

Natalie Hockham

St. John's College

Supervised by Prof. Constantin-C. Coussios

Spatio-Temporal Control of Acoustic Cavitation During High-Intensity Focused Ultrasound Therapy

A thesis submitted for the degree of Doctor of Philosophy

Hilary 2013

Abstract

High-intensity focused ultrasound (HIFU) is rapidly emerging as a viable alternative to conventional therapies in the treatment of deep-seated, solid tumours. In contrast to surgical methods, extracorporeal HIFU transducers non-invasively target pathogenic tissue deep beneath the skin, inducing thermal necrosis of a volume of tissue typically coincident with the ultrasound focus. More recently, cavitation activity has been observed to enhance focal heating, whilst providing a unique opportunity for real-time treatment monitoring. Unfortunately, the stochastic nature of cavitation makes it difficult to initiate and sustain the level of cavitation activity required for enhanced heating, and to confine the spatial extent of cavitation to the focal volume.

The overall aim of this thesis is to design and implement a real-time, closed-loop controller for sustaining thermally relevant cavitation within the HIFU focal region. This is intended to improve the speed and reproducibility of tissue ablation, whilst providing clinicians with real-time feedback as to the extent and location of the ablated region.

A quantitative relationship between the level of cavitation activity and associated temperature rise is first sought experimentally, by investigating cavitation-enhanced heating in two different tissue-mimicking materials (TMM) that yield different levels of cavitation for the same HIFU exposure conditions. It is found that a minimum level of inertial cavitation activity is required for cavitation-enhanced heating to dominate the heating process, which is achieved in the first material but not the second. However, the introduction of exogenous, artificial nuclei to the second material is seen to augment cavitation levels to the extent that cavitation-enhanced heating becomes dominant.

Subsequently, HIFU experimentation is extended to non-perfused, *ex vivo* bovine liver, into which a variety of cavitation nuclei are introduced to augment cavitation levels, and hence heating. Commercially available lipid-shelled microbubbles are contrasted with custom-made sonosensitive nanoparticles for their ability to seed cavitation events, culminating in an empirical relationship between inertial cavitation and heating that is common to both types of exogenous nuclei, and which agrees with the *in vitro* results. Moreover, the abnormally large lesions produced are found to correlate with a broad spatial distribution of inertial cavitation events, as seen on two-dimensional passive acoustic maps.

Based on these encouraging results, a novel negative-feedback, real-time control system is implemented to sustain inertial cavitation within the focal region for extended periods of time. The controller is designed to be both asymmetric and

adaptive, deploying different feedback gains to adjust the peak rarefactional focal pressure (PRFP), depending on whether cavitation activity is above or below the level required for cavitation-enhanced heating. With active cavitation control *in vitro*, the associated focal temperature elevation is maintained at a cytotoxic level for 20 seconds using less than half the energy input required in the absence of cavitation control.

In order to test the applicability of the novel controller to a near-physiological environment, HIFU exposures are eventually performed in a unique normothermic perfused liver model that accounts for both heat advection and nuclei replenishment. Following preliminary experimentation, the controller is modified to account for the inherent variability in the cavitation threshold of perfused tissue, whilst the cavitation demand is also increased to account for heat advection. Following these modifications, use of the controller is found to enable greatly improved reproducibility of HIFU-induced lesions compared to those achieved without cavitation control, with a lesion size that is directly related to the cavitation demand. A cost-effective method for enabling caviation-enhanced, cavitation-controlled and cavitation-monitored HIFU therapy has thus been developed, which enables successful tissue ablation at acoustic energies lower than in current clinical use.

Statement of Originality

I hereby declare that this submission is my own work and, to the best of my knowledge, it contains no materials previously published or written by another person, or substantial proportions of material which have been accepted for the award of any other degree or diploma at the University of Oxford or any other educational institution, except where due acknowledgement is made in the thesis.

Any contribution made to the research by others, with whom I have worked at the University of Oxford or elsewhere, is explicitly acknowledged in the thesis.

I also declare that the intellectual content of this thesis is the product of my own work, except to the extent that assistance from others in the project's design and conception or in style, presentation and linguistic expression is acknowledged.

Natalie Hockham
Hilary 2013

Acknowledgements

The work of this thesis would not have been possible were it not for the support that I have received from the BUBBL group over the last four years. Foremostly, I would like to thank my supervisor, Prof. Constantin-C. Coussios, whose infectious enthusiasm and vast technical expertise have made my post-graduate experience all the more enjoyable. Moreover, he has established and nurtured a research group filled with awesome scientists who also happen to be great friends and I can only hope to find a similar working environment elsewhere.

The *in vitro* portion of the experimental work was carried out with the help of Dr. Manish Arora, whose hands-on approach to teaching eased my transition from undergraduate to research work. Dr. Sarah Wagstaffe spent many an hour demonstrating the sonosensitive nanoparticles fabrication procedure, whilst Dr. Carl Jensen's assistance with implementation of the passive acoustic mapping algorithm was very much appreciated. The perfusion experiments were made possible by clinician Dr. David Holroyd, and I cannot fault the quality of service provided by workshop technicians Mr. Jim Fisk and Mr. David Salisbury.

Finally, although my family has been a huge source of moral support, it has taken a good man, in the form of Dr. Stuart Faragher, to maintain my spirits on a day-to-day basis. I can't thank him enough.

I would also like to gratefully acknowledge the generous support of the UK Engineering Physical Sciences Research Council.

Dissemination

Peer-Reviewed Journal Papers

N. Hockham, C.-C. Coussios, M. Arora, "A Real-Time Controller for Sustaining Thermally Relevant Acoustic Cavitation during Ultrasound Therapy," IEEE Transactions on Ultrasonics, Ferroelectrics and Frequency Control, 2010, 57(12), p.2685-2694

Conference Presentations (presenting author underlined)

N. Hockham, S. Wagstaffe, C.-C. Coussios, "Enhancement of HIFU Ablation by Use of Cavitation-Promoting, Sonosensitive Nanoparticles," 12th International Symposium on Therapeutic Ultrasound, June 2012

N. Hockham, M. Arora, C.-C. Coussios, "Closed-Loop Adaptive Feedback Control of Cavitation during High-Intensity, Focused Ultrasound Therapy," 158th Meeting of the Acoustical Society of America, vol. 126, iss. 4, October 2009

N. Hockham, M. Arora, C.-C. Coussios, "A Real-Time Controller for Sustaining Thermally Relevant Cavitation during HIFU Exposure," 9th International Symposium on Therapeutic Ultrasound, September 2009

Patents

N. Hockham, C.-C. Coussios, M. Arora, R. Roy, "Adaptive and Spatial Control of Acoustic Cavitation," WO/2011/036475

CONTENTS

Contents vii

List of Figures xi

List of Tables xv

Acronyms xvi

1 Introduction 1
- 1.1 Diagnostic Ultrasound . . . 2
- 1.2 Therapeutic Ultrasound . . . 4
- 1.3 Tumour Physiology and Management . . . 8
  - 1.3.1 Vascular Network . . . 9
  - 1.3.2 Physiological Gas Concentrations . . . 11
- 1.4 Thermal Effects and Dosimetry . . . 12
  - 1.4.1 Bioheat Transfer . . . 13
  - 1.4.2 Thermal Ablation . . . 14
  - 1.4.3 Thermal Dose Metrics . . . 15
- 1.5 Treatment Monitoring . . . 17
  - 1.5.1 Magnetic Resonance Imaging . . . 18
  - 1.5.2 Ultrasound Imaging . . . 19
  - 1.5.3 Elastography . . . 21
  - 1.5.4 Photoacoustic Imaging . . . 22
  - 1.5.5 Passive Acoustic Mapping . . . 23
- 1.6 Contributions of the Current Work . . . 24

2 Literature Review 28
- 2.1 Linear Sound Propagation . . . 29
- 2.2 Non-Linear Sound Propagation . . . 30
- 2.3 Cavitation Inception . . . 34

2.3.1 Homogeneous Nucleation . . . 34
2.3.2 Endogenous Nuclei . . . 35
2.3.3 Exogenous Nuclei . . . 36
2.4 Cavitation Dynamics . . . 41
2.4.1 Bubble Resonance . . . 44
2.4.2 Inertial Cavitation Threshold . . . 45
2.4.3 Rectified Diffusion . . . 47
2.4.4 Shape Oscillations . . . 49
2.5 Cavitation Detection and Monitoring . . . 51
2.5.1 Frequency Response of Shelled Microbubbles . . . 54
2.6 Cavitation-Enhanced Heating . . . 55
2.7 Controlling Cavitation . . . 58
2.7.1 Peak Rarefactional Focal Pressure . . . 59
2.7.2 Excitation Frequency . . . 60
2.7.3 Duty Cycle and Pulse Repetition Period . . . 61
2.7.4 Temperature-Dependent Effects . . . 62
2.8 Gap in Knowledge . . . 63

3 Cavitation-Enhanced Heating *In Vitro* 64
3.1 Experimental Setup . . . 65
3.1.1 Tissue-Mimicking Media . . . 66
3.1.2 HIFU Generation . . . 69
3.1.3 Passive Cavitation Detection . . . 70
3.1.4 Temperature Recording . . . 72
3.2 Controlling Software . . . 73
3.3 Data Analysis . . . 74
3.3.1 Quantifying Cavitation Activity . . . 75
3.3.2 Spectral Decomposition of PCD Data . . . 75
3.3.3 Passive Cavitation Localisation . . . 77
3.4 Results and Discussion . . . 78
3.4.1 Cavitation Threshold Measurements . . . 79
3.4.2 Dependence of Cavitation on PRFP . . . 81
3.4.3 Dependence of Cavitation on Nuclei Distribution . . . 85
3.4.4 Correlation of Temperature Elevation with Cavitation . . . 88
3.4.5 Cavitation Enhancement in Polyacrylamide . . . 89
3.5 Summary . . . 95

4 Cavitation-Enhanced Heating *Ex Vivo* 97
4.1 Optimisation of HIFU Insonation Conditions . . . 99

4.1.1 Experimental Setup . . . 99
4.1.2 Data Analysis . . . 102
4.1.3 Results and Discussion . . . 103
4.2 Introducing Exogenous Nuclei . . . 109
4.2.1 Experimental Setup . . . 109
4.2.2 Data Analysis . . . 113
4.2.3 Results and Discussion . . . 114
4.3 Validation using Passive Acoustic Mapping . . . 122
4.3.1 Experimental Setup . . . 122
4.3.2 Controlling Software . . . 125
4.3.3 Data Analysis . . . 126
4.3.4 Results and Discussion . . . 128
4.4 Summary . . . 134

5 Thermally Relevant Cavitation Control *In Vitro* 137
5.1 Basic Control Theory . . . 138
5.2 Experimental Setup . . . 140
5.3 Controlling Software . . . 141
5.4 Data Analysis . . . 141
5.5 Results and Discussion . . . 142
5.5.1 Proof of Concept . . . 142
5.5.2 Controller Design . . . 143
5.5.3 Volumetric Temperature Variation . . . 148
5.6 Summary . . . 152

6 Therapeutically Relevant Cavitation Control in a Perfused Liver Model 155
6.1 Introduction to Perfusion Effects . . . 156
6.1.1 Vascular Supply and Drainage of the Liver . . . 157
6.1.2 Cavitation Nuclei Replenishment . . . 158
6.2 Experimental Setup . . . 159
6.2.1 Liver Procurement . . . 159
6.2.2 Normothermic Perfusion . . . 160
6.2.3 Experimental Protocol . . . 162
6.3 Data Analysis . . . 163
6.4 Results and Discussion . . . 163
6.4.1 Cavitation Threshold Measurements . . . 163
6.4.2 HIFU Sonication in Liver Microvasculature without Cavitation Control . . . 165
6.4.3 Controller Implementation . . . 167

6.4.4 Controller Tuning 170
6.4.5 Effect of Cavitation Control on Lesion Size 176
6.5 Summary 176

7 Conclusions and Future Work **179**
7.1 Conclusions 179
7.2 Future Work 184
7.2.1 Use of Exogenous Nuclei in Perfused Liver 184
7.2.2 Development of a Tumour Model 185
7.2.3 Consideration of Non-Linear Effects 185
7.2.4 Improvements to TEA Beamforming Algorithm 186

References **188**

LIST OF FIGURES

1.1 Illustration of the principles of HIFU 6
1.2 The JC HIFU system, a commercially available HIFU device 7
1.3 The six hallmarks of cancer 8
1.4 Normal vasculature and tumour vasculature 10
1.5 Shear modulus measured at various temperatures in bovine tissue 15
1.6 Theoretically generated temperature profiles demonstrating the concept of CEM 16
1.7 Comparison of passive acoustic mapping and B-mode hyperecho 24

2.1 Illustration of the principles of non-linear sound propagation 31
2.2 Size distribution of SonoVue® 38
2.3 Surface morphology of core-shell nanoparticles 39
2.4 Comparison of stable and inertial bubble oscillations 43
2.5 Bifurcation diagram of bubble behaviour 44
2.6 Inertial cavitation threshold versus inital bubble radius for various frequencies of insonification 47
2.7 Rectified diffusion and inertial cavitation thresholds at 1 MHz for a range of bubble sizes 49
2.8 Rectified diffusion, shape instability and inertial cavitation thresholds . . 50
2.9 Frequency spectra of secondary acoustic emissions 52
2.10 Spectrogram of secondary acoustic emissions 53
2.11 Interaction of ultrasound with shelled microbubbles 54
2.12 Peak focal temperature elevation in a tissue-mimicking phantom for a range of HIFU intensities 56
2.13 Temperature elevation plots from sequential HIFU exposures in agar gel . 57
2.14 Thermal power deposited by bubbles undergoing cavitation 58
2.15 Pressure versus time curve for an idealised ultrasound waveform 59
2.16 HIFU beam profile along the transverse axis of a spherically focused HIFU transducer 60

3.1 Overview of the experimental setup for acquiring cavitation and thermal data . . . 66
3.2 Photographs of agar- and PAA-based tissue-mimicking phantoms . . . 68
3.3 Spherically focused HIFU transducer . . . 70
3.4 Longitudinal and transverse pressure profile sections of a 1.067 MHz spherically focused HIFU transducer . . . 70
3.5 Example of a raw PCD data trace and its frequency spectrum . . . 76
3.6 PCD signal variance versus PRFP for determining cavitation thresholds . 79
3.7 PCD voltage trace demonstrating single bubble inertial collapse in PAA . 81
3.8 Illustration of the variation of cavitation activity and temperature elevation with PRFP in agar and PAA . . . 82
3.9 Summary of the effect of PRFP on maximum temperature elevation in agar and PAA . . . 84
3.10 Passive localisation of ultrasound-induced bubble clouds in agar and PAA at a range of PRFPs . . . 85
3.11 Illustration of the variation of cavitation activity and temperature elevation with repeated HIFU exposures in agar and PAA . . . 86
3.12 Passive localisation of ultrasound-induced bubble clouds in agar and PAA subjected to repeated HIFU sonications . . . 87
3.13 Maximum cavitation-induced temperature elevation in agar as a function of total broadband energy . . . 89
3.14 PCD signal variance versus PRFP for determining the cavitation threshold in talc-infused PAA . . . 91
3.15 Illustration of the variation of cavitation activity and temperature elevation with PRFP in talc-infused PAA . . . 92
3.16 Illustration of the variation of cavitation activity and temperature elevation with repeated HIFU exposures in talc-infused PAA . . . 93
3.17 Maximum cavitation-induced temperature elevation in talc-infused PAA as a function of total broadband energy . . . 94

4.1 Overview of the experimental setup for acquiring cavitation and thermal data during *ex vivo* experimentation . . . 100
4.2 Photographs of liver holder and tissue cutting device . . . 101
4.3 Longitudinal and transverse pressure profile sections of a 0.508 MHz spherically focused HIFU transducer . . . 102
4.4 Photographs of HIFU-induced lesions in bovine liver at a range of frequencies and PRFPs . . . 103
4.5 Cavitation data from HIFU excitation in bovine liver at a range of frequencies and PRFPs . . . 105

4.6 Probability of inertial cavitation occurring both instantaneously and within the first second of HIFU insonation in bovine liver 107
4.7 Illustration of the variation of cavitation activity and temperature elevation with cavitation history in bovine liver 108
4.8 Overview of the experimental setup for acquiring cavitation data during *ex vivo* testing of exogenous nuclei 110
4.9 Size distribution of custom-made sonosensitive nanoparticles 111
4.10 PCD signal variance versus PRFP for determining cavitation thresholds . 115
4.11 Photographs of lesions resulting from 10 s HIFU sonication both in the presence and absence of a foreign nucleation agent 117
4.12 Cavitation data from 10 s HIFU exposures utilising both SonoVue® and sonosensitive nanoparticles as cavitation-promoting agents 118
4.13 Photographs of lesions resulting from 2 s HIFU sonication both in the presence and absence of a foreign nucleation agent 119
4.14 Cavitation data from 2 s HIFU exposures utilising both SonoVue® and sonosensitive nanoparticles as cavitation-promoting agents 120
4.15 Comparison of nucleation agents and their effects on lesion formation . . 121
4.16 Overview of the experimental setup for acquiring cavitation data in two dimensions during *ex vivo* testing of exogenous nuclei 123
4.17 Spherically focused HIFU transducer with rectangular central void 123
4.18 Longitudinal and transverse pressure profile sections of a 1.06 MHz spherically focused HIFU transducer with rectangular central void 124
4.19 Geometry for the implementation of the TEA algorithm 127
4.20 Reconstructed source maps from HIFU exposures in bovine liver in the presence and absence of exogenous cavitation nuclei 130
4.21 Evolution of broadband emissions recorded solely at the focal depth . . . 131
4.22 Comparison of nucleation agents and their effects on lesion formation using the linear array in echo mode 132
4.23 Demonstration of thresholding techniques used for cavitation maps and corresponding lesion photographs 133
4.24 Comparison of lesion widths predicted from thresholded passive acoustic maps and lesion photographs 134

5.1 Schematic representation of a negative-feedback control system 138
5.2 Overview of the experimental setup for acquiring cavitation and thermal data 140
5.3 PCD signal variance and temperature elevation profiles from proof-of-concept controller experiments 143
5.4 Schematic diagram of the first iteration control system design 144

5.5 Implementation of a closed-loop negative-feedback controller 145
5.6 Validation of controller efficacy by comparison with single-PRFP HIFU excitation at 3.38 MPa 146
5.7 Validation of controller efficacy by comparison with single-PRFP HIFU excitation at 4.79 MPa 147
5.8 Pressure amplitude profiles along the transverse and longitudinal axes of the 1.067 MHz HIFU transducer 149
5.9 Spatio-temporal temperature elevation in the transverse plane through the HIFU focus 151
5.10 Spatio-temporal temperature elevation in the longitudinal plane through the HIFU focus 152

6.1 Main anatomical features of liver 157
6.2 Demonstration of cavitation nuclei replenishment in perfused porcine liver 158
6.3 Schematic of the extracorporeal liver perfusion device 160
6.4 Photograph of the extracorporeal liver perfusion device 161
6.5 Overview of the experimental setup for acquiring cavitation data from the perfused liver model 162
6.6 PCD signal variance versus PRFP for each of the four livers experimented upon 164
6.7 Cavitation data from HIFU excitation in perfused liver microvasculature . 166
6.8 Cavitation data from preliminary controller operation 168
6.9 Cavitation data from modified controller operation 169
6.10 Photograph of the liver cross section subsequent to dissection 169
6.11 Repeats of controller experiment in perfused liver 172
6.12 Repeats of controller experiment with modified cavitation reference demand 173
6.13 Validation of controller experiment using constant-PRFP HIFU insonation 174
6.14 Comparison of lesion sizes in the presence and absence of cavitation control 175

LIST OF TABLES

2.1 B/A for various biological tissues 33

3.1 Summary of acoustic properties for various experimental media 68

4.1 Summary of exogenous nuclei used for cavitation enhancement 112

ACRONYMS

HIFU	High-Intensity Focused Ultrasound
BBB	Blood-Brain Barrier
ESWL	Extracorporeal Shock Wave Lithotripsy
IFP	Interstitial Fluid Pressure
H&E	Hematoxylin and Eosin
FDA	Food and Drug Administration
CEM	Cumulative Equivalent-Minutes
MRI	Magnetic Resonance Imaging
MR	Magnetic Resonance
PRF	Proton Resonance Frequency
RF	Radio Frequency
ARFI	Acoustic Radiation Force Impulse
HMI	Harmonic Motion Imaging
PCD	Passive Cavitation Detector
TMM	Tissue-Mimicking Medium
UCA	Ultrasound Contrast Agent
PFC	Perfluorocarbon
LbL	Layer-by-Layer
ADV	Acoustic Droplet Vaporisation
PRFP	Peak Rarefactional Focal Pressure
PRP	Pulse Repetition Period
CW	Continuous Wave
PAA	Polyacrylamide
BSA	Bovine Serum Albumin
DAQ	Data Acquisition
GPIB	General Purpose Interface Bus
FFT	Fast Fourier Transform
ARF	Acoustic Radiation Force
boPET	Biaxially Oriented Polyethylene Terephthalate
PBS	Phosphate Buffered Saline
PDADMAC	Poly(Diallyldimethylammonium Chloride)

IQ	In-phase/Quadrature
PSF	Point Spread Function
TEA	Time Exposure Acoustics
SNR	Signal-to-Noise Ratio
DRB	Dynamic Receive Beamforming
ECLPD	Extracorporeal Liver Perfusion Device
IVC	Inferior Vena Cava
PVDF	Polyvinylidene Fluoride
GPU	Graphics Processing Unit



CHAPTER 1

INTRODUCTION

Cancer is a leading cause of death worldwide, and considerable research effort is presently being directed towards improving treatment options and therapeutic outcomes for a disease that would otherwise yield an estimated 13.1 million deaths in 2030 (Society, 2008). Ultrasound has a major role to play in this capacity, both as a diagnostic tool and as a therapeutic modality. This chapter gives a brief overview of our current understanding of cancer, including its progression, diagnosis and treatment. Clinical applications of ultrasound are discussed, with a particular focus on an emerging therapy involving the use of ultrasound waves focused to a point inside the body, commonly referred to as high-intensity focused ultrasound (HIFU).

Traditionally perceived as a diagnostic modality, ultrasound has undergone something of a rebirth in recent years. Therapeutic bioeffects such as momentum transfer for drug delivery to tumours and blood clots (Mitragotri, 2005; Datta et al., 2006) and mechanical disruption of the blood-brain barrier (BBB) (Meairs and Alonso, 2007) have thrust ultrasound into prominence as a plausible alternative to otherwise invasive procedures in a broad range of clinical applications. In particular, high-intensity focused ultrasound (HIFU), generated by an extracorporeal transducer, has been shown to enable localised energy deposition at depths of up to 20 cm beneath the skin surface by converging high-amplitude, high-frequency pressure waves to a focal region similar in size and shape to a grain of rice (Lynn

et al., 1942). The resulting bioeffects are wide-ranging, depending on the parameters of the ultrasound source and the physical characteristics of the target media (Hill et al., 2004).

At moderate to high acoustic intensities, long-pulse HIFU can be used to thermally ablate deep-seated cancerous tumours without requiring surgical access to the affected region. In contrast to laparoscopic surgery and other minimally-invasive techniques, such as laser ablation and cryoablation (Weber and Lee, 2005), HIFU is the only truly non-invasive alternative to open surgery, thus presenting a number of important advantages: surgical complications such as haemorrhaging from visceral or vascular puncture are avoided, as is perioperative metastatic seeding of the primary tumour when it gains access to the vasculature (Kennedy, 2005).

A major shortcoming of HIFU therapy is the present lack of accurate real-time treatment monitoring, meaning that HIFU treatment times are currently in no way comparable to those of conventional surgery: a 10 cm diameter liver tumour can take in excess of 6 hours to fully ablate (Kennedy, 2005). Concurrent monitoring is especially important given the tendency for pre-focal heating at the insonation conditions typically required for HIFU ablation at the focus. The aim of the present work is, therefore, twofold: to investigate the HIFU parameters required to achieve preferential energy deposition at the focus compared with the pre-focal region and, subsequently, to develop a feedback control system which optimises said parameters during treatment.

1.1 Diagnostic Ultrasound

The use of ultrasound for brain tumour detection can be traced as far back as the 1930s (Dussik, 1942); however, it was not until the late 1940s that ultrasound really

began its ascent to become one of the most widely used diagnostic tools in modern medicine (Ludwig, 1949). Originally used for metal flaw detection (Firestone, 1942), ultrasonography uses the acoustic contrast between features, such as muscles, tendons, internal organs and pathological lesions, to produce tomographic images of the body. Acoustic contrast arises due to differences in density and compressibility, resulting in an incident ultrasound pulse being partly reflected and partly transmitted at the interface between acoustically disparate media, the extent of which depends on their respective acoustic properties. Ludwig was the first to study and document the difference in sound waves as they travelled through animal tissue compared with foreign bodies, namely gallstones (Ludwig, 1949). He used the echo times of the reflected waves and the relative magnitudes of the observed peaks to generate estimates for the speed of sound in adjacent media and the depths at which the corresponding interfaces occurred. Ultrasound imaging conducted in this manner - that is, along a single line extended radially or perpendicularly from the face of a pulse-echo transducer - is commonly referred to as A-mode. By scanning the transducer along either a straight line or an arc, all of the lines can be scan-converted to form a B-mode pulse-echo image where the lines are arranged in their proper geometric orientation, thereby delineating structures in two dimensions (Szabo, 2004).

Of course, ultrasound has progressed over the years and scanners have been adapted to visualise blood flow through arteries and veins (Gill, 1985; Hecher et al., 1995), as well as to produce three-dimensional images of foetuses and breast tissue (Steiner et al., 1994). Notably, there has been a gradual shift in research focus from diagnostic to therapeutic applications of ultrasound, prompted by numerous studies into the destructive effects of diagnostic ultrasound at higher acoustic powers (Barnett et al., 1994, 2000). The field of ultrasound therapeutics seeks to harness

these bioeffects in a controlled manner for a variety of useful applications.

1.2 THERAPEUTIC ULTRASOUND

The global healthcare industry is experiencing a gradual shift towards less invasive curative therapies that not only minimise patient discomfort, but also reduce the considerable costs associated with long patient recovery times. In the context of cancer therapy, this means deviating from the traditional "slash, burn and poison" culture that still dominates this particular field. Ultrasound fits in rather nicely with this mantra due to its non-invasive delivery and, as such, has generated significant interest over a broad spectrum of clinical specialities, be it low-intensity ultrasound used to stimulate tissue and bone repair (Brookes and Dyson, 1985) or focused ultrasound used for cataract treatment by phacoemulsification (Fine et al., 2001).

Acoustic cavitation is an important phenomenon in ultrasonics and is defined as the volumetric oscillation and subsequent collapse of acoustically formed or pre-existing gas- and vapour-filled nuclei under the action of an acoustic stimulus (Leighton, 1994). There exists a vast body of research advocating its controlled use for improved therapeutic outcomes.

Extracorporeal shock wave lithotripsy (ESWL) is one such application, which has dramatically improved the treatment of nephrolithiasis and cholelithiasis. ESWL was pioneered in the 1980s and utilises high-amplitude, focused acoustic shock waves to fragment biliary, and previously renal, stones so that they can be passed safely through the cystic duct and ureters respectively (Lingeman et al., 1986). Stone fragmentation results from a combination of shearing forces and cavitation (Madaan and Joyce, 2007).

Therapeutic ultrasound is also known to enable targeted drug delivery and lo-

calised enhancement of drug activity by the combination of thermal and mechanical effects (Coussios and Roy, 2008). In the treatment of cancer, ultrasound can be used in conjunction with systemically-administered chemotherapy drugs to reduce the dose required for effective cytotoxicity in tumours and, therefore, minimise unwanted side effects in patients (Peterson and Siegel, 1998). Similarly, anticancer agents encapsulated within lipid or polymer spheres can be released under the action of focused ultrasound, enabling highly localised chemotherapeutic activity (Dromi et al., 2007; Mylonopoulou et al., 2010).

Furthermore, pulsed ultrasound has been shown to enhance thrombolysis in the treatment of ischemic stroke. Stroke therapy relies on timely penetration of thrombolytic drugs into the obstructing thrombus, which activate the enzyme plasminogen to clear the fibrin mesh supporting the clot (Datta et al., 2006). Cavitation-induced acoustic streaming and micro-jetting are thought to be largely responsible for the observed enhancement in drug penetration. Interestingly, the reverse effect is possible under different operating conditions: ultrasound has been used to induce haemostasis by non-invasive cauterisation of blood vessels to control internal bleeding (Vaezy et al., 1998).

The present work relates to the use of therapeutic ultrasound for the remote treatment of deep-seated, cancerous tumours (see Figure 1.1). The shearing motion of particles along the path of propagation of a HIFU wave provides a mechanism for the conversion of acoustic energy into heat, commonly referred to as viscous absorption. Moreover, the procedure for focusing ultrasound beams into small, clinically relevant volumes enables rapid, localised heating at the treatment site, whilst leaving tissue in the pre-focal region relatively unscathed (Kennedy, 2005; Kennedy et al., 2004; Wu et al., 2004). Irreversible cell death through coagulative necrosis may ensue, depending on the temperature elevation induced and the exposure duration.

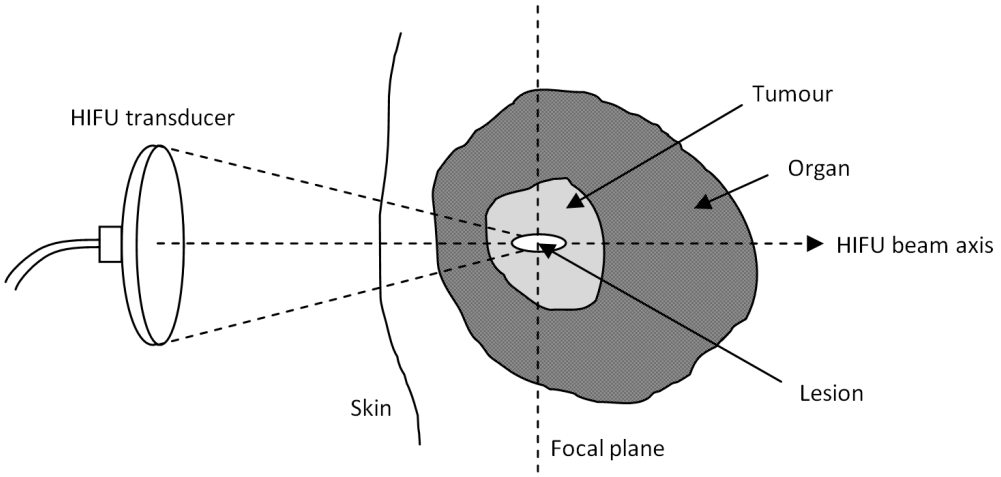


Figure 1.1: Illustration of the principles of HIFU. An extracorporeal HIFU transducer focuses ultrasound waves deep within tissue. Rapid, localised heating raises the temperature at the focus to a cytotoxic level, leading to irreversible cell death by thermal necrosis.

Though still in the development phase, HIFU clinical trials targeting a range of tumour types (kidney, liver, pancreas, prostate) have yielded some encouraging results (Wu et al., 2001a, 2004; Thüroff et al., 2003). This has been made possible by the introduction to market of a range of commercially produced HIFU devices, such as the JC HIFU system developed by the Haifu Technology Company (Chongquing, People's Republic of China) shown in Fig 1.2. This device is currently in use at the Churchill Hospital (Oxford, UK), where clinical trials have shown the technique to be effective in 100% of hepatic and 67% of renal tumour treatments (Illing et al., 2005; Ritchie et al., 2010).

Cavitation-enhanced thermal ablation is a recent extension to this technology. Cavitation has the effect of increasing the amount of energy deposition in the vicinity of a bubble, both by redistributing the incident acoustic radiation to higher frequencies, for which conversion of acoustic energy into heat is more efficient, and by the exertion of mechanical stresses on the molecular structure of the tissue by oscil-



Figure 1.2: The JC HIFU system developed by the Haifu Technology Company (Chongquing, People's Republic of China) and currently in use at the Chuchill Hospital (Oxford, UK). The HIFU transducer, located beneath the hole in the patient's cot, is coupled to the patient using deionised and degassed water, whilst a separate diagnostic ultrasound array is used to track treatment progress (reproduced with permission from company literature).

lating microbubbles (Holt and Roy, 2001; Hynynen, 1991a; Wu and Nyborg, 2006). Moreover, it has been postulated that the secondary acoustic emissions radiated from the focal region of a HIFU transducer may provide a unique opportunity for in-line treatment monitoring and guidance (Coussios et al., 2007a).

Enhanced heating by cavitating microbubbles forms the crux of the work presented in this thesis. Whilst this chapter looks primarily at those concepts and phenomena generic to localised hyperthermia for cancer therapy, the following chapter delves further into the dynamics of cavitating bubbles, including their production, oscillation, detection and opportunities for control.

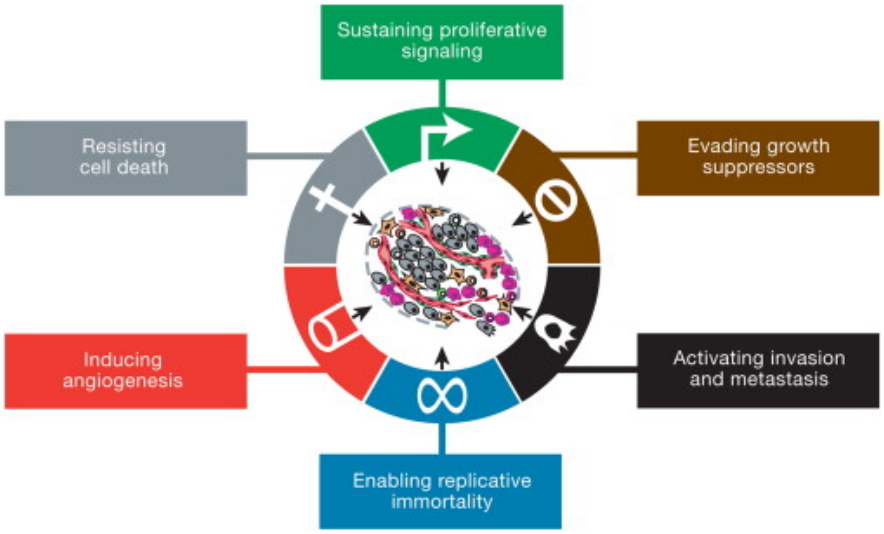


Figure 1.3: The six hallmarks of cancer proposed by Hanahan and Weinberg (Hanahan and Weinberg, 2011). It is believed that most, if not all, cancers acquire the same set of biological capabilities during their development, albeit through various mechanistic strategies.

1.3 Tumour Physiology and Management

Cancer is primarily an environmental disease, characterised by failure of regulation of tissue growth. Malignant cells develop when the genes responsible for growth and differentiation of healthy cells undergo a succession of mutations, resulting in the activation of proto-oncogenes and the deactivation of tumour suppressor genes (Knudson, 1971; Tannock, 2005). Cells thus acquire a range of biological capabilities that collectively describe the so-called "hallmarks of cancer" (see Figure 1.3) (Hanahan and Weinberg, 2011). The net effect is a state of rapid, uncontrolled cell proliferation, which forms an extraneous mass called a tumour. Whereas benign tumours do not invade adjacent tissues or metastasise to remote locations, malignant tumours exhibit both of these traits and can, therefore, become life-threatening. Most cancer deaths are attributable to metastatic disease and so prompt removal of the primary tumour is preferable (Talmadge and Fidler, 2010).

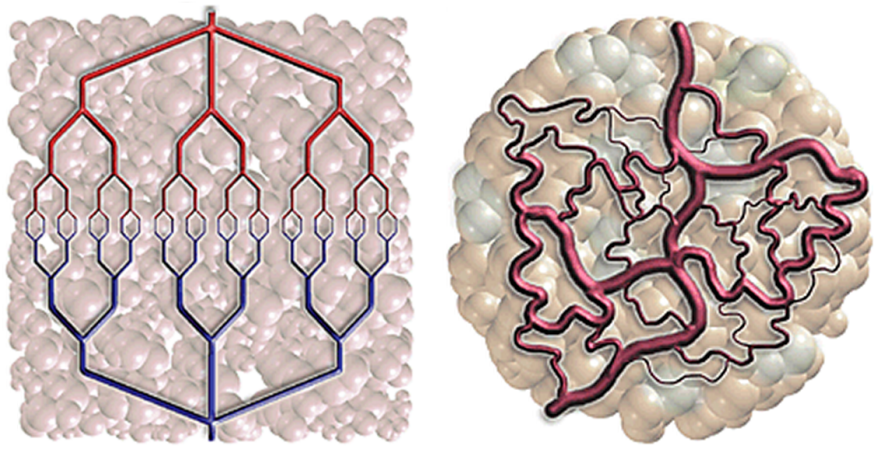
Because cancer is an umbrella term covering a range of conditions, treatment

options often vary from case to case. The end goal of all cancer treatments is, of course, complete removal of the cancer with minimal damage to healthy tissue. Often, this involves the use of potent, systemically administered drugs in combination with ionising radiation to selectively destroy cancer cells; however, the reality is that many healthy cells are targeted in the process (Ragaz et al., 1997; Stadtmauer et al., 2000). Furthermore, it is common to include surgery in intervention schemes, which itself is associated with a number of possible complications (Roth et al., 1994).

In order for HIFU to compete with the better established curative techniques, it needs to illicit confidence in clinicians that the cancer cells can be fully eradicated. This requires not only that the HIFU delivery system is capable of achieving cytotoxic levels of heating but also that a reliable means exists for verifying that the entire tumour volume has been successfully treated. Sections 1.4 and 1.5 consider thermal dosimetry for tumour therapy and the various technologies available for treatment monitoring. To begin with, however, it is instructive to discuss the physiological changes that occur during the progression to malignancy. Of particular interest are changes in vascularity, which determine the extent of drug and dissolved gas delivery to the interstitial space surrounding the cancer cells.

1.3.1 Vascular Network

The growth and metastasis of a solid tumour is dependent on its ability to (i) maintain nutrient and oxygen supply and (ii) evacuate metabolic waste and carbon dioxide. To achieve this, a vascular network is established via a process known as angiogenesis. Often, the emergent network is unable to meet the demands of the growing mass, resulting in regions of neoplastic tissue that are hypoxic, acidotic and exposed to increased interstitial fluid pressure (IFP) (Vaupel et al., 1989). Somewhat paradoxically, this harsh environment offers protection for malignant cells from the



(a) (b)

Figure 1.4: (a) Normal vasculature comprising a highly structured network of mature vessels and (b) abnormal tumour vasculature in which vessels are elongated and arranged in a disorderly manner, with high tortuosity and unusually large diameters (Jain, 2001).

conventional treatment modalities of chemotherapy and radiotherapy, by providing a barrier to efficient drug delivery and reducing radiosensitivity (Thomlinson and Gray, 1955; Dvorak et al., 1991).

Though tumour vasculature shows considerable spatial and temporal heterogeneity, there are several key structural and functional abnormalities that are commonly observed. These abnormalities typically affect the vascular architecture, its density and the structure of the vessel wall itself. Vessels are often elongated and arranged in a disorderly manner, with high tortuosity and unusually large diameters (Cairns et al., 2006), as demonstrated in Figure 1.4. Moreover, the heterogeneous distribution of the vascular network leads to the appearance of avascular areas, with the expansion of the intercapillary space acting to increase diffusion distances.

Vessel walls within a tumour are commonly leaky, or "fenestrated", due to: an incomplete endothelial lining; a lack of pericytes; and/or a compromised basement membrane. Consequently, permeability to osmotic proteins increases, which acts

to elevate the IFP. Reinforced by a lack of lymphatics to drain excess fluid, this elevated IFP often matches, or surpasses, the opposing hydrostatic pressure from within the vessel, thereby limiting the delivery of vascular contents, including cytotoxic drugs, to the interstitial compartment. HIFU fields have been shown to improve the extravasation and distribution of drugs during chemotherapeutic treatment in mice (Bazan-Peregrino et al., 2012); however, the technique is yet to be extended to humans.

1.3.2 Physiological Gas Concentrations

Central to the work of this thesis is the role of cavitation in enhancing HIFU-induced thermal ablation. The efficacy of cavitation-assisted HIFU therapy depends largely on the availability of sources from which bubbles may emerge. Whilst Section 2.3 provides a detailed review of endogenous and exogenous cavitation nuclei, it is important to consider the effects of the tumour microenvironment on the availability of dissolved gases.

In humans, the energy required for daily activity is largely derived from oxidative metabolism of foodstuffs. During this process, oxygen is consumed by cellular mitochondria and carbon dioxide is produced. Replenishment of the oxygen reserve and removal of waste carbon dioxide is achieved by gaseous exchange with the atmosphere via the lungs. These metabolically active gases have highly specialised transport systems, which facilitate the carriage of much higher quantities of gas within blood than could be achieved by dissolution alone. In contrast, inert gases, such as nitrogen, are transported uniquely in the dissolved phase, so that the equilibrium concentration of dissolved gas, c_i, is directly proportional to the gas partial pressure, p_i, as given by Henry's law:

$$p_i = k_H c_i, \tag{1.1}$$

where the constant of proportionality, k_H, is a function of temperature. The dissolved gas concentration within a given tissue is, therefore, dependent on a number of contributing factors, including metabolic state, gas solubility and temperature. In arterial blood, oxygen content may be as high as 20 mL/dL (though only around 2% of this exists in the dissolved phase), whilst venous carbon dioxide levels may reach 50 ml/dL (similarly, only around 5% of this will exist in the dissolved phase). Nitrogen is largely insoluble in blood, with typical concentrations in the region of 1 mL/dL; however, its comparatively high solubility in fat explains its propensity to accumulate in tissues with high fat content (Miller, 1982; Divertie and McMichan, 1984; Riley et al., 1951; Harrop, 1919; Lesser et al., 1960).

In tumours, regions of hypoxic and acidotic tissue are, by definition, deprived of oxygen and rich in carbon dioxide, whilst the metabolically inactive nitrogen reserve remains at its basal concentration (Fukumura and Jain, 2007). As such, though there may be a shift in the availability of metabolically active dissolved gases, inert gas concentrations remain largely unchanged.

1.4 Thermal Effects and Dosimetry

In the USA, the Food and Drug Administration (FDA) presently requires that all clinical HIFU devices be capable of monitoring temperature in real-time, a limitation which is not currently imposed by European regulatory authorities. This section reviews the mechanisms for heat transfer and the various ways in which temperature measurements may be used to compute the delivered thermal dose. Thermal dosimetry is potentially important, not only for determining the effectiveness

of HIFU treatment, but also for warning against the onset of collateral damage to healthy tissue (Rivens et al., 2007).

1.4.1 Bioheat Transfer

In order to predict the bioeffects induced during hyperthermia therapy, it is important to consider not only external sources of heat but also thermal losses experienced due to tissue conduction and blood perfusion. Heat transfer in biological systems may be modelled using Pennes' bioheat transfer equation, adapted to account for different heat sources and sinks (Pennes, 1948). In the case of ultrasound-induced hyperthermia without cavitation:

$$\rho_t C_t \frac{dT_t}{dt} = k_t \nabla^2 T_t - w_b C_b (T_t - T_b) + \dot{Q}_m + \dot{Q}_{ac}, \tag{1.2}$$

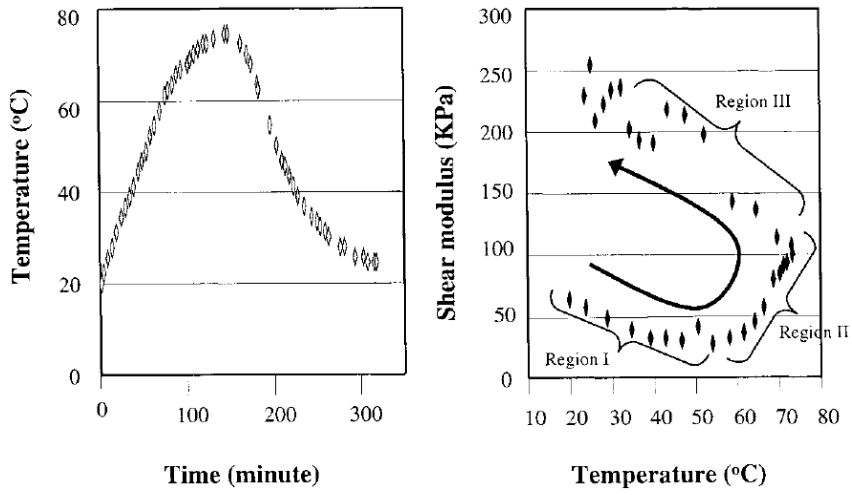
where ρ_t, C_t, T_t and k_t are the density, heat capacity, temperature and thermal conductivity of tissue, w_b, C_b and T_b are the perfusion rate, heat capacity and ambient temperature of blood, $\dot{Q}_m$ is the metabolic heat rate, $\dot{Q}_{ac}$ is the rate of heat deposition by ultrasound, and t is time.

Modelling cavitation-enhanced heating is somewhat more complicated. In particular, two further terms must be appended to Equation 1.2 to account for (i) the power dissipated through viscous heating at the bubble wall and (ii) the power deposited by the absorption of secondary acoustic emissions into the tissue (Coussios and Roy, 2008). These terms are particularly difficult to evaluate as they rely upon precise knowledge of the extent of the radial oscillation of each and every bubble in the field, assuming a range of bubble sizes initially present in the target medium.

1.4.2 Thermal Ablation

Characterising tissue behaviour in response to heat application is notoriously difficult due to the combined effects of increasing temperature and protein coagulation. Proteins are long-chain molecules that play a central role in the human body. Amongst other things, they help to maintain the integrity of cells by providing structure, controlling ion concentrations, and producing a variety of substances essential for cell function. Protein function is dictated largely by protein structure and folding, maintained by strong peptide bonds and comparatively weak hydrogen and hydrophobic bonds. Heat application tends to break the weaker bonds, thereby disrupting the secondary and tertiary structures of the protein molecules in a process known as denaturation (Ellis and Hartl, 1999). Renaturation is sometimes possible; however, prolonged heating is often associated with precipitation or coagulation of the protein, rendering it irreversibly ineffective. Protein coagulation is used synonymously with thermal ablation and manifests as white, opaque regions in exteriorised tissue (Despa et al., 2005).

Wu et al. were able to demonstrate the various thermal regimes experimentally by assessing changes in the shear modulus of *ex vivo* bovine muscle exposed to the heating-cooling curve shown in Figure 1.5 (a) (Wu et al., 2001b). According to Figure 1.5 (b), there exist three distinct regions of protein behaviour. Up to 55 °C, the tissue is seen to soften gradually and return to its native stiffness on cooling, thereby demarcating a region of reversible denaturation. Above 60 °C, stiffness is seen to increase rapidly and irreversibly, and continues in this manner up to the maximum temperature of 75 °C. Protein coagulation and hence cell death is thought to occur in this region. The third and final stage of the hysteretic curve represents cooling back down to room temperature. In this region, the tissue gradually stiffens, reaching a final stiffness much greater than that of its original state.



(a) (b)

Figure 1.5: (a) Heating profile and (b) corresponding variation in shear modulus in *ex vivo* bovine muscle. The arrow depicts the time order of shear modulus change during the heating and cooling processes (Wu et al., 2001b).

These results highlight the importance of considering the thermal history of tissue when predicting the physiological effects induced.

1.4.3 Thermal Dose Metrics

The growing popularity of controlled clinical hyperthermia necessitates a standard method for quantifying the thermal dose in relation to the desired bioeffect. Whereas Kennedy suggests a minimum cytotoxic temperature of 56 °C for at least one second (Kennedy, 2005), cell lysis has been observed at temperatures as low as 41.5 °C (Henle and Dethlefsen, 1980). Determining a threshold value of temperature for thermal necrosis is, therefore, somewhat arbitrary.

Accordingly, Sapareto and Dewey have proposed a model to quantify the thermal dose based on the notion of cumulative equivalent-minutes (CEM). They propose that an exponential relationship exists between temperature and exposure time. More specifically, using 43 °C as an arbitrary reference temperature, a one

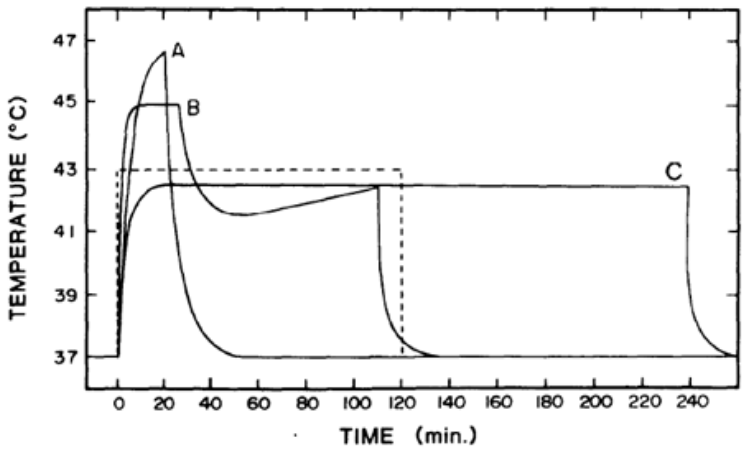


Figure 1.6: Theoretically generated temperature profiles demonstrating the concept of CEM. Profiles A, B and C are all equivalent to 120 minutes at 43 °C (represented by the dashed line). Notably, the areas beneath the curves are not equal (Sapareto and Dewey, 1984).

degree increase in tissue temperature necessitates a twofold decrease in time to achieve the same effect, and a fourfold increase in time for temperatures below 43 °C (Sapareto and Dewey, 1984). This is an Arrhenius-based model derived from first-order reaction kinetics, which is represented mathematically by:

$$CEM_{43} = \int R^{43-T(t)} dt, \tag{1.3}$$

where R is a temperature-dependent parameter approximated as 0.25 below 43 °C and 0.5 above (Sapareto and Dewey, 1984). Figure 1.6 depicts a family of equivalent temperature profiles, with exposure durations ranging from 20 minutes to 240 minutes. A CEM_{43} value of 240 minutes is generally accepted as sufficient to achieve thermal ablation, though the applicability of this measure becomes uncertain at temperatures above 57°C (Borrelli et al., 1990).

The two-state model is an alternative metric of thermal dose (Feng et al., 2008), which is based on assigning each cell to one of two microstates: *viable* (live) and *damaged* (dead). Utilising parameters derived from experimental data, it is possi-

ble to determine the probability of damage of a specific cell type within a given volume based on temperature measurements. This method is less sensitive and more robust than CEM due to its well-behaved model parameters and its adaptability to higher order reaction kinetics. More recently, a three-state model has been proposed, which includes a *vulnerable* state positioned between the *viable* and *damaged* states to account for slow cell death (O'Neil, 1949).

1.5 Treatment Monitoring

Clinical HIFU procedures are typically image-guided to enable the accurate placement of successive lesions and to monitor the overall extent of cell damage both on- and off-target (Vaezy et al., 2001). Due to the unreliability of the CEM_{43} thermal dose formulation at high temperatures, lesion identification is generally preferred over thermometry-based imaging modalities. Unfortunately, this usually requires interlaced operation of the therapy transducer and the diagnostic equipment and, as a result, HIFU treatment times are presently lengthy compared with conventional methods for cancer removal (Illing et al., 2005).

The two most established methods for non-invasively monitoring HIFU-induced thermal lesioning *in situ* are magnetic resonance imaging (MRI) and ultrasound imaging. Both methods utilise changes in the mechanical properties of the insonated medium to either quantify the thermal dose delivered (Rivens et al., 2007) or provide a qualitative assessment of lesion formation, without the danger of ionising radiation. These modalities, and a few sub-modalities, are discussed in detail in the following sections, in addition to a relatively new ultrasound-based monitoring method which utilises cavitation emissions to delineate the treated region.

1.5.1 Magnetic Resonance Imaging

Currently the gold standard for non-invasive HIFU treatment monitoring, MRI exploits the magnetic resonance (MR) of hydrogen nuclei, present primarily in water molecules and organic compounds, to image inside the human body (Hornak, 1996; Hashemi and Bradley, 1997). The technique is renowned for producing superior images with good contrast between different tissue types (Hynynen et al., 2001; Jolesz, 2009). In order to understand some of the shortcomings of this modality, it is instructive to consider briefly the underlying science.

From classical electrodynamics, a spinning charged particle, such as a hydrogen nucleus (i.e. a proton), possesses a magnetic dipole moment with an associated magnetic field that is co-directional with its angular momentum. In the absence of an external magnetic field, the nuclear magnetisations are randomly and evenly aligned, yielding a zero net magnetic field. When a strong magnetic field is applied, the nuclei precess about the field direction (i.e. the dipole magnets align with the field in either a high or low energy state) at the so-called proton resonance frequency (PRF), yielding a non-zero net magnetic field (Hornak, 1996; Hashemi and Bradley, 1997).

Applying an external radio frequency (RF) field at the PRF systematically alters the alignment of magnetisation of hydrogen nuclei in the low energy state by allowing them to absorb energy and precess in phase at the flip angle, thereby decreasing the net magnetisation in the static magnetic field direction. When the RF field is removed, the nuclei gradually return to their equilibrium state and the bulk magnetisation becomes realigned with the static magnetic field. The RF signal generated during this relaxation phase can thence be used to construct the appropriate image. Importantly, the rate of relaxation along the axis of the static magnetic field (T1 or spin-lattice relaxation time) and in the transverse plane (T2 or spin-spin relaxation

time) differs between tissue types (Hornak, 1996; Hashemi and Bradley, 1997).

MRI can be used in various ways to infer information about the treated region. Specialised systems do exist which allow imaging concurrent with the surgical procedure but such systems are based on local temperature measurements, as opposed to lesion identification, and are unreliable. As an example, T1 weighted imaging is said to vary accurately with temperature up to a maximum of 50 °C, making it unsuitable for use alongside ablative therapies (Rivens et al., 2007). T2 weighted images, on the other hand, accurately delineate ablated regions but require that the surgical procedure be temporarily interrupted to allow the tissue to cool down prior to lesion identification (Damianou et al., 2004). Of course, many more MRI-based treatment monitoring techniques exist, from diffusion MRI (Tuch, 2002; Le Bihan, 2003) to MR elastography (Sinkus et al., 2000), each with its own limitations.

Ultimately, a trade-off exists between spatial and temporal resolution: the need for sub-millimetric spatial resolution, as dictated by a typical HIFU focal width of 1 mm, is not readily achievable at the sub-second image acquisition intervals required to prevent overtreatment. Moreover, the inordinate expense of acquiring and running MRI hardware is limiting in itself, making MR-guided HIFU a less appealing alternative to current ultrasound-based practices (ter Haar, 2009).

1.5.2 Ultrasound Imaging

In contrast to MRI, ultrasound is relatively inexpensive, relying on changes in the acoustic properties of tissue with both temperature and lesion formation. A major advantage of using the same diagnostic and therapeutic modality is the common attenuation and distortion parameters along the path of propagation of the acoustic wave (Rivens et al., 2007). However, due to the significant differential in the diagnostic and therapeutic intensities employed, HIFU insonation must be interrupted

periodically to allow imaging to take place without interference from the therapeutic beam.

Active ultrasound imaging methods vary immensely in the types of information they provide to the clinician. In the context of HIFU treatment monitoring, conventional B-mode imaging, introduced previously in Section 1.1, utilises hyperechoes, or "bright-ups", brought about by stabilised boiling bubbles that exist beyond the end of the HIFU pulse for guidance (Fry et al., 1986; Lizzi et al., 1986). The locations of these highly scattering bubbles on an ultrasound image are assumed to coincide with the lesion itself. Inevitably, the technique is only useful when local temperatures exceed that required for boiling, meaning that transient changes in stiffness are not readily detectable. Moreover, boiling bubbles are comparatively large and hence adept at scattering a significant proportion of the incident HIFU beam, thereby shielding the focus and leading to undesirable pre-focal attenuation. The net effect is the formation of tadpole-shaped lesions, weighted towards the ultrasound source (Bailey et al., 2001; Rabkin et al., 2005, 2006).

Echo-shift thermometry attempts to overcome some of these problems by using thermally induced changes in the positions of salient image features to predict the local temperature. These changes arise due to the combined effects of thermal expansion and changes in the compressibility and density of the medium (Bamber and Hill, 1979; Simon et al., 1998; Miller et al., 2004). The apparent echo displacement as seen on a B-mode image can be converted to temperature via a positive linear relationship in which the constant of proportionality is a function of the linear coefficient of thermal expansion of, and the speed of sound in, the medium (Souchon et al., 2005). The technique in its present stage of development does have certain limitations that restrict its usefulness. Foremostly, the relationship between displacement and temperature in non-fatty tissue is only linear up

to 50 °C (Techavipoo et al., 2004), beyond which the speed of sound starts to decrease and echo displacements become indifferentiable. Moreover, at temperatures exceeding 50 °C, the onset of irreversible denaturation means that the thermal history of the tissue becomes important. Temperature dependence varies significantly between tissues, primarily due to variations in lipid content (Nasoni et al., 1979), which makes mapping from displacement to temperature somewhat difficult. Importantly, echo-shift thermometry is not suitable for imaging a cavitating region due to the complex relationship between speed of sound and void fraction in bubbly liquids (McWilliam and Duggins, 1969).

1.5.3 Elastography

Remote palpation by elastography is a relatively new concept in which tissue stiffness is inferred by tracking the displacement of image features during the application of some force. Because different tissue elements have different stiffness parameters, the level of strain experienced when a mechanical compression or vibration is applied is spatially and temporally variant: a stiffer tissue element will generally experience less strain than a softer one. Importantly, in the context of HIFU therapy, due consideration must be given to variations in temperature, and hence speed of sound, when calculating feature displacements.

Elastographic lesion identification is possible using both MRI and ultrasound as the imaging modality. Ultrasound-based elastography has proven successful in the diagnostic assessment of HIFU-induced prostate lesions, comparing favourably with post-therapy MRI and providing much more information than currently afforded by conventional B-mode hyperecho imaging (Souchon et al., 2003). Unfortunately, as with other B-mode monitoring techniques, the requirement for interlaced operation of the therapeutic and diagnostic transducers prevents real-time visuali-

sation of the treated region. Alternatively, MR-based elastography utilises an MR sequence that is phase-locked to the mechanical excitation to spatially map displacements (Sinkus et al., 2000), but suffers from slow acquisition times (on the order of 20-120 s) (Fatemi et al., 2003).

Two promising techniques that enable localised elastography are acoustic radiation force impulse (ARFI) imaging (Bing et al., 2009) and harmonic motion imaging (HMI) (Maleke and Konofagou, 2008). The former technique involves the use of an acoustic square wave for palpation, whilst in the latter case the applied stress is sinusoidal. Moreover, real-time versions of these methods are possible during HIFU therapy if the incident HIFU signal is modulated with the palpation functions.

1.5.4 Photoacoustic Imaging

Photoacoustic imaging relies on the absorption of electromagnetic energy, such as optical or RF waves, by biological tissue to generate acoustic waves, otherwise known as the "photoacoustic effect" (Bell, 1880; Rosencwaig, 1980; Mandelis, 1992). Optical absorption is closely associated with physiological properties, such as hemoglobin concentration and oxygen saturation, which allows for functional as well as structural imaging. In pure optical imaging methodologies, however, optical scattering degrades spatial resolution significantly with depth. Conversely, ultrasound imaging relies principally on changes in mechanical properties, the contrast of which is not always sufficient to detect small changes, as is often the case with early stage tumours (Xu and Wang, 2006). The motivation for photoacoustic imaging is thus to combine the benefits of both modalities and to overcome the aforementioned problems.

The technique has successfully been used to visualise tumours in small animals (Xu and Wang, 2006; Lao et al., 2008), and there are several groups presently inves-

tigating the use of photoacoustic imaging for breast imaging and cancer detection (Kruger et al., 1999, 2000; Fornage et al., 2005). Research into the use of photoacoustic imaging during HIFU treatment is ongoing (Cui and Yang, 2010); however, the requirement for interlaced operation of the therapy and diagnostic ultrasound transducers extends to this hybrid modality.

1.5.5 Passive Acoustic Mapping

A potential solution to the present lack of in-line HIFU monitoring techniques lies in the utilisation of secondary acoustic emissions, generated during HIFU therapy, to infer information about the treatment region. Most work to date in this field makes use of a single-element passive cavitation detector (PCD), aligned confocally with the HIFU transducer. Limitingly, the sensitivity of this setup is restricted to the PCD focal region, and localisation can only really be achieved along the axis of propagation using time-of-flight information(Kennedy et al., 2009).

Recent work has, however, made it possible to map cavitation activity in two, or even three, dimensions by performing cross-correlations between the signals received passively on each of 64 elements of a standard ultrasound array, positioned coaxially with the HIFU transducer (Gyongy and Coussios, 2010; Jensen et al., 2011). This is demonstrated in Figure 1.7, in which a two-dimensional cavitation map, obtained during *ex vivo* experimentation in bovine liver, is contrasted with B-mode hyperecho. The spatial extent of the thermal lesion is accurately represented using cavitation data, whereas B-mode hyperecho is rather less successful.

In addition to enabling multi-dimensional cavitation mapping, the method has the significant advantage of facilitating classification and quantification of cavitation activity in real-time. However, the usefulness of the resultant maps relies on a thorough understanding of the cavitation dynamics and associated bioeffects. Work

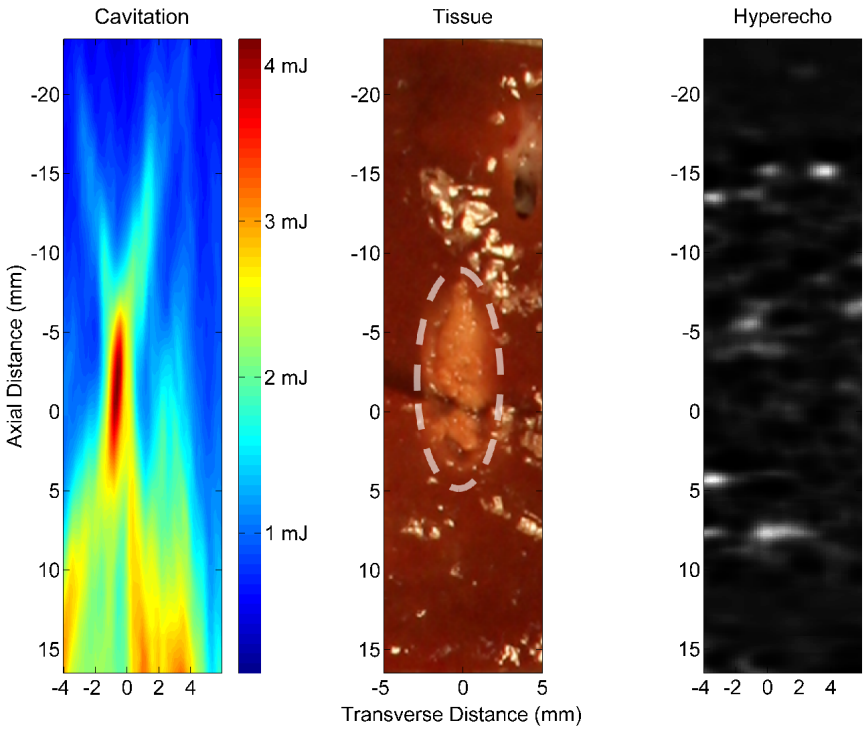


Figure 1.7: Comparison of two-dimensional passive acoustic mapping and B-mode hyperecho with lesion formation in *ex vivo* bovine liver (Jensen et al., 2011), using 1.06 MHz HIFU insonation at 6.3 MPa. The B-mode image was taken immediately after HIFU sonication.

carried out to date in this field is by no means exhaustive and widespread clinical adoption of the technique is therefore unlikely at present. Nevertheless, passive acoustic mapping is an invaluable tool for research into cavitation-enhanced HIFU surgery.

1.6 Contributions of the Current Work

Despite its obvious advantages, the role of HIFU in oncology is presently hindered by (i) lack of specificity and (ii) lack of in-line monitoring techniques. Cavitation-assisted therapies are presently being hailed as potential vectors for widespread HIFU uptake for a variety of reasons. Firstly, cavitation could enable the adoption

of lower acoustic intensities than in current clinical use to achieve the same level of thermal damage. This is an extremely attractive prospect as it suggests more efficient use of the HIFU input energy and, therefore, less collateral damage. Secondly, interpretation of secondary acoustic emissions generated by bubbles occupying the HIFU focal region could provide real-time information regarding treatment progress. This depends not only on safe and reliable cavitation instigation and sustenance but also on there existing an established method for inferring likely bioeffects from cavitation data.

The present work considers the design, implementation and validation of a control system capable of sustaining thermally relevant levels of cavitation using real-time feedback of focal acoustic emissions. Although the primary aim is to demonstrate the heating benefits associated with harnessing cavitation in a controlled manner, the technique could also be used in drug delivery applications, which rely on the mechanical effects of cavitating bubbles.

Having briefly introduced ultrasound as a therapeutic modality, in contrast to its long-established use as a diagnostic tool, and having considered the various facets of hyperthermia in the context of cancer treatment, the following chapter delves deeper into the scientific principles underlying HIFU therapy. This includes the physical mechanisms responsible for viscous absorption and their dependence on the local environment. Acoustic cavitation is explored in more detail, from inception to detection, and its role in ablative therapy explicated. Finally, the dependence of heating and cavitation on each other and on the HIFU insonation parameters are considered, forming the basis of many of the choices made in subsequent chapters.

Thereafter, Chapter 3 considers the effects of HIFU parameters and cavitation history on heating rates in two tissue-mimicking "phantoms" that respond very differently to HIFU sonication. Cavitation-enhanced heating is thus verified *in vitro*

and an empirical relationship between cavitation activity and temperature elevation established. The capacity for exogenous cavitation nuclei to enhance heating rates is also explored, culminating in modified phantom compositions that respond similarly to HIFU insonation.

In Chapter 4, the *in vitro* work from the previous chapter is extended to non-perfused *ex vivo* bovine liver. In the absence of endogenous nuclei, the use of stabilised microbubbles and novel sonosensitive nanoparticles to instigate cavitation activity is examined, and an empirical relationship between cavitation and lesion formation deduced. Bubble activity is monitored in one and, subsequently, two dimensions to investigate what exactly is responsible for the significant lesion sizes observed.

Chapter 5 reverts back to the *in vitro* experimental setup to demonstrate the notion of cavitation control and its associated benefits in a reliable and reproducible tissue model. A closed-loop, negative-feedback controller is implemented to demonstrate how the energy from cavitating bubbles may be harnessed in a controlled manner to deliver consistently superior thermal effects. The temperature elevation is recorded not only at the focus, but also at specific locations adjacent to the focus to investigate the volumetric extent of heating and to rule out the presence of the thermocouple as being wholly responsible for the observed thermal effects.

Finally, the relationship between cavitation and lesioning identified in Chapter 4 and the controller design from Chapter 5 are brought together in Chapter 6 to effect control over cavitation in a perfused *ex vivo* porcine liver. Thermally relevant levels of cavitation are sustained for up to 25 seconds, forming a robust control system capable of achieving ablative levels of heating at lower acoustic intensities than in the absence of cavitation control.

On the basis of these results, Chapter 7 summarises the key findings of this thesis, exploring potential applications for the control system and areas for improvement.



CHAPTER 2

LITERATURE REVIEW

HIFU has the capacity to induce a variety of highly localised bioeffects in a wide range of biomedical applications. In many cases, concurrent acoustic cavitation has been shown to positively reinforce these bioeffects without requiring additional energy input. This chapter considers the physics of ultrasound, from low-amplitude linear sound propagation to non-linear effects induced at higher driving amplitudes. Nucleation strategies are discussed, including the use of exogenous nuclei to encourage cavitation inception, followed by a summary of bubble behaviours and how they derive from the HIFU insonation conditions. Finally, the concept of remote cavitation detection and identification is introduced and its role in cavitation-enhanced thermal ablation examined.

Ultrasound is rapidly emerging as a promising tool for non-invasive therapy and drug delivery, with a wide range of useful bioeffects documented since its initial rise to prominence as a diagnostic modality. Key to the versatility of ultrasound is the acute sensitivity of cells and tissues to subtle changes in the incident ultrasound field. Although simple pressure perturbations are themselves capable of inducing small changes to the cells and tissues along the ultrasound propagation path, it is often the secondary effects of these pressure perturbations which yield the desired bioeffects. In order to understand these effects and to identify critical treatment parameters, it is instructive to first consider the physics of ultrasound.

2.1 Linear Sound Propagation

Sound is a waveform that occurs in elastic media and consists of longitudinal density fluctuations propagating away from a sound source (Leighton, 1994). The generation, transmission and eventual detection of sound relies on the effective transfer of mechanical energy between adjacent particles, which is largely dependent on the elastic and inertial properties of the medium through which sound travels. The term "ultrasound" refers specifically to sound waves at frequencies exceeding the upper limit of human hearing (20 kHz) and, for HIFU, frequencies in the range 0.8-3.5 MHz are typically employed.

In the case of small pressure perturbations of the propagating medium, the nonlinear terms in the equation of continuity, the momentum conservation equation and the equation of state can be ignored, yielding a linearised equation for evaluating the spatio-temporal variation of the pressure field:

$$\frac{\partial^2 p(\mathbf{r},t)}{\partial t^2} = c^2 \nabla^2 p(\mathbf{r},t), \tag{2.1}$$

where p is the pressure fluctuation about the ambient condition, $\mathbf{r}$ is the spatial coordinate, t is the time and c is the phase speed of the wave (Pierce, 1981). By the principle of linear superposition, waves propagating in different directions interfere, giving a spherically focused HIFU transducer its characteristic acoustic field in which the majority of the incident energy is concentrated within an ellipsoidal volume at the HIFU focus.

Realistically, waves propagating through a medium will experience losses, a phenomenon broadly termed "attenuation" (ter Haar, 1995). In a purely visco-thermal medium, attenuation consists solely of *absorption* effects and exhibits quadratic frequency dependence (Hill et al., 2004). Absorption is an umbrella term used to describe the conversion of mechanical energy to thermal energy due to thermal con-

ductivity, viscous effects and molecular relaxation. In tissue, however, *scattering* effects due to inhomogeneities present along the propagation path massively attenuate the incident ultrasound wave, resulting in a frequency relation that is uniquely quasi-linear (Duck, 1990). This is represented mathematically using a power law model:

$$\alpha(f) = \alpha_0 + \alpha_1 f^b, \tag{2.2}$$

where α is the attenuation coefficient, f is the wave frequency, and α_0, α_1 and b are tissue-dependent parameters. Thus, higher frequencies are more readily attenuated than lower ones. This has important implications for the design of therapeutic ultrasound regimens: usually, a compromise is made between treatment depth and the desired rate of energy deposition in an attempt to minimise pre-focal attenuation (ter Haar and Coussios, 2007). This trade-off is considered to be the bane of modern ultrasonics and provides a strong case for research on cavitation aimed at improving energy localisation. This is where cavitation comes in.

2.2 Non-Linear Sound Propagation

In the case of large excitation amplitudes, the local speed of oscillation, u, of individual particles along the propagation path ceases to be small compared to the bulk speed, c. Thus, the zero approximation of non-linear terms in the linear plane wave equation ceases to be valid and the wave deviates from the classical longitudinal case. In particular, waves tend to migrate faster in regions of positive local velocity (compression) and slower in regions of negative particle velocity (rarefaction).

This phenomenon is reinforced by increased bulk modulus and stiffness during phases of compression, leading to increased particle velocity, and the converse effect in regions of rarefaction. The net effect is the gradual distortion of an ini-

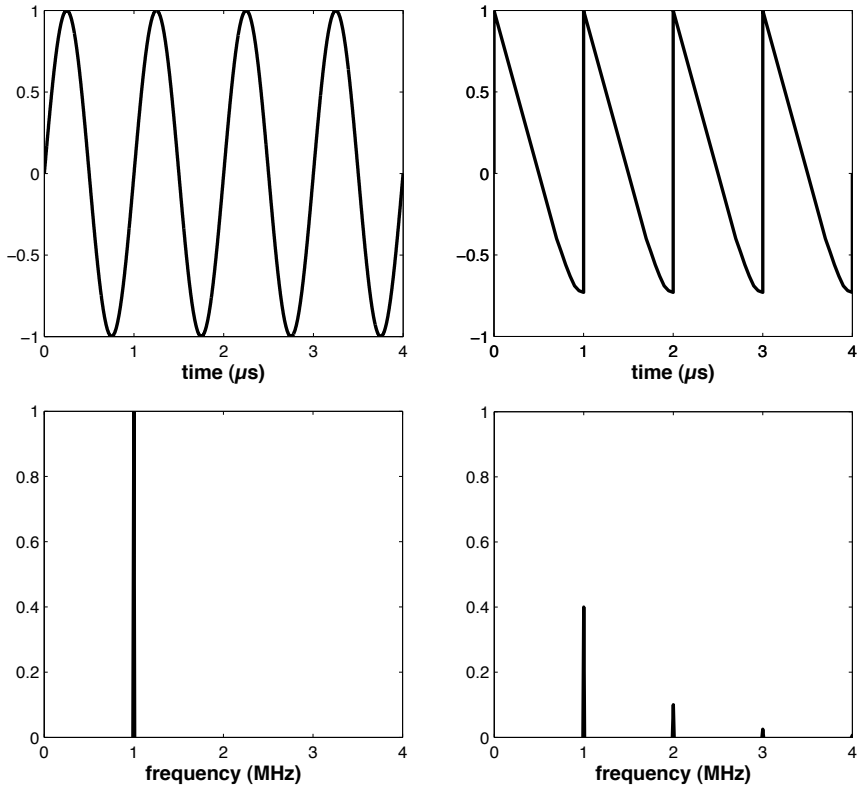


Figure 2.1: Graphical representation of an initially sinusoidal pressure wave before (left) and after (right) shockwave formation due to non-linear sound propagation. The presence of higher harmonics in the latter encourages viscous absorption, leading to enhanced heating along the ultrasound propagation path.

tially sinusoidal pressure wave towards a sawtooth shape and, therefore, magnification of higher harmonic terms in the Fourier domain (Hamilton and Blackstock, 1998; Leighton, 1994), as illustrated in Figure 2.1. Moreover, diffractive effects cause phase shifts in these frequency components and disturb the symmetry of the distorted waveform about the zero line.

The power-law attenuation model dictates that this non-linear behaviour should lead to a net increase in viscous absorption. The propagation distance required for a shockwave to develop is dependent on the source parameters, as well

as the physical properties of the medium itself. For a plane wave:

$$\overline{x}_s = \frac{\rho_0 c^3}{\beta \omega p_0}, \tag{2.3}$$

where $\overline{x}_s$ is the shock formation distance, ρ_0 is the ambient density, β is the coefficient of non-linearity, ω is the angular frequency of the wave source and p_0 is the wave amplitude. The coefficient of non-linearity is a material property that indicates the extent to which a linear wave becomes distorted. It is computed as a function of the coefficients of the first and second order terms, A and B respectively, of the Taylor series expansion of the equation of state $p = p(\rho, s)$:

$$\beta = 1 + \frac{B}{2A}. \tag{2.4}$$

Tissue-mimicking media (TMM) typically have lower coefficients of non-linearity compared with biological tissues (Duck, 1990), as shown in Table 2.1. In a clinical setting, the non-linear properties of biological tissues, specifically those with high lipid content, are an important consideration. Whereas in the context of diagnostic ultrasound, non-linear wave propagation can improve lateral resolution and hence image quality, from a HIFU standpoint, non-linearity can enhance heating both at the HIFU focus and along the path of HIFU propagation. Of course, increased pre-focal attenuation induced by higher frequency spectral components could potentially compromise patient safety.

It is instructive at this point to consider another type of non-linear behaviour observed *in vivo*, which also has the effect of increasing absorption of the incident wave energy. Cavitation is a term that was briefly introduced in Section 1.2 and is expanded upon in the following sections.

Substance	B/A	Reference
Distilled water (20 °C)	5.0	Beyer, 1974
Distilled water (30 °C)	5.2	Beyer, 1974
Distilled water (40 °C)	5.4	Beyer, 1974
Bovine serum albumin (20 g / 100 cm^3, 25 °C)	6.23 (±0.25)	Zhu et al., 1983
Haemoglobin (50%, 30 °C)	7.6	Dunn et al., 1981
Whole porcine blood (12% haemoglobin, 7% plasma proteins, 30 °C)	6.2 (±0.25)	Dunn et al., 1981
Bovine liver (whole, 30 °C)	6.88	Law et al., 1983
Porcine liver (25 °C)	6.7 (±1.5)	Bjorno and Lewin, 1986
Human liver (normal, 30 °C)	7.6 (±0.8)	Cobb, 1983
Porcine fat	10.9	Law et al., 1985

Table 2.1: B/A for distilled water and various biological tissues obtained from both finite amplitude and thermodynamic methods. All values are for atmospheric pressure (Beyer, 1974; Zhu et al., 1983; Dunn et al., 1981; Law et al., 1983; Bjorno and Lewin, 1986; Cobb, 1983; Law et al., 1985).

2.3 Cavitation Inception

Acoustic cavitation is loosely defined as the volumetric oscillation and subsequent collapse of acoustically formed or pre-existing gas- and vapour-filled nuclei, specifically under the action of an acoustic stimulus. The phenomenon is unique to viscous and visco-elastic media and has been heralded as a potential solution to many of the current limitations hindering HIFU therapy, discussed previously in Sections 1.5 and 2.1.

Different HIFU applications exploit different cavitation-induced physical phenomena, be it viscous heating, fluid jetting or streaming in the vicinity of microbubbles. There exist numerous factors governing the type, magnitude, duration and spatial distribution of cavitation events recorded during HIFU therapy. These include: the ultrasound excitation parameters; the size and availability of nucleation sites; the physiological environment; and, crucially, the intricate interaction of all of these. Moreover, with the exception of the ultrasound parameters, these factors can vary significantly between subjects, tissue types and even within the same tissue, creating a non-deterministic problem with multiple outcomes.

This section delves further into the intricacies of cavitation inception and sustenance, with a particular focus on cavitation-assisted thermal ablation for the treatment of deep-seated solid tumours.

2.3.1 Homogeneous Nucleation

Nucleation is the emergence of a distinct thermodynamic phase in a bulk material of contrasting phase (Abraham and Zettlemoyer, 1974). There is a long list of techniques used to induce nucleation, including by neutron radiation (Seitz, 1958) and by laser (Oxtoby, 2002); however, only ultrasound induced nucleation in bulk liquids

is considered in any detail here.

In HIFU systems devoid of pre-existing bubbles, "homogeneous" nucleation is prevalent, wherein stochastically generated cavities are expanded and stabilised by the incident ultrasound field to produce cavitation nuclei. In doing this, it is necessary to first overcome the sizeable intermolecular forces that tend to hold molecules together and prevent the formation of interstitial cavities (Brennen, 1995). In a pure liquid, the net energy, W, required to overcome surface tension and displace the liquid outward to form a spherical bubble is:

$$W = 4\pi R^2\sigma - \frac{4}{3}\pi R^3\Delta p = \frac{4}{3}\pi R^2\sigma = \frac{16\pi\sigma^3}{3(\Delta p)^2}, \tag{2.5}$$

where R is the eventual radius of the bubble, σ is the liquid surface tension and Δp is the threshold static negative pressure required to form the bubble. Bubble formation, therefore, is dependent on the probability that the thermal motions of the molecules would lead to a local energy perturbation of magnitude W. In a physiological environment, stochastically generated cavities are usually on the order of angstroms (Brennen, 1995), which would require pressures in the region of 10 MPa to achieve homogeneous nucleation. Moreover, the application of a dynamic pressure, as opposed to a static one, would necessitate even higher pressures for nucleation to occur over short timescales. To apply an external stimulus of such magnitude would be to encourage uncontrollable bubble behaviour and widespread tissue damage.

2.3.2 Endogenous Nuclei

In practice, cavitation has been observed at considerably lower pressures both *in vitro* and *in vivo*, indicating the pre-existence of cavitation nuclei (ter Haar and Daniels, 1981; Atchley and Prosperetti, 1989; Holland et al., 1996). Free-floating bubbles containing vapour and/or gas are uncommon in clean liquids due to the

combination of buoyancy effects and high dissolution rates, even in liquids supersaturated with dissolved gas (Plesset and Sadhal, 1982; Arora et al., 2007). Instead, nucleation sites are usually tiny crevices of vapour and/or undissolved gas stabilised by attachment to a contacting surface, be it a small solid particle or an endogenous structure, which grow and become detached (Harvey et al., 1944; Apfel, 1970; Crum, 1982). The distribution of these nucleation sites is, of course, dependent on the local density, perfusion and dissolved gas concentration, all of which vary to some extent between subjects and tissues, and with disease progression (Brown and Giaccia, 1998). As such, endogenous nuclei are not always readily available for cavitation instigation, which is obviously problematic when the anticipated bioeffect is cavitation-dependent. Moreover, cavitation has been largely avoided *in vivo* because spatial variations in cavitation thresholds make the likelihood, position and extent of tissue damage unpredictable (Tran et al., 2003).

2.3.3 Exogenous Nuclei

Cavitation onset depends heavily on pre-existing gas bodies to weaken tissue, much like inhomogeneities reduce material strength; however, few such nuclei are present in living tissue. Consequently, systemic administration of artificial cavitation nuclei has been explored as a potential facilitator for cavitation instigation and subsequent control.

Artificial cavitation nuclei employed in biomedical applications can take the form of stabilised microbubbles (Miller and Thomas, 1995; Tran et al., 2003), initially developed for use in specialised imaging modes, surface-modified sonosensitive particles (Wagstaffe et al., 2011) or phase-shift emulsions (Rapoport et al., 2009; Zhang et al., 2011). Of course, clinical optimisation of any one of these systems is challenging because performance indicators such as persistence, biocompatibil-

ity and acoustic response are not usually co-optimal. The following sections summarise the three major classes of synthetic nuclei in finer detail.

2.3.3.1 Ultrasound Contrast Agents

Commercially available ultrasound contrast agents (UCA) are gas-filled microbubbles stabilised against dissolution by either a protein or lipid shell, which can be administered intravenously to the systemic circulation (Lindner, 2004). The encapsulating shell provides a physical resistance to gas leaving the core and reduces the surface tension at the shell-liquid and shell-gas interfaces (Epstein and Plesset, 1950; Borden and Longo, 2002).

Protein-shelled microbubble contrast agents tend to be structurally rigid and, therefore, less stable to ultrasound (Dayton et al., 1999; Weissleder et al., 2010). When subjected to HIFU excitation amplitudes above some threshold value, the shell ruptures and the gas core is released into the tissue matrix, thereby providing a localised source of cavitation nuclei.

The acoustic response of lipid-shelled microbubbles is somewhat different, in that the microbubble itself may be volumetrically excited by the incident HIFU field prior to shell rupture (Ferrara et al., 2007). Crucially, lipids tend to self-assemble into monolayer coatings at a gas-liquid interface, giving lipid-shelled microbubbles their characteristic surface elasticity (Borden and Longo, 2002). This is advantageous not only in imaging applications that specifically harness the non-linear radial response of compliant microbubbles to generate sharper images (de Jong et al., 2000), but also in some therapeutic applications where targeting ligands are conjugated to lipidic particles to achieve microbubble accumulation at diseased sites (Mulder et al., 2006). Moreover, the hydrophilic nature of the lipid "head" group, such as phosphate in the case of a phospholipid, means that lipid-shelled microbubble contrast

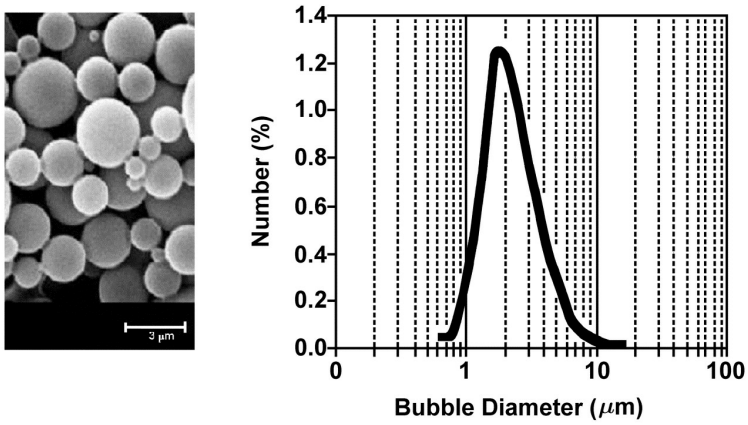
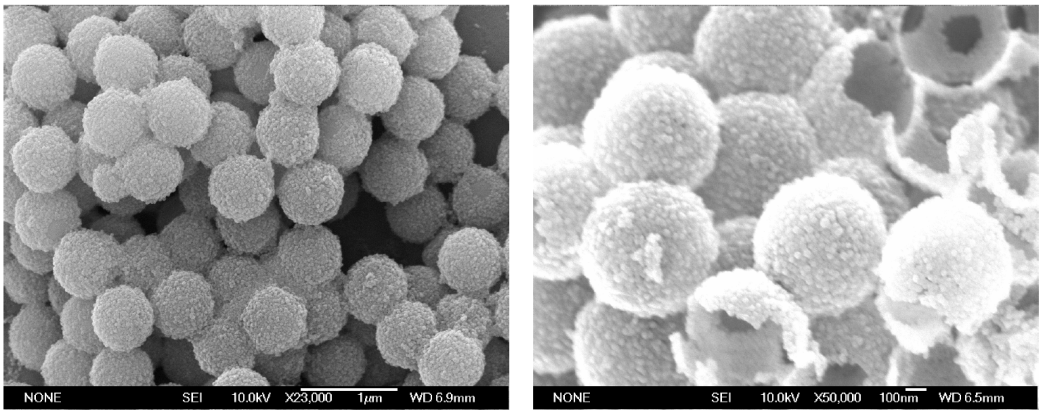


Figure 2.2: (a) Scanning electron microscopy of a SonoVue® microbubble suspension and (b) typical size distribution of a SonoVue® suspension (Stolz and Kaps, 2005).

agents are taken up by the immune system with relative ease, but this is at the expense of reduced microbubble residence time in circulation.

Gas core composition is of equal importance in the design of UCAs. In contrast to first-generation rigid-shelled and air-filled UCAs, modern microbubble contrast agents have evolved to include gases other than air, most commonly perfluorocarbons (PFC). These heavier gases have lower solubilities and diffusivities in water, thereby improving their stability and persistence in the bloodstream without affecting their acoustic response (Kabalnov et al., 1998).

Definity®, Optison® and SonoVue® are all commercially available UCAs, which have been tested for their ability to enhance cavitation activity (Datta et al., 2008; Tran et al., 2003; Luo et al., 2007) with varying amounts of success. Of particular interest here is SonoVue®, a phospholipid-shelled, sulphur hexafluoride-filled contrast agent (see Figure 2.2), which was used as a nucleation agent for the work presented in Chapter 4. Whereas the acoustic properties of UCAs are purposive in monitoring their accumulation at the desired location, their use in cancer therapy is hindered by their size (usually 1-10 μm in diameter), which inhibits extravasation



(a) (b)

Figure 2.3: Scanning electron micrographs showing the surface morphology of (a) core-shell nanoparticles comprising a 600 nm polystyrene core with a surface deposition of Ludox®, and (b) hollow nanoparticles in which the core has been removed by calcination, both of which are prepared by layer-by-layer polyelectrolyte assembly (Wagstaffe et al., 2011).

into cancer tumours (Rifai et al., 2010) and, therefore, limits their use to tumours in close proximity to large blood vessels. This has motivated research into the use of smaller particle types for cavitation instigation.

2.3.3.2 Sonosensitive Nanoparticles

The use of sonosensitive core-shell nanoparticles as cavitation promoters is a relatively new concept that derives from the "crevice model" (Atchley and Prosperetti, 1989), but is yet to be extended to *in vivo* experimentation due to concerns over immunogenicity. The nanoparticles are designed to have specific physical properties, including high hydrophobicity and surface roughness, which allow them to harbour large numbers of surface crevices containing vapour and/or undissolved gas when resuspended in water (see Figure 2.3 (a)). Details of their preparation by layer-by-layer (LbL) polyelectrolyte assembly are provided in Section 4.2.1.1.

Corrugated polystyrene nanoparticles have previously been shown to significantly reduce cavitation thresholds *in vitro* under clinically relevant ultrasound

conditions (Borkent et al., 2007; Rifai et al., 2010; Wagstaffe et al., 2011). These thresholds depend not only on the bulk material properties but also on nanoparticle attributes such as size, wettability and geometry (Borkent et al., 2007), all of which can be precisely tuned by adjusting the synthesis conditions. Importantly, the sub-micron dimensions of sonosensitive nanoparticles makes them ideal for use in the tortuous capillaries of a typical tumour vasculature. Meanwhile, second-generation hollow nanoparticles formed upon calcination of the solid core (Caruso et al., 1998) may additionally provide sufficient contrast to enable localisation using B-mode ultrasound imaging (see Figure 2.3 (b)).

Gold nanoparticles have also been investigated for their potential to instigate cavitation by laser stimulation. This involves the systemic administration of non-reactive gold particles, which cause transient vapour cavities to develop in their vicinity when subjected to moderate laser pulse intensities. These cavities are simultaneously exposed to HIFU, enabling cavitation inception at lower pressures (Farny et al., 2005). The technique is in the early stages of development, but the added complexity of using both laser and ultrasound is likely to hinder its clinical applicability.

2.3.3.3 Nanoemulsions

Acoustic droplet vaporisation (ADV) is an emerging technique for converting biocompatible nanoemulsions into microbubbles, using HIFU to induce the necessary phase transitions (Zhang and Porter, 2010; Zhang et al., 2011). The nanoemulsion usually comprises albumin-coated PFC droplets, which, when insonified with pressure amplitudes exceeding a threshold value, yield gas bubbles approximately five to six times larger in diameter (Kripfgans et al., 2005). Many PFCs are biocompatible and most are associated with relatively low boiling points and enthalpies of vapor-

isation (both of which increase with the number of carbon atoms), making them ideal for this particular application.

ADV-nucleated microbubbles are stable for several minutes or longer and may be volumetrically excited by further HIFU insonation. Despite ADV-assisted HIFU therapy requiring shorter treatment times and lower total acoustic powers, the exact mechanism by which these improvements are made possible is unclear. Viscous damping of non-inertially cavitating microbubbles and/or an increase in the acoustic path length due to scattering have been suggested as plausible explanations. Sizeable vapour pressures may, however, suppress inertial cavitation, which is disappointing given the tremendous thermal advantage proffered by collapsing microbubbles.

Whatever the mechanism for nucleation, the resulting bubbles have common characteristics that govern their response to subsequent HIFU sonication. These are discussed in the following section.

2.4 Cavitation Dynamics

Once nucleated, the behaviour of a bubble subjected to an acoustic stimulus is a complex process involving manifold interactions with other bubbles and the local microenvironment, which serve to constrain expansion and disrupt symmetry. In the interest of simplicity, however, the cavitation dynamics of a single free bubble undergoing radial oscillations in an infinite medium are considered here. Conveniently, these free bubble models may also be applied to compliant lipid-shelled agents for driving pressures up to several hundred kilopascals (Morgan et al., 2000).

The Rayleigh-Plesset equation, derived by applying Newton's Second Law of Motion to a spherical bubble, describes the radial response of the bubble to a time-

varying pressure field, p_{ac}, in an incompressible viscous liquid:

$$R\ddot{R} = -\frac{3}{2}\dot{R}^2 + \frac{p_g + p_v - p_\infty - p_{ac}}{\rho_L} - \frac{2\sigma}{\rho_L R} - \frac{4\nu_L \dot{R}}{R}, \tag{2.6}$$

where R is the bubble radius, p_g and p_v are the bubble gas and vapour pressures respectively, p_∞ is the ambient pressure, ν_L is the kinematic viscosity of the liquid, ρ_L is the liquid density and the dot notation is used to denote differentiation with respect to time (Plesset and Prosperetti, 1977). In the event of large-amplitude bubble oscillations, the Rayleigh-Plesset equation must be modified to include compressibility terms; however, it is used here to elucidate the discerning characteristics of different types of cavitation.

When the three rightmost *pressure* terms of Equation 2.6 are dominant, the bubble is said to be undergoing "stable" cavitation. Stable cavitation is the linear or non-linear pulsation of a bubble subject to acoustic stress about its equilibrium radius: when the instantaneous pressure of the surrounding medium exceeds the internal pressure, the bubble contracts; when the reverse is true, it expands.

At higher acoustic amplitudes, the foremost *inertial* term on the right-hand side of Equation 2.6 dominates over the other terms and the bubble enters the "inertial" cavitation regime. Inertial cavitation is a term used to describe the explosive growth of a cavity followed by its violent collapse, driven by the inertia of the inrushing fluid during the compression phase (Coussios et al., 2007a). This collapse, though brief, is characterised by intense pressures and temperatures within the bubble, which drive its subsequent expansion. The extremes of both stable and inertial cavitation regimes are illustrated in Figure 2.4.

Different HIFU applications exploit different cavitation-induced physical phenomena: microstreaming by bubbles undergoing stable cavitation and sonoporation by inertially cavitating bubbles are pertinent examples. Thus, it is often desir-

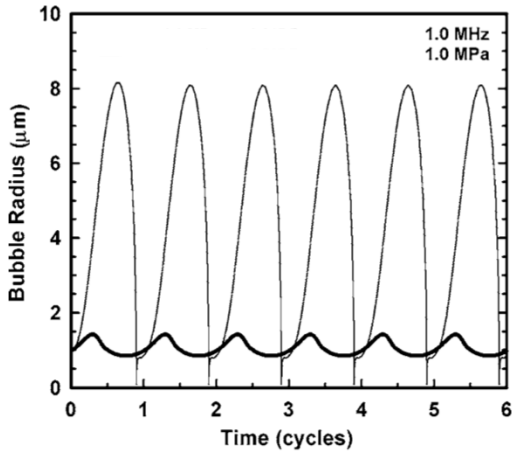


Figure 2.4: Comparison of radial responses of microbubbles undergoing stable (thick line) and inertial (thin line) cavitation (Yang and Church, 2005). Note that radial oscillations of bubbles undergoing stable cavitation are not necessarily sinusoidal.

able to control which type of cavitation is induced. Despite the distinctness implied by their formal definitions, it should be noted that the transition between stable and inertial cavitation is, in fact, a gradual one, as depicted in Figure 2.5. The bifurcation diagram pertains specifically to bubbles smaller than resonance size, for which the initial radius is assumed fixed, and subjected to a constant excitation frequency. Consideration of the transitions that take place with increasing pressure amplitude is crucial to understanding the acoustic signatures of bubbles in a pressure field.

At low pressure amplitudes, a bubble will pulsate linearly, the bubble wall oscillating in phase with the exciting field. Increase the pressure and the amplitude of oscillation is no longer symmetric about the equilibrium radius, a type of nonlinear behaviour which results in the generation of harmonic terms. The bifurcation zone follows in which pulsations transition from periodic to non-periodic by means of a series of period-multiplyling bifurcations. Higher still and the stochastic zone is reached, characterised by chaotic pulsations and the disappearance of the periodic structure altogether in favour of a continuum in the frequency domain

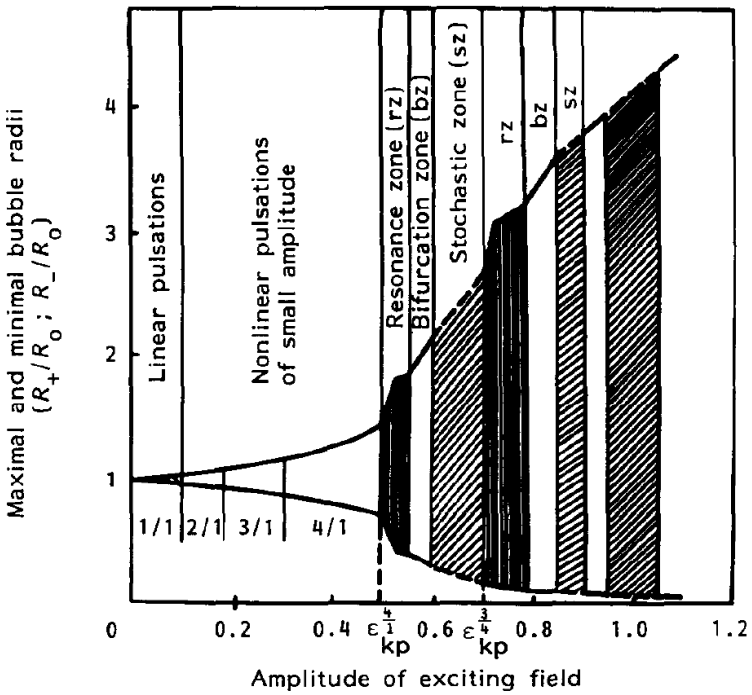


Figure 2.5: Maximal and minimal bubble radii and regimes of oscillation for a bubble excited at a quarter of its resonant frequency (R_0 = 20 μm, f = 36 kHz). ϵ is the non-dimensional pressure, normalised against static pressure (Ilyichev et al., 1989).

(Ilyichev et al., 1989).

Importantly, this ability of inertial cavitation (and to a lesser extent stable cavitation) to redistribute the low-frequency content of the incident pressure field to higher frequencies, predominantly in the focal region, serves to intensify heat deposition during thermal ablation. This potentially enables the use of lower insonating frequencies to achieve cytotoxic levels of heating.

2.4.1 Bubble Resonance

Bubble resonance has already been mentioned in passing, specifically in relation to bubble size. Much like any oscillator, a bubble in an acoustic field will have a natural

frequency, or Minnaert resonance frequency, f_M:

$$f_M = \frac{1}{2\pi R_0}\sqrt{\frac{3\gamma_g p_0}{\rho_L} - \frac{2\sigma}{\rho_L R_0}} \tag{2.7}$$

where R_0 is the equilibrium bubble radius and γ_g is the ratio of specific heats of gas (Minnaert, 1933). It is important to note that the mapping is unique - that is, each insonation frequency has a unique resonance bubble size or, to paraphrase, each bubble size has a unique resonance frequency.

Bubbles much smaller than resonance size for a given frequency of acoustic excitation - that is, those excited at a frequency well below resonance - will oscillate in phase with the incident pressure waves. Bubble oscillations at frequencies close to resonance are characterised by large amplitude bubble wall displacements and the onset of asymmetric shape oscillations. These asphericities can lead to many important phenomena, including the emission of tiny bubble fragments from the surface ripples on the bubble wall (Leighton, 1994). Finally, bubbles significantly larger than resonance size, though not encountered in the present work, will oscillate in antiphase with the incident acoustic field.

2.4.2 Inertial Cavitation Threshold

The onset of inertial cavitation is often loosely described in terms of the minimum acoustic pressure required to initiate explosive growth of a nucleus into a transient cavity during the foremost rarefaction phase of the incident pressure wave, resulting in violent collapse and associated broadband emissions during the compression phase. This so-called "inertial cavitation threshold" is dependent on: the viscoelastic properties of the host medium; the size and number distributions of nucleation sites; the surface tension of cavitation nuclei; the acoustic parameters; as well as the local temperature. Pinpointing this minimum pressure within a continuum

of bubble behaviours is somewhat subjective, the three most commonly used criteria being:

- when the bubble expansion radius, R_{max}, is equal to twice the initial radius (Flynn, 1975);
- when the maximum collapse temperature, T_{max}, of the bubble reaches 5000 K (Apfel and Holland, 1991); or
- when the bubble wall collapse speed exceeds the speed of sound in air (Church, 2002).

These criteria are often mutually exclusive and deciding which one to use will depend on the specific application. Based on the T_{max} threshold definition, Apfel and Holland were able to construct a series of computationally derived curves of threshold versus equilibrium bubble radius for various frequencies of insonification (see Figure 2.6). The threshold is shown both to increase with decreasing nucleus size due to the effects of surface tension and to increase with increasing nucleus size due to inertial and viscous effects, thus yielding an optimal bubble size for inertial cavitation inception. It is important to note that the underlying assumptions for this work are particularly simplifying, and the curves presented are only strictly valid for single-cycle excitation in pure water (Apfel and Holland, 1991).

In biological tissue, a subset of bubble sizes would usually be present prior to HIFU insonation, the exact distribution of which cannot be accurately determined. Additionally, variations in contributing factors such as density, perfusion and dissolved gas concentration between subjects means that the pressures required to instigate inertial cavitation at different frequencies are poorly characterised. Fortunately, however, the acoustic emissions generated by cavitating bubbles may be

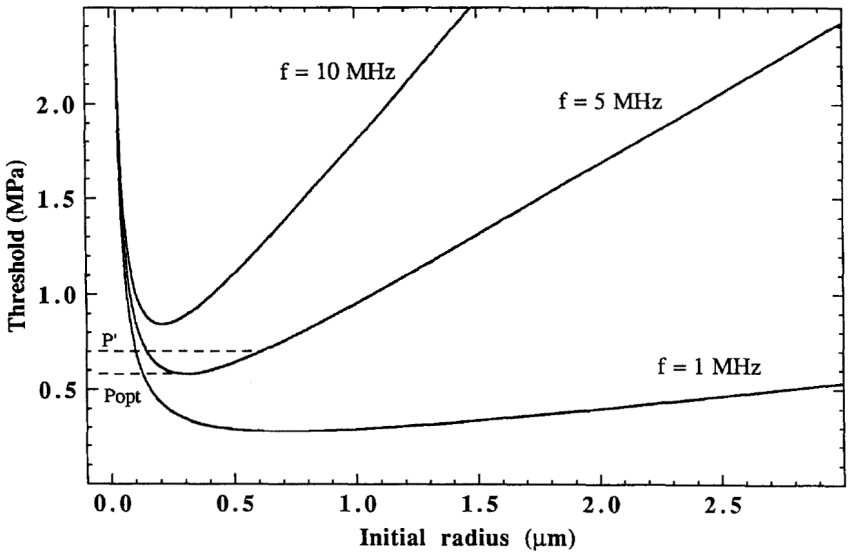


Figure 2.6: Demonstration of stable and inertial cavitation regimes in relation to pressure amplitude and initial bubble radius for various frequencies of insonification. The inertial cavitation threshold is shown to increase with both increasing and decreasing nucleus size due to the effects of surface tension and viscosity respectively, yielding an optimal bubble size for inertial cavitation inception (Apfel and Holland, 1991).

analysed on a case-by-case basis to infer likely bounds on cavitation activity, as will be discussed in Section 2.5.

2.4.3 Rectified Diffusion

In the absence of an acoustic stimulus, the interior pressure of a bubble, p_{int}, must exceed the liquid pressure exterior to it to overcome the surface tension at the interface between liquid and gas. This inevitably leads to a net flux of gas into the liquid (Epstein and Plesset, 1950):

$$p_{int} - p_{\infty} = \Delta p = \frac{2\sigma}{R}, \tag{2.8}$$

where Δp is the "Laplace" pressure of the bubble. Whereas this static diffusion process culminates in eventual bubble dissolution, a bubble undergoing acoustic excitation will grow by rectified diffusion when driven at pressures above a threshold

level. Rectified diffusion impels a net influx of gas over many acoustic cycles under the combined influence of the *area* and *shell* effects (Leighton, 1994; Crum, 1984).

The rate of mass diffusion into or out of a spherical bubble is given by:

$$\frac{dm}{dt} = 4\pi R^2 \delta \frac{\partial \varphi(\gamma, t)}{\partial \gamma}\bigg|_{\gamma=R}, \tag{2.9}$$

where m is the mass of gas inside the bubble, φ is the partial pressure of the dissolved gas and γ is the radial distance from the bubble centre. During the negative part of an acoustic cycle, a bubble contracts and its gas concentration increases, resulting in mass diffusion out of the bubble. During the positive part of the cycle, the direction of mass diffusion is reversed. Since the gas diffusion rate is proportional to the bubble surface area, $4\pi R^2$, more gas enters during expansion than leaves during contraction. This is the area effect. Moreover, when a bubble contracts, the hypothetical constant-volume liquid shell surrounding it thickens, thereby reducing the concentration gradient and thus gas flux out of the bubble. Of course, shell thinning during the expansion phase has the converse effect. This is the shell effect.

Over many cycles, a net influx of gas is realisable and the bubble steadily grows either until it reaches resonance or transient size, whereupon more violent action is usually observed, or until the pressure-radius conditions place it below the threshold. This is demonstrated in Figure 2.7, in which the rectified diffusion and inertial cavitation thresholds are clearly demarcated for a range of bubble sizes in the presence of a 1 MHz acoustic field (Leighton, 1994; Church, 1988). The equilibrium radius-time curve of a bubble in an acoustic field may be obtained by tracking its history along a horizontal line, which intersects the thresholds for rectified diffusion and inertial cavitation.

Recent work by Webb et al. has concluded that the rectified diffusion and inertial cavitation thresholds remain coincident for sub-micron bubble sizes subject to a

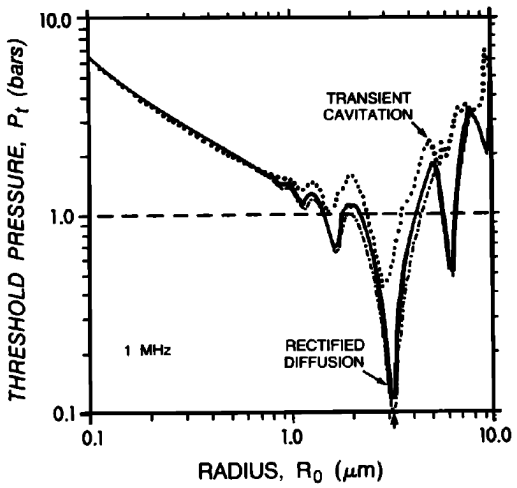
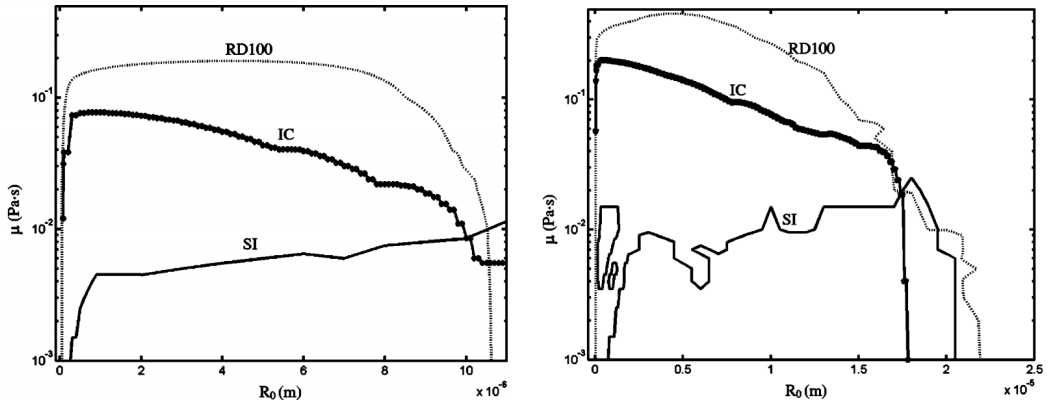


Figure 2.7: Thresholds for rectified diffusion at 90% (dashed line) and 100% (solid line) saturation, and for inertial cavitation (dotted line), for a range of air bubble sizes in water in the presence of a 1 MHz acoustic field (Church, 1988).

1 MHz driving frequency at all temperatures (Webb et al., 2011). Given that most of the work presented in this thesis meets these conditions, rectified diffusion is unlikely to play a major role.

2.4.4 Shape Oscillations

In the case of a static bubble, surface tension causes the bubble to adopt a spherical shape, thereby minimising surface energy. However, an acoustically cavitating bubble can undergo various modes of oscillation, as governed by the acoustic parameters, the liquid viscosity and the contaminants present in the liquid. The simplest mode of oscillation is the "breathing" mode, in which a bubble expands and contracts spherically at frequencies below resonance. At higher frequencies, however, bubbles can be excited to undergo more exotic shape oscillations. In particular, wavy surface perturbations causes shape oscillations of a spherical bubble, as reported extensively in the literature (Plesset, 1954; Eller and Crum, 1970; Prosperetti, 1977), which may or may not lead to breakup of the bubble. The overall shape dis-



(a) (b)

Figure 2.8: Rectified diffusion (RD100), shape instability (SI) and inertial cavitation (IC) thresholds at a frequency of 1 MHz, 100% gas saturation and pressure amplitudes of (a) 1.0 MPa and (b) 2.5 MPa (Yang et al., 2004). Below RD, bubbles grow; below SI, bubbles break up from shape instabilities; and below IC, bubbles collapse inertially.

tortion consists of a superposition of surface oscillations of varying amplitudes.

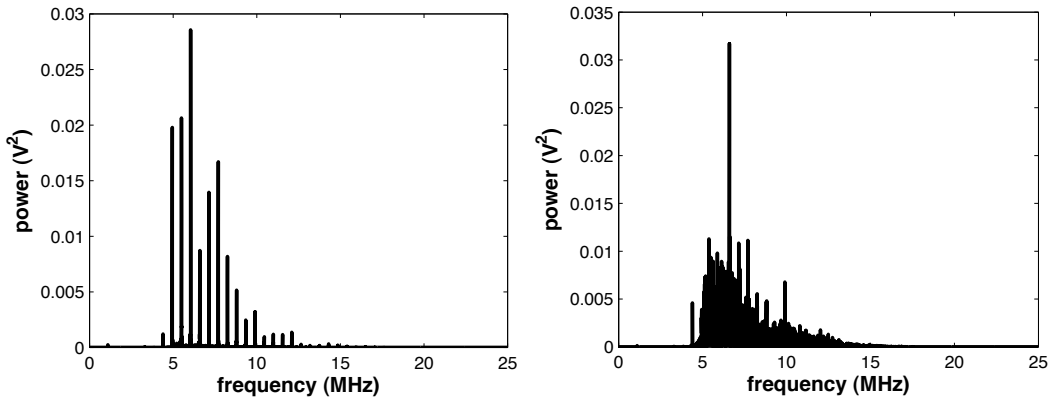
More recently, Yang et al. have published their numerical work on bubble stability boundaries for a parameter space relevant for HIFU (Yang et al., 2004). Figures 2.8 (a) and (b) give an overview of the bubble dynamics for acoustic pressures of 1.0 MPa and 2.5 MPa respectively. The threshold for growth by rectified diffusion, the threshold for break-up via shape instability (calculated for the most unstable mode at each bubble size and viscosity) and the threshold for inertial cavitation (defined as an expansion of the bubble to a size greater than twice the equilibrium radius) are shown. Bubbles below the rectified diffusion threshold lines grow; bubbles below the shape instability threshold lines break up; and bubbles below the inertial cavitation threshold lines collapse inertially.

2.5 Cavitation Detection and Monitoring

A major advantage of cavitation-assisted therapies is the ability to remotely monitor secondary acoustic emissions - that is, the pressure waves propagated by bubbles oscillating in response to therapeutic excitation, rather than the echoes of a diagnostic transmitted pulse - using a PCD. Frequency analysis of these acoustic emissions alludes to the likely bubble behaviour at the HIFU focus (Lauterborn and Cramer, 1981; Ilyichev et al., 1989), providing a unique opportunity for real-time treatment monitoring for both cavitation-enhanced thermal ablation (Coussios et al., 2007a) and cavitation-mediated drug delivery (Datta et al., 2008).

Importantly, cavitation signals represent the superposition of emissions emanating from the entire PCD focal volume, in which a range of bubble sizes exist prior to HIFU insonation. Moreover, both the primary HIFU wave and the secondary acoustic emissions endure significant distortion and attenuation as they propagate through multiple layers of heterogeneous tissue, rendering it near-impossible to extract exactly the type and extent of bubble activity. Nevertheless, previous work has shown that cavitation data obtained in this manner may be empirically correlated with clinically relevant treatment metrics, and hence used for effective treatment guidance (Hockham et al., 2010).

At this point, it is instructive to consider the origins of the various spectral components frequently observed in cavitation data (see Figure 2.9). Because the incident HIFU wave energy is orders of magnitude greater than that of the secondary acoustic emissions, detectable scattering at the fundamental frequency, f_0, by inhomogeneities in the field would ordinarily saturate the received signal. A high-pass filter is, therefore, often used to remove reflections at f_0, improving the dynamic range and thus sensitivity to smaller, more interesting signals.



(a) (b)

Figure 2.9: Frequency spectra of acoustic emissions received by a 15 MHz PCD confocally aligned with a 1.067 MHz focused transducer, subsequent to filtering using a 5 MHz high-pass hardware filter. (a) Typical frequency spectrum for stable cavitation, showing discrete peaks at the harmonics and ultraharmonics. (b) Typical frequency spectrum for inertial cavitation, with broadband noise occurring above 5 MHz.

At higher acoustic intensities, spectral peaks may appear at integer multiples of the fundamental frequency, nf_0/m ($n = 2,3,4,...; m = 1$). These harmonic emissions can be attributed to a variety of sources, namely: scattering of the steepened waveform generated by non-linear propagation of the excitation wave; non-linear radial oscillations of both microbubbles and, to a lesser extent, boiling bubbles; and/or asymmetric shape oscillations of the bubble wall. The latter is also associated with subharmonic ($n = 1; m = 2,3,4,...$) and ultraharmonic emissions, ($n = 2,3,4,...; m = 2,3,4,...$) (Ilyichev et al., 1989; Leighton, 1994), whilst the period-multiplying bifurcations which precurse the stochastic zone manifest as subharmonic emissions. Ultraharmonics may also arise from the non-linear distortion of subharmonic components; however, this is, of course, pressure amplitude dependent.

Inertial cavitation exhibits altogether different spectral characteristics, whereby the rapid collapse of a microbubble in the time domain corresponds to a continuum

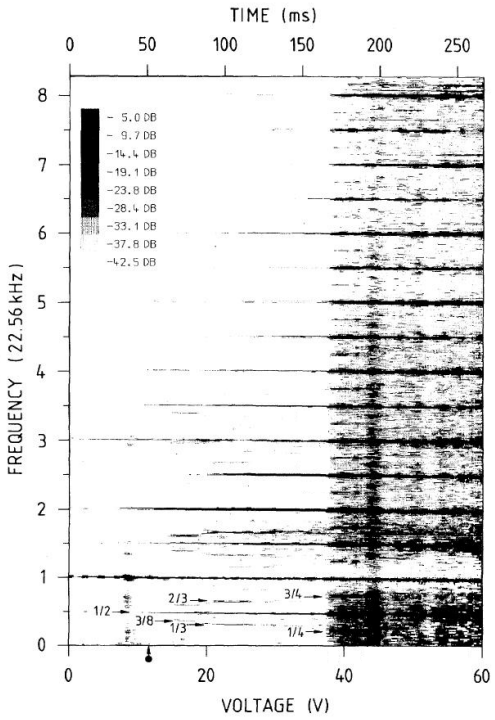


Figure 2.10: Spectrogram of secondary acoustic emissions illustrating the emergence of various spectral components with linearly increasing driving voltage. Harmonic emissions emerge first, followed by subharmonic emissions, ultraharmonic emissions and, finally, broadband emissions (Lauterborn and Cramer, 1981).

in the frequency domain, above the noise floor. Although much of the broadband signal is absorbed in the vicinity of the bubble, the remainder is easily detected and has been shown to scale with the absorbed signal (Collin, 2009). The gradual emergence of each of these oscillating regimes with linearly increasing driving pressure is duly summarised in the spectrogram of Figure 2.10. Crucially, the shift in spectral content from lower to higher frequencies provides a convenient mechanism for enhanced heat deposition at the HIFU focus, where the acoustic intensity is maximum.

In summary, the remote monitoring of acoustic emissions yields a simplified cavitation signal, which may be taken as representative of an inextricably complex system involving a range of bubble sizes distributed throughout the sound field.

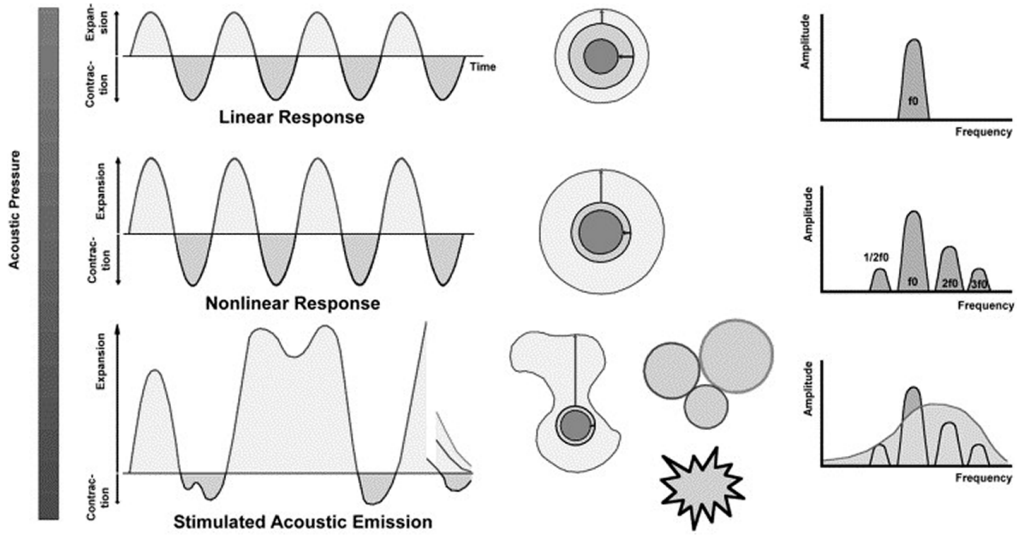


Figure 2.11: Illustration of the interaction of ultrasound with shelled microbubbles. (a) At low acoustic pressures, microbubbles oscillate linearly. (b) At higher pressures, it becomes increasingly difficult to compress rather than expand microbubbles. (c) Highly non-linear bubble oscillations result in the formation of smaller bubbles, bubble coalescence and bubble rupture (Stolz and Kaps, 2005).

Whilst it may not be possible to invert the problem and determine exactly what type of bubble behaviour is responsible for these acoustic emissions, the cavitation signal may nevertheless be empirically correlated with clinically relevant treatment metrics such as lesion formation or drug extravasation.

2.5.1 Frequency Response of Shelled Microbubbles

The frequency response of a shelled microbubble subject to acoustic stress differs from that of its free bubble counterpart on account of the modified boundary conditions. For compliant lipid-shelled microbubbles, of which SonoVue® features prominently in Chapter 4, these boundary conditions become important when the incident acoustic pressure amplitude is increased beyond several hundred kilopascals (Morgan et al., 2000). In this regime, it becomes increasingly difficult to compress, rather than to expand, a microbubble, which results in asymmetric bubble

oscillations about the equilibrium radius. This non-linear behaviour manifests as subharmonic, harmonic and ultraharmonic frequencies in the frequency domain.

Further increasing the acoustic pressure amplitude enhances the non-linear properties of bubble oscillations. Bubble fragmentation, bubble coalescence and bubble rupture are common themes in this regime, and result in the emission of broadband noise, which can be detected above the noise floor of the ultrasound system (see Figure 2.11).

2.6 Cavitation-Enhanced Heating

Pennes' bioheat transfer equation, introduced in Section 1.4.1, is commonly used to predict the temperature response of biological tissues subject to external heating. In a homogeneous medium, the contributive heat deposition term from a plane travelling wave of local intensity, I, is given by:

$$\dot{Q}_{ac} = 2\alpha I = \frac{\alpha}{\rho c} P^2, \tag{2.10}$$

where P is the local pressure amplitude and ρ is the local density. Limitingly, equations 1.2 and 2.10 do not account for cavitation-enhanced heating: to do this, precise knowledge of the extent of radial oscillation of each and every bubble in the field would be required. Instead, researchers often rely upon empirical relationships for predictive purposes.

Figure 2.12 shows the peak focal temperature elevation measured in an agar-graphite tissue-mimicking phantom for a range of HIFU intensities (Holt et al., 2006). The predicted temperature rise in the absence of cavitation activity is also included. At modest pressure amplitudes, there is good agreement between experimental data and the theoretical model. In particular, the temperature elevation is shown to vary quadratically with pressure amplitude and, therefore, linearly with

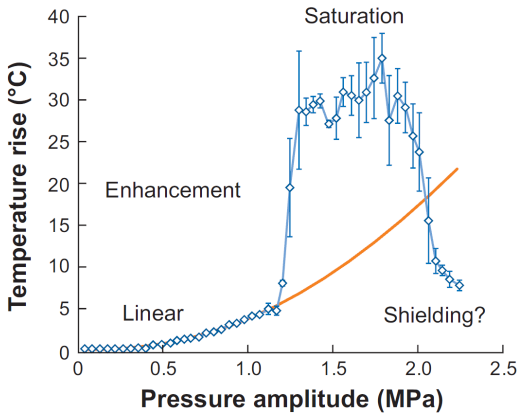
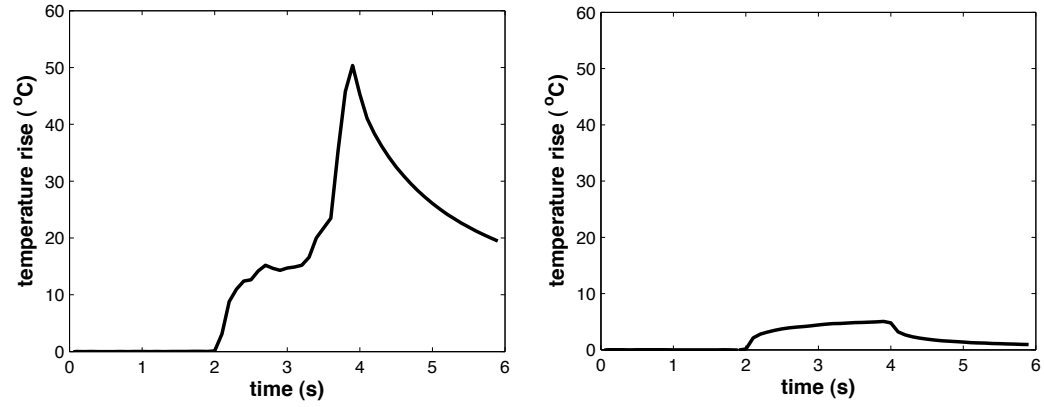


Figure 2.12: Peak focal temperature elevation measured in an agar-graphite tissue-mimicking phantom for 1 s exposures conducted at a range of HIFU intensities (Holt et al., 2006) and a frequency of 1 MHz (blue line). The predicted temperature rise in the absence of cavitation activity is also included (red line). Temperature was measured using a fine wire thermocouple, co-located with the HIFU focus.

acoustic intensity. Beyond a pressure amplitude of approximately 1.1 MPa, however, cavitation activity causes the experimental profile to divert from its predicted course. There is, of course, a limit to the number of bubbles which may occupy the focal volume and, therefore, a cap on the enhancement in heating which may be achieved. Moreover, increased scattering by vapour cavities favours near-field heating, thereby reducing the temperature elevation at the thermocouple-coincident focus.

It is interesting at this point to examine the principal differences between temperature profiles obtained from HIFU exposures in which the contributions from cavitation-enhanced heating are disparate. The graphs in Figure 2.13 pertain to experiments carried out in an agar gel, one with a plentiful source of cavitation nuclei and the other with the nuclei source having been significantly depleted by previous ultrasound excitation. The effect of cavitation is to disrupt the otherwise smooth temperature curve and to enhance the rate of heating.

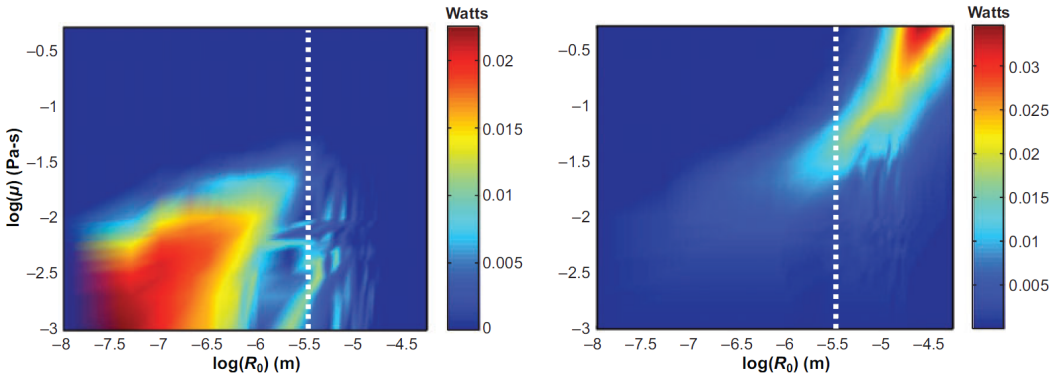


(a) (b)

Figure 2.13: Temperature elevation plots from sequential HIFU exposures in agar gel using a 1.067 MHz HIFU transducer at a pressure amplitude of 2.21 MPa. The HIFU is in an active state between t = 2 s and t = 4 s. (a) Temperature elevation profile with plentiful nucleation sites and (b) temperature elevation profile with depleted nucleation sites.

Artefactual heating, primarily due to viscous forces in the boundary layer of an implantable thermocouple probe, is commonly observed in data obtained during HIFU experimentation. Frictional effects ensue, thence viscous heating. Thermocouple artefact manifests as an artificially steepened gradient coincident with both the onset and termination of HIFU insonation (see Figure 2.13). These effects may be mitigated by ensuring that the probe diameter is an order of magnitude smaller than the excitation wavelength (Rivens et al., 2007).

Previous numerical work has demonstrated that cavitation-enhanced heating observed experimentally can be attributed either to bubbles smaller than resonance size undergoing inertial cavitation or to bubbles larger than resonance size undergoing stable oscillations, as demonstrated in Figure 2.14 (Coussios and Roy, 2008; Holt and Roy, 2006). For water-like viscosities at a frequency of 1 MHz, the allowable bubble size range is between 10 nm and 1 μm, which is considerably smaller than resonance size at the same frequency (Coussios et al., 2007a; Powell, 1971). Most of the work presented in this thesis involves the use of ultrasound source frequen-



(a) (b)

Figure 2.14: Thermal power deposited due to (a) a bubble undergoing inertial cavitation and (b) a bubble undergoing stable cavitation (Holt and Roy, 2006). The dashed white lines indicate the bubble resonance size at an insonation frequency of 1 MHz. The pressure amplitude is 2 MPa.

cies around the 1 MHz mark, which is why the sustenance of broadband acoustic emissions associated with inertial collapse is so desirable.

2.7 Controlling Cavitation

A fundamental obstacle to the widespread use of cavitation in biomedical applications is the stochastic nature of cavitation inception and its tendency to vary unpredictably once instigated. Bubble behaviour in a HIFU field depends not only on the local tumour microenvironment, but also on the ultrasound excitation parameters. The most commonly varied parameters are shown in Figure 2.15 and include: peak rarefactional focal pressure (PRFP); excitation frequency; duty cycle; and pulse repetition period (PRP). Crucially, these parameters can be tuned to induce, and thence control, specific cavitation-dependent bioeffects.

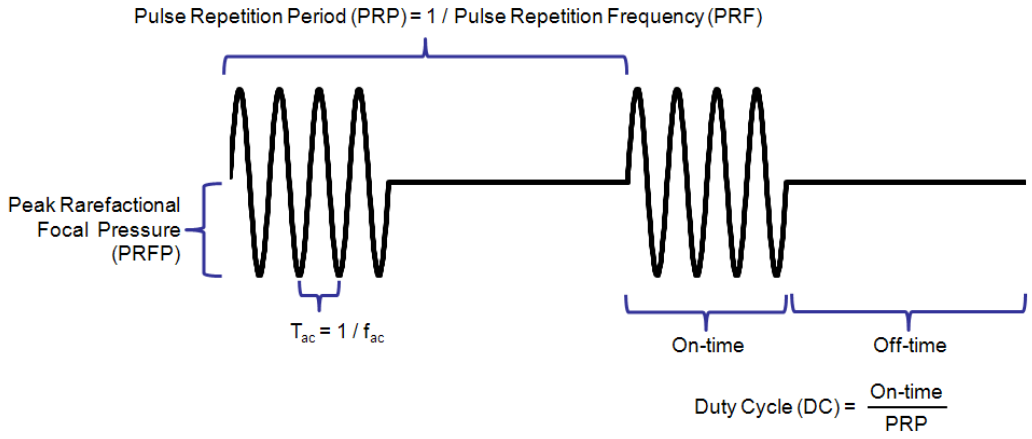


Figure 2.15: Idealised ultrasound insonation waveform (pressure versus time) with commonly varied acoustic parameters indicated.

2.7.1 Peak Rarefactional Focal Pressure

Whilst an initially sinusoidal incident pressure disturbance might be symmetrical about the zero line for low-amplitude HIFU insonation, or for high-amplitude HIFU insonation in the near-field, the relatively high pressures required for thermal ablation are subject to non-linear distortion in the far-field. PRFP is often preferred over its compressional counterpart as a descriptor of waveform amplitude, since it is the rarefactional phase which governs inertial cavitation inception and subsequent bubble growth.

In general, at any given excitation frequency, the probability of an inertial cavitation event occurring, and its corresponding collapse energy, will increase with increasing PRFP until either saturation or shielding occurs. Of course, these events are confined to regions where the local rarefactional pressure exceeds the inertial cavitation threshold and this applies as much to the HIFU side lobes as to the focal volume itself. This is illustrated in Figure 2.16, in which the size of the cavitation region is shown to vary with increasing pressure, and hence beam width.

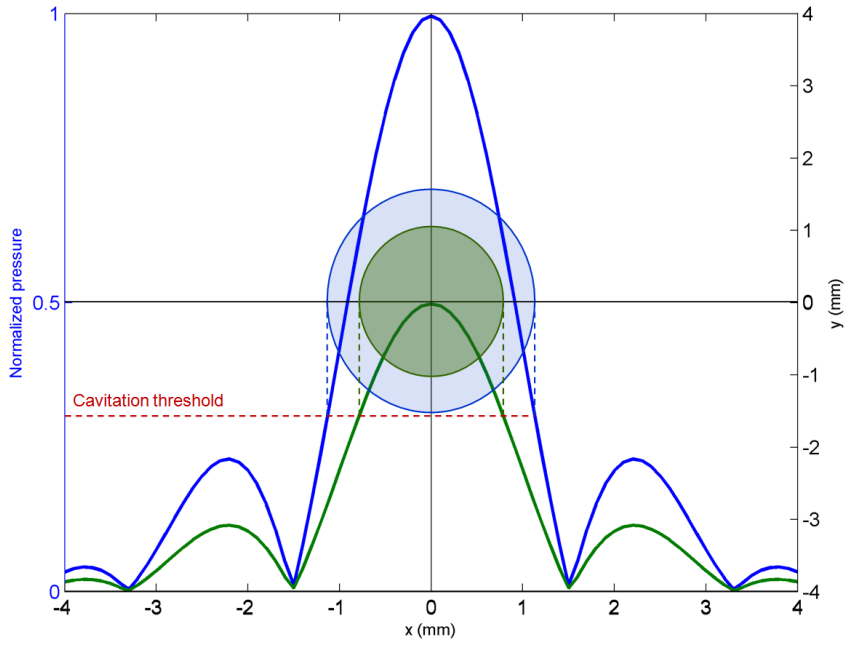


Figure 2.16: A simulated pressure profile along the transverse axis of a spherically focused HIFU transducer. The size of the cavitation region depends on the maximum width of the profile that lies above the inertial cavitation threshold. For low-amplitude HIFU insonation (green), this region is smaller than for high-amplitude HIFU insonation (blue) (Faragher, 2011).

2.7.2 Excitation Frequency

As with all waves, the frequency and wavelength of a sound wave are inversely linked via its phase speed. Thus, in a focused ultrasound field, lower excitation frequencies, and hence longer wavelengths, produce wider focal zones than would be observed at higher frequencies. This results in lower acoustic intensities, and hence focal amplitudes, for a given radiated power and transducer geometry.

Whereas a reduction in PRFP might ordinarily be associated with diminished inertial cavitation activity, the prolonged expansion phase of these waves allows more time for bubble expansion, which favours acoustic cavitation. Of these competing mechanisms, *in vivo* experimentation in canine thigh muscle has shown that the latter takes precedence in the frequency range 0.246 MHz to 1.680 MHz (Hynynen,

1991b) - that is, lower frequencies have the net effect of increasing cavitation yields. Conveniently, this enables deeper penetration of the HIFU beam, whilst minimising pre-focal attenuation.

Interestingly, numerous sources have reported a significant increase in cavitation yield under the combined irradiation of two or more frequencies compared with single frequency excitation (Barati et al., 2007; Iernetti et al., 1997; Feng et al., 2002). The addition of the low frequency component is thought to enable cavitation to occur at lower operational pressures, whilst the high frequency component serves to accelerate mass transfer across the bubble wall. Alternative explanations have also been suggested. Feng et al. explained the effect as the result of a stronger disturbance to the sample solution by the combined irradiation, which enhances both bubble-sound field interactions and bubble-bubble interactions through first- and second-order Bjerknes forces. The resulting surface waves induced on bubbles by their neighbours could cause bubble fragmentation (Feng et al., 2002). In contrast, Carpenedo et al. attributed the effect to a combination resonance in space and time of the two ultrasonic fields (Carpenedo et al., 1987).

2.7.3 Duty Cycle and Pulse Repetition Period

In the absence of thermally relevant cavitation activity, continuous wave (CW) HIFU insonation is preferable for minimising thermal diffusion away from the intended treatment site; however, this requires continual treatment monitoring in order to manage unwarranted pre-focal damage and prevent overtreatment.

Conversely, during cavitation-assisted therapies, the choice of duty cycle, defined as the fraction of time for which the excitation source is in an active state, is an important consideration. Bubble growth during pulsed insonation is limited by the time allowed for dissolution at the end of each pulse. This depends not only on

the duty cycle but also on the PRP (Thomas et al., 2005; Coussios et al., 2007b). As a general rule, lower duty cycles and PRPs yield the highest levels of sustained cavitation activity; however, this is at the expense of increased heat flux away from the target region and, therefore, collateral damage.

Moreover, some passive localisation techniques for identifying the frontal position of a bubble cloud from PCD data fundamentally rely on the use of pulsed HIFU insonation (Kennedy et al., 2009). One such technique is introduced in Section 3.3.3.

2.7.4 Temperature-Dependent Effects

The effect of acoustic heating on cavitation activity *in vivo* is presently poorly understood. It is well established that an increase in local temperature encourages gas expansion within a bubble, whilst the saturation concentration of the surrounding medium decreases. The net effect is mass flux into the bubble from the medium (Webb et al., 2010), a phenomenon that occurs alongside, but which is distinct from, rectified diffusion. In the context of patient safety, significant bubble growth by temperature-dependent effects is undesirable due to the inherent ability of large bubbles to backscatter the incident excitation. This could result in excessive prefocal damage.

Elevated temperatures also reduce the inertial cavitation threshold of target media. Moreover, gradual changes in the material properties of tissue undergoing denaturation affects both the viscous and elastic forces acting upon the bubble wall (Baek et al., 2005). These effects combined could result in a bubble which is more likely to collapse violently due to shape instability.

2.8 Gap in Knowledge

Both the speed and safety of non-invasive tissue ablation by ultrasound depend on the ability to achieve much higher energy deposition efficiencies at the focus compared with the pre-focal region. HIFU-induced cavitation shows great potential as a means of inducing a variety of desirable bioeffects at lower acoustic intensities than might ordinarily be required for HIFU-mediated cancer therapy.

Unfortunately, it is especially difficult to predict how the local tumour environment will react to a given acoustic field in the absence of an accurate model of the cavitation dynamics. The present work thus considers the design, implementation and validation of a negative-feedback control system capable of instigating and sustaining thermally relevant cavitation activity over extended periods of time, based on real-time information pertaining to the focal region in the form of secondary acoustic emissions. Criteria for effective cavitation control include:

- knowledge of an empirical relationship between secondary acoustic emissions and heating;
- instantaneous cavitation instigation and sustained cavitation activity thereafter to enable continual treatment monitoring; and
- thermally relevant bubble oscillation modes that are accessible over a wide range of HIFU parameters.

Whilst the eventual controller design is intended primarily for thermal ablation, it may also be useful for realising other cavitation-assisted bioeffects.



CHAPTER 3

CAVITATION-ENHANCED HEATING *In Vitro*

Cavitation-enhanced heating is an attractive prospect to proponents of HIFU for the mere fact that it could enable tissue ablation at much lower intensities than in current clinical use. Moreover, it brings with it a unique opportunity for real-time treatment monitoring through concurrent passive cavitation detection. This chapter explores the use of different PRFPs to instigate cavitation in both agar and polyacrylamide (PAA) tissue-mimicking phantoms, with a view to establishing an empirical relationship between cavitation levels and the accompanying temperature elevation. Contrasting results in agar and PAA TMMs subjected to identical HIFU insonation conditions are investigated, highlighting the importance of cavitation nuclei distribution in the design of sonication regimens.

Inertial cavitation has a potentially important role to play in the eventual clinical adoption of HIFU. In addition to facilitating heat deposition at clinically feasible insonation conditions, the remote detection of secondary acoustic emissions generated by bubble oscillators provides a unique opportunity for concurrent treatment monitoring.

Biological tissue is inherently inhomogeneous, with marked variations in vascular distribution and acoustic properties commonplace both within and between tissue samples. Compounded with other attributes such as maturity and experimental handling, this creates a complex system with many more degrees of freedom than

might be immediately obvious. Fortunately, the use of a simplified experimental model, in which biological tissue is replaced with moldable tissue-mimicking polymers, allows the system to be stripped of many of its complexities, whilst retaining core elements of the underlying physics. Crucially, TMMs generate reproducible results, whilst their formulations may be adjusted to emulate specific acoustic properties exhibited by biological tissue.

This chapter explores the ability of both agar and polyacrylamide (PAA) tissue-mimicking phantoms to support thermally relevant cavitation under identical HIFU insonation conditions. The effect of initial cavitation nuclei distribution is investigated, culminating in a modified PAA phantom recipe that is optimal for cavitation-enhanced heating. An empirical relationship is thus established between cavitation and temperature elevation, providing the basis for subsequent work into control system design and implementation.

Importantly, the results presented build on previous work by Coussios et al. (Coussios et al., 2007a) and Farny et al. (Farny et al., 2010). Coussios et al. successfully demonstrated the notion of cavitation-enhanced heating using thermocouples embedded in agar-based TMMs at an insonation frequency of 1.1 MHz. Farny et al. further investigated the correlation between broadband acoustic emissions and temperature elevation at the same frequency, concluding that cavitation power is proportional to the rate of temperature rise when HIFU heating is accounted for and when non-linear effects are negligible.

3.1 Experimental Setup

Figure 3.1 is a schematic representation of the experimental setup adopted for the *in vitro* work presented in this chapter. All sonications were conducted inside a water

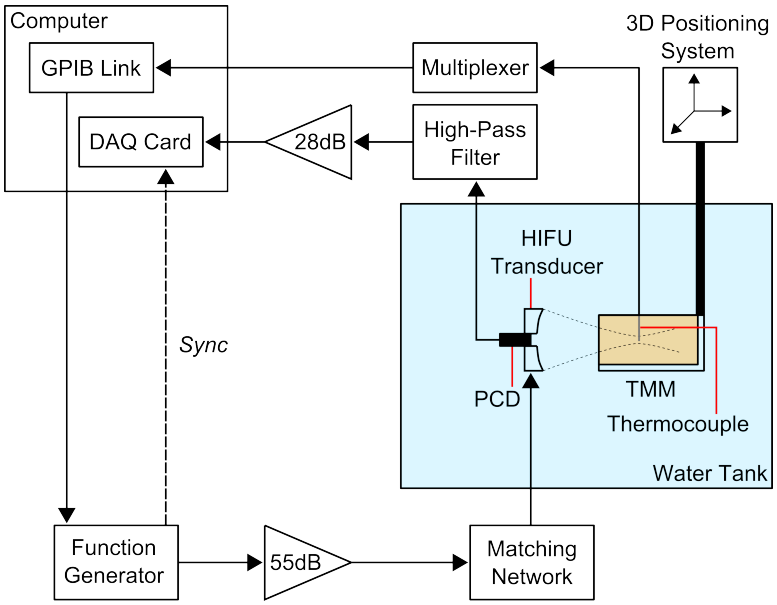


Figure 3.1: Overview of the experimental setup for acquiring cavitation and thermal data. The output signal from a function generator is passed through a series of signal conditioners before reaching the transducer. Acoustic emissions at the focus are recorded by a PCD and thermal data acquired using a thermocouple.

tank maintained at room temperature to enable near-complete wave transmission into the TMM. Degassing the water *a priori* ensured that cavitation occurred preferentially inside the target.

The following sections describe the various components depicted, many of which are pertinent to subsequent chapters also. The reader is, therefore, invited to refer back where necessary.

3.1.1 Tissue-Mimicking Media

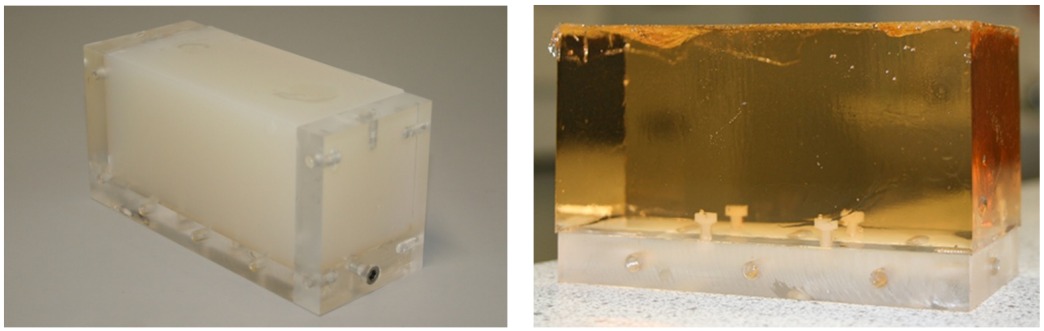
Desirable characteristics of tissue-mimicking phantoms include acoustic and viscoelastic properties that are closely matched to those of biological tissue and structural rigidity for ease of use. Agar-based TMMs of varying concentration are commonly used (Burlew et al., 1980); however, the advent of protein-infused PAA-based test media, which increase in opacity as the protein denatures, has been well re-

ceived by acousticians (Lafon et al., 2005). Both types of TMM are included in this preliminary investigation into the capacity for cavitation-enhanced heating to occur *in vitro* (see Figure 3.2).

Agar is a heterogeneous mixture of the linear polysaccharide *agarose* and other smaller molecules. Agar molds are prepared by suspending agar powder in water, heating to 85 °C to dissolve and allowing to cool to below 35 °C, at which point the polymer strands are held together in a porous gel structure by hydrogen bonding and electrostatic interactions. The application of heat during the dissolution stage results in the formation of large bubbles. Thus, to eliminate uncertainties arising due to variations in initial bubble density, the agar solution was degassed at 0.2 bar for 45 minutes during heat application. 3% agar TMMs have been shown to have material properties (density, compressibility) similar to tissue, with the exception of the attenuation coefficient (see Table 3.1). Although this manifests as reduced heating rates, identifiable trends are of more concern than absolute temperature values in the present work.

Polyacrylamide is a matrix formed from an exothermic polymerisation process involving: acrylamide monomer units dissolved in buffered solution; a polymerising agent; and a catalyst (Lafon et al., 2001, 2005). Bovine serum albumin (BSA), a protein derived from cows, may be gradually added to the mixture prior to catalysis if protein denaturation is of interest, to assist with lesion identification. As with agar, 40% PAA, 7% BSA TMMs have been shown to have material properties similar to those of tissue; however, the attenuation coefficient is, again, relatively low (see Table 3.1).

Phantoms were prepared one day in advance of experimentation and cast in cuboid TMM holders measuring 50 mm x 50 mm x 100 mm. In the ensuing experiments, the TMM was suspended from a three-axis motorised positioning system,



(a) (b)

Figure 3.2: Photographs of (a) an agar TMM and (b) a PAA/BSA TMM, both set in acrylic holders with sides removed.

Material	**Density** (kg/m^3)	**Sound Speed** (m/s)	**Attenuation** (Np/m)	**Reference**
Water (20°C)	1000	1482	0.03	Del Grosso and Mader, 1972
Water (37°C)	990	1524	0.02	Kaye and Laby, 1921
3% Agar (20°C)	1100	1489	1.2	Collin, 2009
40% PAA, 7% BSA (20°C)	1050	1536	1.0	Collin, 2009
Liver (37°C)	1050	1615	2.7	Gyongy, 2010

Table 3.1: Summary of the acoustic properties of water, agar, PAA and liver (Del Grosso and Mader, 1972; Kaye and Laby, 1921; Collin, 2009; Gyongy, 2010). The attenuation coefficient measurements all pertain to 1 MHz HIFU insonation.

square with both the HIFU beam axis and the transducer face, and oriented so that the target volume coincident with the focal region of the transducer was at least 10 mm away from all of the cuboid faces.

3.1.2 HIFU Generation

Effective HIFU generation is reliant upon a series of signal conditioners that transmit, amplify and optimise a predefined driving signal (see Figure 3.1). HIFU transducers vary considerably in their geometry and construction, the combination of which dictates the fundamental frequency of oscillation and, together with the driving conditions, the resultant beam profile.

In the present work, a remotely controlled function generator (Agilent, 33250A) was used to produce a sinusoidal input signal governing the motion of the oscillating face of a rigidly supported, spherically focused, single-element, piezo-ceramic HIFU transducer of resonant frequency 1.067 MHz, active diameter 64.0 mm and focal length 62.6 mm (Sonic Concepts, H102D-SN28). The choice of frequency was motivated by existing clinical HIFU systems, which operate around the 1 MHz mark. The function generator and transducer were connected in series via a 55 dB fixed-gain power amplifier (E&I, A300) and an impedance matching network (Sonic Concepts), yielding electrical signal powers in the range 0-400 W and acoustical powers in the range 0-348 W, based on a transducer efficiency of 87%. A cylindrical void of diameter 13 mm at the centre of the HIFU transducer enabled coaxial alignment of the PCD.

All pressure amplitude values quoted hereafter are based on a free-field calibration of the HIFU transducer in water. This was undertaken using a calibrated membrane hydrophone with an active sensor diameter of 0.2 mm (Precision Acoustics, UT1602). Beam pattern measurements revealed the transducer transverse focal

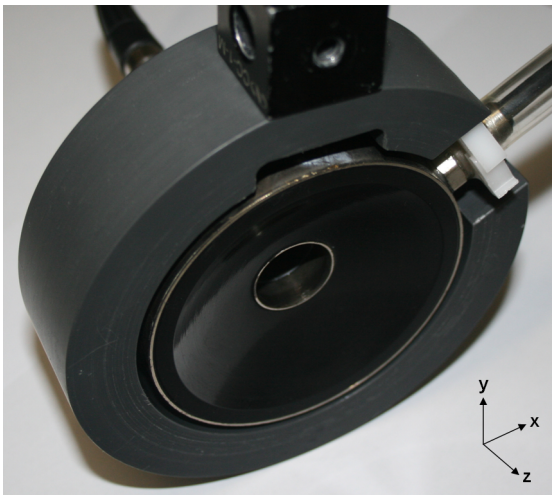


Figure 3.3: Spherically focused HIFU transducer (Sonic Concepts, H102D-SN28) with central cylindrical void for coaxial alignment of a PCD.

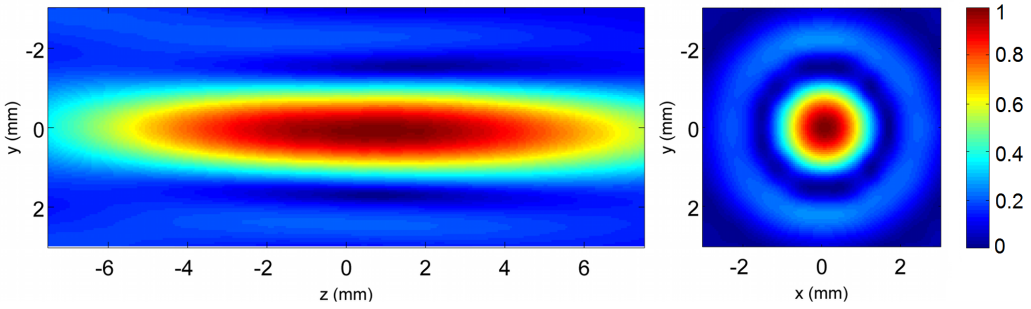


Figure 3.4: Normalised longitudinal and transverse pressure profile sections of the 1.067 MHz focused HIFU transducer, taken through the focal maximum. The focal volume is ellipsoidal, with strong transverse focusing and weak axial focusing.

width and axial focal depth at half maximum to be 2.0 mm and 14.6 mm respectively, as illustrated in Figure 3.4.

3.1.3 Passive Cavitation Detection

Cavitation activity was quantified using a spherically focused PCD transducer of centre frequency 15 MHz, bandwidth 5-25 MHz, diameter 12.5 mm and focal length 75.0 mm (Olympus, V319-SU), coaxially and confocally aligned with the HIFU transducer. The PCD was mounted through the central opening of the HIFU transducer,

a setup which has previously been shown to enable successful quantification and localisation of cavitation activity during HIFU exposure (Kennedy et al. (2009)). Its centre frequency was chosen to be especially sensitive to broadband acoustic emissions, though still capable of detecting the main HIFU frequency and its harmonics, thereby making best use of the available dynamic range.

The raw PCD signals were filtered using a 5 MHz high-pass filter (Allen Avionics) with a roll-off of 176 dB/decade, prior to being amplified using a dedicated 28 dB amplifier (Stanford Research Systems, SR445A). Filtering prevents saturation of the amplifier by acoustic emissions generated at lower harmonics due to limited dynamic range, thus enabling use of the passive cavitation detection apparatus synchronously with HIFU generation.

Once filtered and amplified, the PCD signal was digitised using a 14-bit data acquisition (DAQ) card (National Instruments, NI PCI-5122) operating at a sampling frequency of 100 MHz. This frequency was chosen to conform with the Nyquist-Shannon sampling theorem, thus preventing aliasing of the 5-25 MHz bandwidth PCD signal. Despite sufficient onboard memory to record data continuously for up to 40 ms, data streaming from the DAQ card to the host computer is limited to 110 MB/s. Thus, for exposures exceeding 40 ms, data must be acquired and transferred in discrete 'blocks' at regular acquisition intervals. Of course, there is a trade-off between the lengths of these blocks and their separation: an optimal setting of 40,000 samples recorded every 50 ms was found to contain sufficient information to capably represent cavitation activity over the entire pulse length, and was thus used for all of the experiments performed.

Accurate alignment of the HIFU and PCD transducers is critical in ensuring that the acquired PCD data is representative of focal cavitation activity. Differences in both the geometry and centre frequency of these transducers yields disparately-

sized focal volumes, that of the PCD being dependent on the frequency of the secondary acoustic emissions. The aim, therefore, is to align the points of maximum sensitivity of each device.

Initially, the HIFU transducer was driven in pulse-echo mode using a pulser-receiver (JSR, DPR300), with a 6 mm diameter brass sphere positioned approximately at the focus. In the longitudinal direction, the calibrated HIFU focal length may be converted to a time delay using knowledge of the speed of sound in the transmission medium at the ambient temperature. Monitoring the received signal on an oscillioscope screen (LeCroy, Waverunner 44Xi) thus allowed accurate depth-wise placement of the sphere. In the transverse direction, the sphere was scanned through the HIFU field using the three-axis motorised positioning system to identify the point of maximum echo amplitude. The procedure was repeated for the PCD, with the HIFU transducer and the sphere fixed in place.

3.1.4 Temperature Recording

Temperature measurements were obtained using a T-type fine-needle thermocouple (Omega, HYP0) with an outer diameter of 200 μm, connected to a remotely controlled multiplexer with embedded reference temperature compensation (Agilent, 34970A). Thermal data was outputted to the host computer at 10 Hz via general purpose interface bus (GPIB) interface. The probe was inserted into the phantom via its uppermost face, the thermocouple axis thence normal to the direction of ultrasound wave propagation (see Figure 3.1).

The thermocouple was aligned such that the highly sensitive thermocouple junction was coincident with the HIFU focus, where cavitation activity and heat deposition are assumed to be maximal. In the direction orthogonal to the thermocouple axis, alignment was achieved ultrasonically, whereby the PCD is driven in

pulse-echo mode and the target repositioned so as to maximise the echo amplitude. The HIFU transducer could, of course, have been used to perform this task; however, the relative narrowness of the PCD focus at the HIFU driving frequency is a major advantage, allowing for more precise alignment.

By contrast, alignment in the direction of the thermocouple axis involved the repeated use of CW HIFU at a PRFP below the cavitation threshold for a fixed period of time, to identify the point along the axis where the maximum temperature rise was recorded. Once aligned, the distance between the exposed face of the TMM and the thermocouple probe along the HIFU beam axis was determined using time-of-flight information between the reflections from each of these structures, as viewed on an oscilloscope. To avoid impeding lesion formation and growth, this distance was kept to a minimum of 10 mm.

Importantly, whilst the PCD is sensitive to secondary acoustic emissions originating from a three-dimensional volume, temperature measurements are obtained uniquely at the HIFU-PCD focal point. Deducing empirical relationships between cavitation and thermal data must, therefore, be approached with caution, especially given the non-uniform spatial distribution of cavitation events within and around the focal region.

3.2 Controlling Software

A custom LabView script was developed to control the actuation of the HIFU source and the acquisition of cavitation and thermal data. Some important features of the script include:

- control over the function generator and the capacity to specify a range of excitation waveforms, including ones in which the amplitude is ramped up gradu-

ally over regular time intervals (this is particularly useful for cavitation threshold measurements);

- a network of trigger signals that originate from the function generator and enable cavitation and thermal data to be acquired synchronously with the leading edge of the HIFU envelope;
- graphical representation of the temperature profile post-exposure;
- quasi real-time signal processing capabilities, providing a continually updated account of the PCD signal power and the frontal position of the bubble cloud.

Cavitation and thermal data was obtained for 2 s prior and subsequent to HIFU exposure in order to determine the base noise level on the DAQ card channel and the ambient temperature, and to rule out any artefacts arising from switching the DAQ system and other hardware on/off at the same time. A series of preliminary experiments were conducted in both agar- and PAA-based TMMs to inform the choice of vertical range: cavitation signals can span many orders of magnitude and a compromise must, therefore, be made between artefactual clipping and vertical resolution. The lowest vertical range that avoided clipping was chosen, which was conveniently found to be sufficient for experimentation in tissue also.

3.3 Data Analysis

Offline data processing was performed using Matlab. A range of signal processing techniques were applied to thermal and PCD data in order to extract pertinent information relating to bubble activity at the HIFU focus. These are summarised in the following sections.

3.3.1 Quantifying Cavitation Activity

On account of the 5 MHz high-pass hardware filter located upstream of the DAQ card in the experimental setup, any increase in the amplitude of a PCD signal beyond the base noise level must be the result of non-linear activity, be it cavitation, non-linear sound propagation and/or boiling. As explicated previously in Section 2.5, PCD signals represent the superposition of emissions from a plurality of bubbles occupying the PCD focal volume, rendering it difficult to infer precisely what is occurring in the HIFU field using a single-element PCD. Spectral analysis is, of course, useful for drawing conclusions regarding likely bubble behaviour; however, many spectral features are not unique to a particular type of event. Nevertheless, in the knowledge that something *is* happening, it is certainly useful to monitor the evolution of the PCD signal and its frequency spectrum over the course of an exposure, and to compare these with other exposures.

The PCD signal variance was chosen as a metric for cavitation noise, since it is proportional to the power of the acoustic emissions and devoid of any DC bias introduced by the amplifiers in the DAQ system. Moreover, if inertial cavitation is the dominant heating mechanism, the rate of heating, and hence temperature elevation, should be directly dependent on the power of the broadband acoustic emissions, and hence the broadband component of the PCD signal variance. In practice, the variance was evaluated for each block of samples (akin to an ensemble average), which was taken as representative of the entire pulse length.

3.3.2 Spectral Decomposition of PCD Data

In analysing data in the frequency domain, broadband emissions were associated with inertial cavitation and subharmonic/harmonic/ultraharmonic emissions with stable cavitation and boiling. The application of a digital comb filter to PCD data

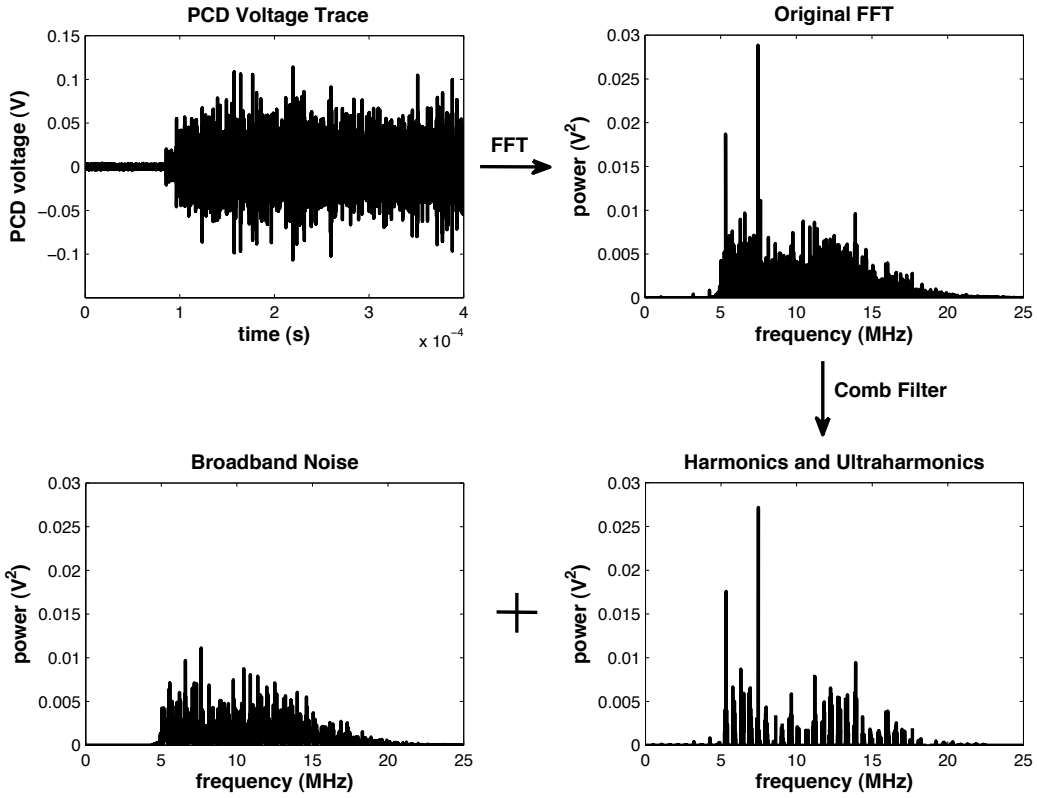


Figure 3.5: An example of a raw PCD data trace (top left) and its corresponding frequency spectrum (top right), which is subsequently decomposed into its various spectral components, as indicated. The data pertains to experimentation in agar using a 1.067 MHz HIFU transducer at 4.14 MPa.

facilitates its decomposition into each of these spectral components, thus alluding to likely bubble behaviour.

Windowed PCD data comprising 25,000 samples was processed using an algorithm that systematically computes the fast Fourier transform (FFT) of the data (based on the Cooley-Tukey algorithm), notch filters out the harmonic content and stores it in a separate array. The subharmonic frequency components are removed by the upstream 5 MHz high-pass hardware filter, whilst the ultraharmonics were found to be indistinguishable from the broadband noise in the *in vitro* work of this chapter. A notch width of 200 kHz was used to remove the harmonic peaks and their principal side lobes, which arise due to leakage. The FFT power level between the

notch limits was subsequently set to zero.

The resulting arrays were plotted in the frequency domain to represent the different components of the original frequency spectrum (see Figure 3.5). The proportions of the PCD signal variance attributable to either inertial or stable cavitation were evaluated subsequent to inversion of the FFTs. Importantly, the relative magnitudes of emissions ascribed to different types of cavitation are largely dependent on the widths of the comb sections and the frequency response of the PCD, amongst other things. Thus, conclusions to the effect of "there is twice as much inertial cavitation as stable cavitation" are without merit.

3.3.3 Passive Cavitation Localisation

A pressure-driven phenomenon, cavitation is not automatically confined to the HIFU focus, just as PCD sensitivity is not entirely restricted to its own focal volume. The spatial extent of the cavitation region may be quantified using time-of-flight information extracted from PCD data.

The method relies upon the time delay between HIFU activation and the detection of a cavitation event by the PCD (refer back to Figure 3.5) (Kennedy et al., 2009). This is attributable to the time of propagation of the incident HIFU beam, from the transducer to an instantaneously excited cavitation nucleus, concatenated with the back-propagation time of the resulting secondary acoustic emissions to the PCD. If the speed of sound in the transmission medium is known, it is a trivial exercise to convert the time to the foremost peak in the corresponding PCD voltage trace to a distance. A threshold of six standard deviations of the foremost 5,000 samples in each data packet was used to distinguish cavitation events from the baseline noise level for bubble localisation purposes.

This "passive localisation" technique is based on two underlying assumptions. Firstly, it is assumed that cavitation is instigated instantaneously - this is particularly valid at excitation pressures in excess of the inertial cavitation threshold. Secondly, cavitation is assumed to occur preferentially along the transducer axis, where the pressure disturbance is greatest. Evidently, the scheme is only useful for identifying the frontal position of a bubble cloud, and is commonly used for warning against pre-focal damage (Kennedy et al., 2009). It gives no indication as to the spatial distribution of individual cavitation events, nor of the relative magnitudes of pre-focal and focal cavitation activity.

To monitor the evolution of a bubble cloud over the course of an exposure, quasi-continuous pulsed insonation is required, leaving upwards of 100 μs between consecutive pulses to ensure that the PCD is recording the basal noise level at the precise moment the HIFU transducer is reactivated.

3.4 Results and Discussion

In this section, the use of different PRFPs to generate thermally relevant levels of cavitation is explored in both agar and PAA TMMs. By isolating the temperature elevation from the PRFP and relating it directly to the cavitation signal, many of the intrinsic factors, such as variations in temperature and nucleation site distribution over the course of an exposure, may be accounted for. Extrinsic factors, including changes in the sensitivities of the insonation and detection equipment over time, are usually managed by good experimental practice. This involves frequent recalibration of experimental equipment.

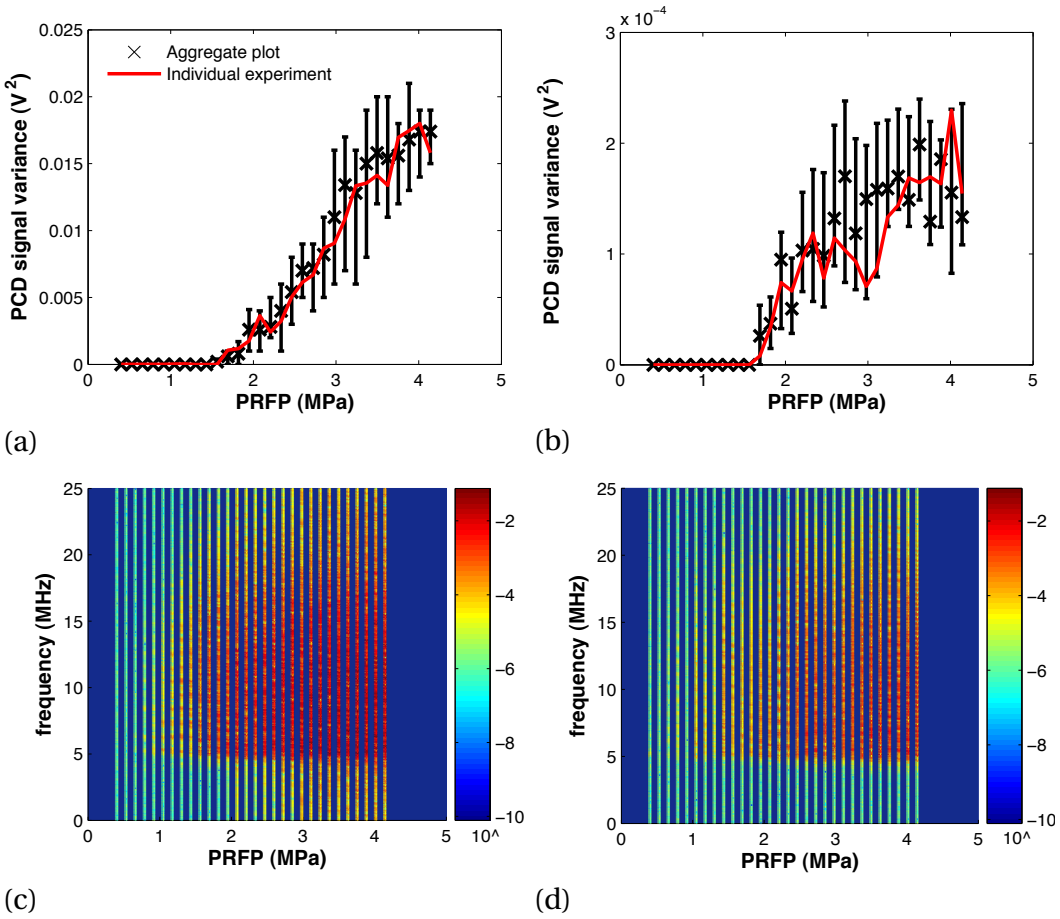


Figure 3.6: (a) and (b) Plots of PCD signal variance (in the absence of digital filtering) versus PRFP for agar and PAA respectively, with exemplary plots obtained from individual experiments overlaid in red. It is important to note that the scale of the abscissa is common to both graphs, whereas the ordinate scales differ by approximately two orders of magnitude. (c) and (d) Corresponding spectrograms from these individual experiments.

3.4.1 Cavitation Threshold Measurements

Preliminary identification of the minimum PRFP required to instigate inertial cavitation over a single HIFU cycle is central to the design of subsequent experimental regimens. Instantaneous cavitation instigation is an essential criterion of the eventual closed-loop feedback controller design, to enable cavitation-based treatment monitoring from start to finish and to maximise the heating benefits proffered by cavitation-inducing HIFU therapy.

Cavitation thresholds were measured by repeatedly exposing each phantom in turn to a sequence of 10-cycle sinusoidal HIFU pulses, gradually increasing in PRFP from 0.40 MPa to 4.14 MPa at 1 s intervals. Remotely detected secondary acoustic emissions were analysed to identify the minimum PRFP above which the PCD signal deviates from the basal noise level. Plots of PCD signal variance (in the absence of digital filtering) versus PRFP for agar and PAA are shown in black in Figures 3.6 (a) and (b), indicating cavitation thresholds of 1.56 MPa and 1.69 MPa respectively. The error bars represent the range of data acquired at each PRFP. Overlaid in red are exemplary plots obtained from individual experiments, whose spectrograms are shown in Figures 3.6 (c) and (d). Interestingly, despite their acoustic similarities, the TMMs yield very different results.

The frequency spectra are clearly dominated by broadband emissions; however, this may be partly due to the short HIFU pulses used: multiplication of the secondary acoustic emissions with a rectangular envelope in the time domain is equivalent to convolution of the frequency spectrum with a sinc function in the frequency domain, the width of which varies inversely with that of the rectangular window. Curiously, the frequency spectrum in PAA at 2.21 MPa comprises a series of peaks located at the harmonics of the fundamental frequency. Examination of the variation of PCD signal voltage with time reveals the periodic occurrence of inertial cavitation events (see Figure 3.7). These events are characterised by sharp impulses, the minima of which are separated by exactly one acoustic cycle. At low pressures, this occurs when the inward force of the inertial collapse is not sufficient to fragment a bubble. Instead, the same bubble grows gradually and contracts violently in synchrony with the ultrasound source. This effect is usually only noticeable when there is a single responsive bubble in the HIFU field.

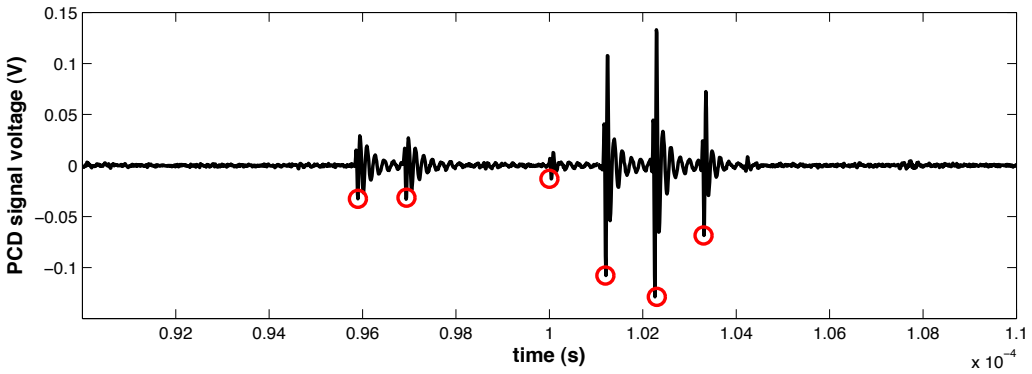


Figure 3.7: PCD voltage trace, demonstrating recursive inertial collapse of a single bubble in PAA subjected to HIFU insonation at a PRFP of 2.21 MPa. Cavitation events are characterised by sharp impulses, the minima of which are highlighted in red.

3.4.2 Dependence of Cavitation on PRFP

Agar and PAA TMMs were exposed to a range of PRFPs at different locations within each phantom using the experimental methods described in Section 3.1. It may be reasonably assumed that the spatial distribution of nucleation sites is initially uniform throughout each phantom and that nuclei depletion during sonication is confined to the focal region. The sonication PRFPs were chosen so as to lie in the pre-threshold, threshold, post-threshold and super-threshold cavitation regimes, whilst all other experimental parameters were kept constant. Each HIFU exposure lasted 2 s, with a 99% duty cycle to enable passive localisation of the frontal position of the ultrasound-induced bubble cloud. Some of the results are presented in Figure 3.8.

Firstly, it is important to note the predominant 4:1 ratio of broadband to harmonic power in the post-threshold and super-threshold regimes. This is a filtering artefact, attributable to the width of the digital notch filter at each harmonic (approximately one fifth of the fundamental frequency), and alludes to mainly broadband activity. In both TMMs, the effect of increasing the PRFP is to increase the corresponding broadband signal variance and local temperature elevation; however,

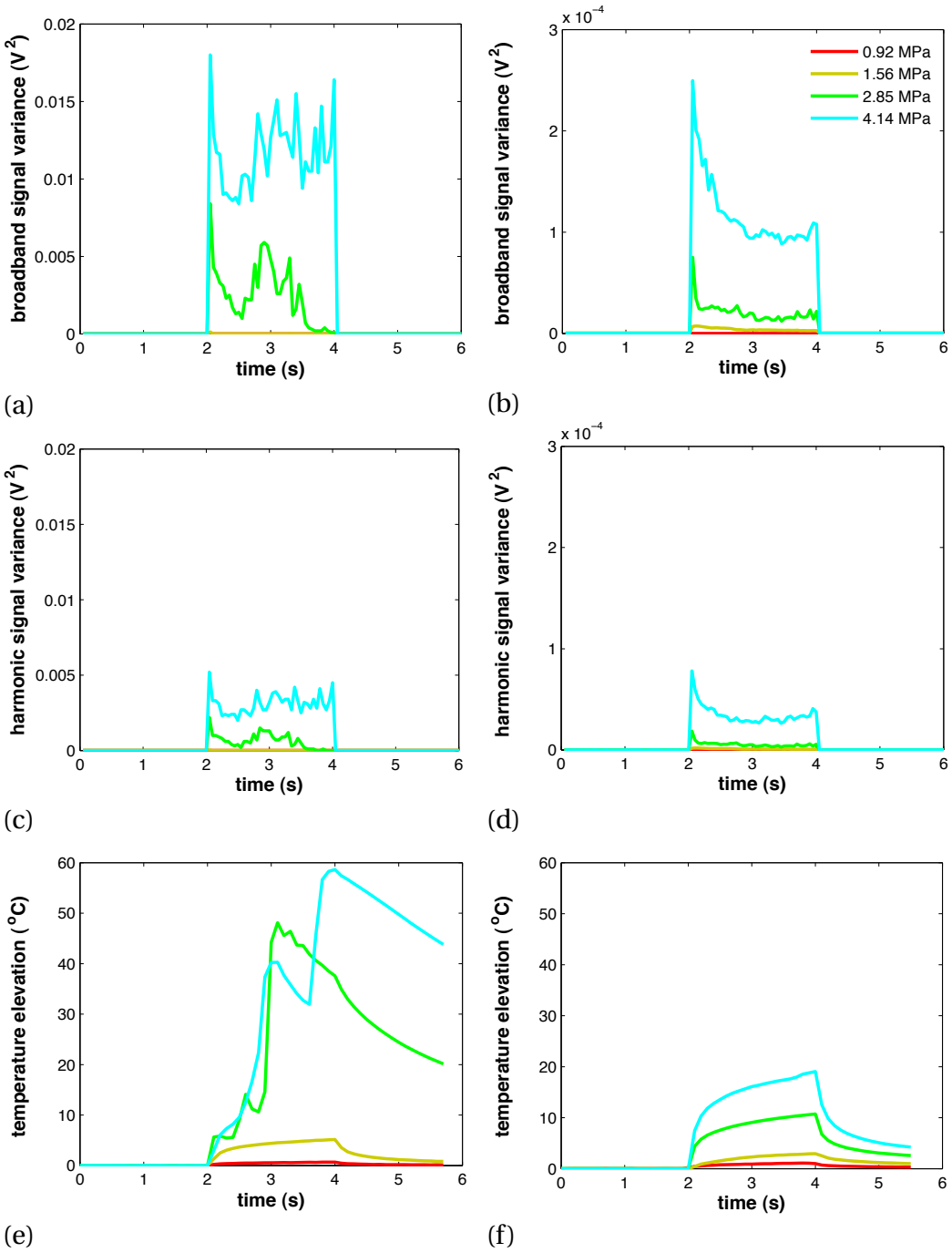


Figure 3.8: Illustration of the variation of cavitation activity (broadband and harmonic) (a to d) and temperature elevation (e,f) with PRFP in agar and PAA TMMs (left and right columns respectively). The effect of increasing the PRFP is to increase the broadband and harmonic signal variances, and the temperature elevation. Note that the ordinate scales are not the same.

this does not necessarily imply that the two are related.

In agar, cavitation levels are consistently higher compared with PAA (the ordinate scales of the broadband and harmonic variance plots in Figures 3.8 (a) and (c) differ from those of PAA by approximately two orders of magnitude). In the pre-threshold and threshold regimes, the broadband signal variances are predictably low, and the corresponding temperature elevations adopt a smooth profile. Doubling the cavitation threshold PRFP amplifies the broadband signal variance by a factor of 100, and causes the temperature elevation to deviate significantly from the characteristic fin shape. A further increase in PRFP yields still higher cavitation levels and an augmented temperature elevation. Importantly, it is not possible to deduce from the graphs whether this augmentation in temperature elevation between the post-threshold and super-threshold regimes is due to visco-thermal heating at the fundamental frequency at different PRFPs, or whether the increase in broadband noise is responsible. Moreover, the effect of increasing PRFP in PAA is at odds with agar, in that there is no obvious thermal advantage induced by cavitation.

Figure 3.9 is a graph of temperature elevation versus PRFP, of which each point represents one of the experiments included in Figure 3.8. The temperature elevation was also computed using a finite-difference time-domain simulation of Equation 1.2 for a homogeneous medium and the focused pressure field as the heat source, where the thermal conductivities and specific heat capacities for both phantoms were assumed to be equivalent to those of water (k = 0.61 $\mathrm{Wm^{-1}K^{-1}}$ and c = 4.18 $\mathrm{kJkg^{-1}K^{-1}}$) (Mills, 1999). Perfusion was omitted and heat absorption was assumed to arise only from ultrasound attenuation. A correction factor was also applied to account for the thermocouple artefact.

In the case of the PAA tissue phantom, the near-parabolic temperature curve points to cavitation-enhanced heating *not* being a dominant heating mechanism.

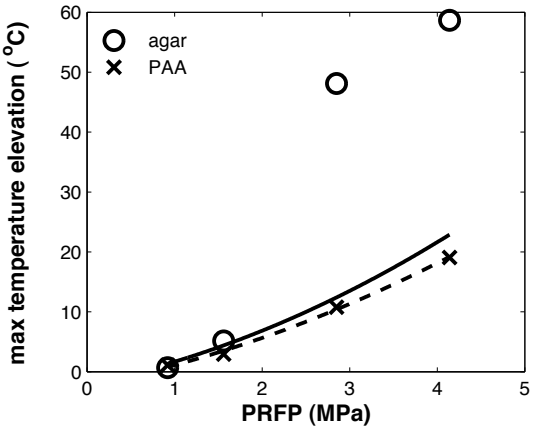
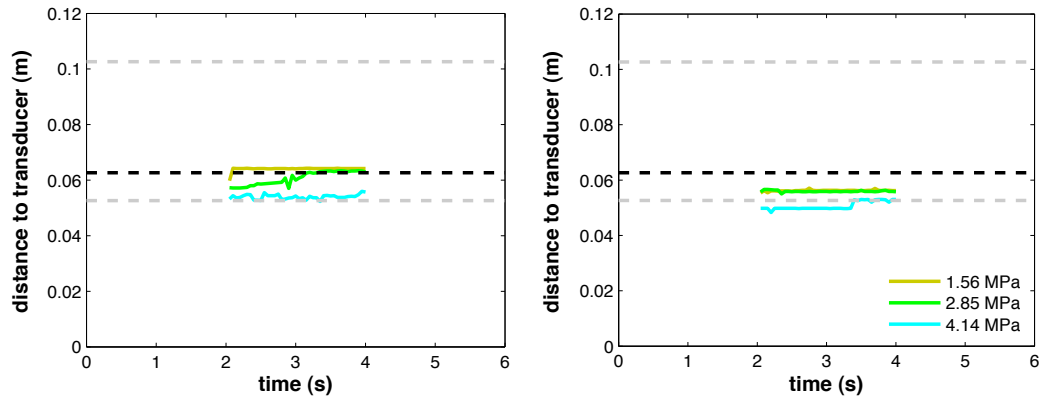


Figure 3.9: Maximum temperature elevation versus PRFP from HIFU exposures undertaken in agar and PAA. This graph summarises the results presented in Figure 3.8, showing how temperature elevation varies parabolically with PRFP in the case of PAA, whilst the curve corresponding to the agar phantom exhibits an altogether different shape. Simulated temperature elevations are also shown for agar (solid line) and PAA (dashed line).

In contrast, the temperature curve corresponding to the agar TMM exhibits an altogether different shape, its deviation from a parabola indicative of significant cavitation-enhanced heating. Though there is some run-to-run variation, this behaviour pattern was consistently observed across all of the phantoms used.

Finally, it is instructive to consider the trajectory of the bubble cloud relative to the HIFU transducer for each of the experiments presented in Figures 3.8 and 3.9, bar those in which cavitation did not occur. The water-phantom interfaces are demarcated in grey and the focal distance in black. In agar, the minimum distance to the bubble cloud decreases with increasing acoustic intensity. Moreover, in contrast to previous studies, in which shielding by the bubble cloud causes it to grow *towards* the HIFU transducer (Bailey et al., 2001), the cavitation onset location does not change significantly over the course of these exposures. On occasion, the bubble cloud even moves *away* from the transducer: this may be due to the sizeable acoustic radiation force (ARF) acting over the time-varying bubble cluster in the direction



(a) (b)

Figure 3.10: Passive localisation of ultrasound-induced bubble clouds in agar (a) and PAA (b) TMMs at different PRFPs. The HIFU transducer is located along the abscissae. The water-phantom interfaces are demarcated in grey and the focal distance in black.

of the HIFU beam and/or liquefaction of the phantom at sufficiently high temperatures - the melting point of agar is 85 °C and, despite the temperatures recorded at the focus exceeding room temperature by around 60 °C in the super-threshold regime, pre-focal temperature elevations may well be higher. In PAA, cavitation always occurs pre-focally, to the extent that, in the super-threshold regime, cavitation was found to occur at the water-phantom interface.

3.4.3 Dependence of Cavitation on Nuclei Distribution

Whilst the previous section has successfully demonstrated that the broadband component of the PCD signal variance may be altered by virtue of the insonating PRFP, this does not take into account the inevitable variation in the population of nucleation sites during the course of an exposure. Subsequent HIFU excitation at previously insonated phantom locations yields very different results, whereby the cavitation signal is dependent not only on the PRFP, but also on the cavitation history of the target medium.

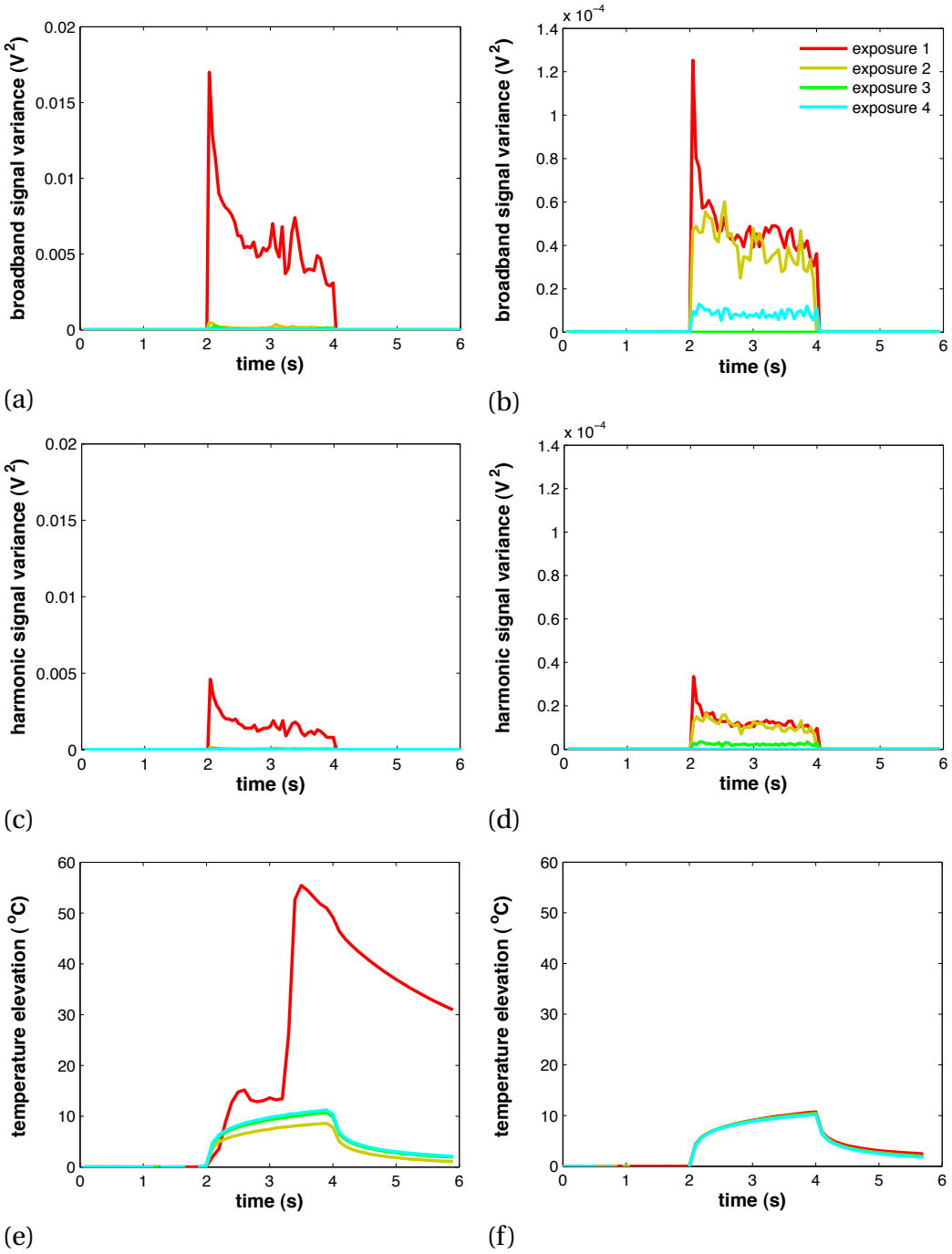
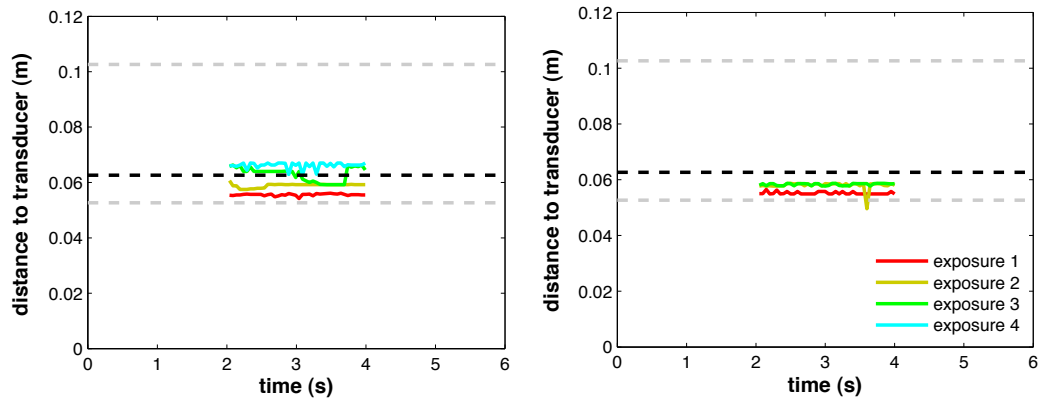


Figure 3.11: Illustration of the variation of cavitation activity (broadband and harmonic) (a to d) and temperature elevation (e,f) with repeated HIFU exposures in agar and PAA (left and right columns respectively) at a PRFP of 2.85 MPa.



(a) (b)

Figure 3.12: Passive localisation of ultrasound-induced bubble clouds in agar (a) and PAA (b) phantoms subjected to repeated HIFU sonications at a PRFP of 2.85 MPa. The HIFU transducer is located along the abscissae. The water-phantom interfaces are demarcated in grey and the focal distance in black.

To investigate the effect of nuclei depletion on cavitation activity and the associated temperature elevation, successive exposures were conducted at a single location. Using the excitation parameters prescribed in Section 3.4.2, each TMM location was used for up to 4 exposures, without modification to the operating conditions between exposures. The results of two such experiments conducted at a PRFP of 2.85 MPa are presented in Figure 3.11. These pertain to both agar (left column) and PAA (right column) TMMs. Predictably, the temperature elevation in PAA is unaffected by variations in cavitation activity; however, a marked decrease in the broadband signal variance between the first and subsequent exposures in agar is seen to have a profound impact on the corresponding temperature elevations.

Moreover, the passive localisation plots provided in Figure 3.12 affirm that the minimum distance to the bubble cloud is not only a function of the PRFP, dependent also on the cavitation history of the exposed region.

3.4.4 Correlation of Temperature Elevation with Cavitation

For PAA phantoms manufactured according to the protocol prescribed in Section 3.1.1, the onset of inertial cavitation does not generate any thermal advantage over and above that induced by viscous absorption at the fundamental frequency. This is in stark contrast to the agar phantom composition, in which massive thermal gains may be realised by choosing a sufficiently high PRFP to induce inertial cavitation, bearing in mind the cavitation history of the target. If an empirical relationship between temperature elevation and inertial cavitation were to be established, it could form the basis of a control system whose primary function is to sustain thermally relevant levels of inertial cavitation.

The effect of the migrating bubble cluster is to complicate any attempt to correlate instantaneous values of temperature rise and inertial cavitation activity because the thermocouple probe location is not necessarily coincident with the region of greatest heat deposition. Figure 3.13 is a graph of *maximum* cavitation-induced temperature elevation in agar plotted against *total* broadband energy for a range of 2 s exposures performed at different PRFPs but with uniform duty cycle (99%). This includes measurements obtained from multiple exposures at a single TMM location. The total broadband energy is evaluated as the integral of the broadband signal variance profile, whilst the temperature elevation in the absence of inertial cavitation - that is, after many HIFU exposures at a single phantom location - has been subtracted from the composite temperature elevation in order to identify the contribution of cavitation-related effects alone.

Crucially, there appears to be a threshold energy (approximately 0.003 V^2s), beyond which the temperature elevation saturates, presumably due to: (i) reaching of an upper limit of the bubble number density that can be sustained within a given volume of material due to bubble-bubble interactions; (ii) suppression of inertial

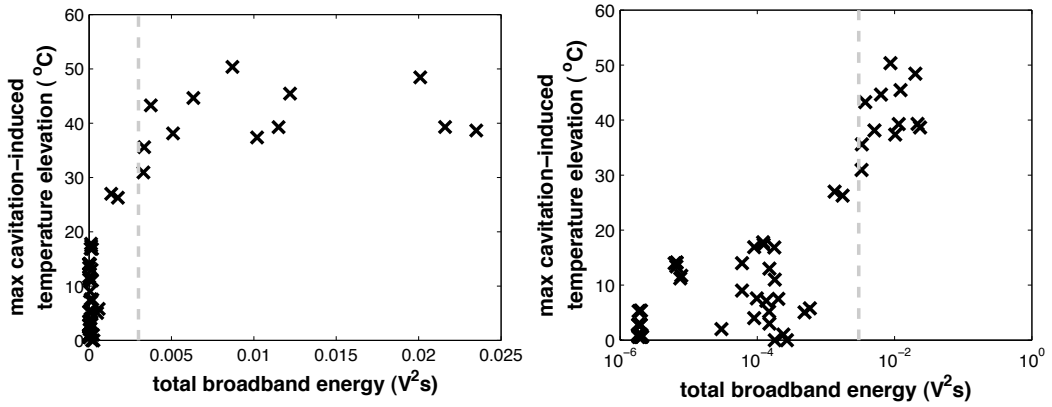


Figure 3.13: Maximum cavitation-induced temperature elevation in agar as a function of total broadband energy using (a) a linear scale along the abscissa and (b) a log scale. There is a threshold energy (grey) beyond which the temperature elevation saturates.

cavitation activity due to increased vapour pressure; and/or (iii) shielding of focal cavitation activity by increasing pre-focal bubble activity. At the range of pressures used in this study, bubble dissolution during acoustic excitation is unlikely. This is an important result as it suggests that HIFU input beyond that required to achieve total broadband energies on the order of 0.003 V^2s is superfluous to requirements *at the focus*. Moreover, below this threshold value, Figure 3.13 (b) shows that there is no obvious relationship between temperature elevation and total broadband energy, although it may well be the case that the experimental procedure and analytical methods adopted are inadequate where low broadband energies are involved.

3.4.5 Cavitation Enhancement in Polyacrylamide

Given the acoustic similarities of agar and PAA (see Table 3.1 for density, sound speed and attenuation properties), it is interesting to discover that they respond quite differently to acoustic stimuli. In particular, significantly higher levels of inertial cavitation are generally observed in agar compared with PAA for the same in-

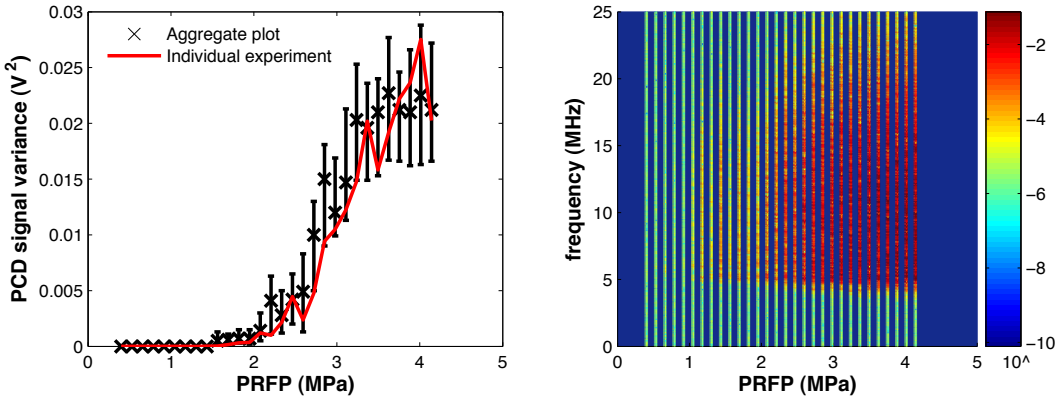
sonation conditions. Disparities in other physical properties, such as porosity, may be responsible for this observation: a more porous TMM would have a higher gas content, which may or may not be replaced with water once suspended in the experimental tank, depending on the diffusion properties of the water-phantom system.

Trying to understand the structural differences between TMM matrices is beyond the scope of the present work; however, it is hypothesised that the contrasting results may be attributed to a fundamental difference in the availability of suitable cavitation nuclei. Previous work has demonstrated that the addition of rough, hydrophobic talc microparticles to PAA-based TMMs can augment cavitation levels by several orders of magnitude (Arora et al., 2011). Thus, it is instructive to explore whether an increase in broadband energy impacts favourably on the corresponding temperature elevation. Accordingly, the PAA phantom composition was adapted to include 3.95 g of talc particles (Johnson & Johnson).

3.4.5.1 Cavitation Threshold Measurements

The cavitation threshold of the modified PAA phantom was determined using the procedure outlined in Section 3.4.1, yielding Figure 3.14. The curve overlaid in red pertains to a single cavitation threshold experiment, for which the corresponding spectrogram is shown alongside.

Whilst the inertial cavitation threshold is not significantly altered by the addition of talc microparticles, there is a marked increase in the magnitude of the recorded cavitation levels, to the extent that they are of the same order of magnitude as previously observed in agar.



(a) (b)

Figure 3.14: (a) Aggregate plot of PCD signal variance versus PRFP for the modified, talc-infused PAA phantom composition, on which the results from an individual cavitation threshold experiment is overlaid in red. (b) Spectrogram corresponding to this experiment.

3.4.5.2 Dependence of Cavitation on PRFP

The results from four HIFU exposures undertaken at a range of PRFPs are summarised in Figure 3.15. All other excitation parameters are as specified in Section 3.4.2. Evidently, the increase in cavitation activity brought about by the addition of talc microparticles is found to have a profound effect on heating rates. The 4:1 ratio of broadband to harmonic power in the post-threshold and super-threshold regimes suggests that the acoustic response is in fact purely broadband, as intimated by the spectrogram in Figure 3.14.

The passive localisation plots are near-identical to those obtained in the unmodified PAA TMM, as are the temperature elevation profiles from the pre-threshold and threshold operating regimes. The latter result indicates that the attenuation of the TMM is unaltered by the addition of talc microparticles. In the post-threshold and super-threshold regimes, the PCD signal variance plots are very similar and there is no obvious thermal advantage at the focus to entering the super-threshold regime. Whilst the contribution to heating from inertial cavitation might at first glance ap-

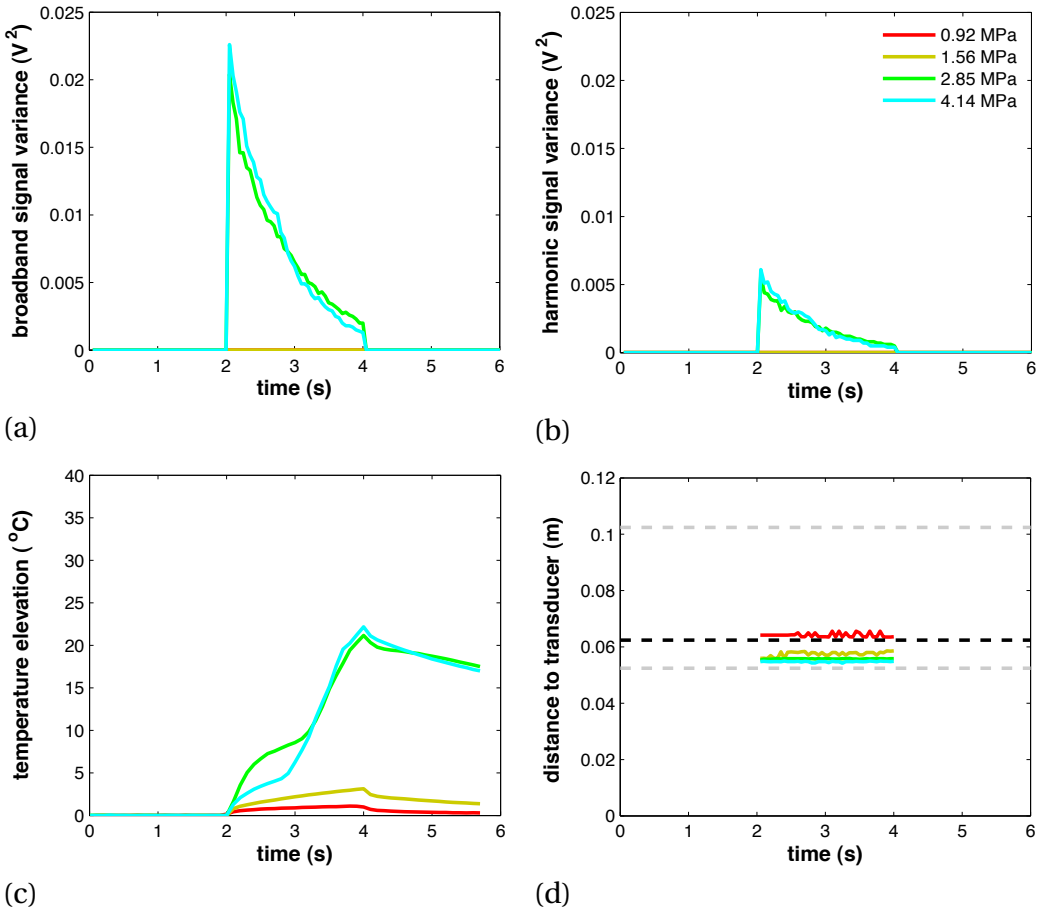


Figure 3.15: Illustration of the variation of cavitation activity (broadband and harmonic) (a and b) and temperature elevation (c) with PRFP in talc-infused PAA TMMs. The effect of increasing the PRFP is to increase the PCD signal variance and the temperature elevation. The trajectories of the bubble clouds are also shown in (d).

pear to be less than that experienced in agar, it is important to remember that temperature is measured at a single location, whereas cavitation events are likely to be spatially distributed.

3.4.5.3 Dependence of Cavitation on Nuclei Distribution

The results presented in Figure 3.16 pertain to a series of four successive exposures undertaken at a PRFP of 2.85 MPa at a single location within a talc-infused PAA phantom. Curiously, despite a gradual reduction in total broadband energy from

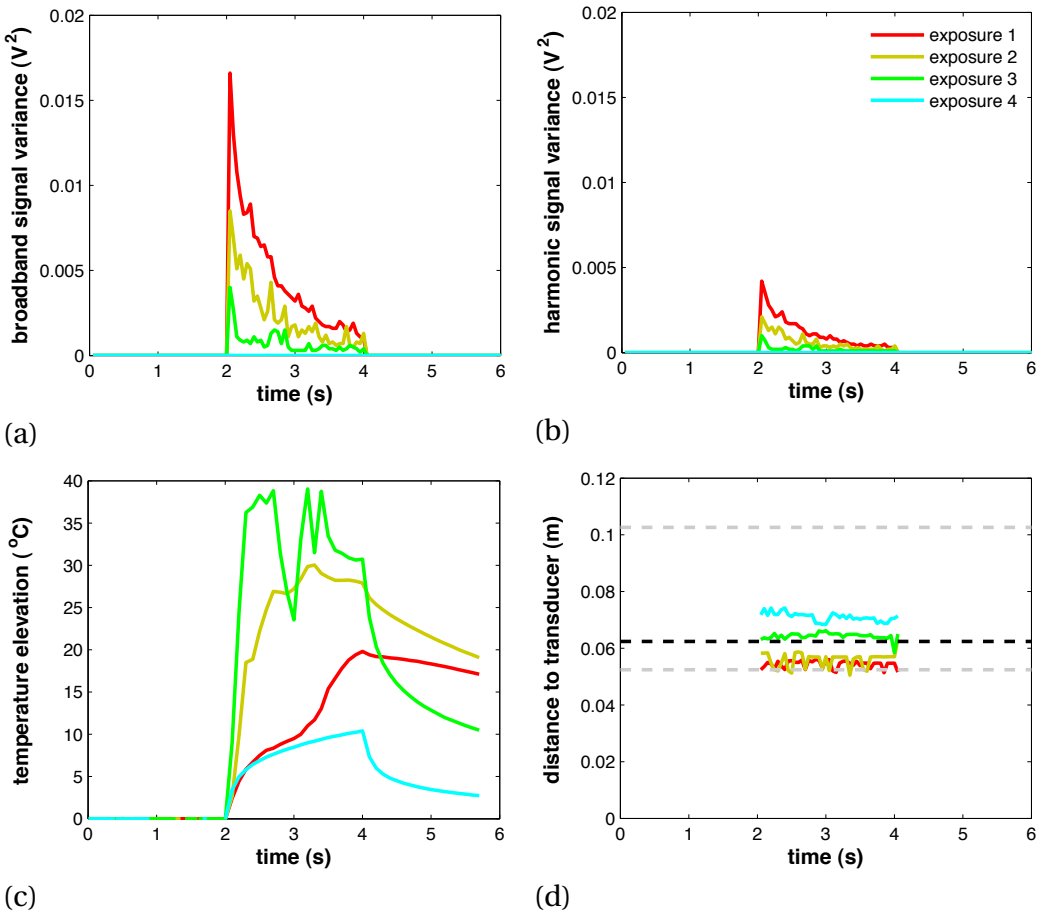
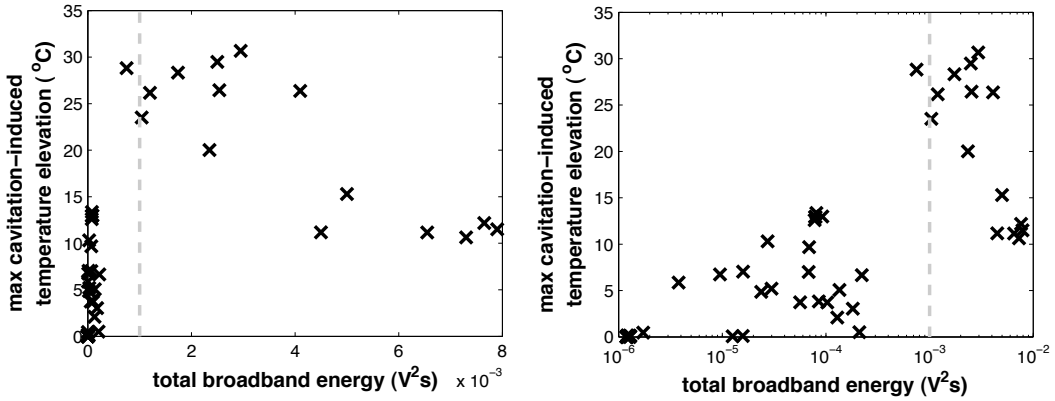


Figure 3.16: Illustration of the variation of cavitation activity (broadband and harmonic) (a and b) and temperature elevation (c) with repeated HIFU exposures in a talc-infused PAA TMM at a PRFP of 2.85 MPa. The trajectories of the bubble clouds are also shown in (d).

one exposure to the next, the temperature elevation actually increases between exposures one to three. This may be explained by way of the passive localisation plots. It is no coincidence that the greatest temperature elevation is recorded during the third exposure, when the cavitation onset location is placed consistently at the focal distance. This is an important result, as it suggests that the thermocouple is not necessarily co-located with the point of maximum heat deposition.



(a) (b)

Figure 3.17: Maximum cavitation-induced temperature elevation in talc-infused PAA as a function of total broadband energy using (a) a linear scale along the abscissa and (b) a log scale. The maximum focal temperature elevation peaks at a total broadband energy of approximately 0.001 V^2s, beyond which it reduces significantly due to increased pre-focal activity.

3.4.5.4 Correlation of Temperature Elevation with Inertial Cavitation

Finally, Figure 3.17 is a graph of *maximum* cavitation-induced temperature elevation plotted against *total* broadband energy for a range of 2 s exposures performed at different PRFPs but with uniform duty cycle, including the results obtained from multiple exposures at a single TMM location. Unlike agar, the focal temperature elevation in talc-infused PAA peaks at a total broadband energy of approximately 0.001 V^2s, beyond which it reduces significantly due to increased pre-focal activity. Moreover, below this threshold value, Figure 3.17 (b) shows that there is no obvious relationship between temperature elevation and total broadband energy, although it may well be the case that the experimental procedure and analytical methods adopted are inadequate where low broadband energies are involved.

These results highlight the importance of monitoring the spatial distribution of cavitation events to ensure preferential heating at the HIFU focus.

3.5 SUMMARY

Though an inherently stochastic phenomenon, cavitation has been shown to occur reliably and reproducibly in both agar- and PAA-based tissue mimicking phantoms subjected to a range of sonication PRFPs spanning the pre-threshold, threshold, post-threshold and super-threshold regimes. Despite their similar acoustic properties, the PCD signals and associated temperature elevations were found to vary considerably between the three different TMM compositions included in this chapter.

In 3% agar phantoms, the secondary acoustic emissions recorded by the PCD transducer were shown to increase in intensity with increasing PRFP. Whereas in the threshold regime cyclic inertial cavitation of lone bubbles was found to generate harmonic spectral components above and beyond the inherent filtering aftefact, in the post-threshold and super-threshold regimes, broadband noise was dominant. Moreover, the results from successive HIFU exposures at a single TMM location revealed there to be a manifest dependence of inertial cavitation on the availability of suitable nucleation sites, in addition to the PRFP. This is an important consideration because clinical HIFU targets do not have pre-defined nuclei populations. An empirical relationship was thus established between focal temperature elevation and inertial cavitation activity, the latter of which depends both on the HIFU parameters and the dynamically evolving nuclei population. Specifically, there has been shown to exist a threshold level of total broadband energy (0.003 V^2s) in agar, beyond which cavitation-enhanced heating *measured at the thermocouple location* emerges as a dominant heating mechanism.

Moreover, a similar outcome was observed in PAA phantoms infused with rough, hydrophobic talc microparticles. The addition of talc served to augment cavita-

tion levels by approximately two orders of magnitude. Broadband emissions were predominant in the post-threshold and super-threshold regimes, causing the corresponding temperature profiles to deviate from the characteristic fin shape. A threshold level of broadband activity for cavitation-enhanced heating was thus similarly established in modified PAA phantoms (0.001 V^2s); however, an upper limit of broadband energy also emerged, beyond which the focal temperature elevation drops off due to pre-focal heating. This is an exciting result as it suggests that more efficient use of acoustic input energy may be possible.

Evidently, a major shortcoming of the experimental setup adopted in this chapter is the assumption that the point of maximum heat deposition must be coincident with the HIFU focus. Whilst this may be true for viscous absorption at the fundamental frequency in the absence of scatterers, the presence of cavitating bubbles greatly complicates the problem. The take-home message is that cavitation-enhanced heating is possible subject to the availability of suitable nucleation sites and sufficiently high collapse energies; however, the broad spatial distribution of cavitation events is not accurately represented by temperature measurements at a single location.

Finally, it is important to consider the findings of this chapter in a clinical context. Cavitation events occurring at the thermocouple boundary layer may result in highly localised temperature elevations with unfeasibly steep gradients. It is presently unclear how this translates to gross effects in mammalian tissue. Moreover, cell damage is not necessarily restricted to thermal effects and mechanical disruption of cell structure must also be considered. The following chapter aims to address some of these uncertainties by extending the *in vitro* work presented here to an *ex vivo* experimental model.



CHAPTER 4

CAVITATION-ENHANCED HEATING *Ex Vivo*

Pinpointing the optimal combination of HIFU parameters for cavitation instigation in animal tissue is notoriously difficult due to the heterogeneous nature of the local microenvironment and the considerable variation in acoustic properties between subjects. This chapter considers the use of different HIFU insonation frequencies and PRFPs to investigate cavitation inception in freshly excised bovine liver tissue. The ability of exogenous cavitation nuclei, including commercially available UCAs and custom-made sonosensitive nanoparticles, to augment cavitation levels is explored and the corresponding secondary acoustic emissions correlated with thermal ablation. The subsequent introduction of a linear array to the experimental setup enables cavitation detection and quantification in two dimensions, albeit at significant computational expense.

A threshold phenomenon, cavitation-enhanced heating has been successfully demonstrated in both agar- and PAA-based tissue-mimicking phantoms. A logical progression is to verify that the emergent empirical relationship between heating and total broadband energy *in vitro* extends to biological tissue. The abundance of inhomogeneities present in the HIFU field tends to distort both the forward- and backward-propagating ultrasound waves. This additional influence confounds an already complex problem.

Experimentation in live animals at this early stage would be highly premature and prohibitively expensive. In contrast, adapting the *in vitro* experimental proto-

col to facilitate *ex vivo* analysis of biological tissue entails minimal modification to the existing setup, and allows direct comparison of the two data sets. This chapter explores the use of different HIFU parameter combinations to reliably instigate cavitation in freshly excised bovine liver, and considers the effect of exogenous nuclei on both cavitation and heating. In addition to passive cavitation monitoring using a single-element PCD, passive acoustic mapping is employed to quantify cavitation activity in two dimensions (Gyongy and Coussios, 2010; Jensen et al., 2011), such that the spatial distribution of cavitation events may be correlated with the extent of lesioning.

The results presented build on previous work by Nandlall et al. (Nandlall et al., 2011) and Jensen et al. (Jensen et al., 2011) involving the use of *ex vivo* hepatic tissue to investigate lesioning following HIFU sonication. Nandlall et al. developed an experimental protocol for assessing tissue damage in bovine liver, whilst Jensen et al. have successfully demonstrated the use of passive acoustic mapping to demarcate lesions. Work published by Tran et al. (Tran et al., 2003) further motivated the decision to investigate the capacity of exogenous nuclei to augment cavitation levels.

Importantly, the work presented in this chapter pertains specifically to healthy tissue due to lack of a suitable bovine carcinoma model. As discussed in Section 1.3, tumour physiology is vastly different to that of healthy tissue. Nevertheless, preliminary work conducted in the absence of a tumour mass is certainly a step in the right direction.

4.1 Optimisation of HIFU Insonation Conditions

Understanding bubble behaviour in animal tissue subjected to a range of HIFU parameter combinations is key to establishing the operational limits of the *ex vivo* system in its present form, and its propensity for inducing cavitation-enhanced heating. This section examines the impact of insonation frequency (0.508 MHz and 1.067 MHz) and PRFP on heat generation and tissue damage.

Bovine liver is readily available, inexpensive to procure, and its relatively large size facilitates extraction of a tissue sample in which multiple exposures may be carried out. Moreover, its biochemistry is similar to that of human liver, as are its acoustic properties, whose broad confidence intervals overlap considerably with those of humans and other mammals.

4.1.1 Experimental Setup

Figure 4.1 is a schematic representation of the experimental setup adopted for the *ex vivo* work presented in this section. Adapted from Figure 3.1, an enclosed bovine liver sample replaces the tissue-mimicking phantom, whilst the water tank was maintained at 37 °C to emulate an *in vivo* environment as far as practicably possible. The top edge of the tissue holder was positioned slightly above the water level in the tank to prevent cross contamination during insertion of a thermocouple probe. The exclusion of perfusion effects is, of course, a limiting factor; however, this would greatly complicate the experimental model and impose further restrictions on the number of exposures that may be undertaken in each tissue sample. The following sections describe the various experimental and analytical procedures pertinent to the revised setup.

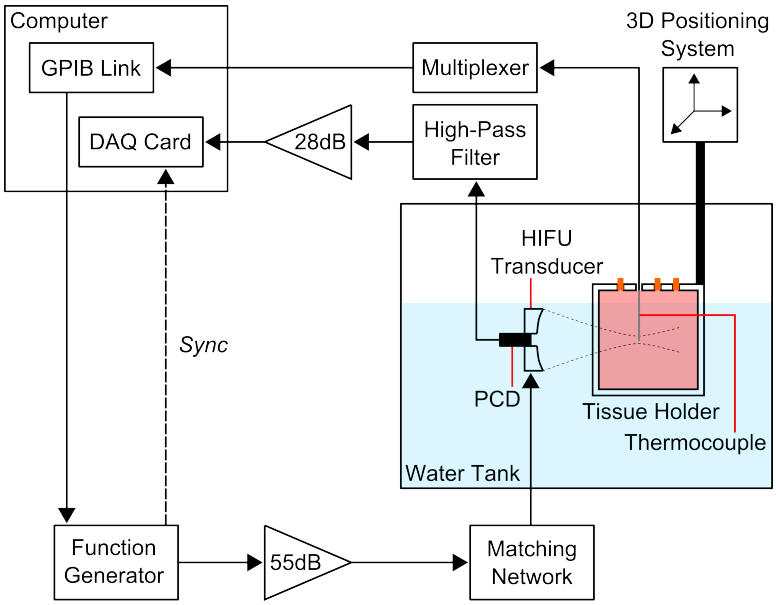
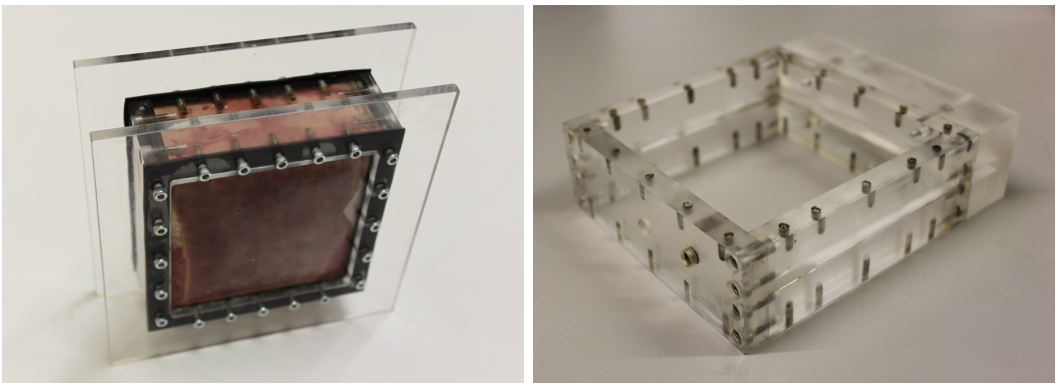


Figure 4.1: Overview of the experimental setup for acquiring cavitation and thermal data during *ex vivo* experimentation. The water level in the tank is maintained below the top edge of the tissue holder to prevent cross contamination.

4.1.1.1 Tissue Preparation and Usage

Experimental data was obtained from adult ox livers, sourced from a nearby abattoir and used within 4 hours of slaughter. The livers were cut to fit snugly inside a custom-made Perspex holder with internal dimensions 100 mm x 100 mm x 40 mm, making sure to retain the collagenous capsule on one of the larger faces of the cuboid. This face was positioned closest to the HIFU transducer during HIFU exposure to mimic the propagation path of an ultrasound wave through the body, and coupled to the water tank using an acoustically transparent biaxially oriented polyethylene terephthalate (boPET) window, or Mylar film. The rear face was sealed in much the same way to prevent saturation of the PCD signal by reflections of the incident HIFU wave.

Prior to HIFU insonation, each tissue sample was immersed in 4 L of 1X Dulbecco's phosphate-buffered saline (PBS) at room temperature and degassed at



(a) (b)

Figure 4.2: (a) Photograph of the Perspex liver holder, including acoustically transparent Mylar windows sealing the front and rear tissue faces. (b) Bespoke liver cutting device, including blade guides.

0.2 bar for 30 minutes to remove some of the bubbles which will have inserted themselves into the tissue matrix during its handling. Once degassed, the tissue was inserted into its holder to form a sealed system devoid of any conspicuous gas bubbles (see Figure 4.2 (a)). When transferring the tissue to the holder, care was taken to ensure that the liver was surrounded by degassed PBS at all times so as to minimise the ingress of air bubbles. A-line ultrasound was subsequently used to confirm the absence of inconspicuous air bubbles along the path of HIFU propagation. On occasions where it was necessary to obtain temperature measurements, one of numerous sealed holes on the uppermost edge of the holder was unplugged and a thermocouple inserted along the mid-plane.

The three-axis motorised positioning system was then used to locate up to 36 irradiation sites on a 10 mm^2 spaced grid at a depth of 20 mm behind the front face of the cuboid. When required, a thermocouple alignment procedure was carried out in the usual way (see Section 3.1.4). Subsequent to HIFU insonation, each liver sample was removed immediately from its holder and bisected along the mid-plane parallel to the front face of the tissue sample using a bespoke cutting device (see Figure 4.2 (b)) for lesion identification. Lesions are clearly identified by regions of

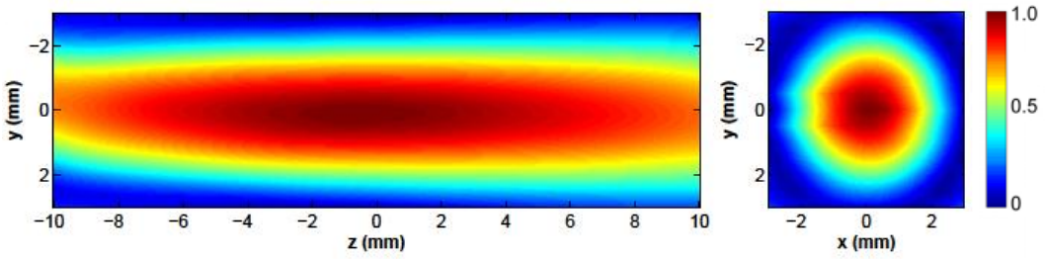


Figure 4.3: Normalised longitudinal and transverse pressure profile sections of the 0.508 MHz focused HIFU transducer, taken through the focal maximum. The focal volume is ellipsoidal, with strong transverse focusing and weak axial focusing.

increased stiffness, blanching, and occasional pitting.

4.1.1.2 HIFU Generation and Passive Cavitation Detection

In addition to the 1.067 MHz HIFU transducer described in Section 3.1.2, a 0.508 MHz transducer (Sonic Concepts, H107D-013) of the same construction and geometry was used to investigate the effect of excitation frequency on cavitation inception and lesion formation. Low-frequency excitation is ideal for deep treatments and is associated with lower cavitation thresholds. In contrast to HIFU insonation at 1.067 MHz, the 0.508 MHz transducer was used in combination with a 5 MHz PCD (Olympus, V309-SU), bandwidth 2-8 MHz, and a 2 MHz high-pass filter (Allen Avionics) to suppress the low-order harmonics whilst retaining broadband sensitivity. Its free-field calibration in water revealed the transverse focal width and axial focal depth at half maximum to be 3.2 mm and 24.0 mm respectively (see Figure 4.3).

4.1.2 Data Analysis

Cavitation and thermal data was processed as per the methods described in the previous chapter (see Section 3.3), with one small modification: the comb filter used to disaggregate the PCD data was modified to include half-harmonics also. The notch width remained unaltered, as did the window function.

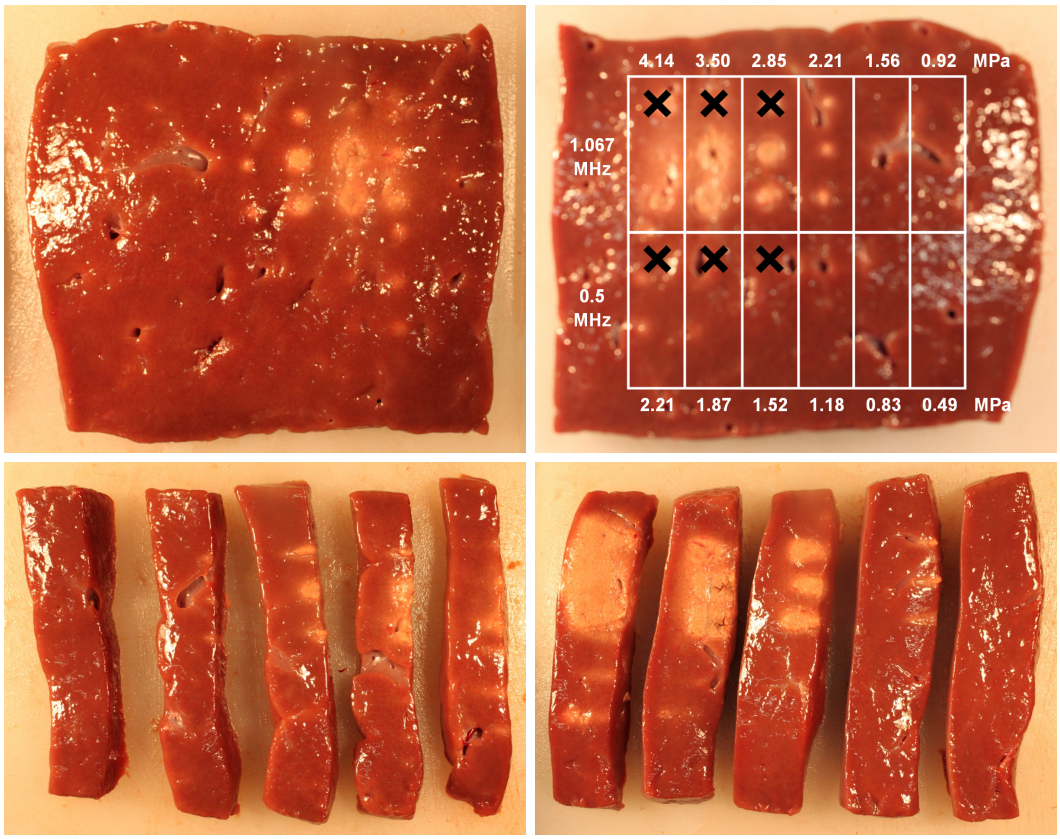


Figure 4.4: Photographs of the rear (top left) and front (top right) portions of a tissue sample subsequent to bisection along its mid-plane. At higher frequencies and pressures, lesions are weighted towards the front half (bottom right) as opposed to the back half (bottom left) of the sample. The duty cycle and exposure duration are uniformly 99% and 30 s respectively.

4.1.3 Results and Discussion

Experimentation in bovine liver lacks the reproducibility of *in vitro* studies due to its inherent heterogeneity and widely variant physical properties. Accordingly, eight bovine livers were experimented upon in this section to provide a broad overview of the effects of HIFU on both cavitation and heating.

4.1.3.1 Dependence of Cavitation on Frequency and PRFP

Figure 4.4 is an example of a liver sample, which has been bisected subsequent to HIFU exposure at two different sonication frequencies (0.508 MHz and 1.067 MHz) and a duty cycle of 99% for 30 s. Importantly, the range of HIFU input voltages is common to both frequencies, yielding inequivalent PRFP ranges. Three identical HIFU exposures were carried out for each parameter combination and, when lesioning did occur, it was found to do so consistently across these multiple exposures. Conversely, cavitation activity was seen to vary considerably. This suggests that cavitation activity is not well correlated with lesion formation.

Cavitation data from the exposures tagged with a black cross in Figure 4.4 is presented in Figure 4.5. The lower halves of the PRFP spectra have been excluded since they do not yield any cavitation events. Importantly, the solid black line, representing the minimum distance to the transducer from the bubble cloud, indicates that the PCD signal has deviated from its basal noise level by at least six standard deviations. Given that the ordinate axes of the PCD signal variance plots have been adjusted to have the same scale, this is a useful tool for identifying whether or not cavitation has occurred.

Current understanding of inertial cavitation predicts that low-frequency HIFU excitation should lead to lower inertial cavitation thresholds. Indeed, cavitation is seen to occur at a PRFP as low as 1.52 MPa in the case of 0.508 MHz insonation, compared with 3.50 MPa at a frequency of 1.067 MHz; however, this is dominated largely by harmonic and ultraharmonic frequency components. At 0.508 MHz, the associated PRFPs are potentially too mild to generate significant non-linear heating effects, whilst the distinct lack of lesioning rules out boiling as a possible explanation for the substantial harmonic and ultraharmonic content.

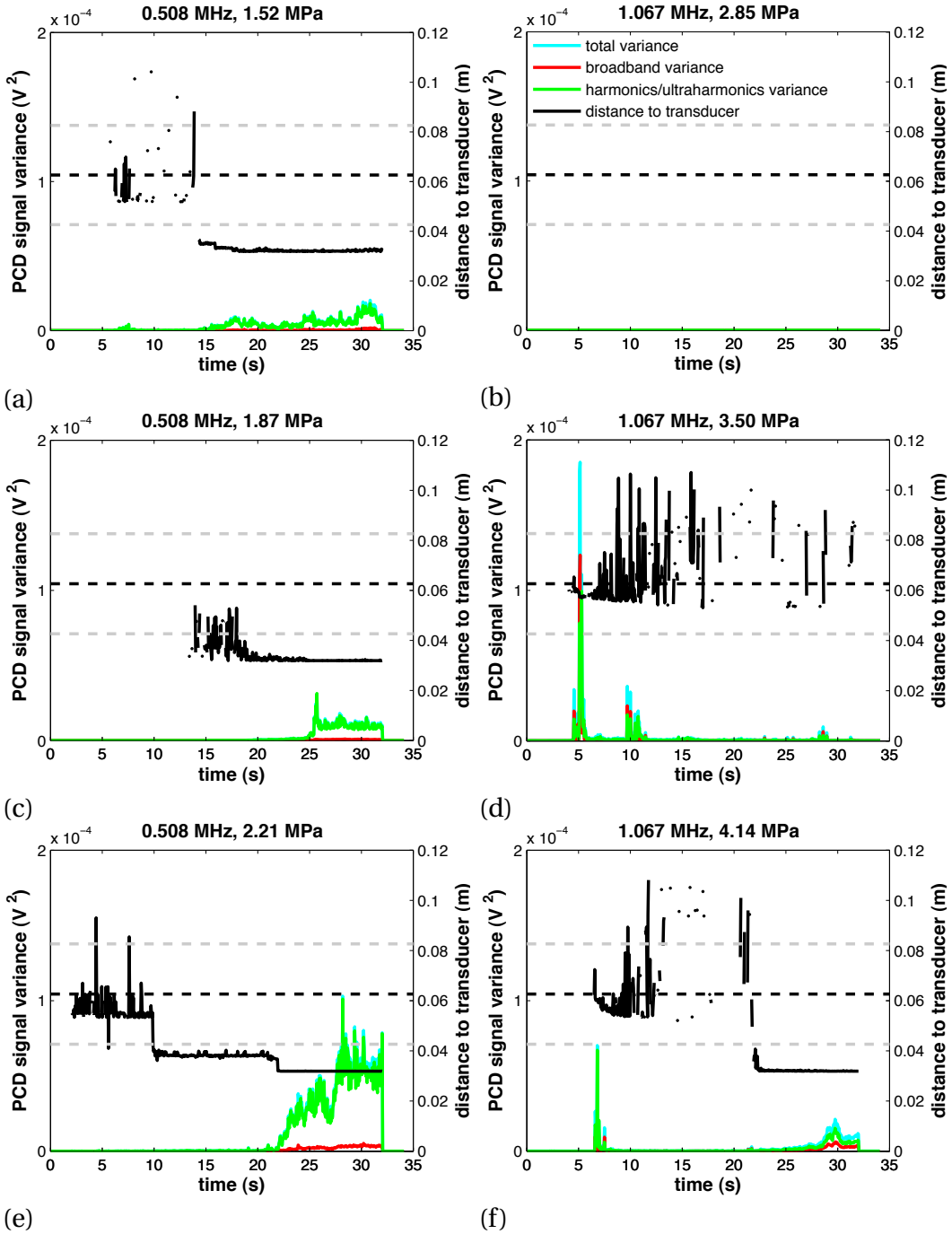


Figure 4.5: Cavitation data from a range of HIFU exposures at 0.508 MHz (left column) and 1.067 MHz (right column). The corresponding PRFPs increase from top to bottom, that is from (a) through (e) and from (b) through (f). The dashed lines represent the positions of the Mylar windows (grey) and the HIFU focal distance (black) along the "distance to transducer" axes.

Fortunately, the passive localisation plots allude to pre-focal activity being a potential source of the detected acoustic emissions, though it is unusual that the emissions are consistently returned from the same location in water. The echo data suggests both the onset of broadband noise and a very stable return from a seemingly stationary bubble or bubble cloud. A potential explanation is the establishment of a one-dimensional standing wave set up between the transducer surface and the proximal face of the sample. The Bjerknes radiation stress associated with such a situation would trap bubbles smaller than resonance size near a pressure maximum. This would both promote inertial cavitation activity and provide a spatially localised scatterer.

At 1.067 MHz, cavitation events are few and far between; however, there is evidence of intermittent inertial cavitation activity, as indicated by the sizeable broadband contributions. Cavitation seldomly occurs in tandem with the first HIFU pulse, let alone the first cycle of subsequent HIFU pulses. The former is likely due to a lack of suitable cavitation nuclei and, therefore, a requirement to elevate the local temperature to a level which favours bubble expansion. The latter is in stark contrast to the *in vitro* work of Chapter 3 and renders ineffective the passive localisation technique initially presented in Section 3.3.3. Moreover, there is significant variation in cavitation activity over the course of each exposure. This does not bode well for the eventual controller design, which will rely on the ability to access PRFPs capable of generating cavitation events instantaneously.

Finally, Figure 4.6 is a graph of probability of cavitation versus PRFP at a sonication frequency of 1.067 MHz, which summarises the propensity for instantaneous cavitation instigation across all eight livers experimented upon. Increasing the PRFP to 4.79 MPa certainly improves upon the results presented in Figure 4.5, in that inertial cavitation is always instigated instantaneously

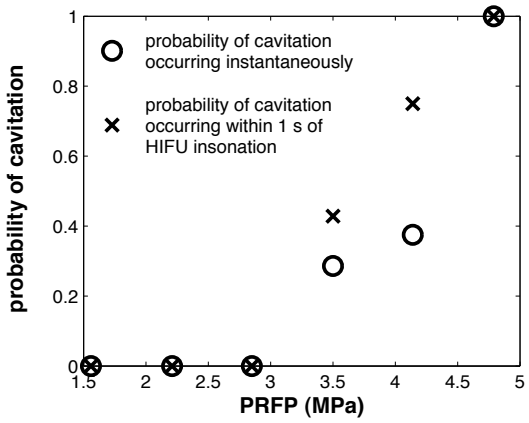


Figure 4.6: Probability of inertial cavitation occurring both instantaneously and within the first second of HIFU insonation in bovine liver at 1.067 MHz and a range of PRFPs.

4.1.3.2 Correlation of Temperature Elevation with Cavitation

It is instructive to examine whether cavitation, when it does occur, impacts favourably on heating. To this effect, bovine liver was exposed to a succession of 1 s HIFU exposures at a frequency of 1.067 MHz, a PRFP of 4.79 MPa and a duty cycle of 99%. These exposure conditions do not cause lesioning, thereby avoiding the added complexity of denaturation effects. It should, however, be noted that in the absence of tissue perfusion, depletion of available nuclei for cavitation over the course of successive HIFU pulses is entirely plausible.

Figure 4.7 presents the results from one such experiment. The gradual decrease in PCD signal variance between successive exposures, which is largely dominated by harmonics and ultraharmonics, strongly suggests that nuclei are indeed getting depleted but that most cavitation activity is not inertial. However, most importantly, despite marked variations in cavitation levels, the temperature elevation is unyielding.

Evidently, it is necessary to adopt a strategy that will (i) enable cavitation at lower

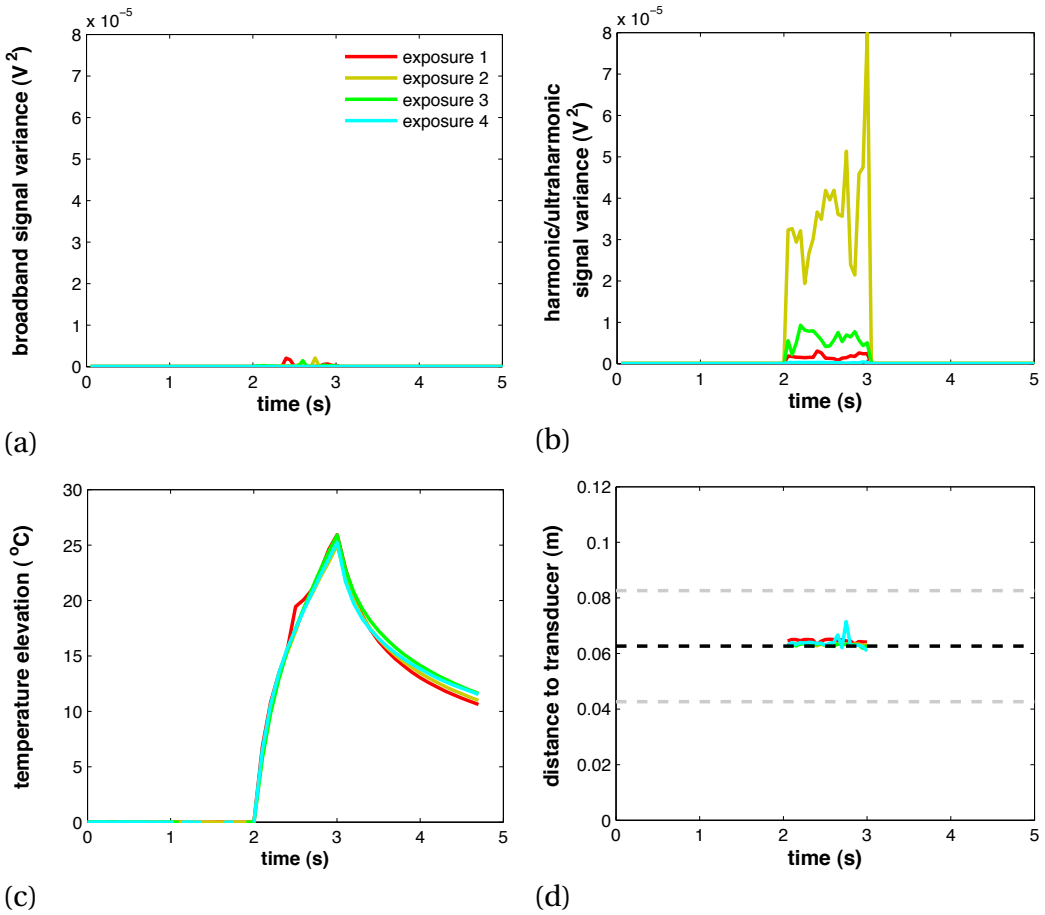


Figure 4.7: Illustration of the variation of cavitation activity (broadband and harmonic/ultraharmonic) (a and b) and temperature elevation (c) with cavitation history in bovine liver at a PRFP of 4.79 MPa. The trajectories of the bubble clouds are also shown in (d), wherein the dashed lines represent the positions of the Mylar windows (grey) and the HIFU focal distance (black) along the "distance to transducer" axis.

pressures and (ii) foster higher levels of inertial cavitation, such that cavitation-enhanced heating becomes the dominant heating mechanism. Due to concerns over excessive pre-focal activity, it was decided to omit the 0.508 MHz HIFU transducer from subsequent lines of investigation.

4.2 INTRODUCING EXOGENOUS NUCLEI

In light of the formidable inertial cavitation threshold of non-perfused bovine liver tissue subjected to 1.067 MHz HIFU sonication, exogenous nuclei were introduced to the tissue matrix in a bid to encourage inertial cavitation. The aim of the present investigation is to determine whether, by achieving adequate levels of cavitation activity in tissue, cavitation can be made to be the dominant heating mechanism and facilitate lesioning at lower acoustic intensities than would otherwise be required.

Previous work in canine kidneys has demonstrated the efficacy of Optison® microspheres as cavitation nuclei, aiding tissue ablation during ultrasound therapy by lowering *in vivo* tissue damage thresholds (Tran et al., 2003). Given the limited scope of these stabilised microbubbles for use in poorly vascularised pathological tissue, the ability of custom-made sonosensitive nanoparticles to promote cavitation was also investigated.

The sonosensitive nanoparticles were contrasted with SonoVue® microbubbles, another popular UCA, in addition to untreated polystyrene nanoparticles, to ascertain their ability to lower the inertial cavitation threshold of bovine liver tissue. Subsequently, the exogenous nuclei were tested for their ability to sustain cavitation over longer HIFU exposure durations.

4.2.1 Experimental Setup

Figure 4.8 is a schematic representation of the experimental setup adopted for the *ex vivo* work presented in this section. The thermocouple and multiplexer have been substituted with a hypodermic needle connected to a syringe containing either microbubbles or nanoparticles in suspension. Concurrent temperature recording would have compromised the integrity of the sealed system, necessitating an

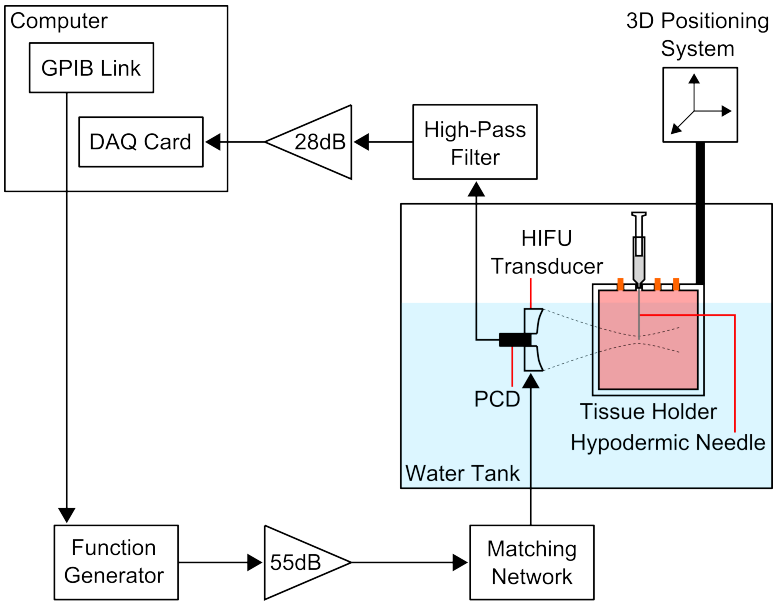


Figure 4.8: Overview of the experimental setup for acquiring cavitation data during *ex vivo* testing of exogenous nuclei. The use of a hypodermic needle to inject either bubble or particle suspensions prevents concurrent temperature measurement.

alternative approach to quantifying thermal effects.

4.2.1.1 Particle Preparation and Usage

Sonosensitive nanoparticles were prepared by LbL polyelectrolyte assembly, each one comprising: a solid polystyrene core with a diameter of 600 nm and a net negative charge; a cationic polymer layer of poly(diallyldimethylammonium chloride) (PDADMAC); and an anionic outer layer of 15 nm diameter Ludox® particles. The size distribution by volume of each batch of particles was measured using a particle characterisation instrument (Malvern Instruments, Zetasizer 3000), as demonstrated in Figure 4.9. The complete manufacturing procedure is explicated in a recent paper by Wagstaffe et al. (Wagstaffe et al., 2011). In theory, binding the Ludox® to a much larger core particle should increase the surface roughness of the emergent nanoparticle, thereby facilitating surface air entrapment during the freeze drying process. Surface crevices containing gas pockets would then constitute cavitation

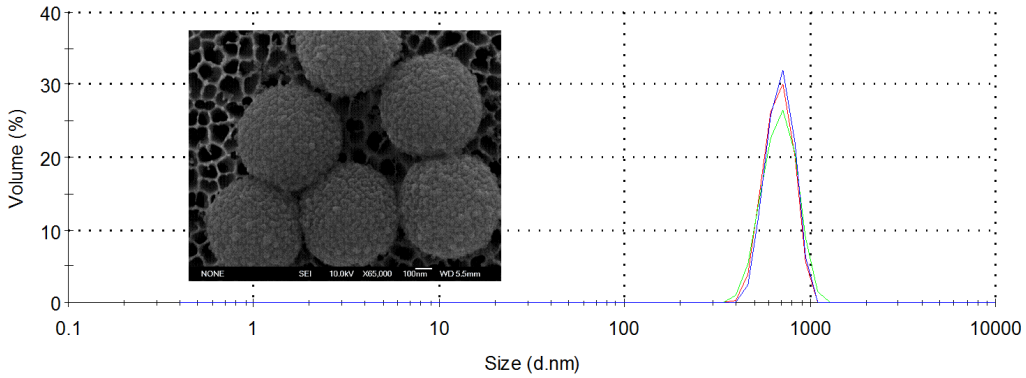


Figure 4.9: Size distribution by volume of custom-made sonosensitive nanoparticles. The graph includes three runs of the sizing procedure, all of which show good agreement. The polydispersity index is approximately 0.3.

nuclei. Whilst the nanoparticles have been successfully tested for their capacity to reduce cavitation thresholds *in vitro* (Molinari, 2012), this work is yet to be extended to biological tissue, until now.

The ability of both SonoVue® microbubbles and unmodified 600 nm diameter polystyrene nanospheres to enhance cavitation levels, and hence heating, was also investigated for comparison purposes. The various suspensions used are summarised in Table 4.1. Whereas the number of SonoVue® microspheres per unit volume is as recommended by the manufacturer for diagnostic applications, a more conservative particle density was arbitrarily chosen for the nanoparticle suspensions, based on batch sizes available and without knowledge of the full range of side effects that can be expected *in vivo*.

In each liver sample, four HIFU exposures were carried out at different locations in the absence of a foreign nucleation agent, and a further four identical exposures, except for the inclusion of exogenous nuclei, undertaken thereafter in the same liver. The three-axis motorised positioning system was used to locate these irradiation sites on a 20 mm^2 spaced grid at a depth of 20 mm behind the front face of

Nucleation Agent	Chemical Composition	External Phase	Cavitation Nucleus ⌀	No. of particles per mL
SonoVue®	SF_6 core; phospholipid shell	9% PBS solution	0.7-10 μm	1-5 x 10^8
SNP	Polystyrene core; Ludox® coating	DI water	630 nm	1 x 10^6
Non-SNP	Polystyrene	DI water	600 nm	1 x 10^6

Table 4.1: Summary of exogenous nuclei used to investigate cavitation enhancement in freshly excised bovine liver. SNP is shorthand for sonosensitive nanoparticles.

the cuboid. An acoustically aligned, standard-bevel hypodermic needle, measuring 18G x 1½" and connected to a 2.5 mL full capacity syringe, was used to inject 2 mL of suspension into the otherwise sealed liver sample via a series of holes along the top edge of the tissue holder. Immediately after injection, the hypodermic needle was withdrawn, the plug replaced and the HIFU transducer activated.

Of all the exogenous nuclei investigated, only SonoVue® was found to be detectable using B-mode ultrasound imaging, at the specified concentration. The microbubbles were seen to gradually diffuse away from the point of suspension injection and into the tissue matrix. This means that all of the exposures in each liver sample and in the presence of exogenous nuclei had a different baseline level of cavitation nuclei; however, in view of the underlying objective to correlate lesion size with cavitation activity, and not with exogenous nuclei concentration, this was deemed acceptable.

4.2.1.2 HIFU Generation and Passive Cavitation Detection

Having already established that 0.508 MHz HIFU excitation is linked to excessive pre-focal cavitation activity and yields little in the way of lesioning, only the 1.067 MHz HIFU transducer and accompanying electronics were used for the experiments presented in this section.

4.2.2 Data Analysis

In the absence of a thermocouple, alternative means of quantifying thermal effects brought about by HIFU sonication were sought. Unfortunately, the significant delay between tissue extraction from the host and lesion formation meant that most, if not all, of the unablated liver cells would have also undergone necrotic death prior to fixation for histopathology. Staining for necrosis from a range of external stimuli is not possible, ruling out microscopic analysis as a method for quantification of thermal effects.

However, localised cytotoxic heating manifests macroscopically as stiff, white lesions, which are distinct from the surrounding parenchyma. Assuming the tissue physical properties to be reasonably uniform both within and between liver samples, lesion cross-sectional area may be used as a coarse indicator of local heating rates. Strictly speaking, tissue damage due to cavitation may be attributed to mechanical, as well as thermal, effects; however, gross examination of the lesions revealed little in the way of mechanical fractionation, as will become clear in Section 4.2.3.2.

Therefore, subsequent to HIFU excitation and liver sample bisection, a photograph was taken of the rear half of the liver sample using an SLR camera (Canon, EOS-400D), showing the extent of lesioning both in the presence and absence of a

foreign nucleation agent. The photographs were later imported into Matlab, regions of interest identified, and the image thresholded to calculate lesion areas in pixels and thence mm^2.

4.2.3 Results and Discussion

The naked threshold for cavitation in the *ex vivo* bovine liver used in the present study is unfeasibly high, whilst cavitation events are erratic and intermittent. The use of hypodermic needles to inject exogenous nuclei greatly improves on these results; however, the number of exposures which may be effected in any one liver sample is significantly reduced. As such, a total of 24 adult ox livers were included in the work presented in this section.

4.2.3.1 Cavitation Threshold Measurements

Bovine liver was exposed repeatedly to 10-cycle HIFU pulses at 1 s intervals and at progressively increasing PRFPs between 0.53 MPa and 2.85 MPa, both in the presence and absence of each of the foreign nucleation agents outlined in Table 4.1. The resulting graph of PCD signal variance versus PRFP is shown in Figure 4.10. Evidently, within the range of PRFPs investigated, experimentation in bovine liver does not yield any cavitation events within the first 10 cycles of HIFU excitation without the inclusion of suitable exogenous nuclei.

The introduction of SonoVue® microbubbles reduces the cavitation threshold of bovine liver appreciably to approximately 0.53 MPa, yielding very high cavitation signals during the short on-time of the HIFU transducer, though with significant uncertainty. Custom-made sonosensitive nanoparticles are also capable of lowering the cavitation threshold of tissue to approximately 0.80 MPa, generating relatively high PCD signals. Moreover, non-sonosensitive polystyrene nanoparticles have lit-

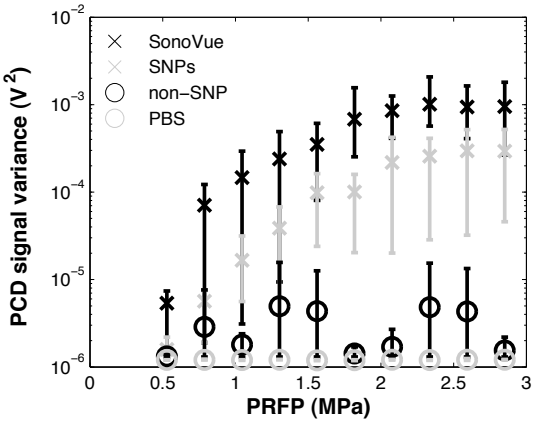


Figure 4.10: PCD signal variance versus PRFP for determining cavitation thresholds in bovine liver, both in the presence and absence of exogenous nuclei and at a frequency of 1.067 MHz.

tle effect on the PCD signal, with cavitation events unpredictable and low in energy. This affirms that the procedure for inserting nuclei into the tissue matrix is not responsible for the increase in cavitation levels observed in the presence of SonoVue® microbubbles and sonosensitive nanoparticles.

4.2.3.2 Assessment of Lesion Formation

Having established that the addition of a foreign nucleation agent to bovine liver can augment cavitation levels, it is instructive to consider the impact that this has on local heating rates. To this effect, a series of HIFU exposures were carried out at a PRFP of 2.85 MPa and a duty cycle of 99% for 10 s. The PRFP was chosen based on the preliminary experiments presented in Section 4.1.3: it is the highest PRFP at which cavitation does not ordinarily occur instantaneously in naked bovine liver (see Figure 4.6). Any cavitation activity observed in the presence of a nucleation agent may thus be attributed solely to the modified nuclei population. Similarly, the exposure duration was chosen such that HIFU sonication in the absence of a nucleation agent would not cause lesioning. Lesion formation in the presence of

one such agent may thus be ascribed to the incumbent nuclei.

The photographs presented in Figure 4.11 are representative of the tissue sections observed during gross examination of the ablated bovine liver samples. Each column pertains to a specific nucleation agent, (SonoVue® microbubbles, sonosensitive polystyrene nanoparticles or non-sonosensitive polystyrene nanoparticles), with PCD data acquired prior and subsequent to introduction of the relevant agent for purposes of comparison. It should be noted that the depth of injection is not exactly equivalent to the length of the needle due to the elasticity of the tissue, meaning that once the needle has been fully inserted into the tissue via the holes in the holder, the tissue rebounds slightly. The effect is different depending on the inhomogeneities present along the needle path.

Foremostly, in all of the control experiments populating the lower halves of the photographs, there is no lesioning. In the presence of either SonoVue® or sonosensitive nanoparticles, sizeable lesions emerge. A key feature of the photographs is the absence of lesioning in tissue regions proximal to large vessels, or in instances where the needle path intersects one such vessel. This provides an escape route for the suspension and significantly enhances the rate of particle diffusion away from the target region. Additionally, a clear demarcation line exists between adjacent lesions in many of the experiments performed, where one might have expected the lesions to merge together. This suggests that the margin of cells separating ablated and unablated tissue is favourably narrow. Moreover, the addition of non-sonosensitive polystyrene nanoparticles does not impact significantly on lesioning compared to the control experiments.

Encouragingly, on occasions where lesioning did occur, the cavitation signal deviated significantly from the basal noise level. The graphs in Figure 4.12 pertain to the HIFU lesions tagged with a black cross in Figure 4.11 and demonstrate the ca-

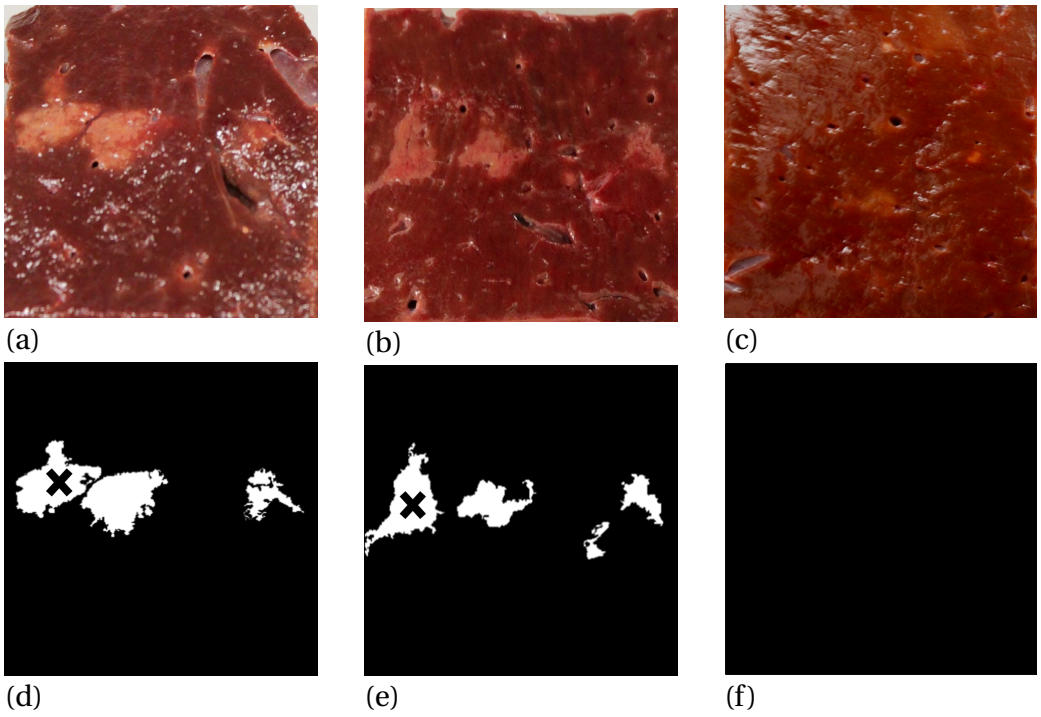


Figure 4.11: Photographs of lesions resulting from 10 s HIFU sonication at a frequency of 1.067 MHz and a PRFP of 2.85 MPa in the presence of (a) SonoVue®, (b) sonosensitive nanoparticles and (c) non-sonosensitive nanoparticles. In each liver sample, a row of four exposures was initially carried out in the lower half of the tissue sample, and a further row of four in the top half subsequent to injection of a foreign nucleation agent. (d), (e) and (f) are thresholded images of the photographs, clearly demarcating the lesion boundaries.

pacity of both SonoVue® and sonosensitive nanoparticles to boost cavitation levels. In both instances, the contribution from the broadband component is significant, primarily at the start of each exposure. There is, of course, a marked difference in the temporal distribution of cavitation events: whereas cavitation activity is confined to the first 500 ms of HIFU exposure in the case of SonoVue®, the PCD signal variance profile is more consistently elevated when utilising sonosensitive nanoparticles to promote cavitation. The harmonic/ultraharmonic spikes which manifest towards the end of the exposure in Figure 4.12 (b) are likely due to boiling.

The exposure duration was subsequently reduced to 2 s to identify whether HIFU insonation beyond that required to fully deplete the nuclei supply is really

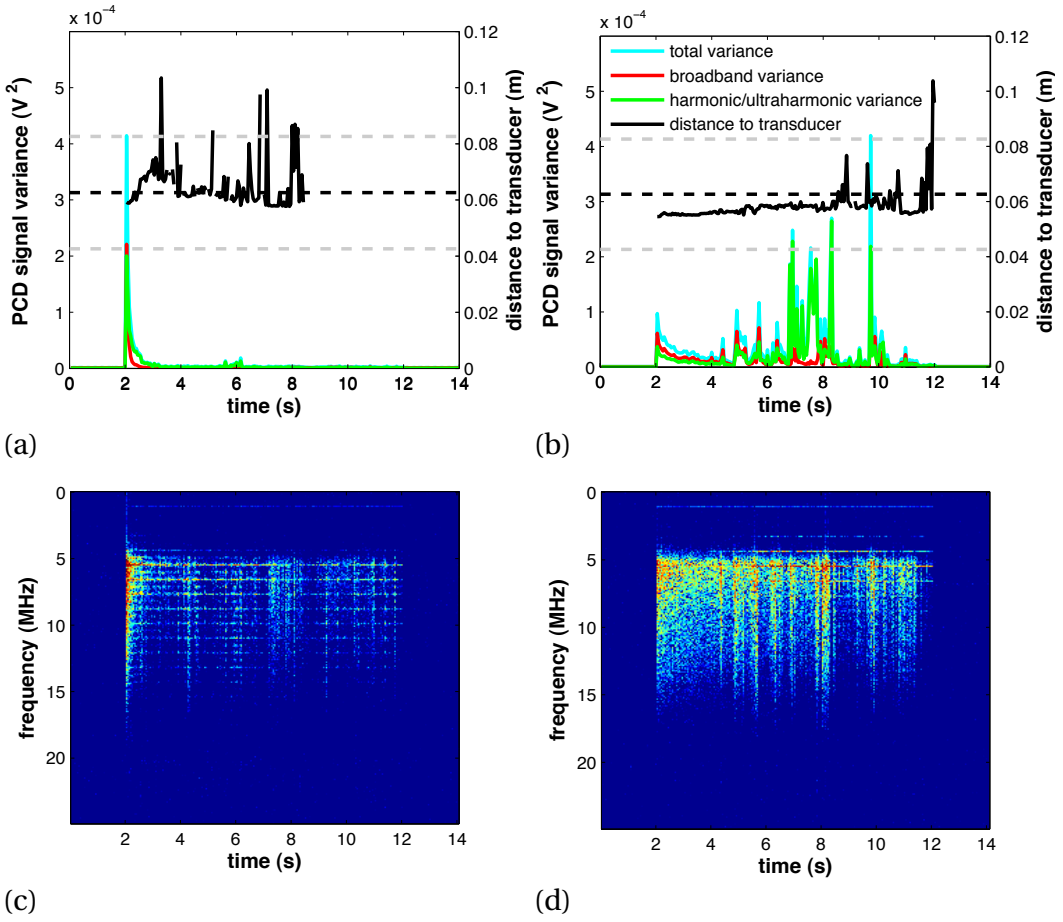


Figure 4.12: Cavitation data from 10 s HIFU exposures at a frequency of 1.067 MHz and a PRFP of 2.85 MPa, utilising both (a) SonoVue® and (b) sonosensitive nanoparticles as cavitation-promoting agents. The dashed lines represent the positions of the Mylar windows (grey) and the HIFU focal distance (black) along the "distance to transducer" axes. The corresponding spectrograms are also provided (c and d), demonstrating the significant contribution from broadband components.

necessary, and to reduce the likelihood of boiling bubble formation. All other experimental parameters remained unaltered. The findings, represented in Figures 4.13 and 4.14, are particularly interesting, in that there is no obvious change in lesion size or opacity, despite an 80% reduction in HIFU input energy. As expected, no lesions were formed in any of the control experiments, nor subsequent to inclusion of non-sonosensitive nanoparticles.

Moreover, in spite of markedly different cavitation profiles between livers im-

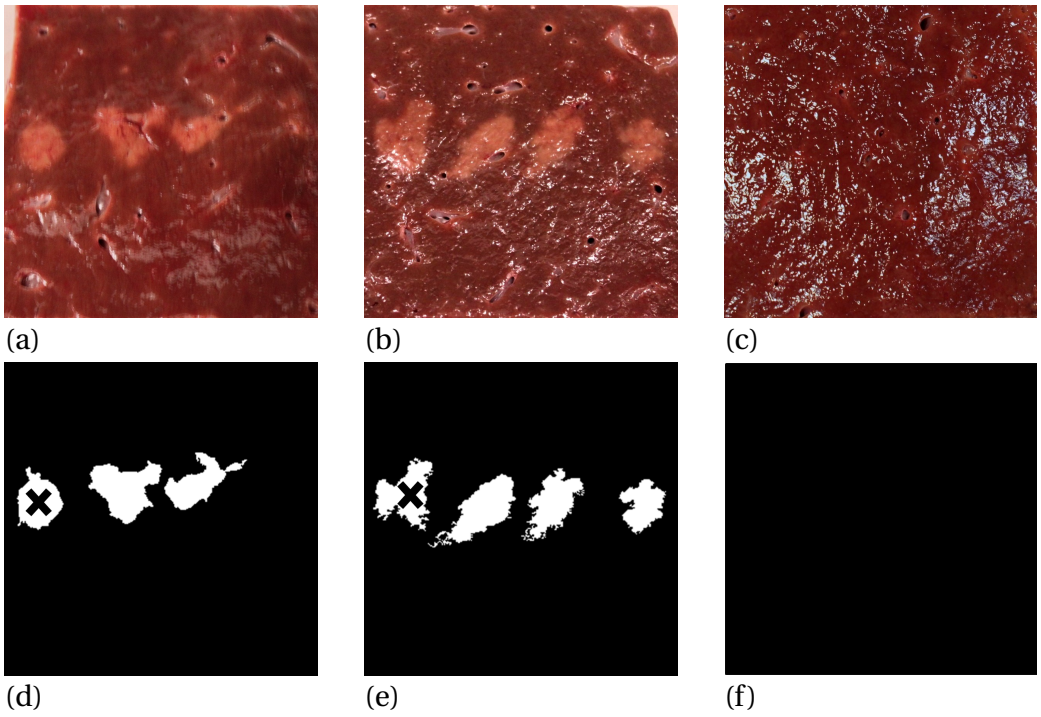


Figure 4.13: Photographs of lesions resulting from 2 s HIFU sonication at a frequency of 1.067 MHz and a PRFP of 2.85 MPa in the presence of (a) SonoVue®, (b) sonosensitive nanoparticles and (c) non-sonosensitive nanoparticles. In each liver sample, a row of four exposures was initially carried out in the lower half of the tissue sample, and a further row of four in the top half subsequent to injection of a foreign nucleation agent. (d), (e) and (f) are thresholded images of the photographs.

pregnated with SonoVue® or sonosensitive nanoparticles, the gross effects are comparable. The SonoVue® PCD signal variance profile is initially dominated by broadband emissions; however, the broadband content rapidly decays, leaving in its wake lipid-shelled microbubbles undergoing stable cavitation (hence the sustained harmonic emissions). These microbubbles are not suitable for inertial collapse due to their size, and will have originated either from the injected microbubble suspension or from fragmentation of larger bubbles. In contrast, exposures involving the use of sonosensitive nanoparticles tend to generate sustained broadband secondary acoustic emissions, albeit at lower intensities. Thus, it is the total broadband content of each exposure which appears to be the common denominator.

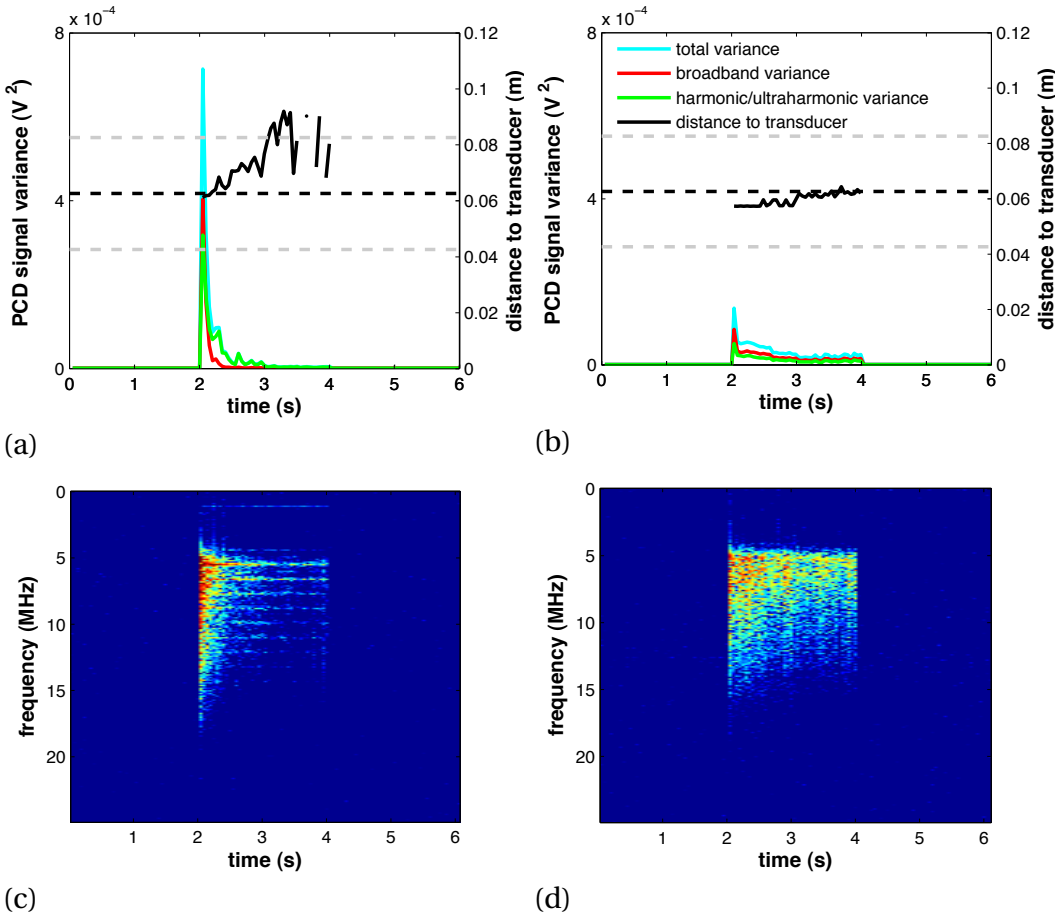


Figure 4.14: Cavitation data from 2 s HIFU exposures at a frequency of 1.067 MHz and a PRFP of 2.85 MPa, utilising both (a) SonoVue® and (b) sonosensitive nanoparticles as cavitation-promoting agents. The dashed lines represent the positions of the Mylar windows (grey) and the HIFU focal distance (black) along the "distance to transducer" axes. The corresponding spectrograms are also provided (c and d), demonstrating the significant contribution from broadband components.

4.2.3.3 Correlation of Lesion Size with Inertial Cavitation

Figures 4.15 (a) and (b) are graphs of lesion cross-sectional area plotted against the total broadband energy of secondary acoustic emissions for all 10 s and 2 s HIFU exposures. The various markers denote different exogenous nuclei. Variations in background noise have been corrected for by comparison with data obtained during the HIFU off-time. Exposures in which harmonic scattering by boiling bubbles was observed have been excluded, representing less than 5% of the data set.

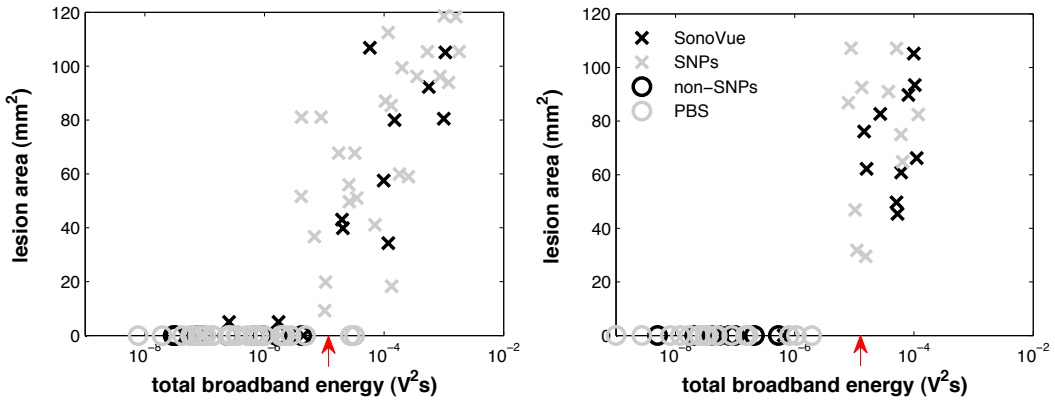


Figure 4.15: Comparison of lesion areas produced using different nucleation agents for (a) 10 s and (b) 2 s HIFU exposures conducted at a frequency of 1.067 MHz, a PRFP of 2.85 MPa and a duty cycle of 99%.

There is an obvious trend for lesion area to increase substantially beyond a threshold level of total broadband energy (approximately 2 x 10^{-5} V^2s); however, once again, the focal region of the PCD is not equivalent to that of the HIFU and the lesions themselves. The control experiments and those conducted in the presence of non-sonosensitive polystyrene nanoparticles occupy a distinct region of the graph, along the abscissae. Both SonoVue® and the sonosensitive polystyrene nanoparticles have the same effect on the *total* broadband content of the PCD signal and the spatial extent of lesioning. This is interesting because the physical properties of these cavitation-promoting agents are vastly different - amongst the most obvious are their respective diffusivities and cavitation nuclei diameters (this is not equivalent to particle diameter in the case of sonosensitive nanoparticles) - and suggests that the threshold level of total broadband energy is largely dependent on the properties of the host medium. Moreover, there appears to be no obvious enhancement to lesioning brought about by extending the HIFU exposure time from 2 seconds to 10 seconds as the difference in lesion cross-sectional area is not statistically significant. In essence, cavitation-enhanced heating is most apt at producing le-

sions in the early part of an exposure.

4.3 Validation using Passive Acoustic Mapping

The introduction of exogenous cavitation nuclei to the tissue matrix clearly impacts favourably on inertial cavitation levels, and hence lesioning. Limitingly, however, the PCD focal volume is not equivalent to that of the HIFU transducer and the lesions themselves. Thus, the PCD signal is not strictly representative of cavitation activity over the entire lesion volume. Two-dimensional passive acoustic mapping is a potential solution to this problem, involving the substitution of the PCD with a standard linear ultrasound array operating in passive mode. This technique is computationally expensive and was not amenable to real-time treatment monitoring at the time of conducting the experiments (see Section 7.2.4 for information on recent developments). Nevertheless, it was instructive to verify that the augmentation in lesion size following injection of a foreign nucleation agent corresponds to a broad spatial distribution of cavitation events, as opposed to extensive thermal diffusion.

4.3.1 Experimental Setup

Figure 4.16 is a schematic representation of the experimental setup adopted for the *ex vivo* work presented in this section. The circular PCD has been replaced by a rectangular linear array, and the HIFU transducer substituted accordingly to accommodate coaxial alignment. This configuration mimics current clinical practice combining HIFU therapy and B-mode treatment monitoring.

4.3.1.1 HIFU generation

To enable passive acoustic mapping, a 1.06 MHz HIFU transducer (Sonic Concepts, H107B-SN22) was used in conjunction with an unfocused linear ultrasound array

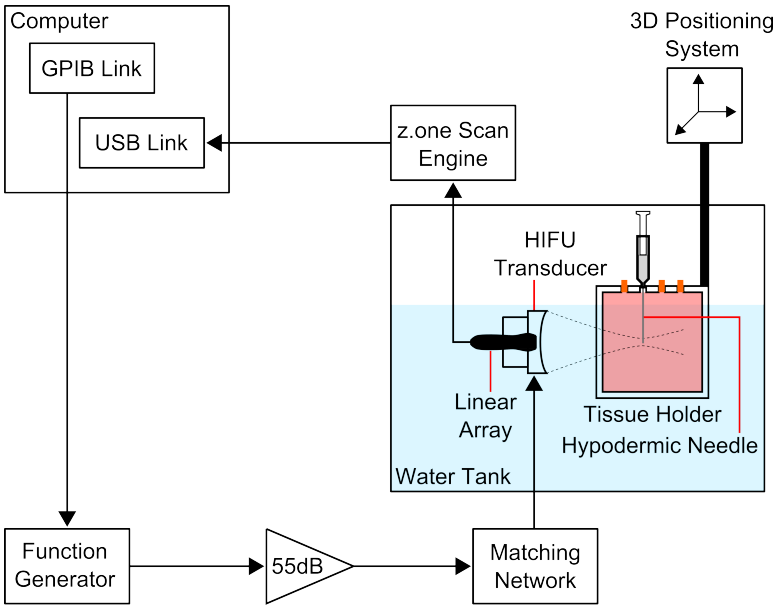


Figure 4.16: Overview of the experimental setup for acquiring cavitation data in two dimensions during *ex vivo* testing of exogenous nuclei. The single element PCD has been replaced with a linear array to enable passive acoustic mapping.

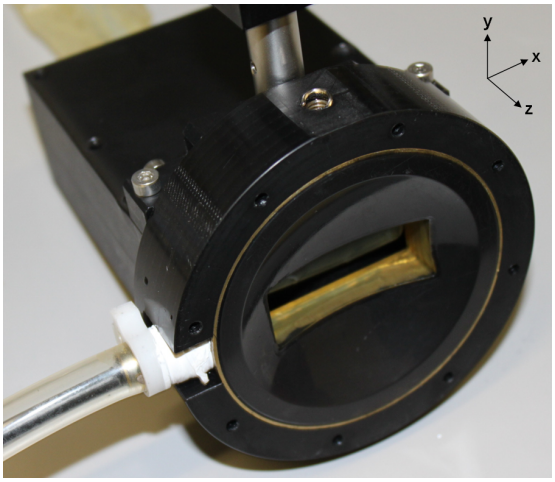


Figure 4.17: Spherically focused HIFU transducer (Sonic Concepts, H107B-SN22) with central rectangular void for coaxial alignment of a diagnostic linear array.

(Zonare, L10-5) for HIFU excitation and cavitation monitoring respectively. Aside from having a rectangular central opening, the transducer construction and geometry are identical to those of the 1.067 MHz and 0.508 MHz HIFU transducers, as are the driving electronics.

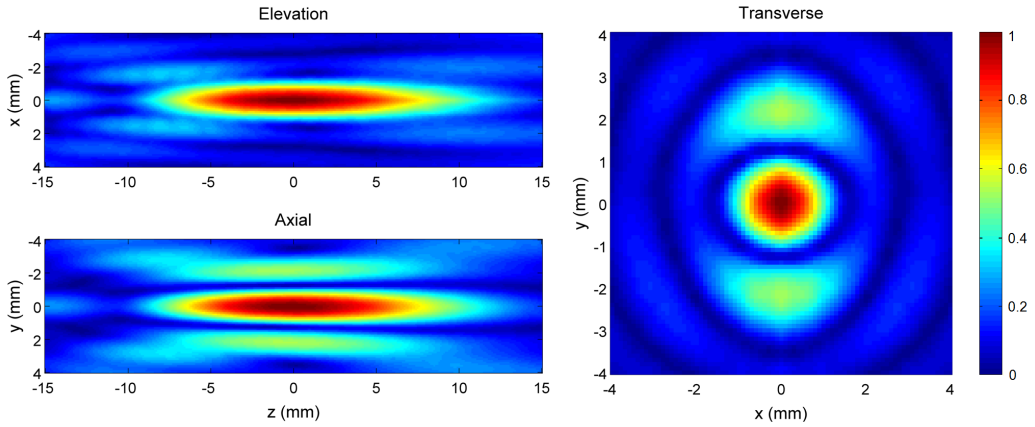


Figure 4.18: Normalised longitudinal and transverse pressure profile sections of the 1.06 MHz focused HIFU transducer, taken through the focal maximum. Note that the side lobes do not take the form of concentric circles in the transverse plane due to the rectangular central void.

The transducer, shown in Figure 4.17, was calibrated in water, from which the transverse and longitudinal scans through the focus are shown in Figure 4.18. The discontinuous side lobes brought about by the rectangular central opening are clearly visible in the axial and transverse planes.

4.3.1.2 Passive Cavitation Detection

The diagnostic linear array used in the following experiments comprises 128 elements, of which 64 may be simultaneously triggered to passively acquire data by the controlling scan engine (Zonare, z.one). The resolution of the reconstructed source maps was maximised by utilising alternate elements, thereby spanning the full 38 mm aperture of the array. Pulse transmission from the scan engine was disabled during cavitation data acquisition to enable purely passive monitoring of secondary acoustic emissions.

Having previously established that extending the exposure duration to 10 s generates no additional benefits as regards cavitation, and hence lesioning, only 2 s

exposures were considered for experimentation using the linear array. The scan engine was configured to acquire data for 3 s at a frame rate of 100 Hz and a maximum imaging depth of 100 mm. This included a 500 ms buffer pre- and post-HIFU operation to provide a measure of the baseline noise level. Cavitation recordings take the form of 5 MHz bandwidth in-phase/quadrature (IQ) data with configurable centre frequency. Of the frequency bands available, 5 to 10 MHz was chosen to sensitise the system to broadband secondary acoustic emissions resulting from 1.06 MHz HIFU insonation.

Coaxial alignment of the focused HIFU transducer and the unfocused linear array was achieved using the array to acquire a B-mode image of a needle hydrophone (Onda, HNA-0400), acoustically positioned at the HIFU focus, and ensuring that the needle was positioned at the transverse midpoint of the array width. The relative positions of the therapeutic and diagnostic transducers are constrained by their geometries, such that the HIFU focus is always located at a minimum imaging depth of 74 mm. Numerical simulation of the point spread function (PSF) has revealed this depth to be associated with transverse and axial -3 dB resolutions of 0.4 mm and 4.9 mm respectively (Gyongy and Coussios, 2010). Once the precise imaging depth to the focus had been ascertained, the hydrophone was removed and replaced by the appropriate tissue sample. Knowledge of this depth is essential for analysing the reconstructed source maps.

4.3.2 Controlling Software

A custom Matlab script was developed to control the actuation of the HIFU source and the acquisition of cavitation data. Communication between the host computer and the scan engine was achieved via USB link, whilst IQ data was saved directly to an external hard drive. A 500 ms delay was imposed between the foremost trigger

signals controlling the scan engine and the function generator, following which a further stream of trigger signals were communicated to the array from the scan engine and the function generator was configured to operate at a 99% duty cycle. Each frame was sampled at 50 MHz, generating approximately 6750 samples per 135 μs frame.

4.3.3 Data Analysis

Time exposure acoustics (TEA) is a passive imaging algorithm, in which new data is incorporated into an image in a recursive fashion such that background noise is made to diminish over time. Originally developed to image subterranean scatterers, the algorithm is becoming increasingly useful for cavitation mapping.

During passive cavitation imaging, acoustic emissions from cavitation events manifest as spatially correlated signals over a receiving array. The coherent summation of these correlated signals over a number of time steps using an appropriate back-propagation algorithm results in the relatively weak secondary acoustic sources growing in strength over time relative to the uncorrelated background noise. Consequently, TEA improves upon the low signal-to-noise ratio (SNR) of dynamic receive beamforming (DRB), employed for B-mode imaging, and thus facilitates accurate mapping of cavitation events.

Mathematically, if $u(\mathbf{r_n}, t)$ denotes the field recorded at the n^{th} element of a receiving array at position $\mathbf{r_n}$, then the image, $I(\mathbf{r})$, generated by back-projection is given by:

$$I(\mathbf{r}) = 4\pi \sum_{n=1}^{N} u(\mathbf{r_n}, |\mathbf{r} - \mathbf{r_n}|/c)|\mathbf{r} - \mathbf{r_n}|, \tag{4.1}$$

where $\mathbf{r}$ is the vector position of the image pixel (see Figure 4.19), and assuming a free space Green's function. Defining $u_n(\mathbf{r}) = 4\pi u(\mathbf{r_n}, |\mathbf{r} - \mathbf{r_n}|/c)|\mathbf{r} - \mathbf{r_n}|$, Equation 4.1

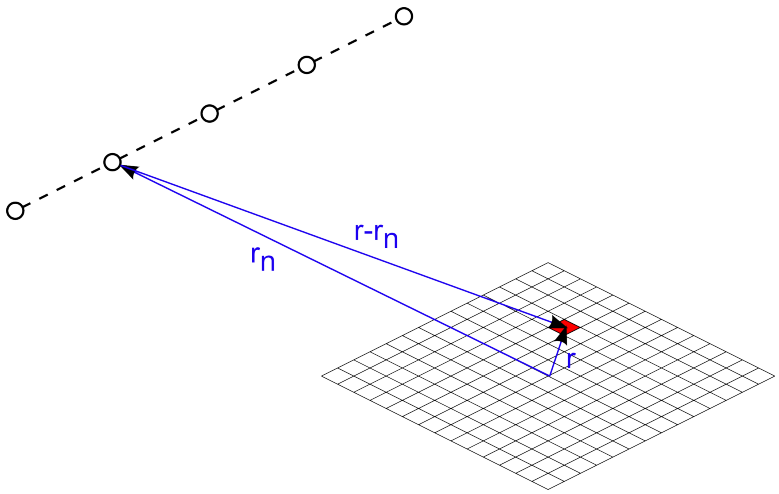


Figure 4.19: Geometry for the implementation of the TEA algorithm, where **r** is the vector position of the image pixel and $\mathbf{r_n}$ is the location of the n^{th} receiving element.

may be rewritten as:

$$I(\mathbf{r}) = \sum_{n=1}^{N} u_n(\mathbf{r}). \tag{4.2}$$

The method assumes that the received noise field is a random variable with zero mean, such that the statistical expectation of the image $E\{I(\mathbf{r})\}$ is equal to zero. Successive realisations of images in the time domain are thus averaged on the basis of intensity squared (i.e. by averaging $|I(\mathbf{r})|^2$). This leads to the accumulation of a DC bias over time, which is removed prior to computation of the mean image as follows:

$$I^k(\mathbf{r}) = \left| \sum_{n=1}^{N} u_n^{(k)}(\mathbf{r}) \right|^2 - \sum_{n=1}^{N} |u_n^{(k)}(\mathbf{r})|^2, \tag{4.3}$$

where $I^{(k)}(\mathbf{r})$ is the k^{th} realisation of the image. The average of M images, $\overline{I}_M(\mathbf{r})$, can then be calculated from:

$$\overline{I}_M(\mathbf{r}) = \frac{1}{M} \sum_{k=1}^{M} I^{(k)}(\mathbf{r}). \tag{4.4}$$

Subsequent to the conversion of IQ data to RF data, the TEA algorithm was implemented across the 64 receiving elements of the linear array using Matlab. Initially, each frame was upsampled to 200 MHz using cubic spline interpolation,

thereby limiting quantisation errors when calculating the appropriate delays for the signals received on each element. Whilst the inherent 5 to 10 MHz bandpass filtering of IQ data negated the use of an additional high-pass filter to remove the low-order harmonics, harmonic and ultraharmonic frequencies within this bandwidth were removed using digital notch filters of width 200 kHz. Integration over time was subsequently conducted at the original sampling rate of 50 MHz over the entire frame duration.

A simplifying assumption of the TEA algorithm implementation in Matlab is that the speed of sound does not vary within the confines of the back-propagation paths. This is reasonable for small lesions; however, temperature- and denaturation-dependent effects become important for larger lesions. Moreover, changes in void fraction due to insertion and/or nucleation of microbubbles could impact on speed of sound calculations. Given that these contributions are likely to have converse effects on the speed of sound, neither was factored into subsequent calculations. In addition, scattering of secondary acoustic emissions from inhomogeneities (including bubbles) in the HIFU field increases the time delay between a cavitation event occurring and being recorded. Converted to a distance, this is perceived to originate from further afield than is actually the case.

4.3.4 Results and Discussion

Two-dimensional passive acoustic mapping has previously been validated both *in vitro* and *ex vivo* (Gyongy, 2010). The present work differs from previous cavitation studies by virtue of the significant cavitation levels involved. This is in spite of using a comparably low input energy to generate thermal effects. It is important to note that, whilst the resultant maps correlate well with lesion formation in the transverse plane (xy), the PSF in the longitudinal direction (z) is too large to extract any mean-

ingful information (Jensen et al., 2011).

4.3.4.1 Passive Acoustic Maps

The images presented in Figure 4.20 are cumulative cavitation maps acquired during experimentation in bovine liver at a PRFP of 2.85 MPa for 2 s, oriented such that the HIFU transducer is located beyond the top edge of each image, pointing downwards. The top and bottom rows of images pertain to broadband and harmonic/ultraharmonic emissions respectively, whilst each column represents a different nucleation environment, namely tissue impregnated with SonoVue® or sonosensitive nanoparticles, and a control devoid of exogenous nuclei. The colour bars are common to all images in each row and represent the energy content of the secondary acoustic emissions in millijoules.

Firstly, there is a marked increase in broadband emissions, indicative of inertial cavitation, brought about by the introduction of exogenous nuclei to the tissue matrix. In the case of sonosensitive nanoparticles, the reconstructed source map bears a strong resemblance to the HIFU field map, in that there is a finite, ellipsoidal region within which inertial cavitation occurs. An interesting feature of Figure 4.20 is that the sonosensitive nanoparticles essentially produce emissions that are exclusively brodband in nature, whilst SonoVue® yields both broadband and harmonic components. As regards SonoVue®, the considerable signal strength at the tail end of the images is thought to be attributable to multiple reflections of secondary acoustic emissions by highly scattering microbubbles. Unfortunately, the reconstruction algorithm perceives the consequent delay in the received signal as due to a cavitation event occurring further away. In general, the harmonic/ultraharmonic emissions vary much more widely between exposures than their broadband counterparts and do not correlate with lesioning.

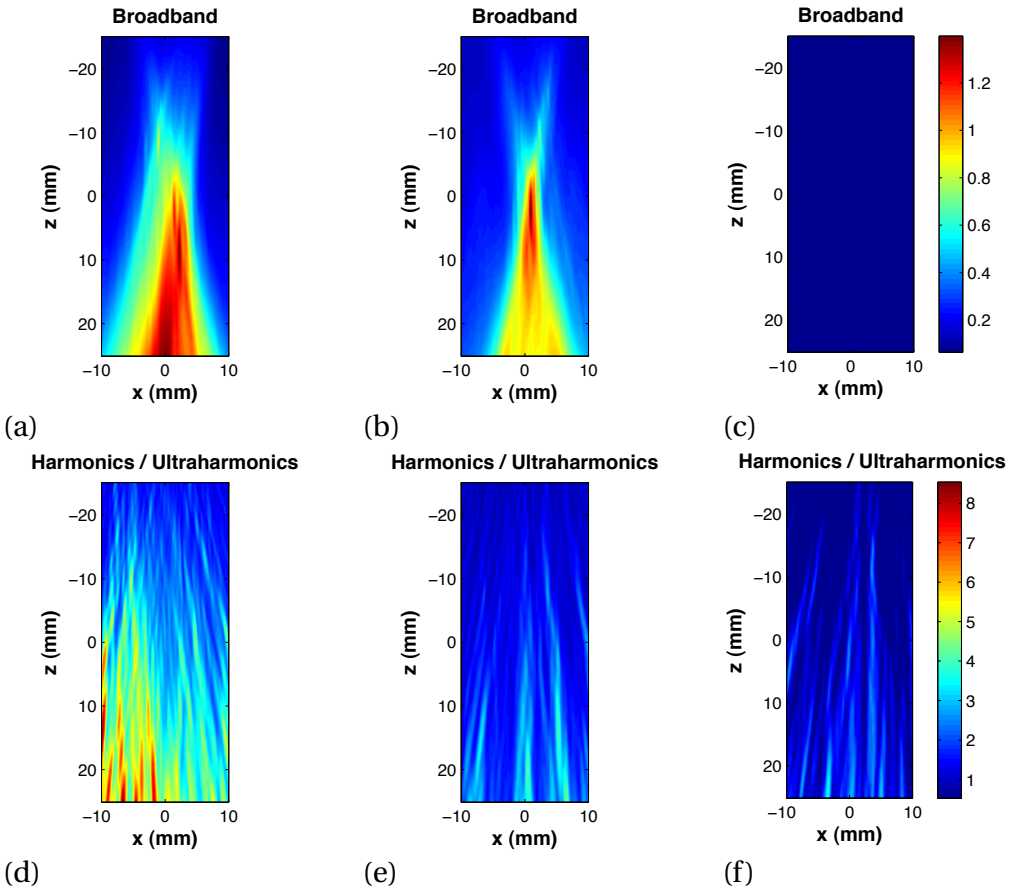
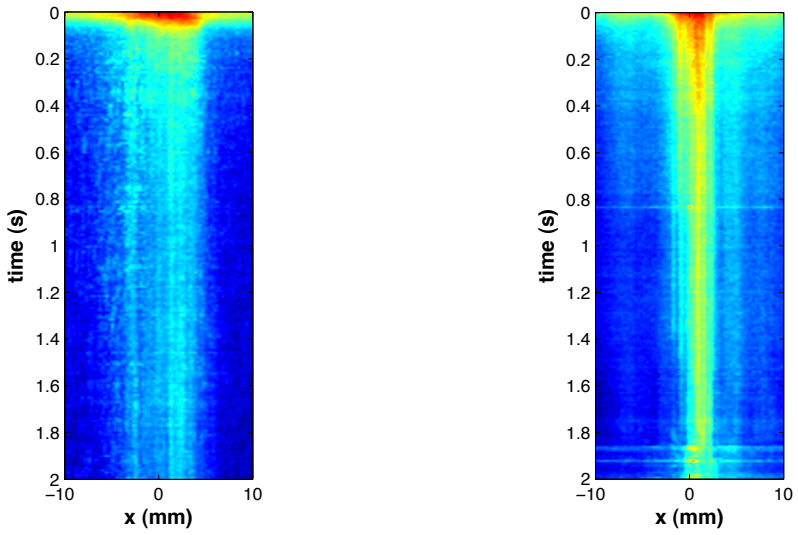


Figure 4.20: Reconstructed source maps from HIFU exposures undertaken in bovine liver at a PRFP of 2.85 MPa for 2 s in the presence of (a and d) SonoVue® and (b and e) sonosensitive nanoparticles, and (c and f) in the absence of exogenous cavitation nuclei. The colour bars are common to all images in each row and represent the energy content of the secondary acoustic emissions in millijoules.

The experimental data summarised in Figures 4.20 (a) and (b) may be alternatively presented by tracking the broadband emissions recorded solely at the focal depth ($z = 0$) over time (see Figure 4.21). As expected, the (inertial) cavitation profiles are widely different, with most of the broadband emissions concentrated at the start of the SonoVue® exposure, whilst the sonosensitive nanoparticles shed their nuclei in a more controlled manner over a longer period of time.



(a) (b)

Figure 4.21: The evolution of broadband emissions recorded solely at the focal depth ($z = 0$) in bovine liver injected with (a) SonoVue® and (b) sonosensitive nanoparticles.

4.3.4.2 Correlation of Lesion Size with Inertial Cavitation

Introducing exogenous cavitation nuclei, namely SonoVue® microbubbles and sonosensitive polystyrene nanoparticles, to tissue prior to HIFU sonication reduces the inertial cavitation threshold and gives rise to a broad spatial distribution of cavitation events. Section 4.2 has revealed there to be a threshold level of total broadband energy, beyond which lesioning occurs for a specific set of HIFU parameters (frequency, duty cycle, PRP). If this threshold can be extended to the cavitation maps, it may be possible to infer lesion dimensions.

Direct comparison of experimental work undertaken using either a single-element PCD or a multi-element linear array should be approached with caution due to differences in sensitivity and frequency response between cavitation detection equipment. However, by using the central element of the linear array as a single-element PCD, it has been possible to deduce a threshold level of total broad-

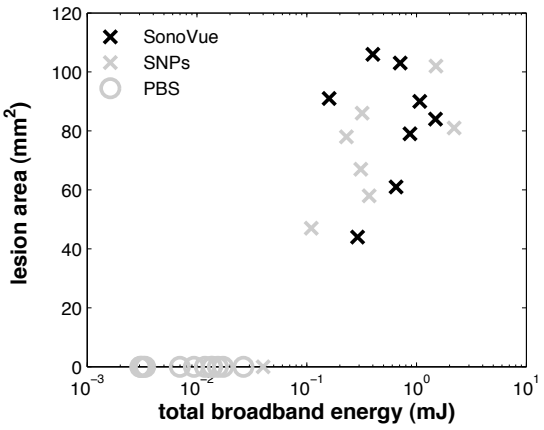


Figure 4.22: Comparison of lesion areas produced using different nucleation agents for 2 s HIFU exposures conducted at a PRFP of 2.85 MPa and a duty cycle of 99%, using the linear array in echo mode for 2 s.

band energy that is relevant to the array and its accompanying amplification and data acquisition systems. Figure 4.22 is a plot of lesion area versus total broadband energy, from which the threshold for lesioning is approximately 0.03 mJ. Conversion between millijoules and V^2s (as used in Section 4.2.3.3) is a trivial task; however, it is hoped that the use of different units will deter direct comparison of absolute values.

Unfortunately, the basal noise level of the source reconstruction algorithm is amplified considerably by summation over multiple frames, such that the vast majority of the cavitation maps presented in Figure 4.20 exceeds the total broadband energy threshold for lesioning. This problem may be circumvented by thresholding each frame prior to summation. Figure 4.23 is a duplicate of the SonoVue® cavitation map shown in Figure 4.20 (a), together with its thresholded equivalent and photographs of the lesion itself. It is important to note that the axes scales and labels differ.

The width of the cavitating region at the HIFU focus may be approximated by the width of the white region in Figure 4.23 (b) at the focal depth (demarcated in red). By assuming the lesion cross-section to be circular and using the area computed

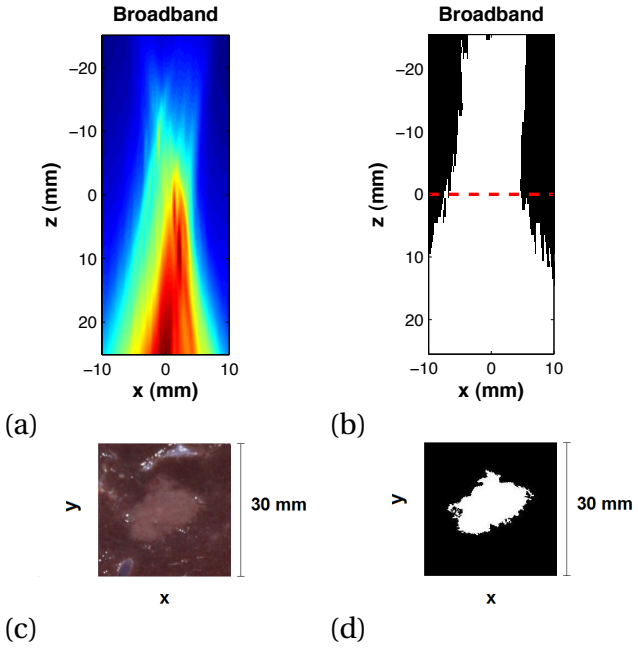


Figure 4.23: Demonstration of thresholding techniques used for cavitation maps (a and b) and corresponding lesion photographs (c and d), using the SonoVue® map from Figure 4.20 as an example.

from the thresholded photographs to estimate the lesion diameter, it is possible to correlate the lesion width predicted from the cavitation maps with the actual lesion properties.

Figure 4.24 compares lesion width estimates from thresholded cavitation maps and thresholded lesion photographs. Interestingly, in tissue injected with SonoVue®, the passive acoustic maps overpredict the lesion widths. The corresponding Pearson's correlation coefficient is 0.436. In contrast, the width of the cavitating region in the presence of sonosensitive nanoparticles underpredicts the lesion dimensions, though there is stronger correlation between the two (Pearson's correlation coefficient = 0.956).

The difference between SonoVue® and sonosensitive nanoparticles is likely due to multiple reflections in the presence of highly scattering SonoVue® microbubbles. Nevertheless, this result confirms that the enhancement in tissue lesioning in the

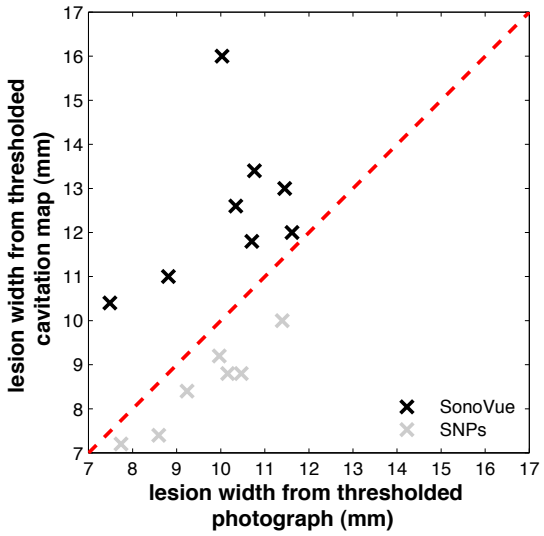


Figure 4.24: Comparison of lesion widths predicted from thresholded passive acoustic maps and photographs of denatured bovine liver tissue. The red line represents the ideal regression line along which the two are identical.

presence of an exogenous nucleation agent is primarily due to a broad spatial distribution of cavitation events whose energies lie above some threshold level. It is unclear whether this relationship would apply to HIFU insonation conditions that favour excessive pre-focal activity.

4.4 SUMMARY

The primary objective of this chapter has been to ascertain whether the empirical relationship between heating and cavitation established *in vitro* in Chapter 3 extends to non-perfused *ex vivo* animal tissue.

Initially, naked bovine liver was experimented upon using a single-element PCD to determine its propensity for cavitation activity at a range of frequencies and PRFPs. At the lower of the two frequencies, pre-focal bubble activity was a major source of concern, whilst cavitation activity at 1.067 MHz was intermittent and lacking in intensity. Unsurprisingly, preliminary temperature elevation measurements

revealed little in the way of cavitation-enhanced heating.

The 0.508 MHz HIFU transducer was subsequently omitted and exogenous nuclei added to the tissue matrix by intra-organ injection. These nuclei took the form of either SonoVue® microbubbles, sonosensitive polystyrene nanoparticles or non-sonosensitive polystyrene nanoparticles. Despite generating markedly different PCD signal variance profiles, the effect of both SonoVue ® and sonosensitive nanoparticles was to lower the inertial cavitation and tissue damage thesholds. Moreover, the extent of lesioning was found to correlate positively with the total broadband energy of these emissions: as with agar and PAA, there exists a threshold level of broadband energy for cavitation-mediated thermal effects to become dominant.

The polystyrene nanoparticles present size advantages over SonoVue®, thereby facilitating extravasation into tortuous tumour capillaries; however, their immunogenicity is presently unknown. Nonetheless, the sonosensitive nanoparticles were extremely effective at producing cavitation activity that was exclusively associated with broadband acoustic emissions, and at sustaining such activity throughout HIFU sonication. It can be concluded that they have potential as an agent for promoting cavitation-enhanced heating and for facilitating cavitation-based monitoring of HIFU therapy by techniques such as passive acoustic mapping. Whilst the work of this chapter shows that lesioning is possible in as little as 2 s, the administration and concentration of exogenous nuclei required to achieve this are by no means clinically relevant.

It is encouraging that the procedure for determining an empirical relationship between cavitation and heating *in vitro* has been successfully replicated *ex vivo*. However, use of a single-element PCD signal to represent cavitation events occurring over a region potentially much larger than the PCD focal volume is question-

able. Passive acoustic mapping was thus used to reconstruct cavitation events in two dimensions using TEA. Whilst the broadband acoustic maps obtained from HIFU exposures involving the use of either SonoVue® or sonosensitive nanoparticles share commonalities compared with the control experiments, the same cannot be said of the harmonic/ultraharmonic component. Application of the broadband energy threshold for lesioning to the reconstructed source maps and comparison with lesion photographs yielded strong positive correlation between the width of the cavitation region and lesion size, particularly in bovine liver impregnated with sonosensitive nanoparticles. This is an important result as it proves that widespread lesioning in the presence of suitable exogenous nuclei may be attributed to a broad spatial distribution of inertial cavitation events.

Finally, it is important to point out that the work presented in this chapter relates to a narrow subset of HIFU operating conditions. At higher intensities, the tendency for pre-focal shielding will skew lesions in the direction of the transducer. Thus, using the width of the cavitation region at the focus to infer likely lesion dimensions is without basis. Moreover, the method adopted for measuring lesion cross-sectional area is somewhat subjective, dependent on the original positioning of the needle, the accuracy of the bisection procedure, and the lighting conditions for photography. However, in the knowledge that cavitation-enhanced heating is achievable in soft animal tissue, the empirical relationship that has emerged forms the basis of ongoing work into this exciting domain.



CHAPTER 5

THERMALLY RELEVANT CAVITATION CONTROL *In Vitro*

Once instigated, there is a tendency for cavitation activity to vary unpredictably on account of the ever changing nucleation environment, which is regrettable given the demonstrable capacity for inertial cavitation to augment heating rates. This chapter considers the implementation of an adaptive PRFP modulation scheme to sustain inertial cavitation, and hence heating, at the HIFU focus over clinically relevant timescales. The eventual controller design is validated in an agar tissue phantom, whose characteristic homogeneity is a helpful simplification of the problem at this development stage.

The previous two results chapters have highlighted the heating benefits of HIFU-induced cavitation, and have shown there to exist a medium-specific level of broadband secondary acoustic emissions beyond which these benefits manifest. This in itself is an important result; however, for cavitation-assisted HIFU to gain clinical acceptance, it is necessary to harness the potential of cavitating microbubbles in a controlled manner, so as to achieve preferential heating at the treatment site. Since an accurate, invertible model of medium response to HIFU is not available, it is necessary to modify the existing setup to include a feedback loop and thus form a control system that is able to stabilise the cavitation signal.

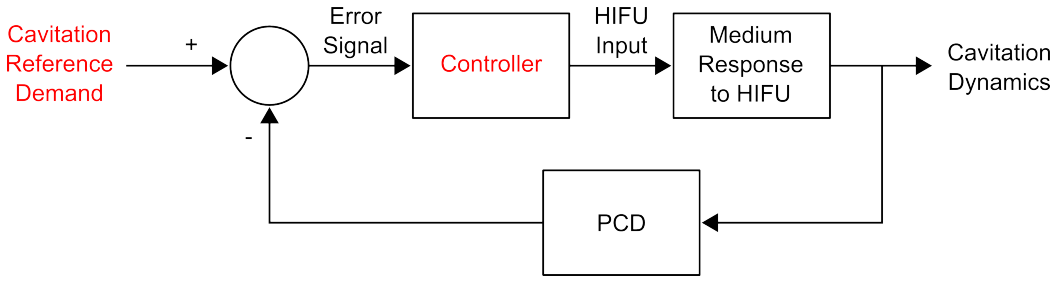


Figure 5.1: Schematic representation of a negative-feedback control system. The cavitation reference demand is equivalent to the threshold total broadband energy level for cavitation-enhanced heating previously identified.

This chapter considers the design, implementation and validation of a proportional gain controller capable of sustaining therapeutic levels of inertial cavitation over clinically relevant timescales. This is achieved *in vitro* by altering the PRFP prescribed by the function generator in response to fluctuations of the PCD signal. The technique shows great promise as a means of effecting cavitation-enhanced, cavitation-controlled and cavitation-monitored thermal ablation at lower HIFU intensities than in current clinical use.

5.1 Basic Control Theory

Figure 5.1 is a schematic of a simple control system, comprising a controller, a dynamical system (the medium response to HIFU), a sensor (the PCD) and a mathematical operator. The purpose of the control system is to force the dynamical system output to follow an external input (the reference demand) by manipulating the dynamical system input based on the error between the reference demand and the system output. Feedback automatically generates an implicit approximate inverse of the dynamical system and can be desensitised to uncertainty in the model.

The elements highlighted in red in Figure 5.1 are those which may be adjusted to generate the desired system output. As regards the cavitation reference demand,

Chapter 3 suggests a threshold *total* broadband energy of 0.003 V^2s for cavitation to emerge as a dominant heating mechanism. However, the control system requires a continuous feed of information - that is, an *instantaneous* measure of inertial cavitation activity - to function. For the 2 s exposures from which the energy threshold was derived, a broadband variance of 0.0015 V^2 is the equivalent quasi-instantaneous system output. Thus, this was identified as a suitable reference demand. Moreover, practical control systems are designed to include a neutral zone above the reference demand where no action occurs to prevent oscillation. The width of this so-called "deadband" was chosen to be 0.003 V^2, based on the significant variation of the PCD signal variance encountered previously.

The controller itself is the subject of the present work, the aim being to sustain thermally relevant levels of inertial cavitation. The 3% agar phantom recipe used in Chapter 3 was considered to be a suitable experimental model for proof-of-concept controller implementation, based on its ease of manufacture and characteristic homogeneity. Previous work has shown that HIFU-induced broadband emissions may be altered by virtue of the sonication parameters. Unfortunately, switching HIFU frequency from the fundamental to the third harmonic, as permitted by the corresponding matching network, is reliant on manual intervention to make the appropriate connections. Moreover, previous work undertaken to investigate the effects of changes in duty cycle on cavitation-enhanced heating has so far proven inconclusive (Hockham, 2009). Thus, the dynamical system input was restricted to a single dimension, the PRFP.

Criteria for the control system were explicated in Section 2.8. Of particular importance is the requirement for cavitation to occur over the entire exposure duration, to enable concurrent cavitation monitoring and, therefore, treatment guidance.

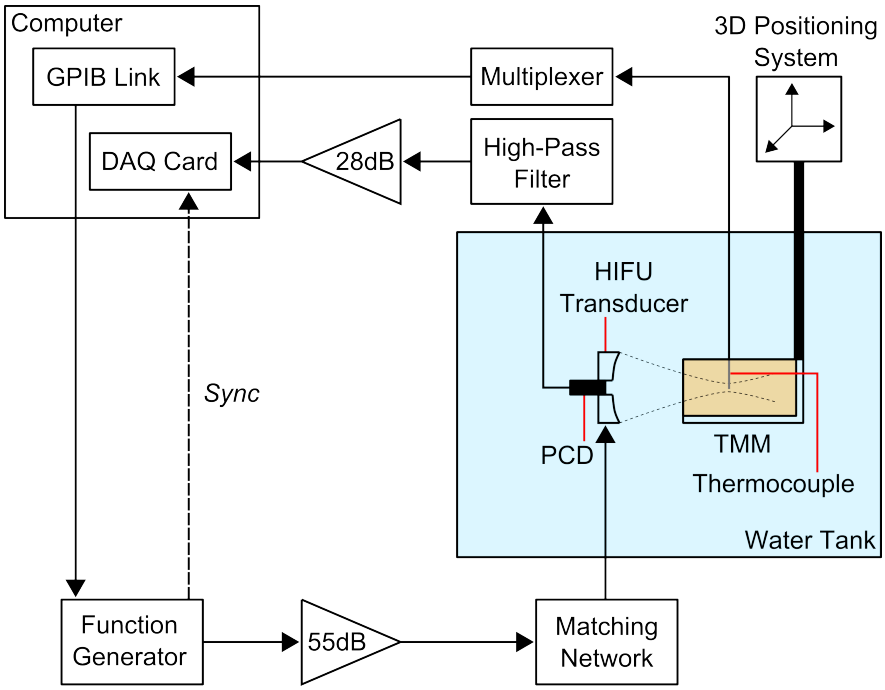


Figure 5.2: Overview of the experimental setup for acquiring cavitation and thermal data. The signal output from a function generator is passed through a series of signal conditioners before reaching the transducer. Acoustic emissions at the focus are recorded by a PCD and thermal data acquired using a thermocouple.

5.2 Experimental Setup

The experimental setup adopted for the work of this chapter is identical to that used in Chapter 3, the schematic of which is replicated in Figure 5.2 for convenience. To summarise, a 1.067 MHz transducer was used in conjunction with a 15 MHz single-element PCD and aligned with an agar-embedded thermocouple located at a depth of 10 mm beyond the front face of the tissue phantom. Moreover, all of the results presented pertain to experiments conducted at room temperature at previously un-exposed phantom locations to standardise the initial cavitation nuclei population as far as practicably possible.

5.3 Controlling Software

The LabVIEW script described in Section 3.2 was systematically modified to include a negative feedback loop. Some additional features of the script include:

- real-time spectral decomposition of PCD data;
- a real-time feed of broadband PCD signal variance (computed in the native LabVIEW environment) to the controller module, which uses the information to amplify/attenuate the PRFP, thus negating the requirement to access data from the hard drive;
- the option to apply asymmetric controller gains, depending on whether the PCD signal variance overshoots or undershoots the reference demand;
- an implicit 8 ms delay between an error signal being detected and the PRFP being reset;
- a hold-off of 100 ms between consecutive amplitude adjustments to prevent saturation of the function generator write buffer and to allow sufficient time for the function generator autoranging feature to switch attenuators;
- an instruction to deactivate the HIFU transducer prior to the pre-selected exposure duration if a specified function generator output voltage is exceeded.

5.4 Data Analysis

Cavitation and thermal data was processed as per the methods described in Chapter 3. This includes the use of a comb filter to remove the harmonics only (and not the ultraharmonics).

5.5 Results and Discussion

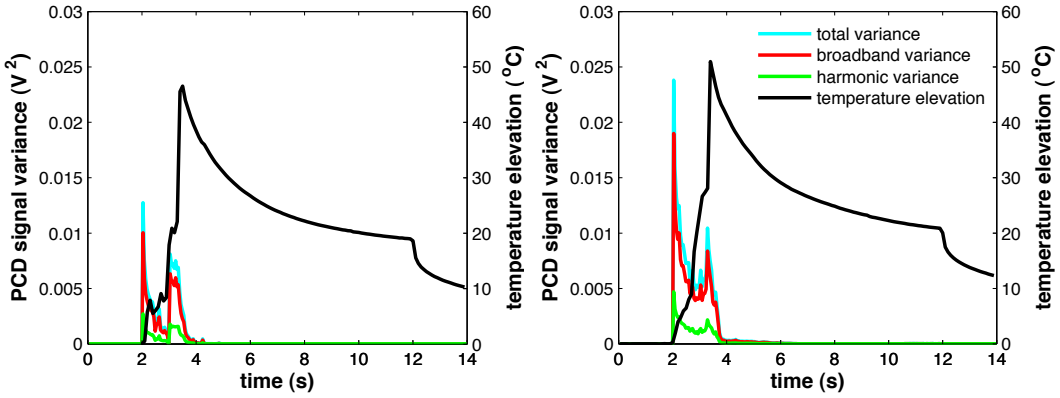
Without any intervention, inertial cavitation in agar, as measured at the focus of a HIFU transducer, tends to decay due to cavitation nuclei depletion. It is hypothesised that, by altering the HIFU parameters part way through an exposure, it may be possible to subsequently target nuclei which were previously unsuitable for inertial cavitation and, therefore, sustain cavitation activity over longer timescales. If the potential for heating enhancement by bubbles undergoing inertial cavitation can be harnessed in a controlled manner, larger volumes of pathological tissue could be treated at each HIFU focus location, thereby reducing treatment times.

5.5.1 Proof of Concept

Prior to designing the controller, an initial proof-of-concept experiment was undertaken, involving a single increase in PRFP triggered by the broadband signal variance dropping to within six standard deviations of the basal noise level. An initial HIFU amplitude of 2.85 MPa was chosen so as to generate a broadband noise signal in excess of that required for cavitation-enhanced heating. Moreover, the duty cycle was maintained at 99% to enable concurrent passive localisation.

Figure 5.3 (a) demonstrates the impact of a triggered increase in PRFP to 3.37 MPa on the cavitation signal and the corresponding temperature elevation profile. This may be contrasted with Figure 5.3 (b), which was conducted at a constant PRFP of 3.37 MPa. Interestingly, the temperature profiles are very similar despite the different energy contents of the incident waves.

This result is encouraging as it suggests that the concept of sustaining inertial cavitation at a pre-defined level to make best use of the incident waveform energy for heating purposes is with merit. Naturally, the next step in the design process is



(a) (b)

Figure 5.3: (a) PCD signal variance and temperature elevation profiles from a HIFU exposure with an initial PRFP of 2.85 MPa, during which the PRFP was incremented once by 0.52 MPa. (b) Results from a HIFU exposure performed at a constant PRFP of 3.37 MPa. The temperature profiles from the two experiments are practically identical, despite different energy contents of the incident waves.

to incorporate more pressure increments.

5.5.2 Controller Design

Figure 5.4 is a schematic of the first iteration controller design, in which the function generator is systematically triggered to increase the amplitude of its output when the broadband signal variance drops below the setpoint (0.0015 V^2) by an amount proportional to the difference. Likewise, when the broadband signal variance exceeds 0.0045 V^2, the function generator is instructed to reduce its output by an amount proportional to the difference. A starting PRFP of 2.21 MPa was chosen for the controller because it consistently yields broadband PCD signals that initially lie within the neutral zone.

Manual tuning of the controller parameters revealed the need to adopt a logarithmic scale and apply asymmetric gains to negative and positive errors to account for the slow response of the cavitation dynamics to a reduction in PRFP. The

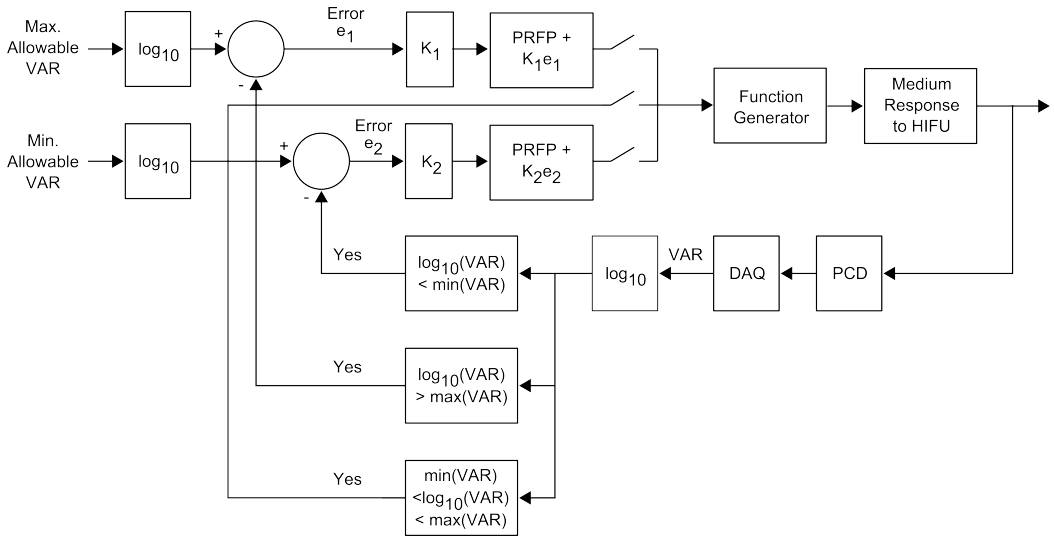


Figure 5.4: Schematic diagram of the first iteration control system design for sustaining thermally relevant cavitation in the focal region of a HIFU transducer. A neutral zone exists between 0.0015 V^2 and 0.0045 V^2 to prevent oscillation.

optimal controller settings for sustaining inertial cavitation activity at the specified level were found to be K_1 = 0.05 and K_2 = 0.005 for negative and positive errors respectively. The graphs presented in Figure 5.5 are typical of HIFU experiments conducted in agar using the control system. Thermally relevant inertial cavitation is sustained for approximately 20 s prior to decay: after 21.5 s of transducer on-time, the PRFP reaches its specified upper limit and the transducer is deactivated. Significant overshooting of the neutral zone at t = 16 s and t = 21 s is likely due to larger bubbles being targeted, which tend to be associated with larger collapse energies.

The grey line overlaid on the temperature elevation profile represents the target focal temperature elevation. It is generally accepted that maintaining cells at a temperature of 56 °C for 1 s (corresponding to a 19 °C temperature rise in tissue initially at 37 °C) results in cell death (Kennedy, 2005). However, several current clinical HIFU treatments rely on hyperecho, which is known to be associated with tissue boiling (Coussios et al., 2007a; Rabkin et al., 2005), thus necessitating a 63 °C temperature rise. The target temperature rise was therefore arbitrarily chosen to be

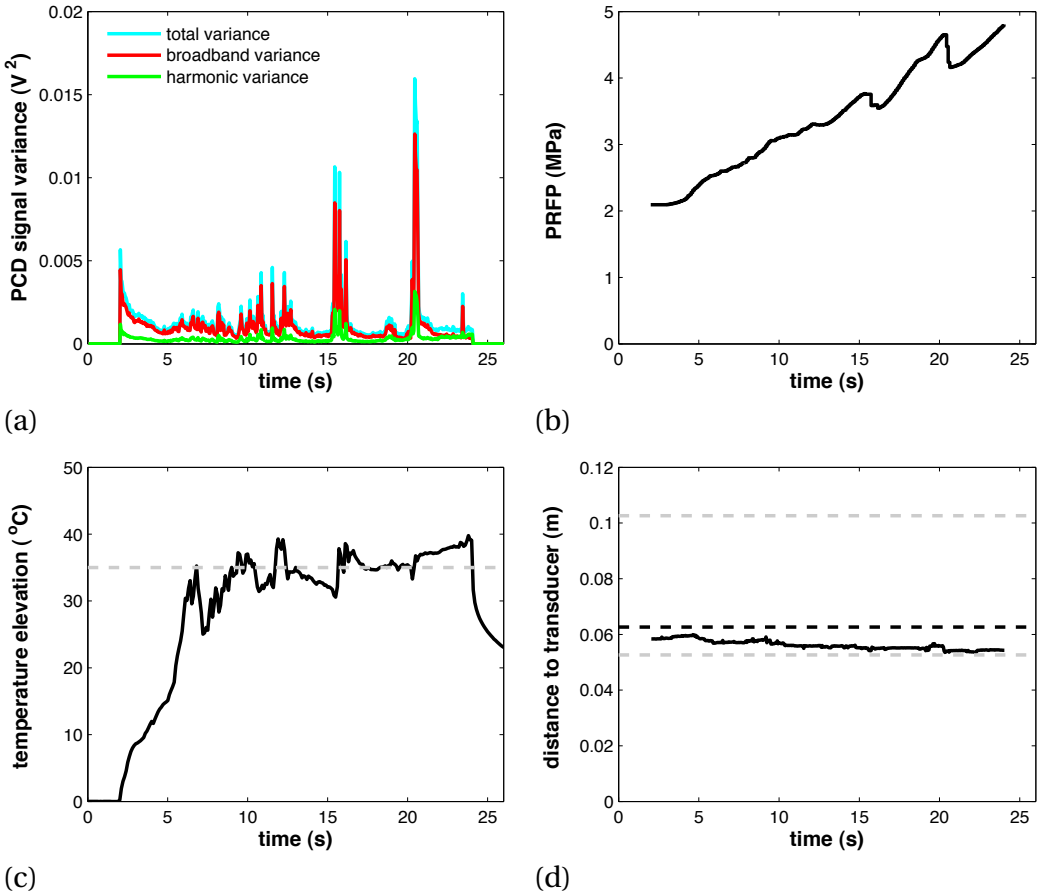


Figure 5.5: Implementation of a closed-loop negative-feedback controller with a starting PRFP of 2.21 MPa. Inertial cavitation is sustained for upwards of 20 seconds (a), yielding a steady temperature profile (c). This is achieved by varying the PRFP (b) using asymmetric proportional gains. The passive localisation plot (d) is indicative of pre-focal cavitation activity, which increases with increasing PRFP, as expected.

35 °C, as an intermediate value between the two extremes. Raising the focal temperature beyond this level is wasteful and counterproductive.

Conversion of the focal PRFP to acoustic intensity and hence power, and integration of the resulting vector yields a focal irradiation energy content of approximately 233 J over the course of this particular exposure. This is equivalent to maintaining the PRFP at 3.38 MPa over the same exposure length. Accordingly, HIFU exposures were also undertaken at constant PRFPs of both 3.38 MPa and 4.79 MPa for 21.5 s

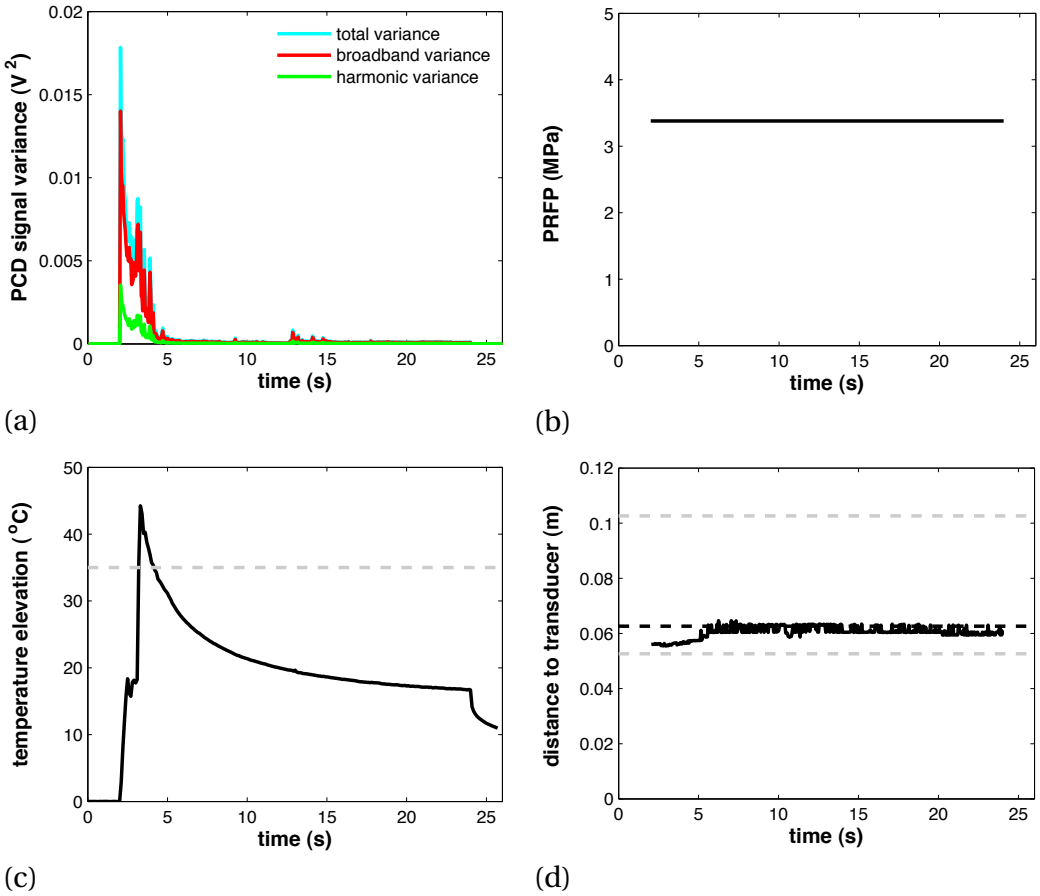


Figure 5.6: Results from a HIFU exposure conducted at a duty cycle of 99% and a PRFP of 3.38 MPa for 21.5 s. Inertial activity decays rapidly (a), which impacts significantly on the corresponding temperature elevation profile (c). The PRFP and localisation profiles are also provided in (b) and (d) for comparison.

in the absence of the feedback loop for validation purposes. The latter value represents the pre-defined upper limit of transducer operation and is equivalent to a focal irradiation energy content of approximately 470 J.

The validation experiments are presented in Figures 5.6 and 5.7. Evidently, inertial cavitation decays rapidly over the first 5 s of HIFU insonation at both PRFPs; however, doubling the focal energy input from 233 J to 470 J is seen to have a positive effect on the temperature elevation profile, which remains close to the target level for the entirety of the exposure duration. This is in contrast to the controller exper-

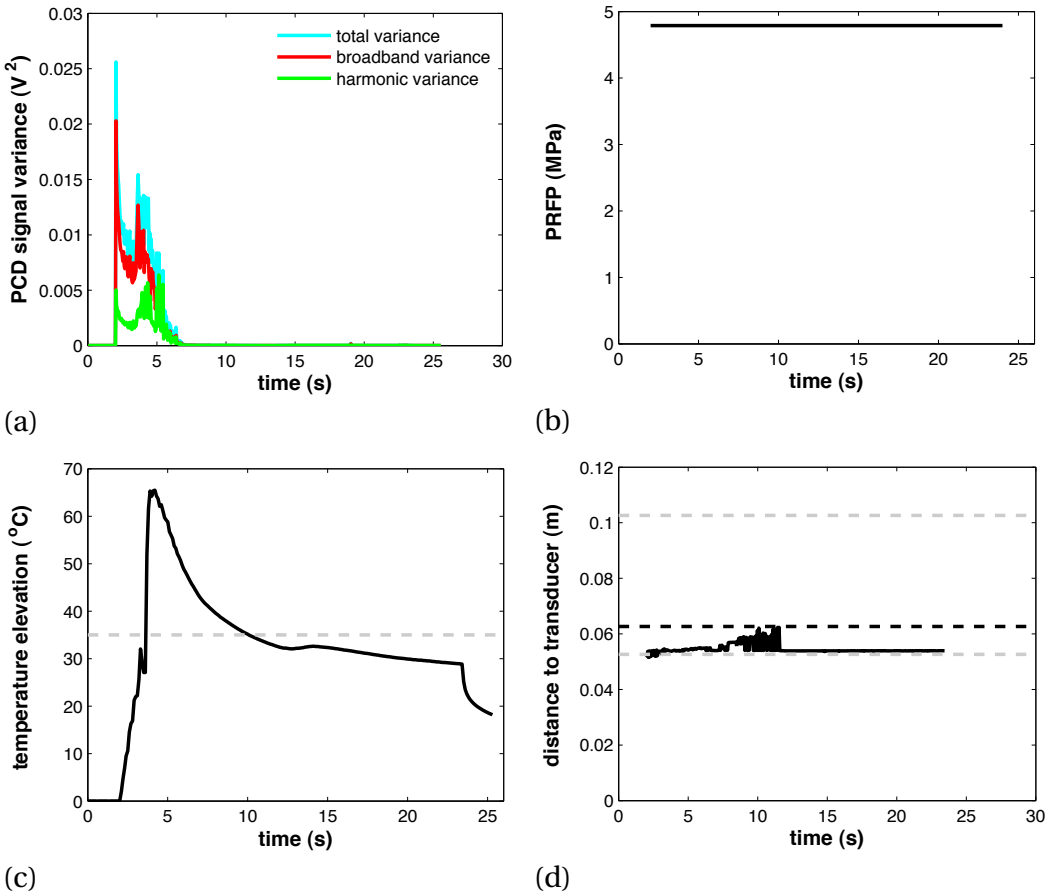


Figure 5.7: Results from a HIFU exposure conducted at a duty cycle of 99% and a PRFP of 4.79 MPa for 21.5 s. Again, inertial activity decays rapidly (a); however, the twofold increase in PRFP is sufficient to sustain thermally relevant levels of heating (c). The PRFP and localisation profiles are also provided in (b) and (d) for comparison. Note the increase in pre-focal activity compared with the controller example.

iment, which employed much lower intensities to achieve the same effect, thereby limiting collateral damage.

In summary, by sustaining inertial cavitation activity above the stipulated threshold value (0.0015 V^2), it has been shown that it is possible to maintain cytotoxic levels of heating at much lower input energies than required in the absence of the controller. The inclusion of a hold-off gives a worst case temporal resolution of approximately 200 ms, which is significantly better than alternative treatment monitoring techniques. Of course, it is plausible that the invasive nature of

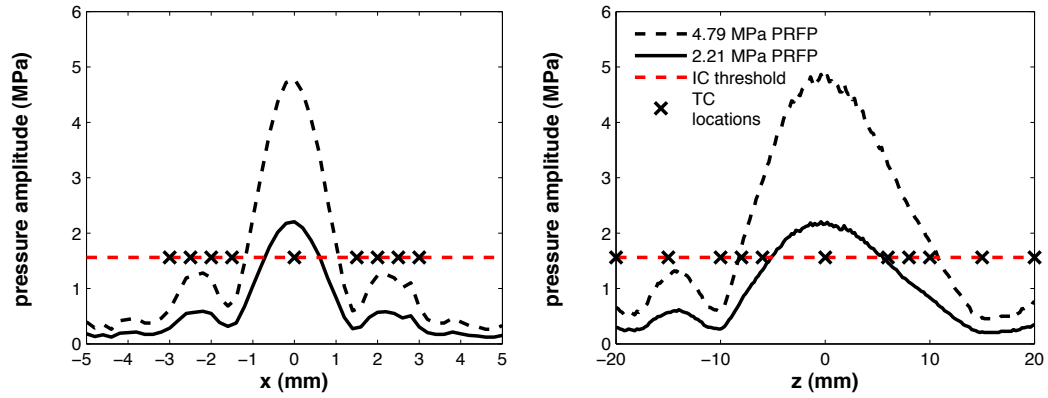
the thermocouple interferes with the cavitation dynamics, and hence focal heating. Moreover, measuring the temperature at a single location is restrictive given the three-dimensional spatial distribution of cavitation events. The following section attempts to address these problems by measuring the temperature elevation off-axis in both the presence and absence of active cavitation control.

5.5.3 Volumetric Temperature Variation

The presence of a foreign object within a HIFU target alters the local microenvironment by increasing viscous forces and promoting bubble formation at its interface. Although HIFU exposures conducted in agar both in the presence and absence of a thermocouple register little difference in the way of cavitation activity, artefactual heating at the thermocouple boundary layer tends to artificially augment the recorded temperatures.

Though it would be difficult to dispute the focal heating benefits brought about by use of the controller over single PRFP HIFU excitation, as demonstrated in Figures 5.5 and 5.6, it is instructive to consider how heating rates compare in regions remote from the HIFU focus, where thermocouple artefact is less significant. Accordingly, off-axis temperature measurements were obtained during both controlled and uncontrolled HIFU sonications to document the three-dimensional evolution of the temperature field. The thermocouple was embedded at different locations within an agar phantom and aligned with the HIFU focus each time. The motorised positioning system was then used to displace the phantom by a known amount.

The various thermocouple locations (relative to the HIFU focus) were chosen to lie mainly in regions where the peak rarefactional pressure lies below the cavitation threshold so as to measure the combined effects of viscous absorption at the fundamenal frequency and thermal diffusion, as opposed to transient temperature



(a) (b)

Figure 5.8: Pressure amplitude profiles along the transverse (a) and longitudinal (b) axes of the 1.067 MHz HIFU transducer. IC is shorthand for inertial cavitation; TC is shorthand for thermocouple.

gradients arising due to cavitation. Figure 5.8 depicts the variation of the HIFU field in the transverse and axial directions, obtained using the membrane hydrophone initially introduced in Section 3.1.2. The solid black lines represent pressure amplitude measurements obtained from within the HIFU field using the membrane hydrophone at the starting HIFU input voltage of the controller (equivalent to a PRFP of 2.21 MPa), whilst the dashed black lines represent extrapolated pressure amplitude values at the pre-defined upper limit of transducer operation (equivalent to 4.79 MPa). The inertial cavitation threshold of 3% agar is demarcated in red, whilst the thermocouple locations are indicated by black crosses.

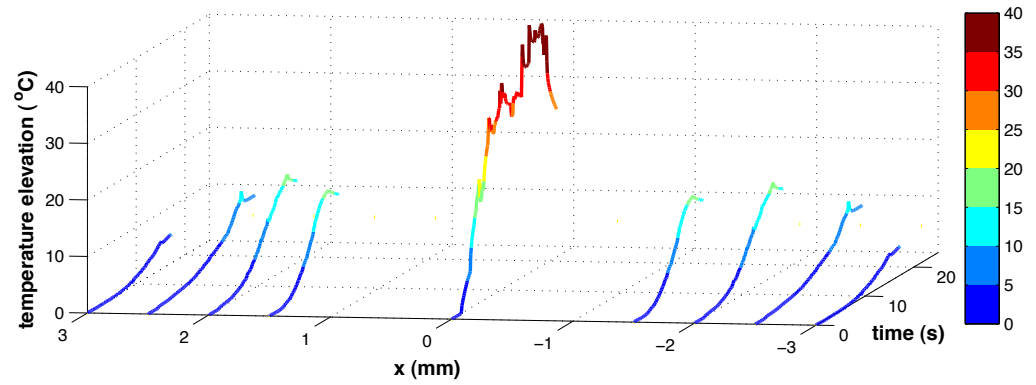
Initially, a series of HIFU exposures were conducted using the controller to sustain inertial cavitation activity at locations (0,0,0), (1.5,0,0), (2,0,0), (2.5,0,0), (3,0,0), (0,0,-20), (0,0,-15), (0,0,-10), (0,0,-8), (0,0,-6), (0,0,6), (0,0,8), (0,0,10), (0,0,15) and (0,0,20), where the coordinates are quoted in millimetres. Subsequently, the mean focal energy input was evaluated for each exposure and an equivalent number of HIFU exposures undertaken in a second phantom without the use of the controller. The associated PRFPs were chosen to deliver the same amount of mechanical en-

ergy to the HIFU focus over the same period of time as the corresponding controlled exposure.

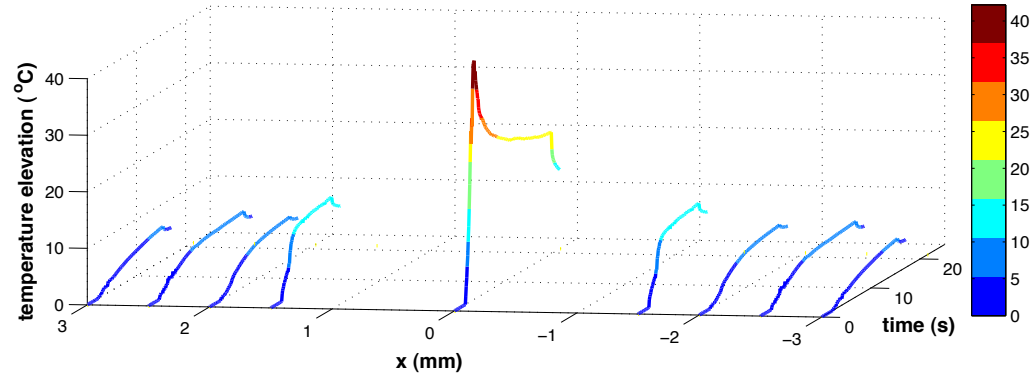
The results from HIFU exposures in which the thermocouple was displaced in the transverse plane are presented in Figure 5.9. The acoustic field profile in this plane is radially symmetric so isotherms may be assumed to take the form of concentric circles originating at the focus. With reference to Figure 5.8, inertial cavitation should not occur at the chosen off-axis thermocouple locations, which would explain the relatively smooth temperature elevation profiles either side of the HIFU focus on both graphs. When the controller is operated, higher temperature elevations are recorded between x = 1.5 and x = 2.5 compared with the constant PRFP equivalents; however, it takes more time for these higher temperature elevations to develop. In contrast, the significant focal temperature elevation recorded at the focus soon after HIFU activation in Figure 5.9 (b) suggests a steep spatial temperature gradient initially, which favours thermal diffusion.

Figure 5.10 is the longitudinal plane equivalent of Figure 5.9. The pressure amplitude profile in the longitudinal direction is distinctly asymmetric, thus the requirement to consider thermocouple placement in the negative and positive directions separately. Importantly, when the thermocouple was positioned between the HIFU-PCD assembly and its geometric focus (z = -6, -8, -10, -15 and -20 mm), the controller was found to halt operation prematurely, after approximately 10 s of HIFU excitation - that is, the PRFP rapidly ramped up to its pre-defined upper limit. It is conceivable that the presence of the thermocouple adversely affects the interference pattern of the transducer and gives rise to a lower PRFP. This would have a cascading effect on focal and off-axis temperature measurements.

Placement of the thermocouple at the distal side of the HIFU focus yielded some interesting results. In particular, significant temperature elevations were recorded



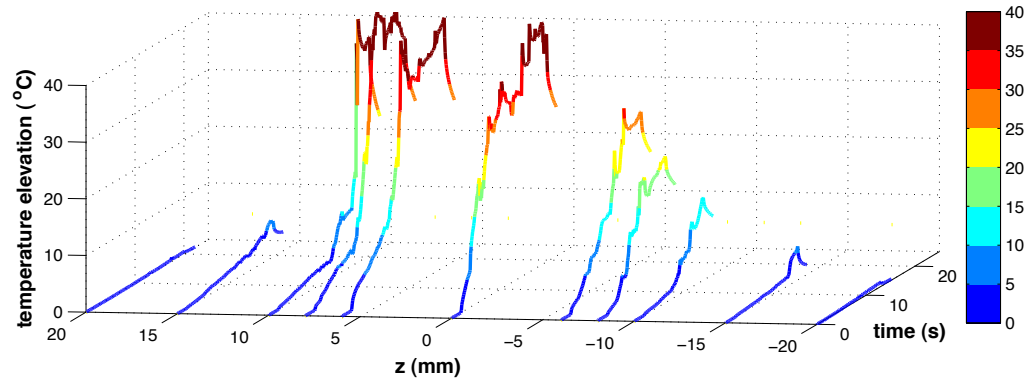
(a)



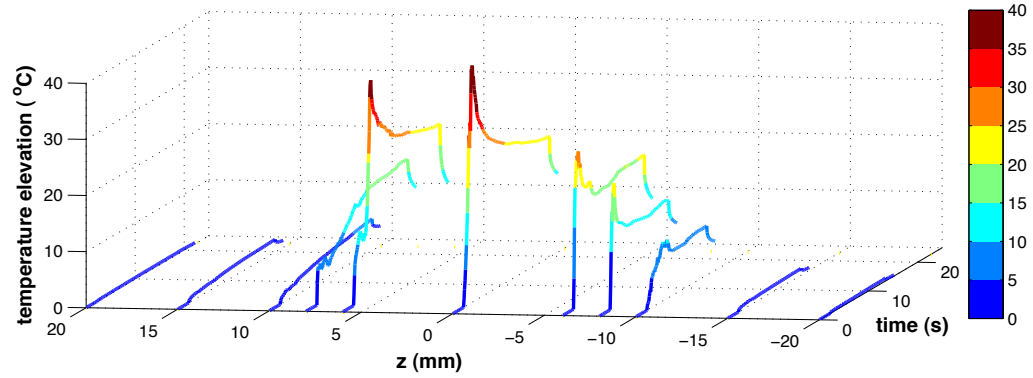
(b)

Figure 5.9: Spatio-temporal temperature elevation in the transverse plane through the HIFU focus with (a) and without (b) use of the controller for sustaining inertial cavitation.

between $z = 5$ and $z = 10$. This suggests that the geometric focus may not have been exactly coincident with the point of maximum PRFP. However, there is also a delay of a few seconds between the temperature elevation entering the cytotoxic regime at $z = 0$ and further field. It is conceivable that some of the agar undergoes a phase change and the resulting liquid is subjected to an ARF, which progressively displaces the cavitation nuclei further afield. Regardless, controller operation is clearly preferable over constant PRFP HIFU exposure of the same focal energy content as it enables higher temperature elevations to be attained in regions remote from the HIFU focus by the combined effects of thermal diffusion from the focus and a progres-



(a)



(b)

Figure 5.10: Spatio-temporal temperature elevation in the longitudinal plane through the HIFU focus with (a) and without (b) use of the controller for sustaining inertial cavitation.

sively expanding cavitation region.

5.6 Summary

Extensive experimental work has already revealed there to be a manifest dependence of heating on inertial cavitation, provided a threshold level of total broadband energy of cavitation emissions is exceeded. Importantly, this relationship has been shown to hold true for a variety of HIFU targets, including agar- and PAA-based tissue-mimicking phantoms, and excised animal tissue. Equipped with this

information, the primary objective of this chapter has been to exploit the empirical relationship between temperature elevation and broadband acoustic emissions to harness the heating benefits of inertial cavitation in a controlled manner.

Systematic modifications to the original LabView script resulted in the evolution of a novel closed-loop feedback control system whose purpose is to sustain inertial cavitation at a steady level for as long as possible using a proportional gain controller. Without the control system, cavitation activity decays rapidly once instigated, but this was found to be preventable by altering the PRFP in response to the broadband variance of the cavitation signal. Validation of the controller design in agar was successful, in that thermally relevant cavitation activity was sustained at the HIFU focus for up to 20 s. This yielded temperature elevations in excess of that which could be achieved without the feedback loop using the same focal energy input, and of the same order of that attained using twice the energy input, again without the controller. These results are particularly encouraging because the use of lower acoustic intensities reduces the likelihood of pre-focal attenuation and greatly improves patient safety.

Furthermore, characterisation of the temperature elevation profile in three dimensions served to eliminate some of the uncertainties surrounding artefactual heating and exogenous nucleation. In particular, it was found that the absence of the thermocouple from the HIFU focus did not impact on cavitation emissions. Moreover, regions adjacent to the HIFU focus were shown to benefit from increased focal activity due to a combination of increased thermal diffusion from the focus and a progressively expanding cavitation region due to the PRFP being gradually increased. Therefore, controller implementation facilitates treatment of a larger volume of tissue, thereby reducing treatment times and moving HIFU one step closer to widespread clinical adoption.

Evidently, the logical progression from this result is to extend the control system to animal tissue. Unfortunately, successful implementation of the controller in non-perfused bovine liver is unlikely given the requirement to insert exogenous nuclei, and the tendency for these nuclei to rapidly diffuse away from the HIFU focus once injected. As such, nuclei depletion occurs over much shorter timescales compared with agar. The following chapter thus involves the use of a perfused liver model, in which the source of cavitation nuclei is continually replenished.



CHAPTER 6

THERAPEUTICALLY RELEVANT CAVITATION CONTROL IN A PERFUSED LIVER MODEL

Thus far, cavitation-enhanced heating has been demonstrated *in vitro* and in non-perfused excised liver, and the notion of cavitation control introduced and validated in an agar tissue phantom. The work of this chapter aims to extend the cavitation controller to a unique perfused liver model, in which blood flow through the tissue vasculature both continually replenishes the supply of cavitation nuclei and removes heat from the target region via the heat sink effect. The cavitation dynamics of the perfused system are initially investigated, followed by implementation of the control system specified in Chapter 5, with the necessary modifications to account for perfusion effects. The overall aim is to determine whether continuous control of inertial cavitation activity during HIFU exposure is capable of achieving controlled lesioning using lower HIFU energies than would be required in the absence of active cavitation control.

The notion of cavitation control to guide HIFU-mediated ablative therapy is a relatively new concept, which has garnered interest from HIFU proponents due to its capacity to deliver superior rates of heating at lower HIFU intensities. The *ex vivo* liver model employed in this chapter has the added complexity of including perfusion effects. Though this arrangement has previously been shown to yield lower cavitation thresholds compared with non-perfused organs due to the continual replenishment of cavitation nuclei, increased heat advection due to blood flow can lead to variability in thermal response and unpredictable perivascular tumour ab-

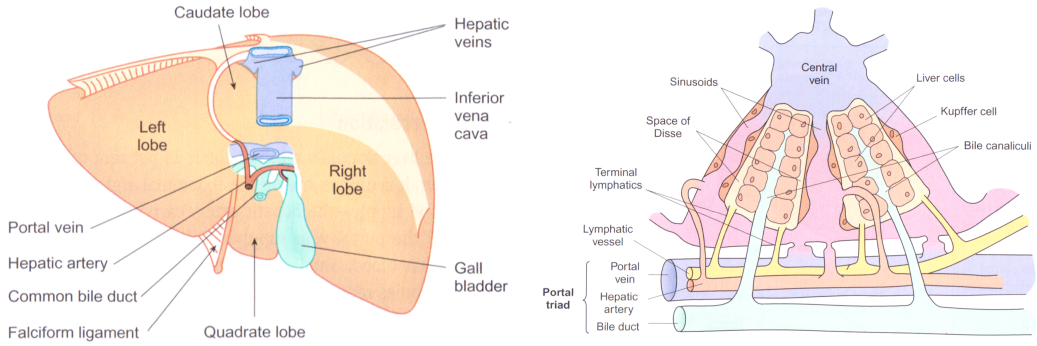
lation (Holroyd et al., 2012).

This chapter considers the implementation of the control system from Chapter 5 in a perfused porcine liver model, the aim being to promote and prolong inertial cavitation to the extent that coagulative necrosis may be induced at lower acoustic energies. Importantly, porcine liver exhibits similar flow rates to human liver (0-2 L/min), and its comparable dimensions present a major advantage over small animal models. The work presented pertains specifically to healthy tissue due to lack of a suitable porcine carcinoma model. As discussed in Section 1.3, tumour physiology is vastly different to that of healthy tissue; however, preliminary work conducted in the absence of a tumour mass is certainly a step in the right direction.

An extracorporeal liver perfusion device (ECLPD) was used to recreate a normothermic environment mimicking that of the human body by continuously perfusing the liver with autologous whole blood at physiological pressures and flows, and providing nutrition. The liver was, therefore, in a quasi-physiological, heamodynamic, synthetic and metabolic state before, during and after HIFU exposure (Butler et al., 2002), enabling direct observation of the effects of tissue perfusion on ablation. The model is largely representative of the *in vivo* environment except for the exclusion of overlying tissue (bone, muscle, fat), which would otherwise attenuate the incident sound field.

6.1 Introduction to Perfusion Effects

As a brief introduction to the work of this chapter, it is instructive to consider the vessels that carry blood to, from and within the liver, in addition to the implications of perfusion effects on bubble nucleation and subsequent oscillation. Heat loss due to blood perfusion was introduced in Section 1.4.1 and is not considered further



(a) (b)

Figure 6.1: (a) Main anatomical features of the liver and (b) basic structure of the liver's functional units (lobules) (Kumar et al., 2010).

here.

6.1.1 Vascular Supply and Drainage of the Liver

The circulatory system of the liver is unlike that seen in any other organ. It receives a dual blood supply from the hepatic artery and the portal vein (see Figure 6.1 (a)), of which the latter accounts for up to 75% of the liver's blood supply but meets only half of its oxygen demand. The rest is met by the hepatic artery. These vessels progressively subdivide into smaller capillaries, the terminal branches of which lead to lobules (see Figure 6.1 (b)).

Lobules are the functional units of the liver, comprising parenchymal cells (hepatocytes) and non-parenchymal cells (Kupffer cells). Blood flows through sinusoids, lined with highly fenestrated endothelial cells and bounded circumferentially by hepatocytes, and into the central vein of each lobule. Central veins coalesce into hepatic veins, which leave the liver and empty into the vena cava. Meanwhile, hepatocytes secrete bile into the canaliculi, which merge into bile ducts. Bile ducts begin in very close proximity to the terminal branches of the portal vein and hepatic artery, the grouping of which is an easily recognisable feature seen in histopatho-

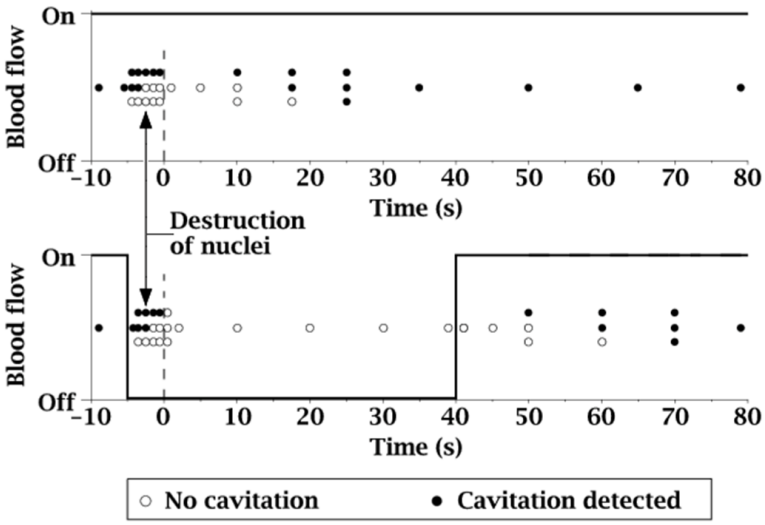


Figure 6.2: Demonstration of cavitation nuclei replenishment, and hence inertial cavitation recurrence, in perfused porcine liver. It takes in excess of 10 s for the supply of cavitation nuclei to be replenished once fully depleted (courtesy of S. Labouret).

logical sections of liver and is commonly referred to as the portal triad (Kumar et al., 2010).

6.1.2 Cavitation Nuclei Replenishment

In contrast to non-perfused systems, blood flow through the tissue vasculature in perfused organs serves to continually replenish the supply of cavitation nuclei. Provided the inertial cavitation threshold of the perfused organ is suitably low, this should facilitate cavitation sustenance for heating applications.

Previous work using 2-cycle, 1.1 MHz HIFU pulses at a PRFP of 9 MPa has shown that it takes in excess of 10 s for inertial cavitation activity to resume once the supply of cavitation nuclei has been fully depleted (Holroyd et al., 2012). This is evident from Figure 6.2, which charts the evolution of inertial cavitation activity when blood flow to the liver is maintained at a steady rate and when it is halted for 45 s (courtesy of S. Labouret). Given the quasi-CW strategy often adopted for ablative therapies,

it is highly likely that cavitation nuclei depletion will occur over shorter timescales; however, the rate of replenishment should not change. In the event of lesion formation, the microcirculation in the vicinity of the lesion may be irreversibly disrupted, thereby impeding cavitation recurrence and limiting the size to which the lesion may grow.

6.2 Experimental Setup

The experimental setup adopted for the *ex vivo* work presented in this chapter consists of two major parts, namely normothermic liver perfusion and ultrasound actuation and detection. Liver retrieval and perfusion were conducted by Dr. David Holroyd, who was present throughout each of the experiments to ensure that the organ was maintained in a physiological state. Details of the relevant procedures, as developed by OrganOx, Oxford, are explained in order in the following sections.

6.2.1 Liver Procurement

Livers were procured from white Landrace pigs weighing between 70 and 85 kg using a standard technique decribed by Brockmann et al., and in accordance with the United Kingdom Animal (Scientific Procedures) Act of 1986 (Brockmann et al., 2009; Jamieson et al., 2011). Blood was initially collected from the pig via the aortic cannula and stored in dextrose-supplemented blood transfusion bags. The liver was subsequently cold-perfused with hyperosmolar citrate solution via the same cannula. Following venesection, the thoracic aorta was cross-clamped and the suprahepatic inferior vena cava (IVC) divided. After 2 L of cold perfusate had been administered, the hepatic vessels and the infrahepatic IVC were divided, allowing the liver to be removed, placed in sterile intestinal bags, and packed with ice in a cool box for transportation.

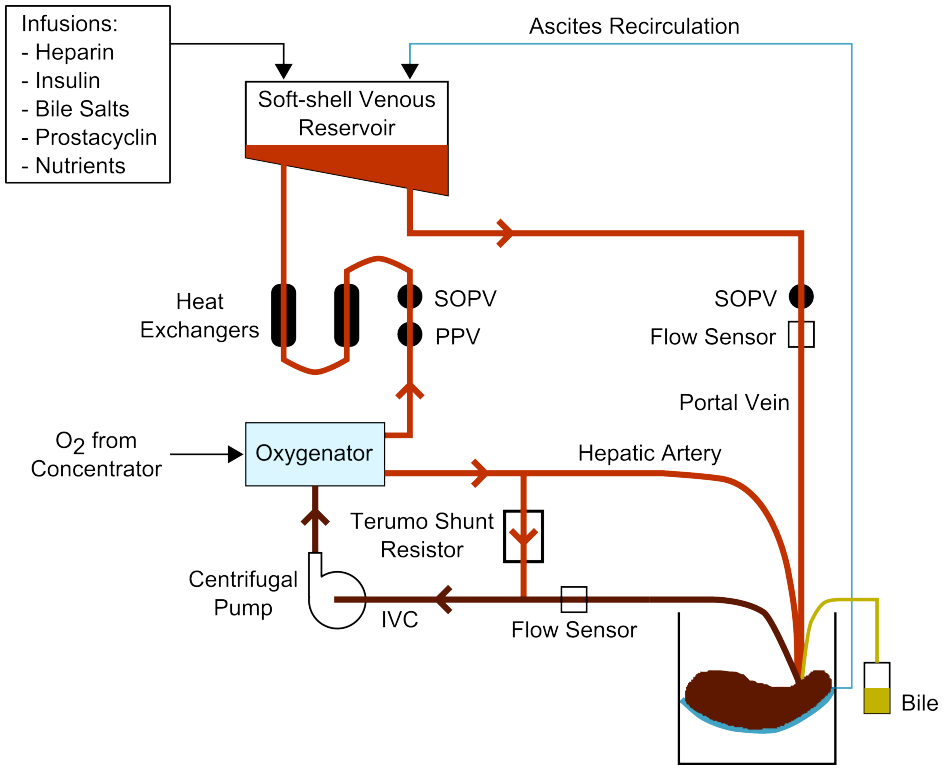


Figure 6.3: Schematic of the ECLPD for organ preservation. The device can maintain an organ in its functional state for up to 72 hours, accounting for relevant haemodynamic, anatomical and physiological characteristics.

6.2.2 Normothermic Perfusion

A total of four livers were surgically explanted under terminal anaesthesia and maintained in a functional state for up to 72 hours by normothermic perfusion. Figure 6.3 is a schematic representation of the ECLPD, showing the various components required to preserve relevant haemodynamic, anatomical and physiological characteristics. Figure 6.4 is the photographic equivalent. The perfusion circuit includes: a hollow-fibre membrane oxygenator (Sorin, EOS ECMO PHISIO M); a centrifugal pump (Medtronic, BPX80); and a soft-shell reservoir (Terumo, Capiox 1500). Blood temperature was maintained between 37 and 39 °C, whilst the portal and arterial flows were automatically controlled to generate pressures within pre-defined limits.

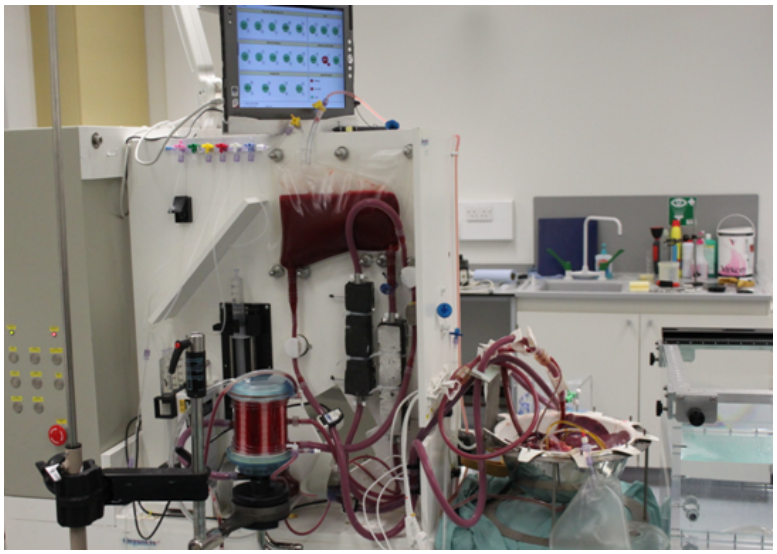


Figure 6.4: Photograph of the ECLPD for organ preservation in operation prior to HIFU sonication.

Prior to attachment of the liver, the circuit was primed with 1.5 L of autologous whole blood to bring it up to a temperature of 36 °C. Immediately before perfusion of the liver, continuous infusions of insulin, heparin, prostacyclin and bile acid were initiated. Prostacyclins increase total blood flow, and hence oxygen transport, following re-perfusion after warm ischemia, whilst bile acid supplementation is necessary to replace enterohepatic recirculation. The liver was subsequently connected to the perfusion circuit and the pump speed gradually increased over the space of a few minutes until an IVC pressure of 0-5 mmHg was achieved. Ascitic fluid produced by the liver was collected in a receptacle and recirculated via a peristaltic pump (Watson Marlow).

Blood gas levels and acid-base status were monitored continuously using an in-line sensor (Terumo, CDI510H). PO2 and PCO2 were automatically maintained within the ranges 12-20 kPa and 3.5-6 kPa respectively, whilst blood glucose analysis was performed at hourly intervals. If the blood glucose level was found to lie below 12 mmol/L, a nutrient infusion was initiated at 15 ml/hr in order to increase

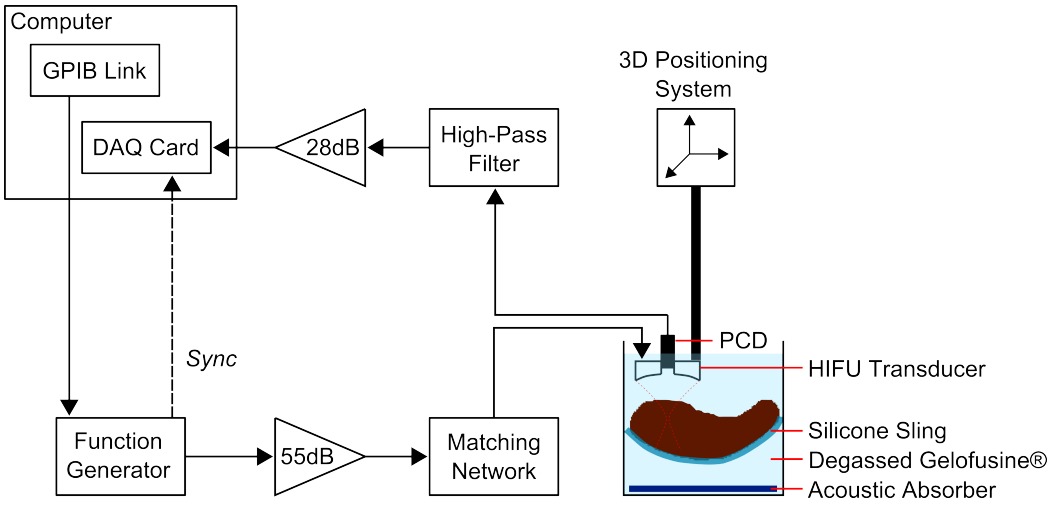


Figure 6.5: Overview of the experimental setup adopted for acquiring cavitation data from the perfused liver model. The HIFU-PCD assembly is supported by a three-axis manual positioning system and oriented face down inside the tank.

the perfusate glucose level to between 4 and 8 mmol/L.

6.2.3 Experimental Protocol

After approximately 30 minutes of normothermic perfusion, the ascites recirculation was terminated and the liver immersed in degassed Gelofusine® maintained at 37 °C. Figure 3.1 is a schematic representation of the experimental setup adopted for the ensuing *ex vivo* work involving the use of ultrasound.

All sonications were conducted using the 1.067 MHz transducer, 15 MHz PCD and accompanying electronics. Given the unwieldiness of the cannula-laiden porcine liver, the HIFU-PCD assembly was supported by a three-axis manual positioning system and oriented face down inside the tank. In addition to the apparatus shown, a linear ultrasound array (Zonare, L14-5sp), operated in both B-mode and colour Doppler mode, was used prior to each exposure to identify inhomogeneities in the HIFU field. Accordingly, all exposures were undertaken at a depth of approximately 10 mm in microperfused regions remote from the cannulae.

In order to avoid any modification of the target tissue region during cavitation-controlled HIFU exposures, no thermocouples were used in the present experimental setup. Instead, the extent of the ablated region was used as a metric to compare exposures with and without cavitation control. Surface lesions were created close to the treatment site following each HIFU exposure, in order to enable identification of the treated region for subsequent dissection and lesion sizing.

6.3 Data Analysis

Cavitation and thermal data was processed as per the methods described in Chapter 4. This includes the use of a comb filter to remove both the harmonics and ultra-harmonics.

6.4 Results and Discussion

With the exception of the cavitation threshold measurements, which were undertaken in all four livers included in this *ex vivo* study, each of the following results sections corresponds to experimentation in a different liver. Access to livers was limited on account of the considerable expense associated with liver procurement, the requirement to coordinate schedules and the long experiment durations.

6.4.1 Cavitation Threshold Measurements

Cavitation threshold measurements were undertaken by repeatedly exposing each of the four livers to a sequence of 10-cycle HIFU pulses at 1 s intervals and at progressively increasing PRFPs between 0.40 MPa and 4.14 MPa. A total of three cavitation threshold measurements were performed at various locations within each liver, the results of which are presented in Figure 6.6. Each graph corresponds to a

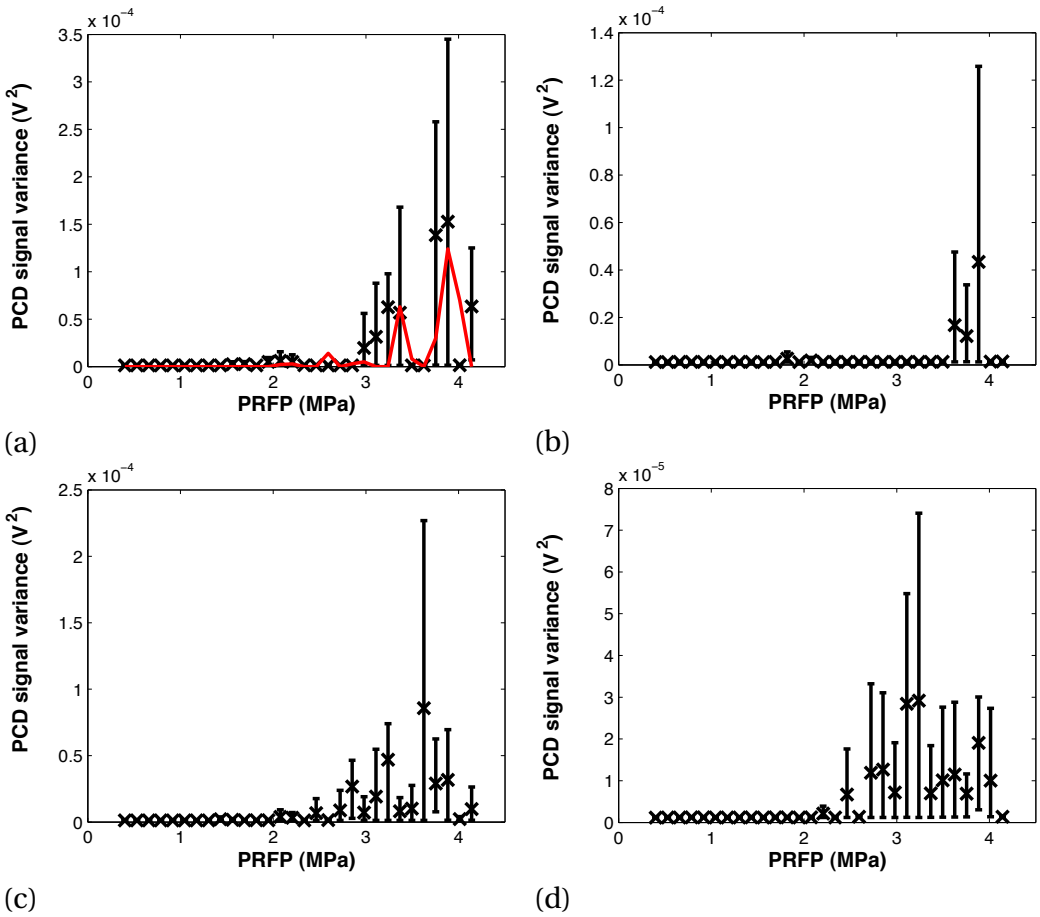


Figure 6.6: PCD signal variance versus PRFP for each of the four livers experimented upon using 1.067 MHz HIFU excitation. Evidently, there is significant variation in cavitation activity both within and between livers. The line plot overlaid in red in (a) was obtained using longer pulse intervals.

particular liver, the error bars spanning the full range of PCD signal variance values recorded. Evidently, there is significant variation both within and between livers.

Cavitation activity is initially detected at approximately 2.00 MPa in all four livers - this is considerably lower than that previously measured in non-perfused liver (3.50 MPa) at the same driving frequency of 1.067 MHz (refer to Section 4.1.3.1). Thereafter, cavitation is intermittent and unpredictable. It was initially presumed that variability in cavitation nuclei depletion and replenishment between successive pulses was responsible for this outcome; however, increasing the time interval

between pulses to 10 s made little difference (see line plot overlaid in red on Figure 6.6 (a)).

6.4.2 HIFU Sonication in Liver Microvasculature without Cavitation Control

Having established that the cavitation threshold of perfused liver is significantly lower than that observed in non-perfused liver, a logical progression is to consider the effects of longer HIFU exposures on both cavitation and lesioning. A series of HIFU sonications were thus undertaken in microperfused regions, where the heat sink effect imparted by major vessels is limited.

Figure 6.7 (a) is a photograph of a liver that was subjected to HIFU excitation without use of the controller at a range of PRFPs and a duty cycle of 99% for 10 s prior to dissection. In contrast to non-perfused liver, it takes in excess of 4.14 MPa over an exposure duration of 10 s for lesioning to occur. Importantly, once disconnected from the perfusion circuit, the liver loses vast amounts of blood, and hence volume. This is evident from the close proximity of the lesion corresponding to 4.79 MPa to the accompanying surface marker, despite all exposures having been undertaken at a depth of 10 mm.

With respect to the secondary acoustic emissions, the graphs of Figures 6.7 (b), (c) and (d) chart the evolution of cavitation activity during each of the HIFU exposures labelled in Figure 6.7 (a). At a PRFP of 3.50 MPa, the PCD signal exceeds the basal noise level by at least six standard deviations for the entire exposure duration, as indicated by the continuous passive localisation plot. This is in stark contrast to the 4.14 MPa HIFU exposure, during which there were no recorded cavitation events. Further increasing the PRFP to 4.79 MPa is seen to have a major impact on

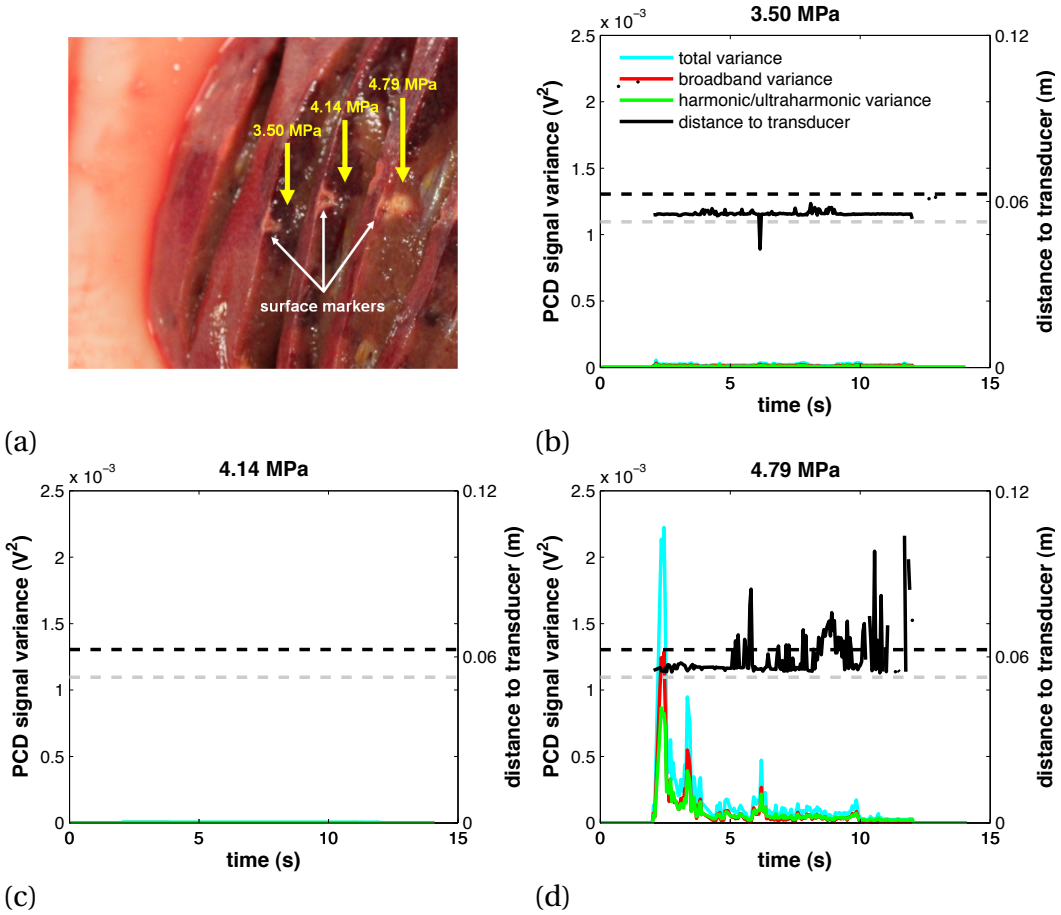


Figure 6.7: (a) Photograph of lesions formed in perfused liver microvasculature at a range of PRFPs, as indicated in yellow. (b, c and d) Corresponding cavitation data for HIFU excitation at 3.50 MPa, 4.14 MPa and 4.79 MPa respectively. The dashed lines represent the exposed liver surface (grey) and the HIFU focal distance (black) along the "distance to transducer" axes.

both broadband and harmonic/ultraharmonic emissions. The prominence of the latter is likely due to the tendency towards non-linear wave propagation at higher acoustic intensities; however, it is also important to remember the filtering artefact associated with the spectral decomposition algorithm.

As with non-perfused liver, there is considerable variation between cavitation data obtained at different locations within the tissue microvasculature. As such, these results are not universally applicable and serve to demonstrate the unpredictable nature of cavitation inception and sustenance.

6.4.3 Controller Implementation

The control system design from Chapter 5 was eventually tested in the perfused liver model, taking care to avoid major vessels so as to encourage lesioning and reduce variability of results. For the PCD apparatus used in the present work, Chapter 4 suggests a threshold total broadband energy of 2 x 10^{-5} V^2s for cavitation to emerge as a dominant heating mechanism in non-perfused liver. For the HIFU exposures from which the energy threshold was derived, a broadband variance of 1 x 10^{-5} V^2 is the equivalent quasi-instantaneous system output (based on an exposure duration of 2 s). Thus, this was identified as a suitable reference demand, whilst the width of the deadband was chosen to be 3 x 10^{-5} V^2. The asymmetric proportional gains were left unaltered.

Figures 6.8 (a) and (b) derive from controller implementation using a duty cycle of 99% and an exposure duration of 10 s. A starting PRFP of 1.82 MPa was chosen, based on the cavitation threshold experiments presented in Figure 6.6 (c). Though it takes in excess of 3 s for cavitation instigation, the broadband variance is sustained close to the specified cavitation reference demand thereafter. Conversion of the focal PRFP to acoustic intensity, and hence power, and integration of the resulting vector over time yields a focal irradiation energy content of approximately 69 J. This is equivalent to maintaining the PRFP at 2.69 MPa over the same exposure length, the results from which are provided in Figures 6.8 (c) and (d). Evidently, the PCD signal variance is much lower compared to Figure 6.8 (a).

The starting PRFP of the controller was subsequently increased to 2.85 MPa, in an attempt to maintain the broadband component of the PCD signal variance within the specified deadband for the entirety of the exposure duration. The results from one such experiment are provided in Figure 6.9, alongside those obtained during HIFU excitation at a constant PRFP of 2.26 MPa for 10 s. Both are equivalent to a

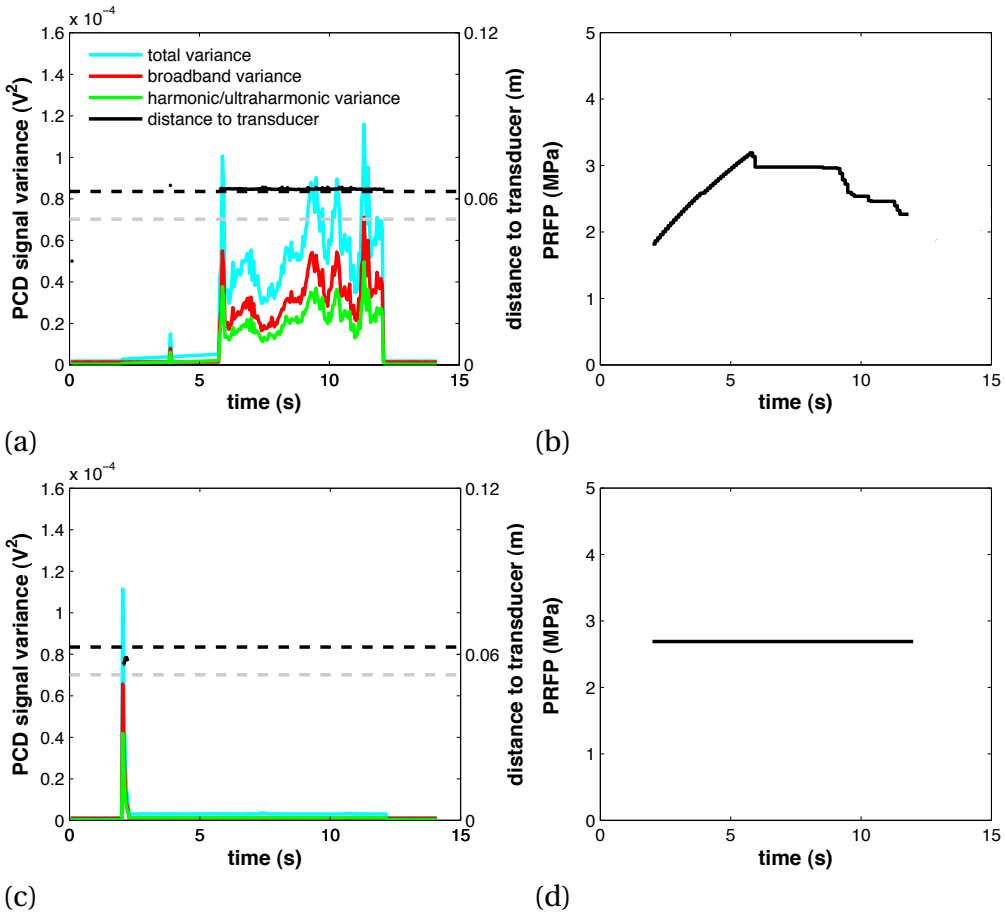


Figure 6.8: (a) Cavitation data from controller operation using a broadband variance threshold of 1 x 10^{-5} V^2 and (b) corresponding PRFP modulation profile. (c) Cavitation data from HIFU excitation at a constant PRFP of 2.69 MPa, as shown in (d). The dashed lines represent the exposed liver surface (grey) and the HIFU focal distance (black) along the "distance to transducer" axes.

total HIFU input energy of 49 J. Though the controller performs well, it is important to note that, in this example, inertial cavitation activity also persists in the absence of cavitation control, albeit below the desired level. Moreover, the latter generates more in the way of inertial cavitation compared with HIFU excitation at 2.69 MPa in the same liver (see Figure 6.8 (c)). This serves to demonstrate the large variation in results obtained at different locations in the absence of cavitation control.

Finally, Figure 6.10 is a photograph of the liver cross section subsequent to dissection. HIFU exposures were undertaken along a straight line at a depth of 10 mm

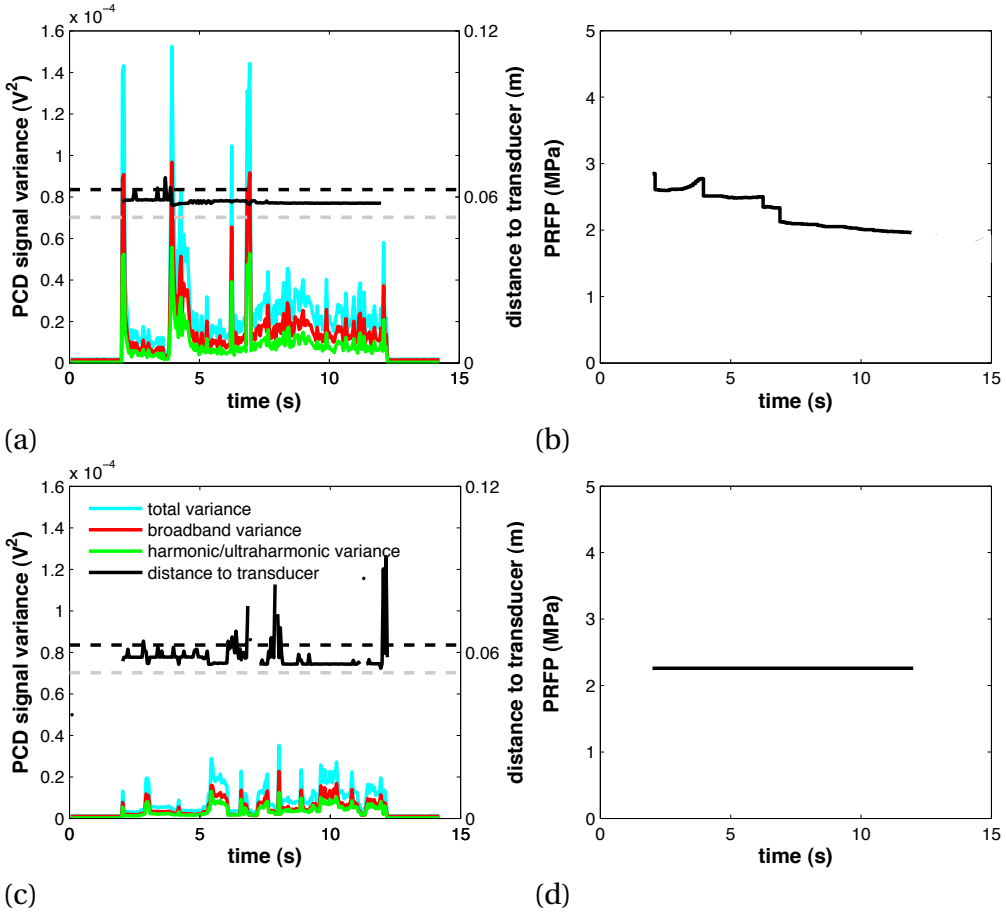


Figure 6.9: (a) Cavitation data from controller operation and (b) corresponding PRFP modulation profile, the starting PRFP having been increased to 2.85 MPa. (c) Cavitation data from HIFU excitation at a constant PRFP of 2.26 MPa, as shown in (d). The dashed lines represent the exposed liver surface (grey) and the HIFU focal distance (black) along the "distance to transducer" axes.

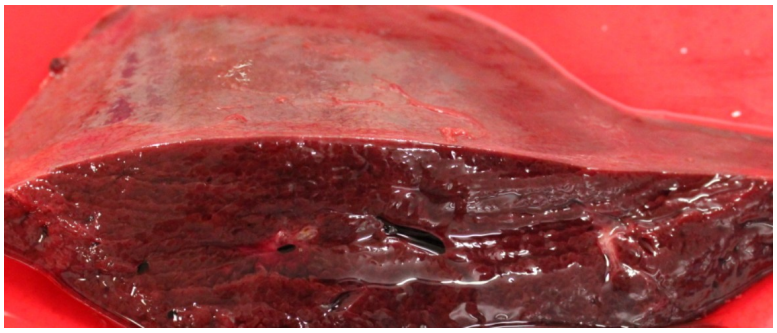


Figure 6.10: Photograph of the liver cross section subsequent to dissection. HIFU exposures were undertaken along a straight line at a depth of 10 mm beneath the liver surface. Evidently, no lesioning was observed.

beneath the liver surface. Unfortunately, no lesions were detected despite successfully sustaining broadband emissions at the desired level for up to 10 s. This may be due to an inadequate exposure duration, a conservative threshold for lesioning or, more likely, a combination of both.

6.4.4 Controller Tuning

Although cavitation control has been successfully demonstrated in the perfused liver model, its capacity to generate superior thermal effects is hitherto unclear. The experimental and control parameters used in Section 6.4.3 were thus modified in an attempt to shed light on the problem. As usual, microperfused regions were customarily targeted to encourage reproducibility of results.

Initially, the controller experiments from Section 6.4.3 were repeated using a longer exposure duration of 30 s. Figure 6.11 comprises a series of graphs obtained from identical HIFU exposures performed using the control system. A logarithmic scale has been adopted along the ordinate axes of the PCD signal variance profiles to capture the wide variation in acoustic emissions recorded over the course of each exposure. The total energy content of the incident HIFU envelope unique to each exposure is indicated on the relevant PRFP profile, and ranges from 250 J to 329 J.

Despite cavitation threshold measurements having indicated the threshold to be in the region of 2 MPa, and having thus chosen a starting PRFP of 2.85 MPa for the controller, it consistently takes in excess of 3 s for the broadband component of the PCD signal variance to reach the cavitation reference demand. Moreover, when the PRFP exceeds approximately 5 MPa, both the broadband and harmonic/ultraharmonic components overshoot the deadband by several orders of magnitude, causing the PRFP to move in the opposite direction to counter the effect. With the exception of the third exposure, inertial cavitation activity is sustained at

the desired level for upwards of 7 s thereafter, beyond which the broadband signal oscillates considerably.

Subsequently, the cavitation reference demand was increased to 1 x 10^{-4} V^2, with a deadband width of 3 x 10^{-4} V^2, in a bid to encourage lesioning: in contrast to the non-perfused model adopted in Chapter 4, from which the original cavitation reference demand was deduced, heat advection by blood flowing through the tissue microvasculature in the perfused liver is likely to increase the tissue damage threshold. A further four identical HIFU exposures were undertaken using the revised control system parameters, the results of which are presented in Figure 6.12. Evidently, the cavitation data is more reproducible, with inertial cavitation activity sustained close to the cavitation reference demand for the majority of the exposure duration in all instances. Whilst the passive localisation profiles do not exhibit the same erratic behaviour previously observed in Figure 6.11, there does appear to be more in the way of pre-focal cavitation activity. As expected, it is necessary to access higher PRFPs in order to meet the cavitation demands of the modified control system, with HIFU input energies ranging from 440 J to 490 J.

Figures 6.11 and 6.12 may be contrasted with cavitation data from HIFU exposures performed at a constant PRFP of 4.14 MPa (see Figure 6.13). Over an exposure duration of 30 s, this is equivalent to a total HIFU input energy of 490 J, which represents the maximum energy input of the preceding controller experiments. Evidently, there is large variation in the PCD signal variance profiles, both over the course of each exposure and between different exposures. More noteworthy, however, is the effect that this has on corresponding lesion size.

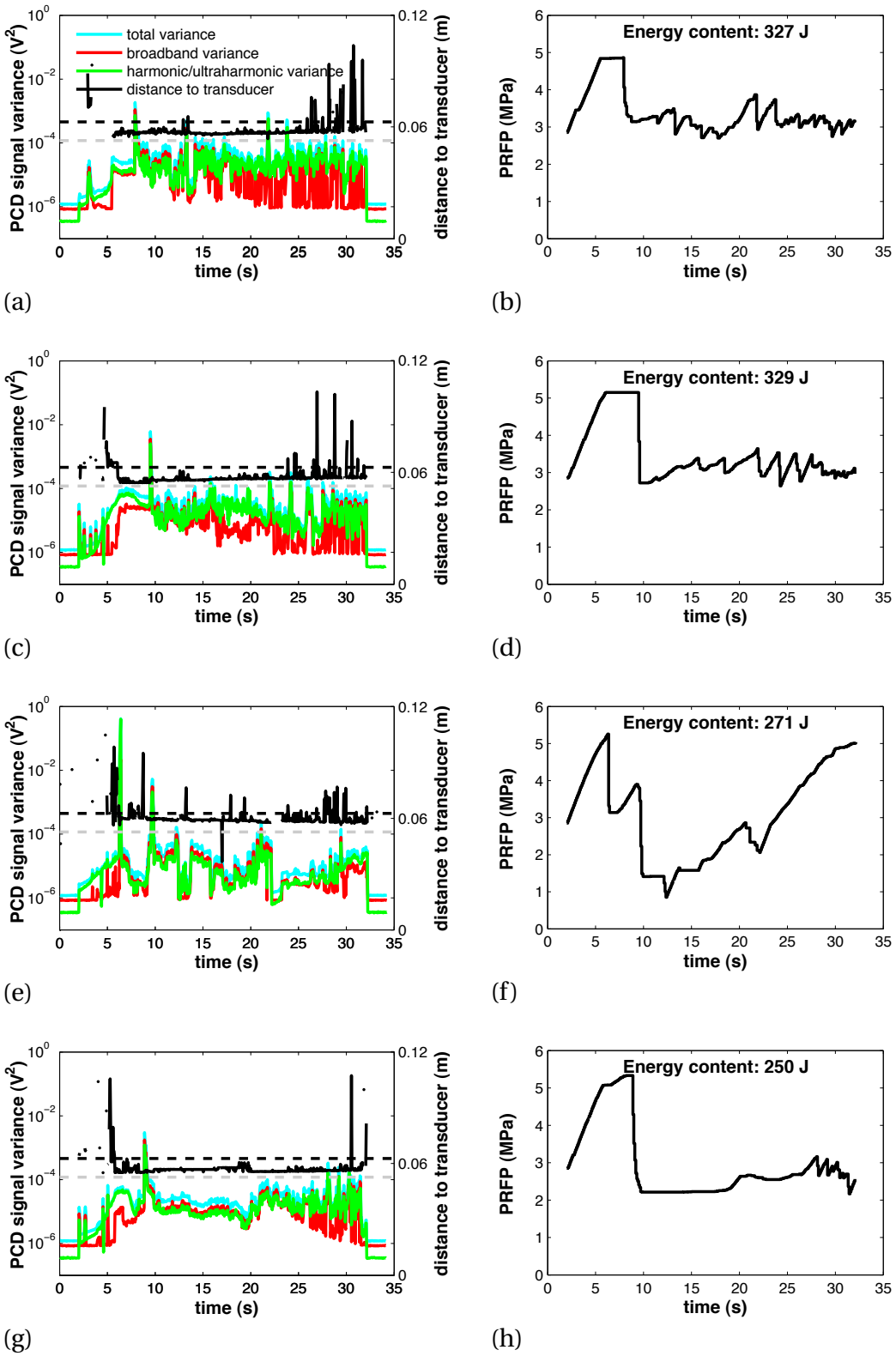


Figure 6.11: Cavitation data from repeated controller implementation in perfused liver with corresponding PRFP profiles (reference demand = 1 x 10^{-5} V^2).

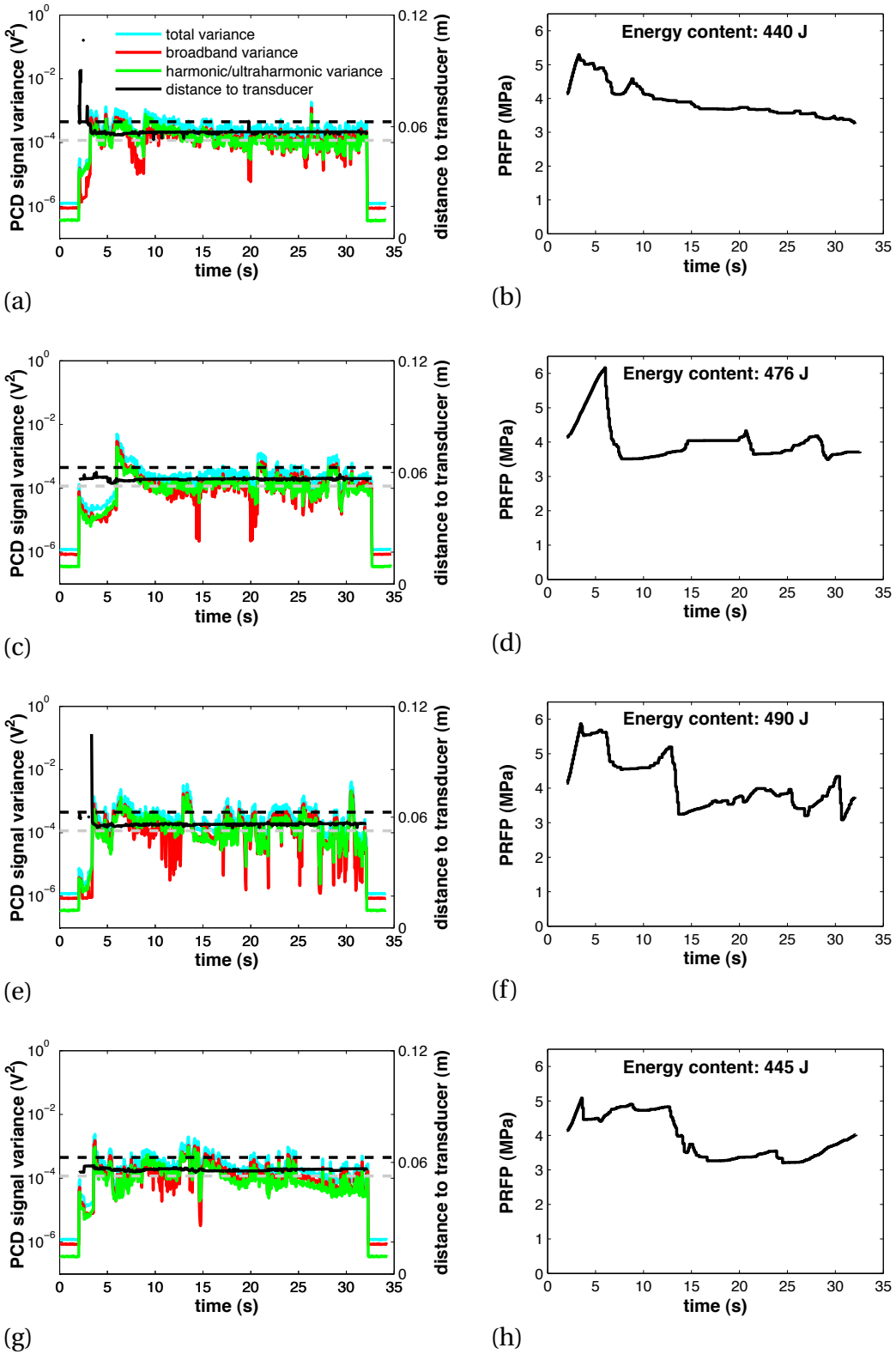


Figure 6.12: Cavitation data from repeated controller implementation in perfused liver with corresponding PRFP profiles (reference demand = 1 x 10^{-4} V^2).

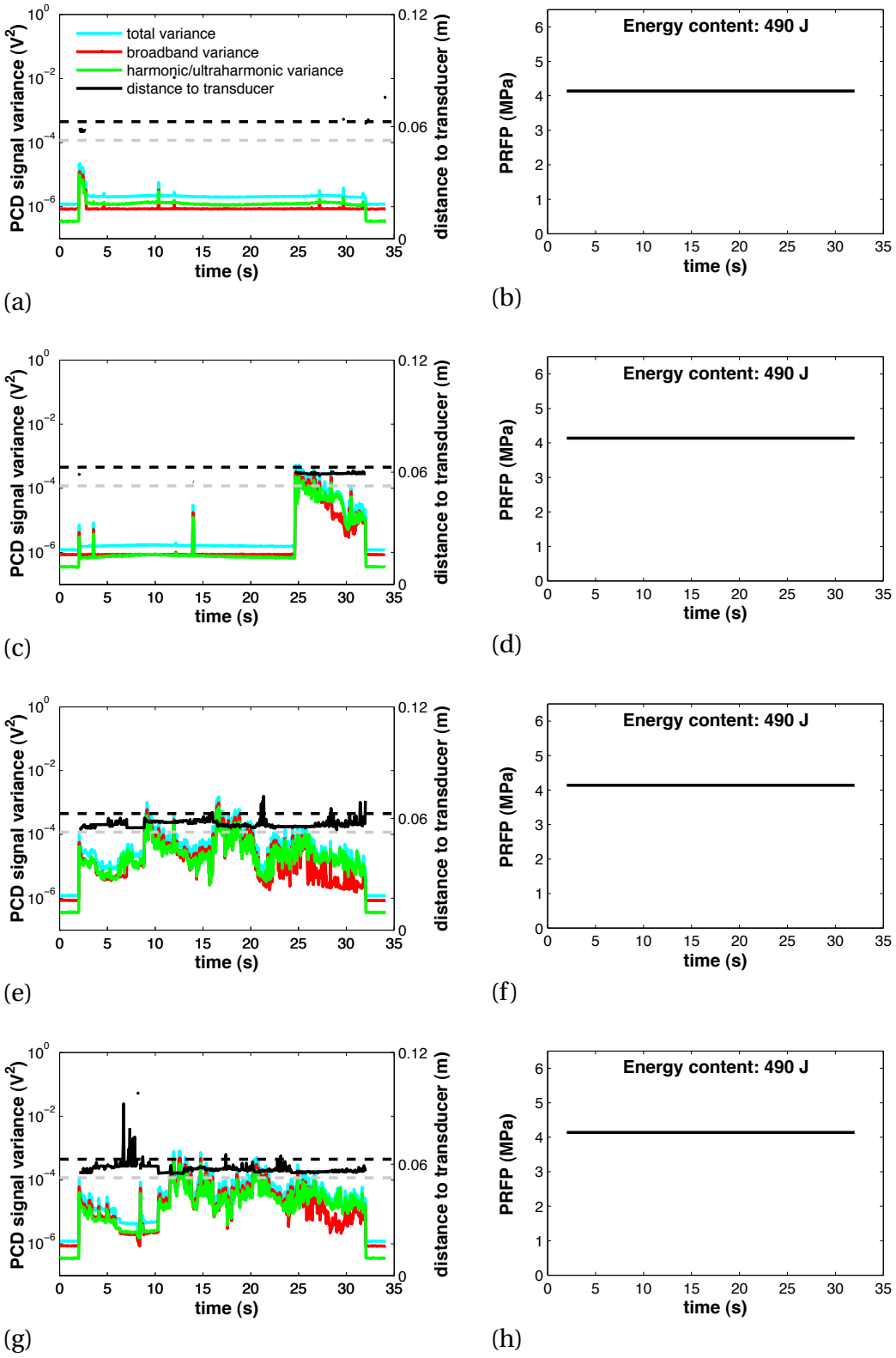
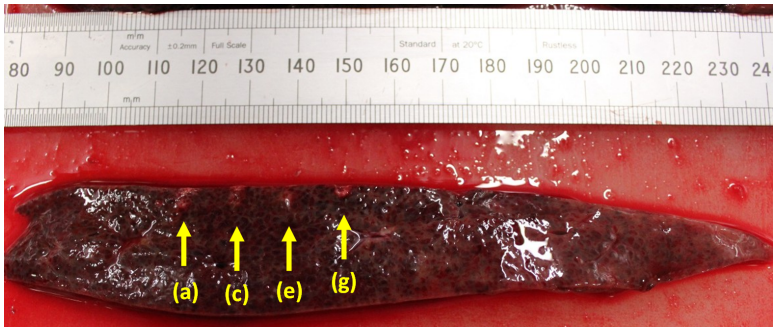
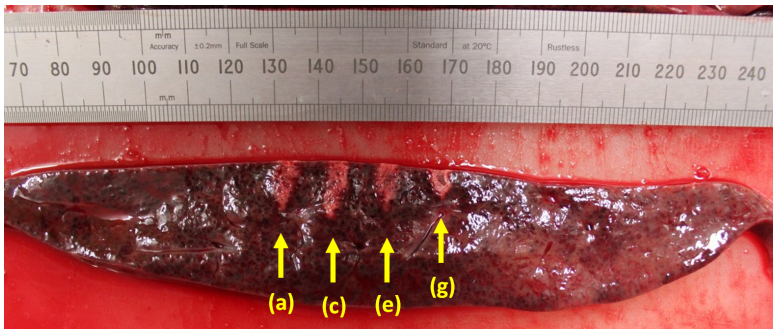


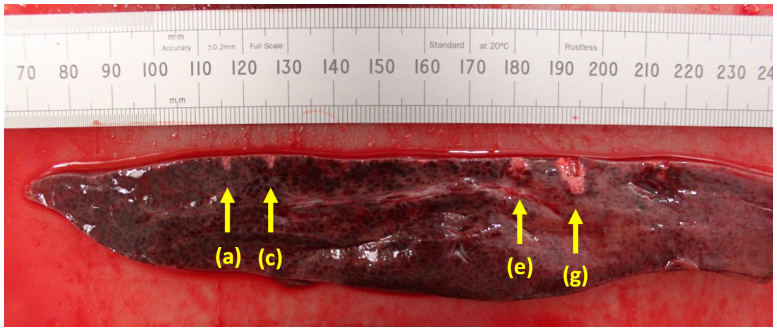
Figure 6.13: Cavitation data from HIFU exposures undertaken at a constant PRFP of 4.14 MPa for 30 s in the absence of active cavitation control.



(a)



(b)



(c)

Figure 6.14: Comparison of lesion sizes in the presence and absence of cavitation control. (a) Lesions corresponding to cavitation data presented in Figure 6.11 (active cavitation control with cavitation reference demand of 1 x 10^{-5} V^2). (b) Lesions corresponding to cavitation data presented in Figure 6.12 (active cavitation control with cavitation reference demand of 1 x 10^{-4} V^2). (c) Lesions corresponding to cavitation data presented in Figure 6.13 (no cavitation control but high incident energy content).

6.4.5 Effect of Cavitation Control on Lesion Size

Figure 6.14 is a series of photographs taken subsequent to dissection of the liver used in Section 6.4.4 - that is, corresponding to active cavitation control with a demand of 1 x 10^{-5} V^2, active control with a demand of 1 x 10^{-4} V^2, and in the absence of active control. Foremostly, irrespective of the level of cavitation demand, cavitation control always results in better controlled lesions in terms of both size and reproducibility. A cavitation reference demand of 1 x 10^{-5} V^2 consistently yields small lesions close to the liver surface. Increasing the reference demand by a factor of ten reproducibly results in larger lesion sizes. Moreover, active cavitation control using a cavitation reference demand of 1 x 10^{-4} V^2 results in larger lesions for the same level of acoustic input energy compared with uncontrolled HIFU exposures.

Finally, it is interesting to note that the HIFU exposures undertaken without active cavitation control yield markedly different lesion sizes, despite all having the same energy input. This variation may be attributed to disparate cavitation profiles, the two larger lesions corresponding to relatively high levels of inertial cavitation activity. Cavitation control has thus been shown to greatly improve the likelihood of achieving the desired level of broadband activity so as to consistently capitalise on the enhanced heating rates proffered by cavitation-assisted HIFU. This is an important result, which validates use of the control system over current HIFU-mediated ablation schemes.

6.5 SUMMARY

The main objective of this chapter has been to consolidate the work of the preceding three results chapters to effect control over HIFU-induced cavitation activity in a manner that promotes focal heating. Use of a normothermically perfused organ

presented significant challenges over *in vitro* and non-perfused models, not least regarding the logistics of procurement and retrieval. However, blood flow through the tissue vasculature is an important consideration when designing clinical HIFU schemes, thus its inclusion here.

Cavitation threshold measurements were initially undertaken in microperfused regions of each of the four livers experimented upon. This was intended not only to inform the choice of subsequent experimental parameters, but also to enable comparison between livers, given the large variation previously observed in bovine liver. Despite strong agreement across all four livers as regards the cavitation threshold, there existed large amounts of variation in cavitation activity at higher PRFPs both within and between livers. This emphasises the need for active cavitation sensing and control.

The effect of perfusion on lesion formation was subsequently investigated, involving the use of quasi-CW HIFU excitation at PRFPs occupying the post-threshold and super-threshold regimes. In contrast to non-perfused liver and in the absence of active cavitation control, it consistently took in excess of 4.14 MPa over an exposure duration of 10 s for lesioning to occur, despite restricting HIFU sonication to the microvasculature. The accompanying cavitation data was highly variable, with no clear trends observed in relation to PRFP.

The control system from Chapter 5 was thus implemented in the perfused liver model, initially using the cavitation reference demand previously identified in Chapter 4 as suitable for lesioning in non-perfused tissue (1×10^{-5} V^2) for 10 s. Although inertial cavitation was successfully sustained at the desired level, there was no evidence of lesioning in the perfused liver. Increasing the cavitation reference demand tenfold to 1×10^{-4} V^2 and extending the exposure duration to 30 s impacted favourably on lesion formation, with broadband emissions consistently

sustained close to the reference demand. This was deemed necessary to account for heat advection by the perfusion circuit. Moreover, when contrasted with HIFU exposures undertaken in the absence of active cavitation control but with the same level of acoustic energy input, cavitation control was shown to reproducibly result in larger lesions, thereby validating use of the controller for effective HIFU-mediated ablation.



CHAPTER 7

CONCLUSIONS AND FUTURE WORK

The work of this thesis addresses the need to improve the heat deposition efficiency during HIFU-mediated tumour ablation by exploiting cavitating bubbles both as promoters and as markers of successful treatment. In this chapter, the various strategies that have been adopted to promote and sustain thermally relevant cavitation are summarised, and future work suggested to further improve the emergent control system.

7.1 CONCLUSIONS

Widespread clinical adoption of HIFU for tumour ablation is presently hindered by long treatment times due to inadequate monitoring techniques and the requirement to manage collateral damage along the HIFU propagation path. This is a great shame given its non-invasive delivery and associated benefits. More recently, cavitation-assisted HIFU has emerged as a plausible solution to many of the shortcomings of conventional HIFU therapy. In particular, oscillating bubbles have the effect of redistributing the incident HIFU frequency to higher order harmonics and broadband noise, which are more readily attenuated. The aim of this thesis has thus been to contain and sustain thermally relevant cavitation activity within the

HIFU focal volume, and hence capitalise on the superior heating rates proffered by cavitation-assisted HIFU. The technique relies on real-time cavitation data for treatment guidance, thereby negating the need for traditional MRI and B-mode imaging modalities.

The experimental setup employed throughout this investigation was intended to represent a clinical HIFU system as far as practicably possible. The notion of cavitation-enhanced heating was initially introduced in Chapter 3, in which two different TMMs (agar- and PAA-based) were subjected to HIFU irradiation at a range of PRFPs. In both phantoms, the power of the acoustic emissions emanating from the focal region was found to correlate positively with PRFP, assuming a uniform initial spatial distribution of cavitation nuclei. A corresponding decrease in the distance between the HIFU transducer and the frontal position of the bubble cloud was also observed, raising concerns over whether the point of maximum temperature elevation coincided with the thermocouple positioning at the HIFU focus.

Whilst there was found to exist a manifest dependence of temperature elevation on inertial cavitation activity in the agar phantom, cavitation-enhanced heating was not observed in PAA, despite both of the TMMs sharing common acoustic properties. The use of exogenous nuclei to promote bubble activity was thus explored, with a positive outcome: by altering the cavitation nuclei distribution in the PAA TMM, corresponding broadband acoustic emissions were successfully augmented to match the inertial cavitation levels observed in the agar TMM, yielding similar temperature rises. Moreover, the temperature elevation at the HIFU focus was found to peak beyond a threshold level of total broadband energy of acoustic emissions in both phantoms.

The *in vitro* work of Chapter 3 was subsequently extended to freshly excised bovine liver. In the absence of perfusion effects, endogenous nuclei were found

to be insufficient to yield focal cavitation events within the range of frequencies and PRFPs investigated, with acoustic emissions unpredictable and intermittent. Placement of a thermocouple at the HIFU focus revealed cavitation-enhanced heating to be non-existent, necessitating the use of exogenous nuclei to augment inertial cavitation levels, and hence heating. To this effect, the UCA SonoVue® was contrasted with custom-made sonosensitive nanoparticles to establish a clinically relevant method for inertial cavitation enhancement. Though their responses to HIFU at a frequency of 1.067 MHz differed considerably on account of their dissimilar constructions, comparable total broadband energies yielded indistinguishable thermal effects, the resulting lesions being far larger than observed in their absence. Furthermore, correlation of lesion size with broadband acoustic emissions revealed there to exist a threshold total broadband energy for lesioning to occur. The threshold was the same regardless of exposure duration and whether SonoVue® or sonosensitive nanoparticles were used as exogenous nuclei. This is a key result, which strongly suggests that achieving cavitation-dominated heating is possible in any medium, for as long as a particular medium-dependent threshold level of cavitation activity is exceeded and maintained.

Having overcome the problem associated with temperature elevation measurement at a single location by using lesion size as a metric for thermal effects, cavitation data acquisition along a single dimension was identified as a further limitation of the experimental setup, especially given the considerable size of the lesions produced. As such, a linear diagnostic ultrasound array was incorporated into the setup, allowing the use of passive acoustic mapping to quantify cavitation activity in two dimensions. Lesion size was thence found to correlate strongly with the extent of the cavitation region, more so for sonosensitive nanoparticles than for SonoVue® microbubbles, which are highly scattering and thus tend to confound the

images. Due to their ability to produce cavitation events which are almost exclusively associated with broadband emissions, sonosensitive nanoparticles are thus better suited to promoting cavitation-guided HIFU therapy and yield a strong correlation between passive acoustic maps acquired during treatment and the ablated tissue region.

Equipped with the knowledge that cavitation-enhanced heating can be achieved in biological tissue, Chapter 5 outlined the design, implementation and validation of a novel closed-loop feedback controller whose primary purpose is to sustain inertial cavitation, and hence temperature elevation, at a pre-defined level. An agar-based phantom was used as an experimental model and the cavitation reference demand thence deduced from Chapter 3, whilst the optimal controller parameters were found by trial and error. An asymmetric proportional gain controller evolved, which modulates the incident PRFP in response to the variance of the broadband secondary acoustic emissions. In the absence of cavitation control, bubble activity is known to diminish over time; however, preliminary controller testing was successful in that thermally relevant cavitation activity could be sustained at the HIFU focus for prolonged periods. This yielded temperature elevations in great excess of those that could be achieved in the absence of active cavitation control using equivalent HIFU input energies. These results are particularly encouraging because the use of lower acoustic intensities enhances patient safety by reducing pre-focal attenuation.

Temperature elevations achievable with and without use of the controller were subsequently measured at a range of off-axis locations in order to (i) quell artefactual heating at the thermocouple-TMM boundary, and (ii) remove any doubts regarding the impact of a foreign object on the nucleation environment. As a result, the thermal benefits brought about by use of the control system were found to ex-

tend beyond the HIFU focal region due to a combination of thermal diffusion and the capacity to target a broader region of cavitation nuclei at higher PRFPs.

In Chapter 6, the control system was extended to a perfused liver model, in which heat advection by blood flow was found to counter the thermal benefits brought about by continual cavitation nuclei replenishment. In the absence of cavitation control, cavitation data was shown to vary considerably both within and between livers, as previously established in the non-perfused model. In contrast, preliminary experimentation using the control system to sustain inertial cavitation levels close to a pre-defined reference demand generated reproducible results. The cavitation reference demand was initially chosen based on the results presented in Chapter 4; however, in the absence of lesioning, it was later increased tenfold to overcome thermal losses due to blood perfusion. The modified control system consistently maintained broadband acoustic emissions at the desired level for up to 30 seconds, accompanied by sizeable lesions. In essence, the greater the cavitation demand, the larger the lesions consistently achieved when active caviation control was deployed.

Finally, the control system was validated by comparison with HIFU exposures undertaken at a constant PRFP of 4.14 MPa. In energy terms, this is equivalent to the upper limit of the preceding controller experiments. On occasions where the nucleation environment was not suitable to sustain adequate broadband acoustic emissions, relatively small lesions were produced. Inertial cavitation levels sometimes lingered close to the cavitation reference demand of their own accord, yielding correspondingly large lesions, but this was by no means assured. Thus, controller implementation consistently enables access to thermally relevant cavitation activity, presenting major advantages over conventional HIFU ablation schemes. It is hoped that the concept of cavitation control to achieve specific bioeffects will prove useful

in a range of cavitation-assisted therapeutic ultrasound applications.

7.2 Future Work

There is, of course, scope to advance on the work of this thesis, which would aid progression towards clinical adoption of cavitation-assisted therapies. The use of exogenous nuclei to reduce cavitation thresholds in perfused liver could be explored, although this would ideally need to be performed in conjunction with a tumour model to assess clinical relevance. The prominence of harmonic and ultraharmonic components in cavitation data obtained from experimentation in biological tissue should also be investigated in more detail to determine the contribution to heating from non-linear effects. Moreover, in the short-term, improvements to implementation of the TEA beamforming algorithm to allow real-time cavitation monitoring in two dimensions would greatly improve the spatial accuracy of cavitation-induced thermal ablation.

7.2.1 Use of Exogenous Nuclei in Perfused Liver

Exogenous nuclei in the form of SonoVue® microbubbles and sonosensitive polystyrene nanoparticles have been shown to lower the inertial cavitation threshold, and hence tissue damage threshold, in a non-perfused *ex vivo* liver model. Systemic administration of exogenous nuclei to the perfused liver could improve the performance of the control system by enabling the use of even lower acoustic intensities to achieve the same level of heat deposition. Sonosensitive nanoparticles present major advantages over SonoVue®, not only in terms of their size, but also in terms of only yielding broadband emissions to facilitate estimation of the lesion size from passive acoustic maps. However, more work needs to be done to ascertain the immunogenicity of these particles in a physiological environment.

Moreover, magnetic microbubbles, which are currently in development for localised imaging and drug delivery applications, may well prove useful to control the concentration of microbubbles at a given site. These microbubbles have magnetic nanoparticles incorporated into their coatings and preliminary results from flow phantom studies and *in vivo* experimentation in a mouse model confirm their successful localisation (Stride et al., 2012; Owen et al., 2012).

7.2.2 Development of a Tumour Model

All of the livers experimented upon over the course of this project have originated from healthy specimen and thus crucially omit the unique physiological and anatomical features characteristic of tumours. These include a highly tortuous vascular network and elevated pressure. This is unfortunate given the intended use of the control system to successfully ablate cancer cells.

The development of a realistic tumour model would help to inform the next iteration of the control system design. This could either take the form of a flow phantom with intrinsic three-dimensional vascular network (Bellan et al., 2009; Mironov et al., 2007) or, ideally, a tumour mass cultivated within the liver itself. Moreover, the presence of an extraneous mass would serve to demarcate the intended treatment site during both treatment and subsequent liver dissection, which would facilitate assessment of targeting accuracy.

7.2.3 Consideration of Non-Linear Effects

Whilst the effect of inertial cavitation activity on heat deposition has been investigated in some detail, the strong presence of harmonic and ultraharmonic frequency components in cavitation data acquired during experimentation in soft biological tissue is also of interest. At thermally relevant PRFPs, it is likely that these compo-

nents arise due to non-linear propagation of the HIFU wave, although stable cavitation and non-linear shape oscillations of large bubbles should not be ruled out.

Further work is thus required to establish the contribution to heating from non-linear wave propagation. This would require modifications to the current data acquistion hardware to sensitise the system to specific frequency ranges and should include complementary theoretical work, given the availability of suitable non-linear propagation models.

7.2.4 Improvements to TEA Beamforming Algorithm

The passive acoustic mapping technique employed in Section 4.3, involving the use of a linear diagnostic array, presently suffers from poor axial resolution due to a combination of the transducer geometry and the TEA beamforming algorithm. Given that the experimental setup adopted is readily implementable in a clinical setting, the most appropriate course of action would be to first explore changes to the software that could yield the necessary gains. Improvements to the TEA algorithm might include modification of the spherical spreading compensation term to reduce shadowing effects at the distal side of the HIFU focus. Alternatively, optimum algorithms, such as the robust Capon beamformer, could be implemented to enhance localisation performance and improve axial resolution to enable improved correlation of cavitation mapping and the extent of lesioning along the HIFU axis (Coviello et al., 2012).

Moreover, the control system would benefit greatly from real-time cavitation data in two, and eventually three, dimensions. Presently, IQ data acquired using the linear array must be transferred to a PC for reconstruction. However, recent developments within the BUBBL laboratory using a two-dimensional polyvinylidene fluoride (PVDF) array and customised digitisers, alongside parallel processing

using a graphics processing unit (GPU), have made it possible to produce three-dimensional cavitation maps at frame rates in excess of 5 Hz (Lyka, 2012). In combination with the controller developed as part of the present work, three-dimensional real-time monitoring and control of cavitation activity for improved HIFU therapy could thus become a clinical reality.

REFERENCES

ABRAHAM, F. F. AND ZETTLEMOYER, A. C. Homogeneous nucleation theory. *Physics Today*, 27:52, 1974.

APFEL, R. E. The role of impurities in cavitation-threshold determination. *The Journal of the Acoustical Society of America*, 48:1179, 1970.

APFEL, R. E. AND HOLLAND, C. K. Gauging the likelihood of cavitation from short-pulse, low-duty cycle diagnostic ultrasound. *Ultrasound in Medicine & Biology*, 17(2):179–185, 1991.

ARORA, M., ARVANITIS, C. D., AND COUSSIOS, C. C. Microparticle-based cavitation nucleation for enhancement of ultrasound therapy. *Ultrasonics*, (in press), 2011.

ARORA, M., OHL, C. D., AND LOHSE, D. Effect of nuclei concentration on cavitation cluster dynamics. *The Journal of the Acoustical Society of America*, 121: 3432, 2007.

ATCHLEY, A. A. AND PROSPERETTI, A. The crevice model of bubble nucleation. *The Journal of the Acoustical Society of America*, 86:1065, 1989.

BAEK, S., WELLS, P. B., RAJAGOPAL, K., AND HUMPHREY, J. D. Heat-induced changes in the finite strain viscoelastic behavior of a collagenous tissue. *Journal of biomechanical engineering*, 127: 580, 2005.

BAILEY, M. R., COURET, L. N., SAPOZHNIKOV, O. A., KHOKHLOVA, V. A., TER HAAR, G. R., VAEZY, S., SHI, X., MARTIN, R., AND CRUM, L. A. Use of overpressure to assess the role of bubbles in focused ultrasound lesion shape in vitro. *Ultrasound in Medicine & Biology*, 27(5):695–708, May 2001. ISSN 0301-5629.

BAMBER, J. C. AND HILL, C. R. Ultrasonic attenuation and propagation speed in mammalian tissues as a function of temperature. *Ultrasound in Medicine & Biology*, 5(2):149–157, 1979. ISSN 0301-5629.

BARATI, A. H., MOKHTARI-DIZAJI, M., MOZDARANI, H., BATHAIE, Z., AND HASSAN, Z. M. Effect of exposure parameters on cavitation induced by low-level dual-frequency ultrasound. *Ultrasonics sonochemistry*, 14(6):783–789, 2007.

BARNETT, S. B., TER HAAR, G. R., ZISKIN, M. C., NYBORG, W. L., MAEDA, K., AND BANG, J. Current status of research on biophysical effects of ultrasound. *Ultrasound in Medicine & Biology*, 20(3):205–218, 1994. ISSN 0301-5629.

BARNETT, S. B., TER HAAR, G. R., ZISKIN, M. C., ROTT, H.-D., DUCK, F. A., AND MAEDA, K. International recommendations and guidelines for the safe use of diagnostic ultrasound in medicine. *Ultrasound in Medicine & Biology*, 26(3):355–366, March 2000. ISSN 0301-5629.

BAZAN-PEREGRINO, M., ARVANITIS, C. D., RIFAI, B., SEYMOUR, L. W., AND COUSSIOS, C. C. Ultrasound-induced cavitation enhances the delivery and therapeutic efficacy of an oncolytic virus in an in vitro model. *Journal of Controlled Release*, 157(2):235–242, January 2012. ISSN 0168-3659.

BELL, A. G. On the production and reproduction of sound by light. *American Journal of Science*, 20: 305–324, 1880.

BELLAN, L. M., SINGH, S. P., HENDERSON, P. W., PORRI, T. J., CRAIGHEAD, H. G., AND SPECTOR, J. A. Fabrication of an artificial 3-dimensional vascular network using sacrificial sugar structures. *Soft Matter*, 5(7):1354–1357, 2009.

BEYER, R. T. Nonlinear acoustics. Technical report, DTIC Document, 1974.

BING, K. F., ROTEMBERG, V. M., PALMERI, M. L., AND NIGHTINGALE, K. R. Concurrent ARFI imaging and HIFU ablation using a diagnostic transducer array and ultrasound system with custom beam sequences. In *Ultrasonics Symposium (IUS), IEEE International*, pages 65–68. IEEE, 2009.

BJORNO, L. AND LEWIN, P. A. Measurement of nonlinear acoustic parameters in tissue. *Tissue characterization with ultrasound*, 1:141–163, 1986.

BORDEN, M. A. AND LONGO, M. L. Dissolution behavior of lipid monolayer-coated, air-filled microbubbles: Effect of lipid hydrophobic chain length. *Langmuir*, 18(24):9225–9233, 2002.

BORKENT, B. M., ARORA, M., AND OHL, C. D. Reproducible cavitation activity in water-particle suspensions. *The Journal of the Acoustical Society of America*, 121:1406, 2007.

BORRELLI, M. J., THOMPSON, L. L., CAIN, C. A., AND DEWEY, W. C. Time-temperature analysis of cell killing of bhk cells heated at temperatures in the range of 43.5 c to 57.0 c. *International Journal of Radiation Oncology Biology Physics*, 19(2):389–399, 1990.

BRENNEN, C. *Cavitation and Bubble Dynamics*. Oxford University Press, 1995.

BROCKMANN, J., REDDY, S., COUSSIOS, C. C., PIGOTT, D., GUIRRIERO, D., HUGHES, D., MOROVAT, A., ROY, D., WINTER, L., AND FRIEND, P. J. Normothermic perfusion: a new paradigm for organ preservation. *Annals of surgery*, 250(1):1–6, 2009.

BROOKES, M. AND DYSON, M. Stimulation of bone repair by ultrasound. *International Journal of Rehabilitation Research*, 8(3):73, 1985.

BROWN, J. M. AND GIACCIA, A. J. The unique physiology of solid tumors: opportunities (and problems) for cancer therapy. *Cancer research*, 58(7): 1408, 1998.

BURLEW, M. M., MADSEN, E. L., ZAGZEBSKI, J. A., BANJAVIC, R. A., AND SUM, S. W. A new ultrasound tissue-equivalent material. *Radiology*, 134(2):517–520, 1980.

BUTLER, A. J., REES, M. A., WIGHT, D. G. D., CASEY, N. D., ALEXANDER, G., WHITE, D. J. G., AND FRIEND, P. J. Successful extracorporeal porcine liver perfusion for 72 hr. *Transplantation*, 73(8): 1212–1218, 2002.

CAIRNS, R., PAPANDREOU, I., AND DENKO, N. Overcoming physiologic barriers to cancer treatment by molecularly targeting the tumor microenvironment. *Molecular cancer research*, 4(2):61, 2006.

CARPENEDO, L., CIUTI, P., FRANCESCUTTO, A., IERNETTI, G., AND JOHRI, G. K. Space-time interaction of two ultrasonic fields and sonoluminescence during transient cavitation in distilled water. *Acoustics letters*, 10(11):178–181, 1987.

CARUSO, F., CARUSO, R. A., AND MÖHWALD, H. Nanoengineering of inorganic and hybrid hollow spheres by colloidal templating. *Science*, 282(5391): 1111–1114, 1998.

CHURCH, C. C. Prediction of rectified diffusion during nonlinear bubble pulsations at biomedical frequencies. *The Journal of the Acoustical Society of America*, 83:2210, 1988.

CHURCH, C. C. Spontaneous homogeneous nucleation, inertial cavitation and the safety of diagnostic ultrasound. *Ultrasound in Medicine & Biology*, 28(10):1349–1364, 2002. ISSN 0301-5629.

COBB, W. N. Finite amplitude method for the determination of the acoustic nonlinearity parameter B/A. *The Journal of the Acoustical Society of America*, 73: 1525, 1983.

COLLIN, J. R. T. *Detection and interpretation of thermally relevant cavitation during HIFU exposure*. PhD thesis, University of Oxford, 2009.

COUSSIOS, C. C., FARNY, C. H., TER HAAR, G. R., AND ROY, R. A. Role of acoustic cavitation in the delivery and monitoring of cancer treatment by high-intensity focused ultrasound. *Int J Hyperthermia*, 23(2), 2007a.

COUSSIOS, C. C., COLLIN, J. R. T., AND MUCKLE, A. P. Non-invasive monitoring and control of inertial cavitation dynamics during HIFU exposure in vitro. *AIP Conference Proceedings*, 911(1):164–170, 2007b.

COUSSIOS, C. C. AND ROY, R. A. Applications of acoustics and cavitation to noninvasive therapy and drug delivery. *Annual Review of Fluid Mechanics*, 40(1), 2008.

COVIELLO, C. T., FARAGHER, S., AND COUSSIOS, C. C. Robust capon beamforming for passive cavitaton detecton during high intensity focused ultrasound therapy. In *The Journal of the Acoustical Society of America*, 2012.

CRUM, L. A. Nucleation and stabilization of microbubbles in liquids. *Applied Scientific Research*, 38(1):101–115, 1982.

CRUM, L. A. Acoustic cavitation series: V. rectified diffusion. *Ultrasonics*, 22(5):215–223, 1984.

CUI, H. AND YANG, X. In vivo imaging and treatment of solid tumor using integrated photoacoustic imaging and high intensity focused ultrasound system. *Medical physics*, 37:4777, 2010.

DAMIANOU, C., PAVLOU, M., VELEV, O., KYRIAKOU, K., AND TRIMIKLINIOTIS, M. High intensity focused ultrasound ablation of kidney guided by MRI. *Ultrasound in Medicine & Biology*, 30(3):397–404, 2004. ISSN 0301-5629.

DATTA, S., COUSSIOS, C. C., AMMI, A. Y., MAST, T. D., DE COURTEN-MYERS, G. M., AND HOLLAND, C. K. Ultrasound-enhanced thrombolysis using Definity as a cavitation nucleation agent. *Ultrasound in Medicine & Biology*, 34(9):1421–1433, 2008. ISSN 0301-5629.

DATTA, S., COUSSIOS, C. C., MCADORY, L. E., TAN, J., PORTER, T., DE COURTEN-MYERS, G., AND HOLLAND, C. K. Correlation of cavitation with ultrasound enhancement of thrombolysis. *Ultrasound in Medicine & Biology*, 32(8):1257–1267, August 2006.

DAYTON, P. A., MORGAN, K. E., KLIBANOV, A. L., BRANDENBURGER, G. H., AND FERRARA, K. W. Optical and acoustical observations of the effects of ultrasound on contrast agents. *Ultrasonics, Ferroelectrics and Frequency Control, IEEE Transactions on*, 46(1):220–232, 1999.

DE JONG, N., BOUAKAZ, A., AND FRINKING, P. Harmonic imaging for ultrasound contrast agents. In *Ultrasonics Symposium, 2000 IEEE*, volume 2, pages 1869–1876. IEEE, 2000.

DEL GROSSO, V. A. AND MADER, C. W. Speed of sound in pure water. *the Journal of the Acoustical Society of America*, 52:1442, 1972.

DESPA, F., ORGILL, D. P., NEUWALDER, J., AND LEE, R. C. The relative thermal stability of tissue macromolecules and cellular structure in burn injury. *Burns*, 31(5):568–577, 2005.

DIVERTIE, M. B. AND MCMICHAN, J. C. Continuous monitoring of mixed venous oxygen saturation. *CHEST Journal*, 85(3):423–428, 1984.

DROMI, S., FRENKEL, V., LUK, A., TRAUGHBER, B., ANGSTADT, M., BUR, M., POFF, J., XIE, J., LIBUTTI, S. K., LI, K. C. P., ET AL. Pulsed-high intensity focused ultrasound and low temperature–sensitive liposomes for enhanced targeted drug delivery and antitumor effect. *Clinical Cancer Research*, 13(9): 2722–2727, 2007.

DUCK, F. A. *Physical properties of tissue: a comprehensive reference book*. Academic Pr, 1990.

DUNN, F., LAW, W. K., AND FRIZZELL, L. A. Nonlinear ultrasonic wave propagation in biological materials. In *Ultrasonics Symposium Proceeding, Chicago, USA*, pages 527–532, 1981.

DUSSIK, K. T. Uber die moglichkeit hochfrequente mechanische schwingungen als diagnostisches hilfsmittel zu verwerten. *Zeitschrift für die gesamte Neurologie und Psychiatrie*, 174(1):153–168, December 1942.

DVORAK, H. F., NAGY, J. A., AND DVORAK, A. M. Structure of solid tumors and their vasculature: implications for therapy with monoclonal antibodies. *Cancer Cells*, 3(3):77–85, March 1991.

ELLER, A. I. AND CRUM, L. A. Instability of the motion of a pulsating bubble in a sound field. *The Journal of the Acoustical Society of America*, 47:762, 1970.

ELLIS, R. J. AND HARTL, F. U. Principles of protein folding in the cellular environment. *Current opinion in structural biology*, 9(1):102–110, 1999.

EPSTEIN, P. S. AND PLESSET, M. S. On the stability of gas bubbles in liquid-gas solutions. *The Journal of Chemical Physics*, 18(11):1505–1509, 1950.

FARAGHER, S. R. *Cavitational Methods for Characterising and Testing Clinical High-Intensity Focused Ultrasound Systems*. PhD thesis, University of Oxford, 2011.

FARNY, C. H., HOLT, R. G., AND ROY, R. A. The correlation between bubble-enhanced hifu heating and cavitation power. *Biomedical Engineering, IEEE Transactions on*, 57(1):175–84, 2010.

FARNY, C. H., WU, T., HOLT, R. G., MURRAY, T. W., AND ROY, R. A. Nucleating cavitation from laser-illuminated nano-particles. *Acoustics Research Letters Online*, 6(3):138–143, 2005.

FATEMI, M., MANDUCA, A., AND GREENLEAF, J. F. Imaging elastic properties of biological tissues by low-frequency harmonic vibration. *Proceedings of the IEEE DOI*, 91(10):1503–1519, 2003. ISSN 0018-9219.

FENG, R., ZHAO, Y., ZHU, C., AND MASON, T. J. Enhancement of ultrasonic cavitation yield by multi-frequency sonication. *Ultrasonics sonochemistry*, 9 (5):231–236, 2002.

FENG, Y., ODEN, J. T., AND RYLANDER, M. N. A two-state cell damage model under hyperthermic conditions: theory and in vitro experiments. *Journal of biomechanical engineering*, 130(4):041016, 2008.

FERRARA, K., POLLARD, R., AND BORDEN, M. Ultrasound microbubble contrast agents: fundamentals and application to gene and drug delivery. *Annu. Rev. Biomed. Eng.*, 9:415–447, 2007.

FINE, I. H., PACKER, M., AND HOFFMAN, R. S. Use of power modulations in phacoemulsification: Choo-choo chop and flip phacoemulsification. *Journal of Cataract & Refractive Surgery*, 27(2):188–197, 2001.

FIRESTONE, F. A. Flaw detecting device and measurement instrument, April 1942. US Patent App. 02/280,226.

FLYNN, H. G. Cavitation dynamics: II. free pulsations and models for cavitation bubbles. *The Journal of the Acoustical Society of America*, 58(6):1160–1170, 1975.

FORNAGE, B. D., JIN, X., XU, M., HUNT, K. K., AND WANG, L. V. Thermoacoustic and photoacoustic tomography of thick biological tissues toward breast imaging. *Technology in cancer research & treatment*, 4(5), 2005.

FRY, F. J., SANGHVI, N. T., MORRIS, R. F., SMITHSON, S., ATKINSON, L., DINES, K., FRANKLIN, T., AND HASTINGS, J. A focused ultrasound system for tissue volume ablation in deep seated brain sites. In *IEEE 1986 Ultrasonics Symposium*, pages 1001–1004. IEEE, 1986.

FUKUMURA, D. AND JAIN, R. K. Tumor microenvironment abnormalities: Causes, consequences, and strategies to normalize. *Journal of Cellular Biochemistry*, 101(4):937–949, 2007. ISSN 1097-4644.

GILL, R. W. Measurement of blood flow by ultrasound: accuracy and sources of error. *Ultrasound in medicine & biology*, 11(4):625–641, 1985.

GYONGY, M. *Passive Cavitation Mapping for Monitoring Ultrasound Therapy*. PhD thesis, University of Oxford, 2010.

GYONGY, M. AND COUSSIOS, C. C. Passive spatial mapping of inertial cavitation during HIFU exposure. *Biomedical Engineering, IEEE Transactions on DOI*, 57(1):48–56, 2010. ISSN 0018-9294.

HAMILTON, M. AND BLACKSTOCK, D., editors. *Nonlinear Acoustics*. Academic Press, 1998.

HANAHAN, D. AND WEINBERG, R. A. Hallmarks of cancer: the next generation. *Cell*, 144(5):646–674, 2011.

HARROP, G. A. The oxygen and carbon dioxide content of arterial and of venous blood in normal individuals and in patients with anemia and heart disease. *The Journal of experimental medicine*, 30(3): 241, 1919.

HARVEY, E. N., BARNES, D. K., MCELROY, W. D., WHITELEY, A. H., PEASE, D. C., AND COOPER, K. W. Bubble formation in animals. *Journal of cellular and comparative physiology*, 24(1):1–22, 1944.

HASHEMI, R. H. AND BRADLEY, W. G. *MRI: the basics*. Williams & Wilkins Baltimore, Md., 1997.

HECHER, K., CAMPBELL, S., DOYLE, P., HARRINGTON, K., AND NICOLAIDES, K. Assessment of fetal compromise by Doppler ultrasound investigation of the fetal circulation: arterial, intracardiac, and venous blood flow velocity studies. *Circulation*, 91(1):129, 1995.

HENLE, K. J. AND DETHLEFSEN, L. A. Time-temperature relationships for heat-induced relationships for heat-induced killing of mammalian cells. *Annals of the New York Academy of Sciences*, 335(1):234–253, 1980.

HILL, C. R., BAMBER, J. C., AND TER HAAR, G. R. *Physical Principles of Medical Ultrasonics*. John Wiley and Sons, Ltd, 2004.

HOCKHAM, N. A realtime controller for sustaining thermally relevant cavitation during ultrasound therapy. Master's thesis, Department of Engineering Science, Oxford University, June 2009.

HOCKHAM, N., COUSSIOS, C. C., AND ARORA, M. A real-time controller for sustaining thermally relevant acoustic cavitation during ultrasound therapy. *Ultrasonics, Ferroelectrics and Frequency Control, IEEE Transactions on*, 57(12):2685–2694, 2010. ISSN 0885-3010.

HOLLAND, C. K., DENG, C. X., APFEL, R. E., ALDERMAN, J. L., FERNANDEZ, L. A., AND TAYLOR, K. J. W. Direct evidence of cavitation in vivo from diagnostic ultrasound. *Ultrasound in Medicine & Biology*, 22(7):917–925, 1996. ISSN 0301-5629.

HOLROYD, D., MYLONOPOULOU, E., CHOI, J., CHUNG, D., JENSEN, C., FRIEND, P. J., AND COUSSIOS, C. C. Effects of perfusion on thermal and cavitational characteristics of HIFU therapy using a

novel normothermic, extracorporeal liver perfusion model. In *International Society for Therapeutic Ultrasound*, 2012.

HOLT, R. G. AND ROY, R. A. *Bubble and Particle Dynamics in Acoustic Fields: Modern Trends and Applications*, chapter Bubble dynamics in therapeutic ultrasound, pages 108–229. Research Signpost, 2006.

HOLT, R. G., ROY, R. A., THOMAS, C. R., FARNY, C., WU, T., YANG, X., AND EDSON, P. Therapeutic bubbles: Basic principles of cavitation in therapeutic ultrasound. In *AIP Conference Proceedings*, volume 829, page 13, 2006.

HOLT, R. G. AND ROY, R. A. Measurements of bubble-enhanced heating from focused, MHz-frequency ultrasound in a tissue-mimicking material. *Ultrasound in Medicine & Biology*, 27(10):1399–1412, October 2001. ISSN 0301-5629.

HORNAK, J. P. *The basics of MRI*. 1996.

HYNYNEN, K. The role of nonlinear ultrasound propagation during hyperthermia treatments. *Medical Physics*, 18(6):1156–1163, 1991a.

HYNYNEN, K. The threshold for thermally significant cavitation in dog's thigh muscle in vivo. *Ultrasound in Medicine & Biology*, 17(2):157–169, 1991b.

HYNYNEN, K., POMEROY, O., SMITH, D. N., HUBER, P. E., MCDANNOLD, N. J., KETTENBACH, J., BAUM, J., SINGER, S., AND JOLESZ, F. A. MR imaging-guided focused ultrasound surgery of fibroadenomas in the breast: A feasibility study. *Radiology*, 219 (1):176–185, 2001.

IERNETTI, G., CIUTI, P., DEZHKUNOV, N. V., REALI, M., FRANCESCUTTO, A., AND JOHRI, G. K. Enhancement of high-frequency acoustic cavitation effects by a low-frequency stimulation. *Ultrasonics sonochemistry*, 4(3):263–268, 1997.

ILLING, R., KENNEDY, J., WU, F., TER HAAR, G., PROTHEROE, A., FRIEND, P., GLEESON, F., CRANSTON, D., PHILLIPS, R., AND MIDDLETON, M. The safety and feasibility of extracorporeal high-intensity focused ultrasound (HIFU) for the treatment of liver and kidney tumours in a western population. *British journal of cancer*, 93(8):890–895, 2005.

ILYICHEV, V. I., KORETZ, V. L., AND MELNIKOV, N. P. Spectral characteristics of acoustic cavitation. *Ultrasonics*, 27(6):357–361, 1989. ISSN 0041-624X.

JAIN, R. K. Normalizing tumor vasculature with anti-angiogenic therapy: a new paradigm for combination therapy. *Nature medicine*, 7(9):987–989, 2001.

JAMIESON, R. W., ZILVETTI, M., ROY, D., HUGHES, D., MOROVAT, A., COUSSIOS, C. C., AND FRIEND, P. J. Hepatic steatosis and normothermic perfusion - preliminary experiments in a porcine model. *Transplantation*, 92(3):289–295, 2011.

JENSEN, C. R., RITCHIE, R. W., GYONGY, M., COLLIN, J. R. T., LESLIE, T., AND COUSSIOS, C. C. Spatiotemporal monitoring of high-intensity focused ultrasound therapy with passive acoustic mapping. *Radiology*, 2011.

JOLESZ, F. A. MRI-guided focused ultrasound surgery. *Medicine*, 60(1):417, 2009.

KABALNOV, A., KLEIN, D., PELURA, T., SCHUTT, E., AND WEERS, J. Dissolution of multicomponent microbubbles in the bloodstream: Theory. *Ultrasound in medicine & biology*, 24(5):739–749, 1998.

KAYE, G. W. C. AND LABY, T. H. *Tables of physical and chemical constants and some mathematical functions*. Longmans, Green and co., 1921.

KENNEDY, J. E., WU, F., TER HAAR, G. R., GLEESON, F. V., PHILLIPS, R. R., MIDDLETON, M. R., AND CRANSTON, D. High-intensity focused ultrasound for the treatment of liver tumours. *Ultrasonics*, 42 (1):931–935, 2004.

KENNEDY, J. E. High-intensity focused ultrasound in the treatment of solid tumours. *Nat Rev Cancer*, 5 (4):321–327, April 2005. ISSN 1474-175X.

KENNEDY, P., ARORA, M., AND COUSSIOS, C. C. Localization and interpretation of bubble activity during HIFU exposure. volume 1113, pages 68–72. AIP, 2009.

KNUDSON, A. G. Mutation and cancer: statistical study of retinoblastoma. *Proceedings of the National Academy of Sciences*, 68(4):820, 1971.

KRIPFGANS, O. D., ORIFICI, C. M., CARSON, P. L., IVES, K. A., ELDEVIK, O. P., AND FOWLKES, J. B. Acoustic droplet vaporization for temporal and spatial control of tissue occlusion: A kidney study. *Ultrasonics, Ferroelectrics and Frequency Control, IEEE Transactions on*, 52(7):1101–1110, 2005.

KRUGER, R. A., MILLER, K. D., REYNOLDS, H. E., KISER, W. L., REINECKE, D. R., AND KRUGER, G. A. Breast cancer in vivo: Contrast enhancement with

thermoacoustic ct at 434 mhz - feasibility study 1. *Radiology*, 216(1):279–283, 2000.

KRUGER, R. A., REINECKE, D. R., AND KRUGER, G. A. Thermoacoustic computed tomography - technical considerations. *Medical Physics*, 26:1832, 1999.

KUMAR, R., ABBAS, A., FAUSTO, N., AND ASTER, J., editors. *Robins and Cotran Pathologic Basis of Disease*. Saunders Elsevier, 8th edition, 2010.

LAFON, C., KACZKOWSKI, P. J., VAEZY, S., NOBLE, M., AND SAPOZHNIKOV, O. A. Development and characterization of an innovative synthetic tissue-mimicking material for high intensity focused ultrasound (HIFU) exposures. In *IEEE Ultrasonics Symposium*, pages 1295–1298. IEEE, IEEE, 2001.

LAFON, C., ZDERIC, V., NOBLE, M. L., YUEN, J. C., KACZKOWSKI, P. J., SAPOZHNIKOV, O. A., CHAVRIER, F., CRUM, L. A., AND VAEZY, S. Gel phantom for use in high-intensity focused ultrasound dosimetry. *Ultrasound in Medicine & Biology*, 10:1383–1389, 2005.

LAO, Y., XING, D., YANG, S., AND XIANG, L. Noninvasive photoacoustic imaging of the developing vasculature during early tumor growth. *Physics in medicine and biology*, 53(15):4203, 2008.

LAUTERBORN, W. AND CRAMER, E. Subharmonic route to chaos observed in acoustics. *Physical Review Letters*, 47(20):1445–1448, 1981.

LAW, W. K., FRIZZELL, L. A., AND DUNN, F. Determination of the nonlinearity parameter B/A of biological media. *Ultrasound in medicine & biology*, 11 (2):307–318, 1985.

LAW, W., FRIZZELL, L., AND DUNN, F. Comparison of thermodynamic and finite amplitude methods of B/A measurement in biological materials. *The Journal of the Acoustical Society of America*, 74:1295, 1983.

LE BIHAN, D. Looking into the functional architecture of the brain with diffusion MRI. *Nature Reviews Neuroscience*, 4(6):469–480, 2003.

LEIGHTON, T. G. *The Acoustic Bubble*. Academic Press, 1994.

LESSER, G. T., PERL, W., AND STEELE, J. M. Determination of total body fat by absorption of an inert gas; measurements and results in normal human subjects. *Journal of Clinical Investigation*, 39(12): 1791, 1960.

LINDNER, J. R. Microbubbles in medical imaging: current applications and future directions. *Nature Reviews Drug Discovery*, 3(6):527–533, 2004.

LINGEMAN, J. E., NEWMAN, D., MERTZ, J. H., MOSBAUGH, P. G., STEELE, R. E., KAHNOSKI, R. J., COURY, T. A., AND WOODS, J. R. Extracorporeal shock wave lithotripsy: the Methodist Hospital of Indiana experience. *J Urol*, 135(6):1134–1137, Jun 1986.

LIZZI, F. L., COLEMAN, D. J., DRILLER, J., SILVERMAN, R., LUCAS, B., AND ROSADO, A. A therapeutic ultrasound system incorporating real-time ultrasonic scanning. In *IEEE 1986 Ultrasonics Symposium*, pages 981–984. IEEE, 1986.

LUDWIG, G. D. Considerations underlying the use of ultrasound to detect gallstones and foreign bodies in tissue. *Bethesda, Md, Naval Medical Research Institute*, 1949.

LUO, W., ZHOU, X., REN, X., ZHENG, M., ZHANG, J., AND HE, G. Enhancing effects of Sonovue, a microbubble sonographic contrast agent, on high-intensity focused ultrasound ablation in rabbit livers in vivo. *Journal of ultrasound in medicine*, 26 (4):469–476, 2007.

LYKA, E. Real-time 3-D passive mapping of inertial cavitation during HIFU therapy. Master's thesis, University of Oxford, 2012.

LYNN, J. G., ZWEMER, R. L., CHICK, A. J., AND MILLER, A. E. A new method for the generation and use of focused ultrasound in experimental biology. *The journal of general physiology*, 26(2):179, 1942.

MADAAN, S. AND JOYCE, A. D. Limitations of extracorporeal shock wave lithotripsy. *Current Opinion in Urology*, 17(2):109, 2007.

MALEKE, C. AND KONOFAGOU, E. E. Harmonic motion imaging for focused ultrasound (HMIFU): a fully integrated technique for sonication and monitoring of thermal ablation in tissues. *Physics in medicine and biology*, 53(6):1773, 2008.

MANDELIS, A. *Principles and perspectives of photothermal and photoacoustic phenomena*. Elsevier New York, 1992.

MCWILLIAM, D. AND DUGGINS, R. K. Speed of sound in bubbly liquids. In *Proceedings of the Institution of Mechanical Engineers, Conference Proceedings*, volume 184, pages 102–107. SAGE Publications, 1969.

MEAIRS, S. AND ALONSO, A. Ultrasound, microbubbles and the blood-brain barrier. *Progress in biophysics and molecular biology*, 93(1):354–362, 2007.

MILLER, D. L. AND THOMAS, R. M. Ultrasound contrast agents nucleate inertial cavitation in vitro. *Ultrasound in medicine & biology*, 21(8):1059–1065, 1995.

MILLER, M. J. Tissue oxygenation in clinical medicine an historical review. *Anesthesia & Analgesia*, 61(6): 527–535, 1982.

MILLER, N. R., BAMBER, J. C., AND TER HAAR, G. R. Imaging of temperature-induced echo strain: preliminary in vitro study to assess feasibility for guiding focused ultrasound surgery. *Ultrasound in medicine & biology*, 30(3):345–356, 2004.

MILLS, A. F. A. *Basic heat and mass transfer*, volume 2. Prentice hall Upper Saddler River, NJ, 1999.

MINNAERT, M. On musical air-bubbles and the sounds of running water. *The London, Edinburgh, and Dublin Philosophical Magazine and Journal of Science*, 16(104):235–248, 1933.

MIRONOV, V., PRESTWICH, G., AND FORGACS, G. Bioprinting living structures. *J. Mater. Chem.*, 17(20): 2054–2060, 2007.

MITRAGOTRI, S. Healing sound: the use of ultrasound in drug delivery and other therapeutic applications. *Nature Reviews Drug Discovery*, 4(3):255–260, 2005.

MOLINARI, M. *Mechanical fractionation of the intervertebral disc*. PhD thesis, University of Oxford, 2012.

MORGAN, K. E., ALLEN, J. S., DAYTON, P. A., CHOMAS, J. E., KLIBAOV, A. L., AND FERRARA, K. W. Experimental and theoretical evaluation of microbubble behavior: Effect of transmitted phase and bubble size. *Ultrasonics, Ferroelectrics and Frequency Control, IEEE Transactions on*, 47(6):1494–1509, 2000.

MULDER, W. J. M., STRIJKERS, G. J., VAN TILBORG, G. A. F., GRIFFIOEN, A. W., AND NICOLAY, K. Lipid-based nanoparticles for contrast-enhanced MRI and molecular imaging. *NMR in Biomedicine*, 19 (1):142–164, 2006.

MYLONOPOULOU, E., ARVANITISA, C. D., BAZAN-PEREGRINOA, M., ARORA, M., AND COUSSIOS, C. C. Ultrasonic activation of thermally sensitive liposomes. In *AIP Conference Proceedings*, volume 1215, page 83, 2010.

NANDLALL, S. D., JACKSON, E., AND COUSSIOS, C. C. Real-time passive acoustic monitoring of hifu-induced tissue damage. *Ultrasound in medicine & biology*, 37(6):922–934, 2011.

NASONI, R. L., BOWEN, T., CONNOR, W. G., AND SHOLES, R. R. In vivo temperature dependence of ultrasound speed in tissue and its application to noninvasive temperature monitoring. *Ultrasonic Imaging*, 1(1):34–43, 1979.

O'NEIL, H. T. Theory of focusing radiators. *The Journal of the Acoustical Society of America*, 21(5):516–526, 1949.

OWEN, J., PANKHURST, Q., AND STRIDE, E. Magnetic targeting and ultrasound mediated drug delivery: Benefits, limitations and combination. *International Journal of Hyperthermia*, 28(4):362–373, 2012.

OXTOBY, D. W. Materials chemistry: Crystals in a flash. *Nature*, 420(6913):277–278, 2002.

PENNES, H. H. Analysis of tissue and arterial blood temperatures in the resting human forearm. *Journal of applied physiology*, 1(2):93–122, 1948.

PETERSON, T. M. AND SIEGEL, R. J. Ultrasound enhanced chemotherapy, November 1998. US Patent App. 09/189,608.

PIERCE, A. D. *Acoustics, An introduction to its physical principles and applications*. McGraw-Hill Book Company, 1981.

PLESSET, M. S. On the stability of fluid flows with spherical symmetry. *Journal of Applied Physics*, 25 (1):96–98, 1954.

PLESSET, M. S. AND PROSPERETTI, A. Bubble dynamics and cavitation. *Annual Review of Fluid Mechanics*, 9(1):145–185, 1977.

PLESSET, M. S. AND SADHAL, S. S. On the stability of gas bubbles in liquid-gas solutions. *Applied Scientific Research*, 38(1):133–141, 1982.

POWELL, M. R. Mechanism and detection of decompression sickness. Technical report, DTIC Document, 1971.

PROSPERETTI, A. On the stability of spherically symmetric flows. *Atti Accad. Naz. Lincei, Cl. Sci. Fis. Mat. Nat. Rend*, 62:196, 1977.

RABKIN, B. A., ZDERIC, V., CRUM, L. A., AND VAEZY, S. Biological and physical mechanisms of HIFU-induced hyperecho in ultrasound images. *Ultrasound in Medicine & Biology*, 32(11):1721–1729, November 2006. ISSN 0301-5629.

RABKIN, B. A., ZDERIC, V., AND VAEZY, S. Hyperecho in ultrasound images of hifu therapy: Involvement of cavitation, 2005. ISSN 0301-5629.

RAGAZ, J., JACKSON, S. M., LE, N., PLENDERLEITH, I. H., SPINELLI, J. J., BASCO, V. E., WILSON, K. S., KNOWLING, M. A., COPPIN, C. M. L., AND PARADIS, M. Adjuvant radiotherapy and chemotherapy in node-positive premenopausal women with breast cancer. *New England Journal of Medicine-Unbound Volume*, 337(14):956–962, 1997.

RAPOPORT, N. Y., KENNEDY, A. M., SHEA, J. E., SCAIFE, C. L., AND NAM, K. H. Controlled and targeted tumor chemotherapy by ultrasound-activated nanoemulsions/microbubbles. *Journal of Controlled Release*, 138(3):268–276, 2009.

RIFAI, B., ARVANITIS, C. D., BAZAN-PEREGRINO, M., AND COUSSIOS, C. C. Cavitation-enhanced delivery of macromolecules into an obstructed vessel. *The Journal of the Acoustical Society of America*, 128 (5):EL310–EL315, 2010.

RILEY, R. L., COURNAND, A., AND DONALD, K. W. Analysis of factors affecting partial pressures of oxygen and carbon dioxide in gas and blood of lungs: methods. *Journal of applied physiology*, 4 (2):102–120, 1951.

RITCHIE, R. W., LESLIE, T., PHILLIPS, R., WU, F., ILLING, R., TER HAAR, G. R., PROTHEROE, A., AND CRANSTON, D. Extracorporeal high intensity focused ultrasound for renal tumours: a 3-year follow-up. *BJU international*, 106(7):1004–1009, 2010.

RIVENS, I., SHAW, A., CIVALE, J., AND MORRIS, H. Treatment monitoring and thermometry for therapeutic focused ultrasound. *International Journal of Hyperthermia*, 23(2):121–139, 2007.

ROSENCWAIG, A. *Photoacoustics and photoacoustic spectroscopy*. Wiley, 1980.

ROTH, J. A., FOSSELLA, F., KOMAKI, R., RYAN, M. B., PUTNAM, J. B., LEE, J. S., DHINGRA, H., DE CARO, L., CHASEN, M., AND MCGAVRAN, M. A randomized trial comparing perioperative chemotherapy and surgery with surgery alone in resectable stage IIIA non-small-cell lung cancer. *Journal of the National Cancer Institute*, 86(9):673, 1994.

SAPARETO, S. A. AND DEWEY, W. C. Thermal dose determination in cancer therapy. *International Journal of Radiation Oncology/Biology/Physics*, 10(6): 787–800, 1984. ISSN 0360-3016.

SEITZ, F. On the theory of the bubble chamber. *Physics of fluids*, 1:2, 1958.

SIMON, C., VANBAREN, P., AND EBBINI, E. S. Two-dimensional temperature estimation using diagnostic ultrasound. *Ultrasonics, Ferroelectrics and Frequency Control, IEEE Transactions on*, 45(4): 1088–1099, 1998.

SINKUS, R., LORENZEN, J., SCHRADER, D., LORENZEN, M., DARGATZ, M., AND HOLZ, D. High-resolution tensor MR elastography for breast tumour detection. *Physics in Medicine and Biology*, 45:1649, 2000.

SOCIETY, A. C. *Cancer facts & figures*. The Society, 2008.

SOUCHON, R., BOUCHOUX, G., MACIEJKO, E., LAFON, C., CATHIGNOL, D., BERTRAND, M., AND CHAPELON, J. Y. Monitoring the formation of thermal lesions with heat-induced echo-strain imaging: A feasibility study. *Ultrasound in medicine & biology*, 31(2):251–259, 2005.

SOUCHON, R., ROUVIÈRE, O., GELET, A., DETTI, V., SRINIVASAN, S., OPHIR, J., AND CHAPELON, J. Y. Visualisation of HIFU lesions using elastography of the human prostate in vivo: preliminary results. *Ultrasound in medicine & biology*, 29(7):1007–1015, 2003.

STADTMAUER, E. A., O'NEILL, A., GOLDSTEIN, L. J., CRILLEY, P. A., MANGAN, K. F., INGLE, J. N., BRODSKY, I., MARTINO, S., LAZARUS, H. M., AND ERBAN, J. K. Conventional-dose chemotherapy compared with high-dose chemotherapy plus autologous hematopoietic stem-cell transplantation for metastatic breast cancer. *cancer*, 342:1069–76, 2000.

STEINER, H., STAUDACH, A., SPITZER, D., AND SCHAFER, H. Diagnostic techniques: Three-dimensional ultrasound in obstetrics and gynaecology: technique, possibilities and limitations. *Human Reproduction*, 9(9):1773, 1994.

STOLZ, E. P. AND KAPS, M. Ultrasound contrast agents and imaging of cerebrovascular disease. In *Seminars in Cerebrovascular Diseases and Stroke*, volume 5, pages 111–131. Elsevier, 2005.

STRIDE, E., OWEN, J., MULVANA, H., PANKHURST, Q., TANG, M., AND ECKERSLEY, R. Magnetic microbubbles for localised imaging and drug delivery: Development, characterisation and preliminary application in vivo. *J Acoust Soc Am*, 131(4):3245, 2012.

SZABO, T. L. *Diagnostic Ultrasound Imaging*. Elsevier Academic Press, 2004.

TALMADGE, J. E. AND FIDLER, I. J. AACR centennial series: the biology of cancer metastasis: historical perspective. *Cancer research*, 70(14):5649, 2010.

TANNOCK, I. *The basic science of oncology*. McGraw-Hill Professional, 2005.

TECHAVIPOO, U., VARGHESE, T., CHEN, Q., STILES, T. A., ZAGZEBSKI, J. A., AND FRANK, G. R. Temperature dependence of ultrasonic propagation speed and attenuation in excised canine liver tissue measured using transmitted and reflected pulses. *The Journal of the Acoustical Society of America*, 115: 2859, 2004.

TER HAAR, G. R. Ultrasound focal beam surgery. *Ultrasound in Medicine & Biology*, 21(9):1089 – 1100, 1995. ISSN 0301-5629.

TER HAAR, G. R. Ultrasound-guided high intensity focused ultrasound therapy - safety concerns from a clinical perspective. *The Journal of the Acoustical Society of America*, 125(4):2741–2741, 2009.

TER HAAR, G. R. AND COUSSIOS, C. C. High intensity focused ultrasound: Physical principles and devices. *International Journal of Hyperthermia*, 23 (2):89–104, 2007. ISSN 0265-6736.

TER HAAR, G. R. AND DANIELS, S. Evidence for ultrasonically induced cavitation in vivo. *Physics in medicine and biology*, 26:1145, 1981.

THOMAS, C., FARNY, C., COUSSIOS, C., ROY, R., AND HOLT, R. Dynamics and control of cavitation during high-intensity focused ultrasound application. *Acoustics Research Letters Online*, 6:182, 2005.

THOMLINSON, R. H. AND GRAY, L. H. The histological structure of some human lung cancers and the possible implications for radiotherapy. *British Journal of Cancer*, 9(4):539, 1955.

THÜROFF, S., CHAUSSY, C., VALLANCIEN, G., WIELAND, W., KIEL, H. J., LE DUC, A., DESGRANDCHAMPS, F., DE LA ROSETTE, J. J., AND GELET, A. High-intensity focused ultrasound and localized prostate cancer: efficacy results from the european multicentric study. *Journal of Endourology*, 17(8):673–677, 2003.

TRAN, B. C., SEO, J., HALL, T. L., FOWLKES, J. B., AND CAIN, C. A. Microbubble-enhanced cavitation for noninvasive ultrasound surgery. *Ultrasonics, Ferroelectrics and Frequency Control, IEEE Transactions on*, 50(10):1296–1304, 2003.

TUCH, D. S. *Diffusion MRI of complex tissue structure*. PhD thesis, Massachusetts Institute of Technology, 2002.

VAEZY, S., ANDREW, M., KACZKOWSKI, P., AND CRUM, L. A. Image-guided acoustic therapy. *Annual review of biomedical engineering*, 3(1):375–390, 2001.

VAEZY, S., MARTIN, R., YAZIJI, H., KACZKOWSKI, P., KEILMAN, G., CARTER, S., CAPS, M., CHI, E. Y., BAILEY, M., AND CRUM, L. A. Hemostasis of punctured blood vessels using high-intensity focused ultrasound. *Ultrasound in medicine & biology*, 24(6): 903–910, 1998.

VAUPEL, P., KALLINOWSKI, F., AND OKUNIEFF, P. Blood flow, oxygen and nutrient supply, and metabolic microenvironment of human tumors: a review. *Cancer research*, 49(23):6449, 1989.

WAGSTAFFE, S. J., ARORA, M., COUSSIOS, C. C., AND SCHIFFTER, H. A. Sonosensitive nanoparticle formulations for cavitation-mediated ultrasonic enhancement of local drug delivery. *Materials Research Society Symposium Proceedings*, 1316, 2011.

WEBB, I. R., ARORA, M., ROY, R. A., PAYNE, S. J., AND COUSSIOS, C. C. Dynamics of gas bubbles in time-variant temperature fields. *Journal of Fluid Mechanics*, 663:209–232, 2010.

WEBB, I. R., PAYNE, S. J., AND COUSSIOS, C. C. Effect of temperature on rectified diffusion during ultrasound-induced heating. *The Journal of the Acoustical Society of America*, 130(5):3450–3457, 2011.

WEBER, S. M. AND LEE, F. T. Expanded treatment of hepatic tumors with radiofrequency ablation and cryoablation. *Oncology*, 19(11):27–32, 2005.

WEISSLEDER, R., ROSS, B. D., REHEMTULLA, A., AND GAMBHIR, S. S. *Molecular imaging: principles and practice*. Pmph USA Ltd, 2010.

WU, F., CHEN, W. Z., BAI, J., ZOU, J. Z., WANG, Z. L., ZHU, H., AND WANG, Z. B. Pathological changes in human malignant carcinoma treated

with high-intensity focused ultrasound. *Ultrasound in Medicine & Biology*, 27(8):1099–1106, August 2001a. ISSN 0301-5629.

WU, F., WANG, Z. B., CHEN, W. Z., WANG, W., GUI, Y., ZHANG, M., ZHENG, G., ZHOU, Y., XU, G., LI, M., ZHANG, C., YE, H., AND FENG, R. Extracorporeal high intensity focused ultrasound ablation in the treatment of 1038 patients with solid carcinomas in China: an overview. *Ultrasonics Sonochemistry*, 11(3-4):149–154, 2004. ISSN 1350-4177. 4th Conference on the Applications of Power Ultrasound in Physical and Chemical Processing.

WU, J. AND NYBORG, W. L. M. *Emerging therapeutic ultrasound*. World Scientific Pub Co Inc., 2006.

WU, T., FELMLEE, J. P., GREENLEAF, J. F., RIEDERER, S. J., AND EHMAN, R. L. Assessment of thermal tissue ablation with MR elastography. *Magnetic resonance in medicine*, 45(1):80–87, 2001b.

XU, M. AND WANG, L. V. Photoacoustic imaging in biomedicine. *Review of scientific instruments*, 77 (4):041101–041101, 2006.

YANG, X., ROY, R. A., AND HOLT, R. G. Bubble dynamics and size distributions during focused ultrasound insonation. *The Journal of the Acoustical Society of America*, 116:3423, 2004.

YANG, X. AND CHURCH, C. C. A model for the dynamics of gas bubbles in soft tissue. *The Journal of the Acoustical Society of America*, 118(6):3595–3606, 2005.

ZHANG, M., FABIILLI, M. L., HAWORTH, K. J., PADILLA, F., SWANSON, S. D., KRIPFGANS, O. D., CARSON, P. L., AND FOWLKES, J. B. Acoustic droplet vaporization for enhancement of thermal ablation by high intensity focused ultrasound. *Academic radiology*, 2011.

ZHANG, P. AND PORTER, T. An in vitro study of a phase-shift nanoemulsion: A potential nucleation agent for bubble-enhanced HIFU tumor ablation. *Ultrasound in medicine & biology*, 36(11):1856–1866, 2010.

ZHU, Z., ROOS, M. S., COBB, W. N., AND JENSEN, K. Determination of the acoustic nonlinearity parameter B/A from phase measurements. *The Journal of the Acoustical Society of America*, 74:1518, 1983.